

THE UNIVERSITY OF HULL

Fabrication of Novel Sensors from Nanomaterials

being a Thesis submitted for the Degree of
in the University of Hull

by

William Richard Small, MChem

January 2009

Abstract

This thesis describes the fabrication and characterisation of novel sensors from nanomaterials. These are materials that have at least one length scale in the nanometre region, and in many cases they exhibit fascinating electrical, mechanical or optical properties due to their small size. While their small size makes them candidates for miniaturising macro-scale technologies, many researchers are concerned with exploiting their unique properties in larger scale applications. These might include strong, lightweight building materials based on their mechanical properties, or visual displays based on their electrical and/or optical properties. To achieve transfer of the properties from the nano-scale to the macro-scale however is not straight forward, and there are a number of obstacles that must be overcome. One obstacle is that of processing the nanomaterials, ensuring that their properties do not become lost when they are incorporated into bulk materials or composites due to aggregation or poor interactions with their host matrix. This obstacle will also be addressed in the thesis, as we fabricate and characterise composites incorporating nanomaterials, and develop methods to process these materials into novel sensors.

The synthesis and characterisation of a number of different composites has been achieved, incorporating either carbon nanotubes or silver nanowires as the nanomaterials of interest. These have been fabricated using either mixing or *in situ* polymerisation routes, with surfactants, polysaccharides or conducting polymers as the dispersant. The composites are all soluble in either water or organic solvents to give stable dispersions, and show interesting properties including optical activity, high loading fractions of the nanomaterials and electrochromic behaviour.

The methods that we have developed for processing the dispersions are drop deposition, inkjet printing and dielectrophoretic assembly. Drop deposition has been performed as it forms the basis of numerous solution-based processing techniques, and we have investigated specifically the effects of substrate hydrophobicity and the effect of aggregates in the dispersion on the resulting composite films that are formed. We have reported for the first time the inkjet printing of single wall carbon nanotubes, and have printed composite films that show good transparency and high conductivity. A novel method for arresting the structures formed through dielectrophoretic assembly

within a gel solution has also been developed. This has led to the fabrication of electrically anisotropic gels, and free-standing ‘strings’ of yeast cells.

Novel sensors have been fabricated through two of our processing methods. Thin films containing carbon nanotubes have been inkjet printed, and show sensitivity to water vapour (with gellan gum as the composite material) and alcohol vapour (with a water soluble conducting polymer as the composite material). A sensor based on biotin-functionalised silver nanowires assembled into a microwire and encapsulated within agarose gel has also been fabricated. This sensor showed sensitivity to streptavidin when the response was measured parallel to the formed microwire, but gave a much lower signal when the response was measured perpendicular to the microwire. This provides a proof of concept that a whole range of biosensors based on assembled silver nanowires into an anisotropic gel can be produced by employing an antigen-antibody strategy, similar to the one shown for biotin-streptavidin.

Acknowledgements

I would like to thank my supervisors, Dr Vesko Paunov and Dr Marc in het Panhuis for their encouragement, guidance, excellent supervision and seemingly never ending stream of ideas!

I would like to thank Dr Wolfgang Maser, Dr Ana Benito, Dr Raquel Sainz and everybody else at the Instituto de Carboquímica, Zaragoza, Spain. I would also like to thank Professor Gordon Wallace, Dr Fatemeh Masdarolomoor and everybody else at the Intelligent Polymer Research Institute (IPRI), University of Wollongong, Australia.

I am grateful to the EPSRC for funding this PhD. The Royal Society is thanked for financial support towards the visits to the Instituto de Carboquímica. I also thank the Australian Research Council Centre of Excellence for Electromaterials Science for funding the visit to the IPRI.

I would like to thank those that have contributed work to this thesis (University of Hull, unless otherwise stated); Dr Carol Lynam (IPRI) and Mrs Janice Haller for TEM images, Dr Joachim Loos (Eindhoven University of Technology, Netherlands) for SEM images and Dr Chris Walton for scanning white light interferometry. Dr Khue Tian Lai is thanked for his assistance with setting up electrical equipment.

I am grateful for the help and support of all my friends and colleagues in the Surfactant and Colloid Group, past and present, for making my time there so enjoyable. Particular thanks must go to Andy, selflessly sacrificing his own studies (!) to join me on regular breaks for fried breakfasts, pool, beer and crisps.

Finally, without the continued love and support of my parents, Richard and Ann, I would not have been able to achieve any of this. Thank you for everything. Regular coffee intervals, physiotherapy and general advice in all matters are greatly appreciated from my sister, Katie, a true hero of mine. Last but not least I thank my partner, Louise, because she's special.

Publications and presentations

The work contained in this thesis has given rise to the following publications and presentations:

- 1 *Carbon nanotube network formation from an evaporating sessile drop*, W. R. Small, C. D. Walton, J. Loos and M. in het Panhuis, *J. Phys. Chem. B*, **2006**, *110*, 13029.
- 2 *Synthesis and properties of optically active polyaniline carbon nanotube composites*, R. Sainz, W. R. Small, N. A. Young, C. Vallés, A. M. Benito, W. K. Maser and M. in het Panhuis, *Macromol.*, **2006**, *39*, 7324.
- 3 *Inkjet printed water sensitive transparent films from natural gum-carbon nanotube composites*, M. in het Panhuis, A. Heurtematte, W. R. Small and V. N. Paunov, *Soft Matter*, **2007**, *3*, 840.
- 4 *Inkjet printing of transparent, electrically conducting single-walled carbon-nanotube composites*, W. R. Small and M. in het Panhuis, *Small*, **2007**, *3*, 1500.
- 5 *Inkjet deposition and characterization of transparent conducting electroactive polyaniline composite films with a high carbon nanotube loading fraction*, W. R. Small, F. Masdarolomoor, G. G. Wallace and M. in het Panhuis, *J. Mater. Chem.*, **2007**, *17*, 4359.
- 6 *Fabrication of electrically anisotropic agarose gels by dielectrophoretic assembly and encapsulation of silver nanowires*, W. R. Small and V. N. Paunov, *J. Mater. Chem.*, **2008**, *18*, 2082.
- 7 Conference proceedings *Inkjet printing: a viable tool for processing polymer carbon nanotube composites*, M. in het Panhuis and W. R. Small, *SPIE Conf. Proc.*, **2008**, *6800*, 80007.
- 8 Poster presentation “*Soluble and optically active polyaniline-carbon nanotube composite*” at the 3rd NanoSpain Workshop, Pamplona, Spain, 20th - 23rd March 2006.
- 9 Poster presentation “*Inkjet printing PMAS/Pan/MWNT composite*” at the ACES Electromaterials Science Symposium, University of Wollongong, Australia, 7th - 9th February 2007.

10 Oral presentation “*The design and fabrication of novel nanomaterials*” at the Hull University Research Colloquia, Department of Chemistry, University of Hull, Hull, UK, 16th June 2008.

List of abbreviations

The following is a list of the abbreviations that can be found throughout this thesis.

AC	Alternating current
An	Aniline
APS	Ammonium persulphate
CD	Circular dichroism
CMC	Critical micelle concentration
CMCell	Carboxymethylcellulose
CNTs	Carbon nanotubes
CNTFET	Carbon nanotube field effect transistor
CSA	Camphorsulfonic acid
CTAB	Cetyltremethyl ammonium bromide
CVD	Chemical vapour deposition
DC	Direct current
DEP	Dielectrophoresis
DMSO	Dimethyl sulfoxide
DNA	Deoxyribonucleic acid
DWNT	Double wall carbon nanotube
FDA	Fluorescein diacetate
FET	Field effect transistor
GG	Gellan gum
HE	Hydroxyethyl
HiPco	High pressure decomposition of carbon monoxide
IPRI	Intelligent Polymer Research Institute
ITO	Indium tin oxide
<i>I-V</i>	Current-voltage
LbL	Layer-by-layer
MAS	3-amino-4-methoxy benzenesulfonic acid
MWNT	Multi wall carbon nanotube
NWs	Nanowires

OLEDs	Organic light emitting diodes
OTS	Octadecyltrichlorosilane
PAH	Polyallylamine hydrochloride
PAni	Polyaniline
PDMS	Polydimethyl siloxane
PET	Poly(ethylene terephthalate)
PMAS	Poly(2-methoxyaniline-5-sulfonic acid)
PTFE	Polytetrafluoroethylene
PVA	Poly(vinyl alcohol)
PVDF	Poly(vinylidene fluoride)
rpm	Revolutions per minute
SDBS	Sodium dodecylbenzenesulphonate
SDS	Sodium dodecyl sulphate
SEM	Scanning electron microscopy
SWNT	Single wall carbon nanotube
TGA	Thermogravimetric analysis
TEM	Transmission electron microscopy
UV-vis	Ultraviolet-visible

FABRICATION OF NOVEL SENSORS FROM NANOMATERIALS

Contents

CHAPTER 1	INTRODUCTION	1
1.1	Introduction to nanotechnology and nanomaterials	2
1.2	CNTs - a unique material	2
1.2.1	<i>Synthesis of CNTs</i>	3
1.2.2	<i>Properties of CNTs</i>	6
	1.2.2.1 <i>Electrical properties of CNTs</i>	6
	1.2.2.2 <i>Mechanical properties of CNTs</i>	9
1.2.3	<i>Applications of CNTs</i>	10
1.3	Sensors - an introduction	11
1.3.1	<i>Sensing mechanisms for sensors based on nanomaterials and CNTs</i>	12
1.3.2	<i>Examples of sensors based on nanomaterials and CNTs</i>	13
1.4	Aims of the thesis	17
1.5	Overview of the thesis	18
1.6	References	20
CHAPTER 2	EXPERIMENTAL	26
2.1	Materials	26
2.1.1	<i>Water</i>	26
2.1.2	<i>Organic solvents</i>	26
2.1.3	<i>Carbon nanotubes and silver nanowires</i>	26
2.1.4	<i>Gelling agents</i>	27
2.1.5	<i>Other materials</i>	27
2.1.6	<i>Substrates for sessile drop evaporation, supported films and inkjet printing</i>	29
2.2	Methods	30
2.2.1	<i>Polymer and polymer-CNT composite synthesis</i>	30
	2.2.1.1 <i>Synthesis of PANi and PANi-MWNT composites</i>	30

2.2.1.2	<i>Synthesis of PMAS</i>	30
2.2.1.3	<i>Synthesis of PMAS-PAni-MWNT composites</i>	31
2.2.2	<i>Dispersion preparation</i>	31
2.2.2.1	<i>Preparation of CNT dispersions</i>	31
2.2.2.2	<i>Preparation of Ag NW dispersions</i>	32
2.2.2.3	<i>Yeast cell dispersions</i>	32
2.2.3	<i>Drop deposition</i>	33
2.2.4	<i>Inkjet printing</i>	33
2.2.4.1	<i>Inkjet printing gellan gum-CNT and PMAS-CNT dispersions</i>	33
2.2.4.2	<i>Inkjet printing PMAS-PAni-MWNT dispersions</i>	33
2.2.5	<i>Dielectrophoretic assembly in agarose solutions</i>	33
2.2.5.1	<i>DEP cell</i>	33
2.2.5.2	<i>Dielectrophoretic assembly of Ag NWs in agarose solution</i>	33
2.2.5.3	<i>Dielectrophoretic assembly of yeast cells in agarose solution</i>	34
2.3	Characterisation	34
2.3.1	<i>Characterisation of solutions and dispersions</i>	34
2.3.1.1	<i>UV-visible spectroscopy</i>	34
2.3.1.2	<i>Contact angle analysis</i>	35
2.3.1.3	<i>Rheology</i>	35
2.3.1.4	<i>Surface tension</i>	36
2.3.1.5	<i>Gas phase chromatography</i>	36
2.3.1.6	<i>Circular dichroism</i>	36
2.3.2	<i>Characterisation of supported, free-standing and printed films</i>	36
2.3.2.1	<i>UV-visible spectroscopy</i>	36
2.3.2.2	<i>Circular dichroism</i>	37
2.3.2.3	<i>Raman spectroscopy</i>	37
2.3.2.4	<i>Thermogravimetric analysis (TGA)</i>	37
2.3.2.5	<i>Optical microscopy</i>	37
2.3.2.6	<i>Transmission electron microscopy (TEM)</i>	37
2.3.2.7	<i>Scanning electron microscopy (SEM)</i>	38
2.3.2.8	<i>Cyclic voltammetry</i>	38
2.3.2.9	<i>Topographical analysis</i>	38
2.3.2.10	<i>Electrical characterisation</i>	39

2.3.3	<i>Sensing studies</i>	39
2.3.4	<i>Treatment of living yeast cell strings</i>	41
2.3.4.1	<i>Fixing yeast cell strings</i>	41
2.3.4.2	<i>Imaging yeast cell strings</i>	41
2.4	References	43
CHAPTER 3 CARBON NANOTUBE NETWORK FORMATION FROM AN EVAPORATING SESSILE DROP		44
3.1	Introduction	44
3.1.1	<i>Interactions between carbon nanotubes and surfactants</i>	44
3.1.2	<i>Sessile drop evaporation on a substrate</i>	48
3.2	Surfactant drops on silicon substrates	49
3.3	Surfactant-CNT drops on substrates	52
3.3.1	<i>SDS-SWNT dispersions</i>	52
3.3.2	<i>Optical microscopy</i>	53
3.3.3	<i>Contact angle analysis</i>	55
3.3.4	<i>SDS-SWNT film formation</i>	60
3.3.5	<i>Raman spectroscopy</i>	68
3.3.6	<i>Scanning electron microscopy</i>	69
3.3.7	<i>Optical profiling</i>	71
3.4	Conclusions	75
3.5	References	77
CHAPTER 4 PREPARATION AND CHARACTERISATION OF CARBON NANOTUBE COMPOSITES IN AQUEOUS AND ORGANIC SOLVENTS		79
4.1	Introduction	79
4.1.1	<i>Conducting polymers</i>	79
4.1.2	<i>Conductivity of conducting polymers</i>	80
4.1.3	<i>Polyaniline</i>	81
4.1.4	<i>Water soluble polyaniline</i>	82
4.1.5	<i>Conducting polymer-CNT composites</i>	83
4.2	PAni-CNT composites	84
4.2.1	<i>PAni-MWNT composite dispersions in DMSO</i>	84

4.2.2	<i>Transmission electron microscopy of PAni-MWNT composites</i>	86
4.2.3	<i>Thermogravimetric analysis of PAni-MWNT composites</i>	87
4.2.4	<i>Optical activity of PAni-MWNT composites</i>	89
4.2.4.1	<i>Optical activity and circular dichroism</i>	89
4.2.4.2	<i>Circular dichroism of PAni-MWNT composites</i>	89
4.3	PMAS-CNT composites	93
4.3.1	<i>Effects of sonicating time on the molecular weight of PMAS</i>	94
4.3.2	<i>Investigating PMAS-CNT interactions</i>	95
4.4	Characterisation of PMAS-PAni-MWNT composites	100
4.4.1	<i>PMAS-PAni-MWNT solution properties</i>	101
4.4.2	<i>TGA of PMAS-PAni-MWNT</i>	103
4.4.3	<i>Electrical properties of PMAS-PAni-MWNT free-standing films</i>	104
4.4.4	<i>Electrochromic behaviour of PMAS-PAni-MWNT composites</i>	106
4.4.4.1	<i>Cyclic voltammetry</i>	106
4.4.4.2	<i>Electrochromic behaviour of PMAS-PAni-MWNT composites</i>	106
4.5	Conclusions	108
4.6	References	109
CHAPTER 5 INKJET PRINTING FUNCTIONAL CARBON NANOTUBE COMPOSITES		113
5.1	Introduction	113
5.1.1	<i>Inkjet printing and fluid properties</i>	113
5.1.2	<i>Inkjet printing polymers and other materials</i>	115
5.1.3	<i>Inkjet printing carbon nanotubes</i>	117
5.1.4	<i>Gellan gum- a naturally occurring polysaccharide</i>	117
5.2	Gellan gum-CNT composites	118
5.2.1	<i>Characterisation of gellan gum-CNT dispersions</i>	118
5.2.1.1	<i>Comparison of gellan gum-SWNT dispersions with SDS-SWNT dispersions</i>	118
5.2.1.2	<i>Effect of pH on gellan gum-SWNT dispersions</i>	120
5.2.1.3	<i>Effect of NaCl on gellan gum-SWNT dispersions</i>	122
5.2.2	<i>Inkjet printing gellan gum-CNT composites</i>	123
5.2.2.1	<i>Optical transmittance</i>	123

5.2.2.2	<i>Electrical and sensing properties</i>	124
5.3	PMAS-CNT composites	128
5.3.1	<i>UV-vis spectroscopy of composite inks and films</i>	128
5.3.2	<i>Raman spectroscopy of printed films</i>	130
5.3.3	<i>Electrical and sensing properties of printed films</i>	131
5.3.4	<i>Sensing mechanism of PMAS-SWNT films</i>	143
5.4	PMAS-PAni-MWNT composites	144
5.4.1	<i>Suitability of the composites for printing</i>	144
5.4.2	<i>Optical and electrical characterisation of the printed films</i>	147
5.4.3	<i>Electrochromic behaviour of PMAS-PAni-MWNT films</i>	151
5.5	Conclusions	152
5.6	References	154
CHAPTER 6 ELECTRICALLY ANISOTROPIC GELS AND ORGANISED ASSEMBLIES FORMED BY ARRESTED DIELECTROPHORETIC ASSEMBLY		157
6.1	Introduction	157
6.1.1	<i>Theory of dielectrophoresis</i>	157
6.1.2	<i>Practical applications of dielectrophoresis</i>	160
6.1.3	<i>Agarose gel</i>	163
6.2	The effects of an electric field on the gelling transition of agarose	164
6.2.1	<i>Strategy for measuring the effect of an AC field on agarose gelation</i>	165
6.2.2	<i>Effect of an AC field on the gelation of agarose solutions</i>	166
6.3	Dielectrophoretic assembly and encapsulation of nanoparticles in a solution	170
6.3.1	<i>New strategy for carrying out dielectrophoretic assembly in a gelling solution</i>	171
6.3.2	<i>Microwire growth diagram of the dielectrophoretic assembly of Ag NWs in agarose gel</i>	173
6.3.3	<i>Optical microscopy of dielectrophoretically assembled Ag microwires</i>	176
6.3.4	<i>Electrical properties of assembled microwires and gels after DEP</i>	179
6.4	Fabrication of a novel biosensor from Ag NWs assembled with DEP	184
6.4.1	<i>NW functionalisation and strategy for novel biosensor fabrication</i>	184

6.4.2	<i>Sensitivity of the novel biosensor to streptavidin</i>	186
6.5	Assembly of yeast cell ‘strings’ through DEP in agarose gel	187
6.5.1	<i>Strategy for the assembly of yeast cell strings through DEP</i>	188
6.5.2	<i>DEP of yeast cells in an unmodified agarose gel</i>	189
6.5.3	<i>DEP of yeast cells in a hydroxyethylated agarose gel</i>	191
6.6	Conclusions	195
6.7	References	197
CHAPTER 7 MAIN CONCLUSIONS AND FUTURE WORK		199
7.1	Main conclusions	199
7.2	Future work	202
7.3	References	204

CHAPTER 1

INTRODUCTION

Nanomaterials are structures whose building blocks have dimensions in the nanometer domain, and possess many interesting and unique properties which make them candidates for a great number of potential applications. The electrical and mechanical properties of nanomaterials could be exploited in, for example, sensors, electrical devices such as transistors, optical displays for televisions and computers, strong, lightweight building materials and artificial muscles. There are challenges to overcome however, such as how to accomplish the large scale, financially viable production of nanomaterials that possess uniform and precisely determined properties. This thesis will address another major challenge, which is how to take these nanomaterials from their as-produced state and process them into materials that best exploit their phenomenal properties. Topics that will be discussed include studies on the interactions between nanomaterials and a range of different dispersants, novel processing techniques for these materials such as inkjet printing and dielectrophoretic assembly, and characterisation of the processed materials that display properties such as optical activity, electrochromic behaviour and sensitivity to a range of analytes.

This chapter introduces some of the basic knowledge required for the understanding of the research work presented in this thesis. First, a general introduction to nanotechnology and nanomaterials will be presented, followed by a discussion on carbon nanotubes (CNTs), which feature heavily throughout this thesis and are a nanomaterial of interest in a number of different disciplines. Then, an introduction to sensors will be presented, reviewing the current technologies employed and explaining why sensors based on nanomaterials may be advantageous. Previous works on sensors based on nanomaterials and CNTs will also be discussed. Finally, a brief overview of the following chapters introduces the reader to the general trend of the thesis.

1.1 Introduction to nanotechnology and nanomaterials

The term ‘nanotechnology’ has, over the past few decades, been the subject of much debate, speculation, discussion and even controversy. Like few other areas of science it has captured the attention of the general public, and yet there is no firm definition of what nanotechnology actually is. Perhaps this is due to the fact that nanotechnology could be classed as a sub-section of diverse disciplines including chemistry, physics, biology and materials science. Many leading researchers in the field however feel that nanotechnology is an interdisciplinary area, where collaboration and cooperation will be key factors in pushing nanotechnology forward and making many of the theories and proposed applications a reality.

Nanomaterials themselves can be classed as materials that have at least one length scale in the region of 1 to 100 nm, where one nanometer is a billionth of a meter, or 10^{-9} m. The interest in nanomaterials arises for a number of reasons related to their size. For instance, some materials display unique and interesting properties when they are scaled down to the nanometer domain that are not apparent in the bulk or even on the micron scale. There is also a general interest in miniaturising technologies in a number of different areas, so that enhanced functionality can be condensed into smaller spaces. One logical way to do this would of course be to use nanostructured materials.

1.2 CNTs – a unique material

CNTs, discovered by Iijima in 1991,¹ are an allotrope of carbon just as diamond, graphite and fullerenes² are. In diamond, each carbon atom forms bonds with another four carbon atoms in a tetrahedral fashion, which accounts for the exceptional strength of diamond. In graphite however, each carbon atom bonds to another three atoms in a hexagonal lattice, with layers of the lattice held together by relatively weak forces. As each of the carbon-carbon bonds is sp^2 hybridised, electrons are easily transported in the plane of the lattice, but not perpendicular to it. The relatively weak forces between the hexagonal lattice layers allow them to slide over each other, and graphite is used in pencils and as a lubricant because of its ‘slip’ nature. Fullerenes are spherical ‘cages’ of carbon atoms, where again each carbon atom is bonded to another three atoms. Typically the rings that make up the fullerene are hexagonal, but five-membered (pentagonal) and seven-membered (heptagonal) rings are also present. CNTs combine

the properties of exceptional strength, like diamond, with electrical conduction, like graphite, and have a structure that is similar to that of graphite and fullerenes. They are hollow cylinders of carbon, best envisaged by rolling up a graphene sheet (one of the layers of carbon atoms that make up graphite) to form a seamless cylinder, and then capping the ends with fullerene-type caps. This would give a single wall carbon nanotube (SWNT), though double wall and multiwall CNTs (MWNT) can be produced, which comprise a two or more different sized nanotubes stacked within each other, much like Russian dolls (Figure 1.1). CNTs typically have diameters ranging from one to tens of nanometers, with lengths that in some cases have approached centimeters,³ though are more typically several micrometers. They therefore have high aspect ratios, large surface areas and low densities, though this is only the beginning of their extraordinary properties, which include unique electrical and mechanical characteristics that make them desirable for any number of potential applications.

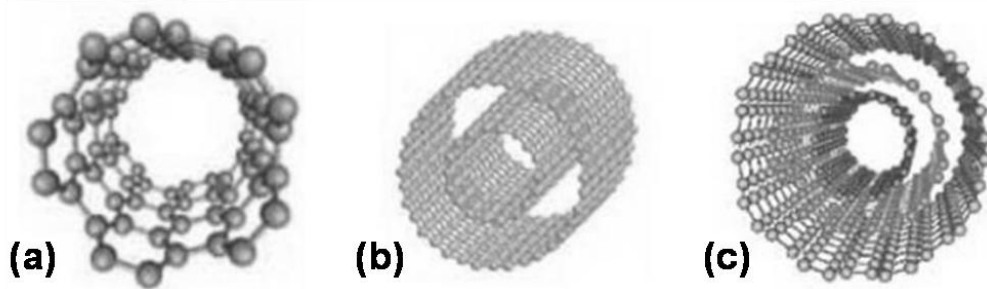


Figure 1.1 Image of (a) single wall, (b) double wall and (c) multi wall carbon nanotube. Image adapted from reference 4.

1.2.1 Synthesis of CNTs

When first discovered in 1991, CNTs were observed deposited on the negative electrode during the direct current (DC) arcing of graphite for the production of fullerenes.¹ This production process involved the ablation of graphite, which then reformed into the organised, spherical cage-like structures that became known as fullerenes. The synthesis of CNTs is based on similar principles, with a carbon source undergoing ablation followed by the recombination of short fragments to form nanotubes. Depending on the size of the nanotube and the number of walls that are required, four different techniques have been developed for their synthesis, based upon this same basic principle.

Technique 1: *Arc discharge*. A large current (approximately 60 – 100 A across a potential drop of around 30 - 35 V)⁵ is applied between two graphite rods that make up the anode and the cathode. At the high temperatures generated, the carbon anode sublimates and is deposited on the cathode as CNTs and amorphous carbon.⁶ An inter-electrode gap of around 1 mm is usually maintained by gradually moving the anode towards the cathode as it sublimates. The discharge is usually carried out in the presence of some inert gas, typically helium, argon or methane. Methane is thought to be particularly good for the synthesis of nanotubes high in crystallinity, and the presence of hydrogen is also believed to inhibit the formation of unwanted carbon nanoparticles and fullerenes.⁷ Typically, CNTs produced through this technique are MWNTs, though it is possible to obtain SWNTs if metal nanoparticles are present as a catalyst. Common catalysts employed are based on molybdenum, iron, cobalt and nickel, or combinations of two or more of these metals.^{8,9} The method is similar to that for producing MWNTs, but the anode is hollowed out and filled with the catalyst, while the cathode remains a pure graphite rod. A number of groups have studied the effects of different catalysts and inert gases, catalyst ratios when present in mixtures, and the pressure of the gas on the quality and diameter of the nanotubes obtained.¹⁰⁻¹²

Technique 2: *Chemical vapour deposition (CVD)*. In this technique, a hydrocarbon gas is decomposed by high temperature (650 – 900 °C) in a sealed chamber, in which a substrate is also placed. The chamber is then cooled, resulting in the carbon atoms recombining to give nanotubes on the substrate, which is often coated with a specific catalyst. Typical catalysts for the production of MWNTs are similar to those used in arc discharge, and include cobalt, nickel, copper and iron.^{13,14} The choice of catalyst and length of reaction time have both been reported as influencing the diameter and length of the resulting nanotubes.¹⁵ José-Yacamán and co-workers have synthesised MWNTs from acetylene at a temperature of 700 °C,¹⁶ while Endo and co-workers have reported their synthesis from benzene at 1100 °C.¹⁷ The production of SWNTs using CVD has also been reported, with Dai and co-workers employing carbon monoxide for the synthesis of tubes with diameters of 1 - 5 nm.¹⁸ They suggest that elevated temperatures of 1200 °C are necessary to reduce the amount of defects in the growing nanotubes. Further advances have seen dense nanotube ‘forests’ grown on substrates, where the nanotubes can either be vertically aligned¹⁹ or present as randomly oriented networks.²⁰ The patterning of substrates with catalyst particles also allows a

degree of control over the position of nanotube growth, which is not possible with some other methods of synthesis.^{21, 22}

Technique 3: *Laser ablation*. The laser ablation technique was pioneered by Smalley and co-workers at Rice University, Texas.²³ Graphite is placed in a temperature controlled furnace, through which a flow of helium or argon is continuously passed. A laser is then scanned across the surface of the graphite target, vaporizing the graphite into small fragments that are carried to a copper collector where they recombine as nanotubes. Thess and co-workers introduced a second laser pulse to be applied just after the first, which breaks up the larger particles ablated by the first pulse to reduce the amount of unwanted soot formed.²⁴ Two types of laser that are commonly used in laser ablation are neodymium-doped yttrium aluminium garnet (Nd:YAG) and carbon dioxide (CO₂) lasers.²⁵ Yudasaka and co-workers report that CO₂ lasers are capable of room temperature SWNT production,²⁶ while Nd:YAG lasers require elevated temperatures as they do not deliver sufficient power for the laser alone to account for graphite vaporisation. As in the arc discharge method of production, pure graphite sources give MWNTs, while the presence of a catalyst gives SWNTs.⁵ It has been reported by a number of authors that the catalyst influences the yield of nanotubes formed in this process. Mixtures of nickel/cobalt, nickel/platinum and cobalt/platinum all give good yields of nanotubes, but platinum and copper when used alone give small yields.^{23, 24, 27}

Technique 4: *High-pressure decomposition of carbon monoxide (CO), known as the HiPco process*.²⁸ CO is the feedstock gas, which flows over a heater with a small amount of iron pentacarbonyl (Fe(CO)₅) acting as a catalyst. Iron catalyst particles are liberated at high temperature, which catalyse the decomposition of CO and act as nucleation sites for the growth of CNTs which grow in the gas phase. The rate of CO decomposition is increased at high pressure, hence the importance of this parameter, and it also influences the diameter of the nanotubes that form. To increase the efficiency of this process, a feedback system has been introduced to return un-reacted CO back into the system, rather than releasing it into the atmosphere. Using this method, SWNTs have been produced at rates of 450 mg h⁻¹, which is in excess of other production methods.²⁹ SWNTs with diameters of 0.7 nm, which is thought to be the smallest possible diameter for a stable SWNT, have also been synthesised using this method.³⁰

1.2.2 Properties of CNTs

The unique properties of CNTs are what make them of such interest. Here we will describe some of these properties, and discuss why they are so unique to CNTs.

1.2.2.1 Electrical properties of CNTs

Before discussing the electrical properties of CNTs, it is first important to understand a little more about their structure. It was mentioned previously that a CNT could be envisaged by rolling a graphene sheet to form a seamless cylinder. There are however different ways in which we could roll up the graphene sheet, which affects the ‘twist’ of the hexagonal lattice with respect to the axis along the length of the nanotube. We refer to this twist as the ‘chirality’ of the nanotube, with each carbon nanotube defined by a chiral angle θ and a chiral vector $C_h = n\mathbf{a}_1 + m\mathbf{a}_2$, where n and m are integers and \mathbf{a}_1 and \mathbf{a}_2 are unit vectors (Figure 1.2).³¹ The nanotube axis T refers to the axis that runs parallel with the length of the nanotube.

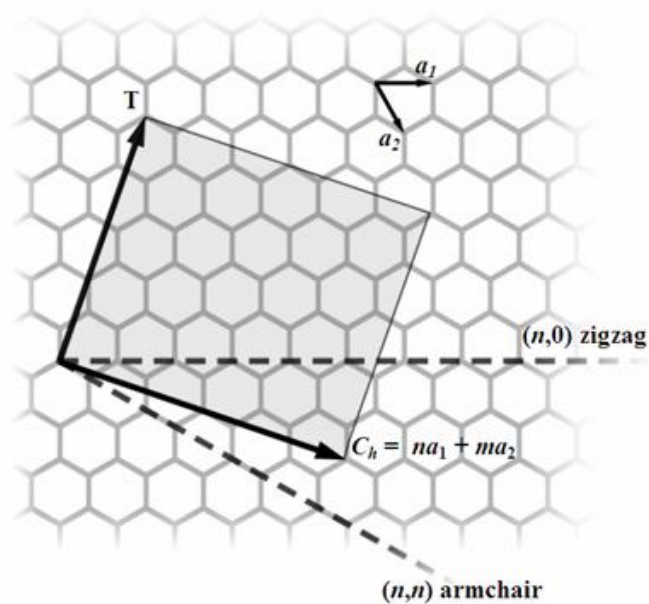


Figure 1.2 A 2D graphene sheet, showing the chiral vector C_h . T denotes the nanotube axis. Image reproduced from reference 32.

SWNTs that have a chiral angle of zero, and where either n or m is also zero are referred to as ‘zigzag’ nanotubes. Where the chiral angle is 30° and $n = m$, nanotubes are referred to as ‘armchair’ nanotubes, with large values of n and m giving nanotubes

of large diameter. Both zigzag and armchair nanotubes have high symmetry, with a mirror symmetry plane normal to the axis of the nanotube. Nanotubes that have a chiral angle between zero and 30° , and where n and m are different values, are called ‘chiral’ nanotubes. Images of armchair, zigzag and chiral nanotubes are shown in Figure 1.3.

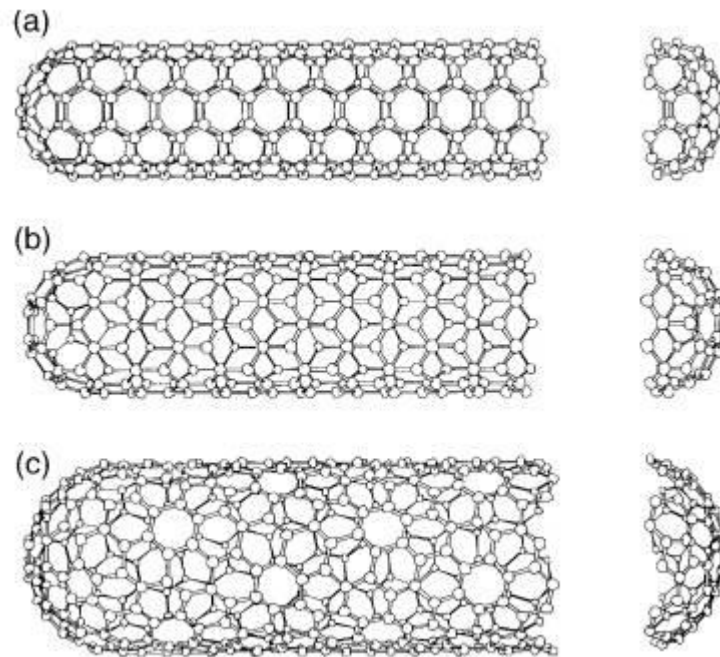


Figure 1.3 Models of (a) armchair, (b) zigzag and (c) chiral SWNT. Image reproduced from reference 33.

The values of n and m can drastically affect the electrical properties of the carbon nanotube. Specifically, a carbon nanotube can either be classed as a conductor or a semi-conductor, based upon these structural properties. A detailed explanation of this phenomenon falls outside the scope of this thesis, but briefly, we can attribute this to the periodic overlapping of the molecular orbitals of carbon atoms when the graphene sheet is arranged in a cylindrical geometry.³⁴ This overlapping only occurs at certain diameters and chiralities of the nanotube, and it has been shown that two thirds of CNTs will be semi-conducting while the remaining one third will be electrically conducting. In fact, all armchair nanotubes are conducting, and one third of zigzag and chiral nanotubes are conducting when $n - m = 3q$, where q is an integer.³⁵ A more detailed explanation regarding the dependence of nanotube conductivity on its structure is given in reference 6, and references therein.

That CNTs can either be metallic or semi-conducting is in itself a noteworthy property, but it is even more impressive when we consider the actual properties of each of these classes of nanotubes. Mann and co-workers have measured the resistance for an individual SWNT of 32 k Ω at 290 K,³⁶ which from the length and diameter of the nanotube has been calculated elsewhere to have a conductivity of $0.9 \times 10^6 \text{ S cm}^{-1}$,³⁷ which is comparable to silver and copper. Theoretical predictions suggest however that the conductivity of longer and thinner ideal SWNTs should be greater than this,³⁸ so if produced, a metallic SWNT would have the highest conductivity of any known material (with the exception of superconductors). Networks and fibres of CNTs have also been measured as having conductivities of the order 10^3 S cm^{-1} .^{39,40} MWNTs are thought to have similarly high conductivities despite the close proximity of the concentric tubes, due to weak coupling between the cylinders.⁴¹ Yao and co-workers have measured a current carrying capacity for SWNTs of the order 10^9 A cm^{-2} ,⁴² which is several orders of magnitude larger than for many metal wires ($\sim 10^3 \text{ A cm}^{-2}$ for copper wires). In semi-conducting nanotubes, the band gap is inversely proportional to the nanotube diameter,³⁵ which opens up the possibility for devices with well defined electrical properties if this parameter can be controlled. The charge carrier mobility of CNTs has been measured by Durkop and co-workers, who quote a value of the order $10^5 \text{ cm}^2 \text{ V}^{-1} \text{ s}^{-1}$ (typical charge carrier mobilities for silicon are of the order $10^4 \text{ cm}^2 \text{ V}^{-1} \text{ s}^{-1}$).⁴³ Individual semiconducting SWNTs have shown $I_{\text{ON}}/I_{\text{OFF}}$ ratios of the order 10^6 ,⁴⁴ (recent silicon based field effect transistors (FETs) are approaching ratios of 10^5) which coupled with their high charge carrier mobilities make them promising candidates for semi-conductor devices. Networks of many CNTs do not yield such good $I_{\text{ON}}/I_{\text{OFF}}$ ratios, however, with typical values of the order 10^4 .⁴⁵

Although it is possible to have some control over the diameter of CNTs during their synthesis, there is not currently a method to control the precise chirality of CNTs from their growth. This is a significant obstacle that researchers are aiming to overcome, as commercial samples therefore exist as a mixture of both metallic and semi-conducting CNTs. This is problematic for applications where only metallic or semi-conducting nanotubes are required (in FETs for example), or where semi-conducting nanotubes of a precise band gap are desired. Developments have been made however for the separation of metallic from semi-conducting nanotubes, or the elimination of one type of nanotube from a mixture. For example, Chattopadhyay and co-workers report the non-destructive separation of metallic from semi-conducting

SWNT in the bulk, based on their differing interactions with the dispersant octadecylamine in the solvent tetrahydrofuran.⁴⁶ This work is built upon by Maeda and co-workers, who report a similar separation where the concentration of metallic SWNTs obtained in a sample approaches 87 %.⁴⁷ Ménard-Moyon and co-workers report the covalent functionalisation of semi-conducting SWNTs based on their cycloaddition reactions with azomethine ylides.⁴⁸ Elsewhere, An and co-workers describe the fabrication of nanotube devices where the metallic nanotubes have been eliminated through treatment with a diazonium reagent,⁴⁹ based on the previous work of Strano and co-workers.⁵⁰ More recently, an electrochemical method of identifying semi-conducting and metallic SWNT in a mixture has been developed by Yu and co-workers.⁵¹

1.2.2.2 Mechanical properties of CNTs

The mechanical properties of CNTs that make them stand out particularly from other materials are their Young's modulus and the tensile strength. Briefly, the Young's modulus is the measure of stiffness of a material, while the tensile strength is the point at which a material undergoes breakage or irreversible deformity, due to the stress of an applied force. The strength of CNTs is attributed to the bond structure between the sp^2 hybridised carbon atoms: to break a carbon nanotube, these covalent bonds must be broken mechanically.

Many values have been reported for both the Young's modulus and tensile strength of SWNTs and MWNTs since their discovery.⁵² Yu and co-workers report a Young's modulus of 1 TPa and a tensile strength of ~ 30 GPa for an individual SWNT,⁵³ while the Young's modulus for a bundle of SWNTs is believed to be lower, at around 640 GPa.⁵⁴ For comparison, the Young's modulus of silicon carbide is approximately 450 GPa, while the tensile strength of Kevlar is approximately 3 GPa. For MWNTs, Yu and co-workers have reported a tensile strength of ~ 37 GPa, where they observed that the MWNT breaking mechanism was that of 'sword in sheath'.⁵⁵ In this mechanism, as the MWNT was pulled between two AFM tips, the outer walls of the nanotube slipped past the inner walls prior to breaking. Dalton and co-workers have produced SWNT containing fibres, which have a tensile strength of 1.8 GPa, formed from a coagulation process.⁵⁶ Elsewhere, Zhang and co-workers report the fabrication and characterisation of MWNT sheets, formed by drawing a post-it note away from a 'forest' of CVD produced MWNTs.⁵⁷ They observed alignment of the nanotubes in the direction of the draw, giving sheets that could support 50,000 times their own weight.

However, it remains a challenge to fabricate materials that possess the same mechanical properties as the individual nanotubes.

1.2.3 Applications of CNTs

Potential applications for CNTs are based on their small size, coupled with their electrical or mechanical properties.⁵⁸ For example, semi-conducting CNTs are believed to be ideal components for FETs (the operation of these devices is described in detail later), where the performance of conventional FETs based on silicon is expected to reach a limit in the near future.⁵⁹ FET sensors based on CNTs are also predicted, which will be discussed in more detail in the next section. Field emission devices for electron sources, flat panel displays and microwave generators are also envisaged, based on the electrical properties and high aspect ratios of CNTs.

Composites that contain CNTs are expected to exploit both their electrical and mechanical properties. Due to the high aspect ratio of CNTs, they are expected to form a conducting, percolating network (an interconnected network of CNTs that spans the composite) within insulating matrixes at far lower loading fractions than traditional conducting fillers, such as carbon black or carbon fibers.⁶⁰ Their low density and mechanical properties also make CNTs an obvious choice for strong, lightweight composite materials, which might be used in car body parts or building materials for example. Several groups have also reported the production of CNT fibres,^{56, 61} which might then be woven together to produce ultra-strong fabrics or cables. Such CNT cables or wires might then find applications in actuators and artificial muscles.⁶²

There are however a number of technical obstacles that have prevented these potential applications of CNTs from becoming a reality. It has already been mentioned that semi-conducting CNTs cannot be selectively synthesised, and therefore must be separated from the metallic nanotubes if they are to be used in FETs. There is also the problem of processing CNTs, for example how to separate an individual nanotube from an aggregate and position it accurately between two electrodes. Similarly for composite materials, bundles of CNTs would need to be separated into individual nanotubes, making best use of their surface area and aspect ratios for conducting composites and sensors, while ensuring better matrix-nanotube interactions for composites exploiting the mechanical properties of CNTs. These are just some of the issues that must be addressed.

1.3 Sensors – an introduction

A sensor, according to the IUPAC definition,^{*} is a device that transforms information into an analytically useful signal.⁶³ They have found widespread applications, as they can give us accurate and real-time information about a vast number of parameters. For example in our cars we have sensors to tell us how fast we are going, how much petrol we have left and how hot or cold it is outside. Sensors are also used extensively in other areas such as medicine (to probe what is happening in our bodies), industry (to measure the progress and safety of reactions), and the environment (to measure levels of pollutants in the air or water). There is a demand however for improvements in sensors, and in particular for lower limits of detection, faster response and recovery times, selectivity and the ability to work under extreme conditions. For example, sensors that can detect low levels of toxins in the air and that can communicate this information rapidly will provide early warnings against chemical warfare, while sensors that can operate at high temperatures and/or pressures will be of use in the automotive industry. Therefore there is much research in this area, searching for new materials that will be able to meet these demands.

Sensors essentially comprise two basic functions: a *receptor*, which is the sensitive element in the sensor, and a *transducer*, which transforms the response into a signal that can be measured analytically or observed by a user. They generally fall in to two main categories: *physical* sensors, which detect a physical change, such as temperature or pressure, and *chemical* sensors, which detect the presence of a chemical reaction. A sub-class of chemical sensors that has attracted a lot of attention is *biochemical* sensors, also known as *biosensors*, which detect a biochemical process. There are also sensors that do not quite belong in either the chemical or physical sensor categories, for example where the sensing is caused by an *adsorption* process. In this summary we will not discuss physical sensors, instead focusing on chemical and biochemical sensors. Sensors that detect an adsorption process are also of interest, as it is this mechanism that accounts for many examples of sensors based on nanomaterials and CNTs in particular.

Sensors can be further classified based on the operating mechanism of the transducer - the part of the sensor that transforms the response into a signal. For

^{*} IUPAC is the International Union of Pure and Applied Chemistry

example, sensors with optical transducers might signal a response as a change in the absorbance, fluorescence or refractive index of a material. Mass sensitive transducers include piezoelectric devices, where a change in the adsorption of an analyte from either a gas or solution medium is signalled by a change in the frequency. Responses can also be signalled as a change in the materials magnetic, thermal or radiation properties.⁶⁴ Many sensors however rely on electrochemical or electrical transducers, which signal a change in the electrical properties of the receptor based upon either the detection of an electrochemical process, or the interaction of an analyte directly with the receptor. This type of sensing is of particular interest in the field of sensors based on nanomaterials and CNTs, with many examples reported in the literature, which will be discussed below.

1.3.1 Sensing mechanisms for sensors based on nanomaterials and CNTs

Many of the reported sensors based on nanomaterials and CNTs respond either to an electrochemical process, or to an interaction between an analyte and receptor that results in a change in the electrical properties of the receptor. This second process can include adsorption of the analyte onto the receptor, mentioned briefly earlier. There appear to be two main transduction mechanisms for measuring this interaction. One method is to measure the electrical properties of the receptor while it is exposed to an analyte. For example, the current might be measured at a constant voltage through the device, with a response signalled as a change in the current. Where an individual CNT or network are the sensing element, these types of sensors are known as ‘CNT chemiresistors’.⁶⁵ The second, widely encountered method is to employ a FET as the transducer. An interaction, whether it is an adsorption or electrochemical reaction, can either affect with the gate material which then results in a change in the source-drain current, or it can affect the source-drain channel, and thus the current, itself.⁶⁶ FETs are devices where the current flowing through a semi-conducting material is controlled by another, often much smaller, electric field. They form the basis of integrated circuits and microprocessors that are used in computers all over the world, and have been recently investigated as miniature sensors.

1.3.2 *Examples of sensors based on nanomaterials and CNTs*

In one of the first studies on CNTs as components in FETs, Tans and co-workers constructed twenty devices with individual CNTs as the source-drain channel between two platinum electrodes.⁶⁷ Silicon was the gate material, separated from the nanotube by an insulating layer of silicon dioxide. They observed two distinct types of behaviour, with some devices exhibiting linear current-voltage plots with no dependence on the gate voltage, characteristic of metallic CNTs, and other devices showing a dependence on the gate voltage that was attributed to semi-conducting CNTs. Their study and that of Avouris and co-workers revealed that the nanotubes displayed p-type semi-conductivity, and that holes were the majority charge carrier.⁶⁸ Several groups have sought to address the question of whether the holes are inherent to the CNTs, or whether they are induced by doping of the nanotube. Wildöer and co-workers attributed the presence of holes in semi-conducting CNTs to doping from the electrodes that they were connected to. In their study, gold electrodes were used which have a higher work function than CNTs. They reported that this causes electron transfer from the nanotube to the electrodes, leaving holes in the nanotube. However a study by Collins and co-workers suggested that the doping of CNTs could be attributed to their surroundings, as they found differences in the electrical properties of CNT bundles and films when transferred from air to a vacuum.⁶⁹ The resistance of the CNTs was lower when exposed to air than it was in the vacuum, and after exposure to the pure constituent gases in air they attributed the lower resistance to the presence of oxygen, which induces holes in the nanotube through electron transfer to the adsorbed oxygen. Kang and co-workers report that doping of the nanotube might depend upon its length, as they find that for long nanotubes the presence of oxygen causes doping, but that for shorter nanotubes the nanotube-electrode junction may determine the doping.⁷⁰

With these reports of p-type CNTs, several groups have tried to alter the doping so that the nanotubes became n-type, and in doing so the first basic sensors based on a CNTFET were produced. Kang and co-workers reported n-type semi-conductivity after exposure to ammonia gas,⁷⁰ in agreement with Kong and co-workers.⁷¹ Two mechanisms of doping by ammonia are postulated in the Kong report; one being interaction between ammonia and the silicon dioxide substrate, thus altering the properties of the gate, and the second being an interaction between ammonia and oxygen already adsorbed onto the CNTs. Other dopants that have been found to induce

n-type semi-conducting behaviour in CNTs are alkali metals such as potassium,⁷² polyethylene imine⁷³ and an amphiphilic synthetic peptide.⁴⁵

CNTFET sensors (see Figure 1.4) generally fall into two groups. In the first group of sensors that will be discussed, the sensing element of the device, or receptor, is the CNT itself, and the sensing interaction is directly between the CNT and the analyte. Later we will discuss the second group of sensors, where the CNTs are functionalised with another particle or molecule that interacts with the analyte, which can be useful for analytes that CNTs are otherwise inert to.

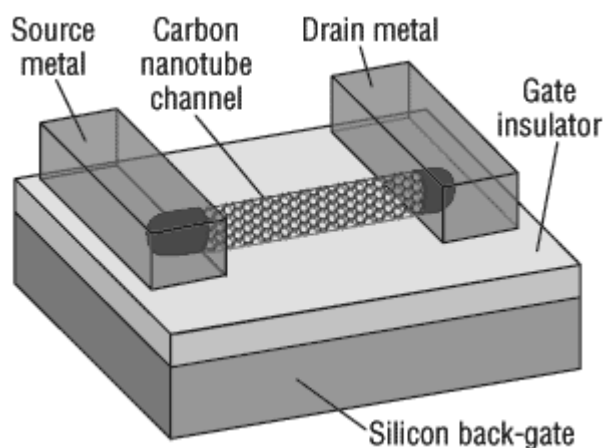


Figure 1.4 Illustration of a simple CNTFET. Image adapted from reference 74.

Many reports of CNT sensors describe their use in the detection of gaseous analytes. Kong and co-workers reported the use of CNTFET devices as chemical sensors for ammonia and nitrogen dioxide gases, based on a single CNT as the sensing element.⁷¹ Nitrogen dioxide could be measured by the device, at room temperatures, at a concentration of 200 parts-per-million (ppm) with a response time of 2 - 10 s, and at a concentration of 2 ppm in a time of 5 minutes. The recovery time for the device in a flow of argon was around 12 hours, but this could be speeded up to 1 hour with heating to 200 °C in air. This compares favourably with existing metal oxide sensors that can detect 100 ppm nitrogen dioxide with a response time of 50 s, but at an operating temperature of 250 °C.⁷⁵ Ammonia was measured at a concentration of 10000 ppm in a time of 1 - 2 minutes, and at 1000 ppm in 10 minutes, also at room temperature. Again this compares favourably with an existing metal oxide sensor, which has a response time of 1 minute for 10000 ppm ammonia, but at an operating temperature of 500 °C.⁷⁶

The Kong study reports that the response of the device was different for exposure to each of the gases ammonia and nitrogen dioxide, with ammonia giving a fall in the nanotube conductivity and nitrogen dioxide giving a rise in the conductivity. They attribute this to the electron withdrawing properties of nitrogen dioxide, which leads to the creation of more holes in the nanotube and thus increases the number of the majority charge carriers. The observed fall in conductivity meanwhile is attributed to the electron donating properties of ammonia, where electrons fill the holes and thus reduce the number of charge carriers. Similar responses were observed for mats of SWNTs, though the responses were not so large. This was attributed to averaging of the interactions for metallic and semi-conducting CNTs, and some nanotubes being 'hidden' within aggregates, so that their surfaces were not available to interact directly with the analyte.

Someya and co-workers have reported the fabrication of CNTFETs for the detection of various alcoholic vapours, finding that the same device may be able to differentiate between a range of alcohols.⁷⁷ Star and co-workers also demonstrated the ability of CNTFETs to sense in solution, exposing devices to benzene derivatives dissolved in cyclohexane.⁷⁸ They reported that the shift in the electrical properties of the device could be related to the relative electron withdrawing and donating groups of the substituents on the ring.

One example of the need to functionalise CNTs for sensing is given by Kong and co-workers, who report functionalised SWNT devices for hydrogen detection.⁷⁹ CNTs are inert to hydrogen, so a 5 Å thick layer of palladium was evaporated onto the walls of an individual SWNT, which provided a catalyst for hydrogen dissociation. This dissociation led to a lowering of the work function of the palladium, which in turn caused a decrease in the number of holes in the nanotube. This resulted in a measurable decrease in the conductance of the device at hydrogen concentrations as low as 4 ppm. Figure 1.3a shows the graph of a typical response of the palladium-functionalised sensor, responding to hydrogen at a concentration of 400 ppm. Star and co-workers have also investigated the sensitivity of SWNT network FETs decorated with metal nanoparticles, including platinum, gold and rhodium, to gases such as ammonia, nitrogen dioxide, hydrogen sulphide and hydrogen.⁸⁰

Qi and co-workers functionalised SWNT with polyethyleneimine, which changed the doping of the nanotubes from p-type to n-type.⁸¹ These CNTFET devices could detect nitrogen dioxide at a concentration of 100 parts-per-trillion (ppt), but were insensitive to ammonia, carbon dioxide, methane and hydrogen. Figure 1.5b shows a

typical graph of the sensor responding to nitrogen dioxide. However by changing the functional polymer adsorbed to the nanotube, replacing polyethyleneimine with Nafion (a sulfonated tetrafluoroethylene polymer), the devices could be made sensitive to ammonia gas, but not nitrogen dioxide. This demonstrates one of the advantages of functionalising CNTs for sensing - their ability to become more selective in what they will detect.

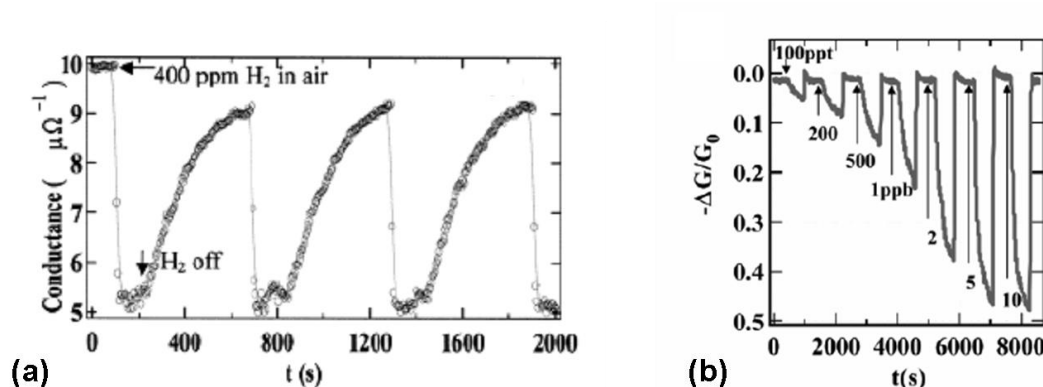


Figure 1.5 (a) Graph of the typical response of a palladium-functionalised SWNT sensor to hydrogen (reproduced from reference 79). (b) Graph of the typical response of a polyethylimine-functionalised SWNT sensor to increasing concentrations of nitrogen dioxide (reproduced from reference 81).

CNT sensors that operate based on the chemiresistor principle have also been fabricated for the detection of a range of analytes. Valentini and co-workers fabricated CNT mats on top of prefabricated platinum electrodes, which could detect nitrogen dioxide at concentrations as low as 10 parts-per-billion (ppb).⁸² However the device was found to be at its most sensitive at an operating temperature of 165 °C. The detection of nitrogen dioxide is also reported by Li and co-workers, who quote detection limits of 44 ppb at room temperature.⁸³ They also quote limits of detection of 262 ppb for nitrotoluene, for their devices fabricated by drop-casting a SWNT dispersion onto interdigitated gold electrodes. Dielectrophoretic assembly has been used to construct CNT chemiresistors from both SWNT and MWNT networks. Suehiro and co-workers fabricated an ammonia sensor from MWNT,⁸⁴ while Lee describes the fabrication of a SWNT device that is sensitive to thionyl chloride and dimethyl methylphosphonate.⁸⁵ Kordás and co-workers have recently described a novel method for fabricating CNT

chemiresistors, by inkjet printing networks of covalently functionalised MWNTs from aqueous dispersions onto paper and polymer surfaces.⁸⁶ Their devices showed sensitivity to the vapours of water, ammonia and several alcohols.

CNT chemiresistors where the nanotubes are functionalised have also been reported. Bekyarova and co-workers report the covalent functionalisation of SWNT with poly(*m*-aminobenzene sulfonic acid), which are processed into networks between interdigitated gold electrodes.⁸⁷ These sensors showed better sensitivity to ammonia gas compared to similar sensors with carboxylated SWNT, which they attribute to protonation of the ammonia by the sulfonic acid group on the functional group. This induces hole depletion of the CNTs, resulting in the observed drop in conductance of the sensor upon exposure to ammonia. A chemiresistor sensor to nitrogen dioxide has also been fabricated, based on CNT-polymer composites of SWNT with polypyrrole.⁸⁸ The composite was spin-coated onto prefabricated electrodes, for the detection of nitrogen dioxide at concentrations down to 200 ppm. Oakley and co-workers have also reported the construction of SWNT films through vacuum filtering, onto which palladium nanoparticles were evaporated for the detection of hydrogen at 100 ppm.⁸⁹ Glucose sensors based on CNT chemiresistors have also been fabricated, for the measurement of glucose concentrations in biological samples. This requires the functionalisation of CNTs with glucose oxidase enzyme, which catalyses the oxidation of glucose and forms hydrogen peroxide as a by-product. Sotiropoulou and co-workers report the non-covalent functionalisation of MWNT arrays with the enzyme, resulting in devices that can detect 19 mM glucose,⁹⁰ while Lin and co-workers covalently functionalise the CNTs in their study.⁹¹ There is however some debate as to the mechanism of sensing, with some researchers suggesting that the removal of oxygen in the reaction changes the conductance of the nanotubes, while others believe that the nanotubes have a catalytic effect on the hydrogen peroxide by-product.

1.4 Aims of the thesis

The aim of the work undertaken for this thesis has been to fabricate novel sensors based on nanomaterials, particularly CNTs. This will contribute to the understanding of how these unique materials can be incorporated into applications that make use of their exceptional properties. However to achieve this ultimate aim, a number of other factors have also been considered. These include a study of the

interactions between nanomaterials and dispersants or functional groups, such as surfactants and conducting polymers. These are materials that can facilitate processing, and in some cases they can even enhance the properties or functionality of the nanomaterials. An important part of the study therefore is to synthesise and characterise composites that incorporate the nanomaterials. Our aim is also to develop existing and novel techniques for processing relevant nanomaterials and their composites. The focus here is on solution-based processing techniques, such as drop deposition, inkjet printing and dielectrophoresis, which are expected to become increasingly important in the future of nanomaterials processing.

1.5 Overview of the thesis

The materials and methods that have been used throughout this thesis will be outlined in Chapter 2, covering some of the more generic techniques that have been used, such as optical microscopy and UV-vis spectroscopy. Methods that have been developed as part of this thesis will be described in detail at the appropriate point in Chapters 3 – 6.

In Chapter 3 we will explore some of the factors affecting the formation of thin carbon nanotube films from a sessile drop deposited onto a substrate. This is a process that is of fundamental importance to solvent based nanomaterial processing, as the deposition of a liquid drop on a substrate forms the basis of processing techniques such as inkjet printing, targeted drop deposition and spraying. The effects of substrate hydrophobicity and dispersion treatment (*i.e.* centrifugation) will be discussed, as we explore the distribution of nanotubes over the films. In addition, we develop a novel, non-destructive method for the topographical characterisation of these thin films, where more established methods have not been possible to perform due to the optical properties of the films.

The synthesis and characterisation of a number of different carbon nanotube composites is discussed in Chapter 4. We assess dispersing efficiency of CNTs by several aqueous and non-aqueous dispersants, using both physical mixing (sonication) and *in situ* polymerisation methods of composite synthesis. This is with the aim of producing composites that have enhanced properties due to the presence of the nanotubes, but that are also easy to process due to the dispersant. For the composites with conducting polymers as the dispersants, we describe the electrical properties of the

composite, and also the optical activity where an optically active polymer is employed as the dispersant.

In Chapter 5, we process some of the composites described in Chapter 4 using inkjet printing, fabricating thin carbon nanotube composite films. We consider both widely available desk-top inkjet printers, as well as research-grade inkjet printers that are particularly well suited for the printing of novel materials. Our aim here is to develop inkjet printing as a tool for processing CNTs, showing that it is a fast and reproducible technique suitable for fabricating carbon nanotube thin films. The electrical properties of the films are characterised, and we study the ability of the films to act as sensors for a range of analytes, and as electrochromic CNT-containing films.

The fabrication of gels with anisotropic electrical properties, and freestanding strings of living yeast cells is described in Chapter 6. These novel materials are prepared due to a method that we have developed of performing dielectrophoretic assembly of nano and micro structures in a gel solution above its gelling point. When the solution is cooled, the organised or aligned structures are encapsulated within the gel, even when the electric field is removed. This represents an efficient way of arresting the structures formed through dielectrophoresis, without the need for modification of the building blocks structure. Where the building blocks were functionalised with biotin however, we were able to fabricate a novel biosensor based on this functionalisation and the anisotropic nature of the gel. This suggests the possibility for the fabrication of novel biosensors based on gels with anisotropically aligned, functionalised structures embedded within them.

Finally, Chapter 7 concludes on all of the results and findings presented earlier in the thesis, regarding the processing and development of nanomaterials for novel sensors. Possible future work that could be performed in this area is also discussed.

1.6 References

- 1 Iijima, S., *Nature*, 1991, **354**, 56.
- 2 Kroto, H. W., Heath, J. R., O'Brien, S. C., Curl, R. F. and Smalley, R. E., *Nature*, 1985, **318**, 162.
- 3 Zheng, L. X., O'Connell, M. J., Doorn, S. K., Liao, X. Z., Zhao, Y. H., Akhadov, E. A., Hoffbauer, M. A., Roop, B. J., Jia, Q. X., Dye, R. C., Peterson, D. E., Huang, S. M. Liu, J. and Zhu, Y. T., *Nat. Mater.*, 2004, **3**, 673.
- 4 www.nanotube.korea.ac.kr, checked 25th April 2009.
- 5 Journet, C and Bernier, P., *Appl. Phys. A.*, 1998, **67**, 1.
- 6 Rao, C. N. R. and Govindaraj, A., *Nanotubes And Nanowires*, RSC Publishing, Cambridge, 2005.
- 7 Tai, Y., Inukai, K., Osaki, T., Tazawa, M., Murakami, J., Tanemura, S. and Ando, Y., *Chem. Phys. Lett.*, 1994, **224**, 118.
- 8 Bethune, D. S., Klang, C. H., de Vries, M. S., Gorman, G., Savoy, R., Vazquez, J. and Beyers, R., *Nature*, 1993, **363**, 605.
- 9 Iijima, S. and Ichihashi, T., *Nature*, 1993, **363**, 603.
- 10 Farhat, S., de La Chapelle, M. L., Loiseau, A., Scott, C. D., Lefrant, S., Journet, C. and Bernier, P., *J. Chem. Phys.*, 2001, **115**, 6752.
- 11 Journet, C., Maser, W. K., Bernier, P., Loiseau, A., de La Chapelle, M. L., Lefrant, S., Deniard, P., Lee, R. and Fischer, J. E., *Nature*, 1997, **388**, 756.
- 12 Saito, Y., Kawabata, K. and Okuda, M., *J. Phys. Chem.*, 1995, **99**, 16076.
- 13 Ivanov, V., Nagy, J. B., Lambin, P., Lucas, A., Zhang, X. B., Zhang, X. F., Bernaerts, D., Van Tendeloo, G., Amelinckx, S. and Van Landuyt, J., *Chem. Phys. Lett.*, 1994, **223**, 329.
- 14 Ivanov, V., Fonseca, A., Nagy, J. B., Lucas, A., Lambin, P., Bernaerts, S. and Zhang, X. B., *Carbon*, 1995, **33**, 1727.
- 15 Ago, H., Komatsu, T., Ohshima, S., Kuriki, Y. and Yumura, M., *Appl. Phys. Lett.*, 2000, **77**, 79.
- 16 José-Yacamán, M., Miki-Yoshida, M. and Rendón, L., *Appl. Phys. Lett.*, 1993, **62**, 657.
- 17 Endo, M., Takeuchi, K., Igarashi, S., Kobori, K., Shiraishi, M. and Kroto, H. W., *J. Phys. Chem. Solids*, 1993, **54**, 1841.

-
- 18 Dai, H., Rinzler, A. Z., Nikolaev, P., Thess, A., Colbert, D. T. and Smalley, R. E., *Chem. Phys. Lett.*, 1996, **260**, 471.
- 19 Ren, Z. F., Huang, Z. P., Xu, J. W., Wang, J. H., Bush, P., Siegal, M. P. and Provencio, P. N., *Science*, 1998, **282**, 1105.
- 20 Chen, J., Minett, A. I., Liu, Y., Lynam, C., Sherrell, P., Wang, C. and Wallace, G. G., *Adv. Mater.*, 2008, **20**, 566.
- 21 Fan, S., Chapline, M. G., Franklin, N. R., Tombler, T. W., Cassell, A. M. and Dai, H., *Science*, 1999, **283**, 512.
- 22 Merkulov, V. I., Lowndes, D. H., Wei, Y. Y., Eres, E. and Voelkl, G., *Appl. Phys. Lett.*, 2000, **76**, 3555.
- 23 Guo, T., Nikolaev, P., Rinzler, A. G., Tomanek, D., Colbert, D. T. and Smalley, R. E., *J. Phys. Chem.*, 1995, **99**, 10694.
- 24 Thess, A., Lee, R., Nikolaev, P., Dai, H., Petit, P., Robert, J., Xu, C., Hee Lee, Y., Kim, S. G., Rinzler, A. G., Colbert, D. T., Scuseria, G. E., Tomanek, D., Fischer, J. E. and Smalley, R. E., *Science*, 1996, **273**, 483.
- 25 Hornbostel, B., Haluska, M., Cech, J., Dettlaff, U. and Roth, S., *Arc Discharge And Laser Ablation Synthesis Of Singlewalled CNTs*, Springer, Netherlands, 2006.
- 26 Yudasaka, M., Fokai, F., Takahashi, K., Yamada, R., Sensui, N., Ichihashi, T. and Iijima, S., *J. Phys. Chem. B*, 1999, **103**, 3576.
- 27 Guo, T., Nikolaev, P., Thess, A., Colbert, D. T. and Smalley, R. E., *Chem. Phys. Lett.*, 1995, **243**, 49.
- 28 Nikolaev, P., Bronikowski, M., Bradley, R. K., Rohmund, F., Colbert, D. T., Smith, K. A. and Smalley, R. E., *Chem. Phys. Lett.*, 1999, **313**, 91.
- 29 Bronikowski, M. J., Willis, P. A., Colbert, D. T., Smith, K.A. and Smalley, R. E., *J. Vac. Sci. Technol. A*, 2001, **19**, 1800.
- 30 Smalley, R. E. and Yakobson, B. I., *Solid State Commun.*, 1998, **107**, 597.
- 31 Dresselhaus, M. S., Dresselhaus, G. and Saito, R., *Phys. Rev. B*, 1992, **45**, 6234.
- 32 www.ccnano.com, checked 30th March 2009.
- 33 Dresselhaus, M. S., Dresselhaus, G. and Eklund, P. C., *Science of Fullerenes and Carbon Nanotubes*, Academic Press, New York, 1996.
- 34 Saito, R., Fujita, M., Dresselhaus, M. S. and Dresselhaus, G., *Appl. Phys. Lett.*, 1992, **60**, 2204.

-
- 35 Dresselhaus, M., Dresselhaus, G., Eklund, P. and Saito, R., *Physics World*, 1998, 33.
- 36 Mann, D., Javey, A., Kong, J., Wang, Q. and Dai, H., *Nano Lett.*, 2003, **3**, 1541.
- 37 in het Panhuis, M., *J. Mater. Chem.*, 2006, **16**, 3598.
- 38 White, C. T. and Todorov, T. N., *Nature*, 1998, **393**, 240.
- 39 Dettlaff-Weglikowska, U., Skakalov, V., Graupner, R., Jhang, S. H., Kim, B. H., Lee, H. J., Ley, L., Park, Y. W., Berber, S., Tomanek, D. and Roth, S., *J. Am. Chem. Soc.*, 2005, **127**, 5125.
- 40 Ericson, L. M., Fan, H., Peng, H. W., Davis, V. A., Zhou, W., Sulpizio, J., Wang, Y. H., Booker, R., Vavro, J., Guthy, C., Parra-Vasquez, A. N. G., Kim, M. J., Ramesh, S., Saini, R. K., Kittrell, C., Lavin, G., Schmidt, H., Adams, W. W., Billups, W. E., Pasquali, M., Hwang, W. F., Hague, R. H., Fischer, J. E. and Smalley, R. E., *Science*, 2004, **305**, 1447.
- 41 Baughman, R. H., Zakhidov, A. A. and de Heer, W. A., *Science*, 2002, **297**, 787.
- 42 Yao, Z., Kane, C. L. and Dekker, C., *Phys. Rev. Lett.*, 2000, **84**, 2941.
- 43 Durkop, T., Getty, S. A., Cobas, E. and Fuhrer, M. S., *Nano Lett*, 2004, **4**, 35.
- 44 Javey, A., Guo, J., Wang, Q., Lundstrom, M. and Dai, H., *Nature*, 2003, **424**, 654.
- 45 in het Panhuis, M., Growisanker, S., Vanesko, D. J., Mire, C. A., Jia, H., Xie, H., Baughman, R. H., Musselman, I. H., Gnade, B. E., Dieckmann, G. R. and Draper, R. K., *Small*, 2005, **1**, 820.
- 46 Chattopadhyay, D., Galeska, I. and Papadimitrakopoulos, F., *J. Am. Chem. Soc.*, 2003, **125**, 3370.
- 47 Maeda, Y., Kimura, S. -I., Kanda, M., Hirashima, Y., Hasegawa, T., Wakahara, T., Lian, Y., Nakahodo, T., Tsuchiya, T., Akasaka, T., Lu, J., Zhang, X., Gao, Y., Yu, Y., Nagase, S., Kazaoui, S., Minami, N., Shimizu, T., Tokumoto, H. and Saito, R., *J. Am. Chem. Soc.*, 2005, **127**, 10287.
- 48 Ménard-Moyon, C., Izard, N., Doris, E. and Mioskowski, C., *J. Am. Chem. Soc.*, 2006, **128**, 6552.
- 49 An, L., Fu, Q., Lu, C. and Liu, J., *J. Am. Chem. Soc.*, 2004, **126**, 10520.
- 50 Strano, M. S., Dyke, C. A., Usrey, M. L., Barone, P. W., Allen, M. J., Shan, H., Kittrell, C., Hauge, R. H., Tour, J. M. and Smalley, R. E., *Science*, 2003, **301**, 1519.

-
- 51 Qian, P., Wu, Z., Diao, P., Zhang, G., Zhang, J. and Liu, Z., *J. Phys. Chem. C*, 2008, **112**, 13346.
- 52 Treacy, M. M. J., Ebbesen, T. W. and Gibson, J. M., *Nature*, 1996, **381**, 678.
- 53 Yu, M. F., Files, B. S., Arepalli, S. and Ruoff, R. S., *Phys. Rev. Lett.*, 2000, **84**, 5552.
- 54 Gao, G., Çağın, T. and Goddard, W. A., *Nanotechnology*, 1998, **9**, 184.
- 55 Yu, M. F., Lourie, O., Dyer, M. J., Moloni, K., Kelly, T. F. and Ruoff, R. S., *Science*, 2000, **287**, 637.
- 56 Dalton, A. B., Collins, S., Muñoz, E., Razal, J. M., Ebron, V. H., Ferrais, J. P., Coleman, J. N., Kim, B. G. and Baughman, R. H., *Nature*, 2003, **423**, 703.
- 57 Zhang, M., Fang, S., Zakhidov, A. A., Lee, S. B., Aliev, A. E., Williams, C. D., Atkinson, K. R. and Baughman, R. H., *Science*, 2005, **309**, 1215.
- 58 Baughman, R. H., Zakhidov, A. A. and de Heer, W., *Science*, 2002, **297**, 787, and references therein.
- 59 Kish, L. B., *Phys. Lett. A*, 2002, **305**, 144.
- 60 Biercuk, M. J., Llaguno, M. C., Radosavljevic, M., Hyun, J. K., Johnson, A. T. and Fischer, J. E., *Appl. Phys. Lett.*, 2002, **80**, 2767.
- 61 Vigolo, B., Pénicaud, A., Coulon, C., Sauder, C., Pailler, R., Journet, C., Fischer, J. E. and Smalley, R. E., *Science*, 2000, **290**, 1331.
- 62 Baughman, R. H., Cui, C. X., Zakhidov, A. A., Iqbal, Z., Barisci, J. N., Spinks, G. M., Wallace, G. G., Mazzoldi, A., De Rossi, D., Rinzler, A. G., Jaszinski, O., Roth, S. and Kertesz, M., *Science*, 1999, **284**, 1340.
- 63 Hulanicki, A., Glab, S. and Ingman, F., *Pure & Appl. Chem.*, 1991, **63**, 1247.
- 64 Mandelis, A., *Physics, Chemistry and Technology of Solid State Gas Sensor Devices*, Wiley, New York, 1993.
- 65 Zhang, T., Mubeen, S., Myung, N. V. and Deshusses, M. A., *Nanotechnology*, 2008, **19**, 332001.
- 66 Bradley, K., Cumings, J., Star, A., Gabriel, J. -C., P. and Grüner, G., *Nano Lett.*, 2003, **3**, 639.
- 67 Tans, S. J., Verschueren, A. R. M. and Dekker, C., *Nature*, 1998, **393**, 49.
- 68 Martel, R., Schmidt, T., Shea, H. R., Hertel, T. and Avouris, P., *Appl. Phys. Lett.*, 1998, **73**, 2447.
- 69 Collins, P. G., Bradley, K., Ishigami, M. and Zettl, A., *Science*, 2000, **287**, 1801.

-
- 70 Kang, D., Park, N., Ko, J., Bae, E. and Park, W., *Nanotechnology*, 2005, **16**, 1048.
- 71 Kong, J., Franklin, N. R., Zhou, C., Chapline, M. G., Peng, S., Cho, K. and Dai, H., *Science*, 2000, **287**, 622.
- 72 Lee, R. S., Kim, H. J., Fischer, J. E., Thess, A. and Smalley, R. E., *Nature*, 1997, **388**, 255.
- 73 Shim, M., Javey, A., Shi Kam, N. W. and Dai, H., *J. Am. Chem. Soc.*, 2001, **123**, 11512.
- 74 www.solid-state.com, checked 25th April 2009.
- 75 Sberveglieri, G., Groppelli, S. and Nelli, P., *Sensor. Actuat. B-Chem.*, 1991, **24**, 18.
- 76 Shimizu, Y. and Egashira, M., *MRS Bull.*, 1999, **24**, 18.
- 77 Someya, T., Small, J., Kim, P., Nuckolls, C. and Yardley, J. T., *Nano Lett.*, 2003, **3**, 877.
- 78 Star, A., Han, T. -R., Gabriel, J. -C. P., Bradley, K. and Grüner, G., *Nano Lett.*, 2003, **3**, 1421.
- 79 Kong, J., Chapline, M. G. and Dai, H., *Adv. Mater.*, 2001, **13**, 1384.
- 80 Star, A., Joshi, V., Skarupo, S., Thomas, D. and Gabriel, J. C. P., *J. Phys. Chem. B*, 2006, **110**, 21014.
- 81 Qi, P., Vermesh, O., Grecu, M., Javey, A., Wang, Q., Dai, H., Peng, S. and Cho, K. J., *Nano Lett.*, 2003, **3**, 347.
- 82 Valentini, L., Armentano, I., Kenny, J. M., Cantalini, C., Lozzi, L. and Santucci, S., *Appl. Phys. Lett.*, 2003, **82**, 961.
- 83 Li, J., Lu, Y. J., Ye, Q., Cinke, M., Han, J. and Meyyappan, M., *Nano Lett.*, 2003, **3**, 929.
- 84 Suehiro, J., Zhou, G. B. and Hara, M., *J. Phys. D: Appl. Phys.*, 2003, **36**, 109.
- 85 Lee, C. Y., Baik, S., Zhang, J. Q., Masel, R. I. and Strano, M. S., *J. Phys. Chem. B*, 2006, **110**, 11055.
- 86 Kordás, K., Mustonen, T., Tóth, G., Jantunen, H., Lajunen, M., Soldano, C., Talapatra, S., Kar, S., Vajtai, R. and Ajayan, P. M., *Small*, 2006, **2**, 1021.
- 87 Bekyarova, E., Davis, M., Burch, T., Itkis, M. E., Sunshine, S. and Haddon, R. C., *J. Phys. Chem. B*, 2004, **108**, 19717.

-
- 88 An, K. H., Jeong, S. Y., Hwang, H. R. and Lee, Y. H., *Adv. Mater.*, 2004, **16**, 1005.
- 89 Oakley, J. S., Wang, H. T., Kang, B. S., Wu, Z., Ren, F., Rinzler, A. G. and Pearton, S. J., *Nanotechnology*, 2005, **16**, 2218.
- 90 Sotiropoulou, S. and Chaniotakis, N. A., *Anal. Bioanal. Chem.*, 2003, **375**, 103.
- 91 Lin, Y., Lu, F., Tu, Y. and Ren, Z., *Nano Lett.*, 2004, **4**, 191.

CHAPTER 2

EXPERIMENTAL

2.1 Materials

2.1.1 Water

Water was purified by reverse osmosis and by passage through a Milli-Q reagent water system. The resistivity was always above 18 MΩ cm.

2.1.2 Organic solvents

The organic solvents used in this study are summarised in Table 2.1, together with their purity and source. All solvents used as received.

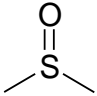
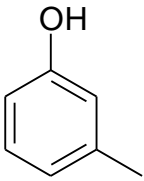
Solvent	Formula	Purity	Source
Dimethyl sulfoxide (DMSO)		≥ 99 %	Alfar Aesar
<i>m</i> -cresol		≥ 99 %	Riedel-de Haën
ethanol	CH ₃ CH ₂ OH	analytical grade	Fisher
methanol	CH ₃ OH	analytical grade	Fisher

Table 2.1 Summary of the solvents used, with their formula, purity and source.

2.1.3 Carbon nanotubes and silver nanowires

SWNTs were prepared by the HiPco method and purchased from Carbon Nanotechnologies Inc., Houston, TX.

MWNTs produced by the Arc discharge and CVD methods have been supplied by researchers at the Instituto de Carboquímica, Zaragoza, Spain. CVD MWNTs were

prepared using a cobalt-molybdenum sol-gel catalyst, with a molybdenum/cobalt ratio of 30. Full details can be found in reference 1. Arc MWNTs were prepared by the arc-discharge induced sublimation of pure graphite rods under a helium atmosphere of 66 kPa using a current of 60 A and a voltage of 25 V.² Sample material was collected from the inner core of the formed cathodic deposit, which consisted of straight, well-graphitised MWNTs of micrometer lengths and diameters of 20 - 30 nm.

MWNTs and DWNTs prepared by the CVD method were purchased from Nanocyl, Belgium.

Silver nanowires (Ag NWs) were purchased from PlasmaChem GmbH, Berlin, Germany. Three samples of NWs were obtained, with lengths of 40 - 50 μm and diameters of 50, 100 and 200 nm.

2.1.4 *Gelling agents*

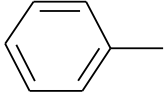
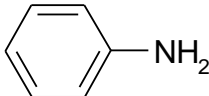
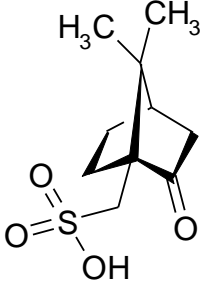
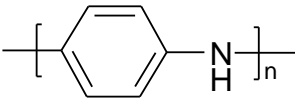
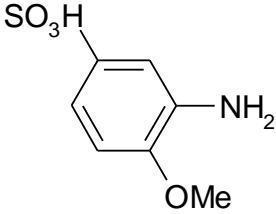
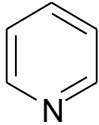
Gellan gum used in this study was a gift from CP Kelco, USA, and used here without further purification.

Agarose (type D5) was purchased from Hispanagar, Spain. This agarose forms gels on cooling at 32 - 40 °C depending on concentration, with the lowest gelling concentration at ~ 0.5 % w/v. D5 is a 'high strength' agarose gel, with a strength of 3200 g cm^{-2} at a concentration of 1.5 % w/v.

SeaPrep agarose (hydroxyethylated) was purchased from Lonza, UK. This has a lower strength than the D5 agarose, $\sim 75 \text{ g cm}^{-2}$ at a concentration of 2.0 % w/v, and also has a low gelling and melting temperature.

2.1.5 *Other materials*

Many other materials have also been used throughout this study. These are summarised in Table 2.2.

Material	Formula	Purity	Source
sodium dodecyl sulphate (SDS)	$C_{12}H_{25}-O-\overset{\overset{O}{\parallel}}{\underset{\underset{O}{\parallel}}{S}}-O^- Na^+$	> 99 %	Aldrich
toluene		99 %	Fisher
octadecyltrichlorosilane (OTS)	$CH_3(CH_2)_{16}CH_2SiCl_3$	≥ 90 %	Aldrich
aniline		99 %	Sigma
ammonium persulphate (APS)	$NH_4^+ O^- \overset{\overset{O}{\parallel}}{\underset{\underset{O}{\parallel}}{S}}-O-O-\overset{\overset{O}{\parallel}}{\underset{\underset{O}{\parallel}}{S}}-O^- NH_4^+$	≥ 98 %	Aldrich
(1 <i>S</i>)-(+)-10- camphorsulphonic acid (CSA)		99 %	Aldrich
polyaniline emeraldine (PAni) base $M_w \sim 50,000$		-	Aldrich
3-amino-4-methoxy benzenesulfonic acid (MAS)		98 %	Aldrich
pyridine		≥ 99 %	Sigma
sodium chloride	NaCl	99.5 %	BDH

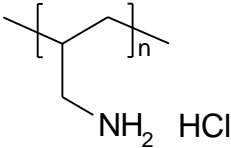
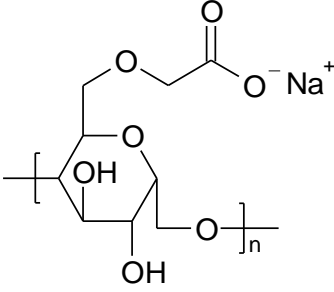
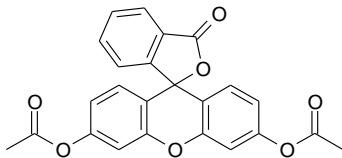
polyallylamine hydrochloride (PAH) $M_w \sim 15,000$		-	Aldrich
carboxymethyl cellulose (CMCell)		-	Fluka
fluorescein diacetate (FDA)		$\geq 98 \%$	Fluka

Table 2.2 Summary of the materials used, with their formula, purity and source.

Biotin-terminated tri(ethylene glycol) hexadecanethiol, purity > 99 %, was purchased from Asemblon, Redmond, WA.

Streptavidin was purchased from Sigma.

Yeast cells were obtained from Allinson's Dried Active Yeast, available at supermarkets.

2.1.6 Substrates for sessile drop evaporation, supported films and inkjet printing

Glass microscope slides (Thermo Scientific) were cleaned in ethanol prior to use. Copper-coated silicon wafers were prepared from silicon wafers sputtered with a 200 nm thick layer of copper, and obtained from Texas Instruments, Richardson, TX.

Hydrophobised silicon wafers were prepared by submerging silicon wafers in a beaker of OTS in toluene, at a concentration of 1.0 % w/v OTS. This was performed in a large bag flushed with nitrogen, and in the presence of phosphorus pentoxide, to remove moisture from the air which causes the polymerisation of OTS. After incubation for 1 hour, the wafers were then washed in toluene and ethanol, before drying in air. The contact angle of a sessile water drop on one of these hydrophobised silicon wafers

was $\sim 110^\circ$, with a contact angle of $\sim 25^\circ$ measured for a water drop on an untreated silicon wafer.

Inkjet printing has been performed on paper, glossy photopaper (Hewlett-Packard (HP)), poly(ethylene terephthalate) (PET) ‘overhead transparency slides’ and gold coated poly(vinylidene fluoride) (Au-PVDF, supplied by the Intelligent Polymer Research Institute (IPRI), University of Wollongong, Australia).

2.2 Methods

The majority of the work in this thesis has been performed at the University of Hull. However, some of this work has been undertaken at other locations, mainly at the Instituto de Carboquímica, Zaragoza, Spain (two periods of three weeks), and at the IPRI, University of Wollongong, Australia (three months). It will be made clear both in this chapter and throughout the rest of the thesis where work has either been performed at another location, either by the author or by a collaborator.

2.2.1 Polymer and polymer-CNT composite synthesis

2.2.1.1 Synthesis of PANi and PANi-MWNT composites

In situ polymerisation of PANi-MWNT composites was carried out according to the method of Kane-Maguire and co-workers.³ Arc or CVD MWNTs (provided by the Instituto de Carboquímica, Zaragoza, Spain) and aniline (An) monomer were added to 100 mL 1 M CSA with stirring. To this, APS dissolved in 5 mL 1 M CSA was slowly added, with continuous stirring. Molar ratios were An:CSA = 0.1:1, An:APS = 4.47:1, and MWNTs were added at a concentration of 10 % w/w with respect to An. After 1 ½ hours, the resulting mixture was filtered under vacuum, washed with 400 mL 0.1 M CSA and dried at room temperature under vacuum for 24 hours. Synthesis of PANi was carried out using an identical procedure, but without the addition of MWNTs. This work was carried out at the Instituto de Carboquímica, Zaragoza, Spain.

2.2.1.2 Synthesis of PMAS

PMAS was synthesised according to the method of Shimizu and co-workers.⁴ MAS (0.2 moles) was dissolved in 2.5 mL 2.5 M pyridine with stirring and in an ice/water bath, forming a yellow/green solution. To this, 4.5 mL APS (0.5 moles) was

added drop wise over 20 minutes, which resulted in a colour change to dark brown, and an increase in viscosity. The reaction proceeded over 17 hours, at which point the polymer was filtered (Whatman filter paper, 15 - 20 μm pore size) under vacuum and washed with 100 mL methanol. After drying under vacuum for 24 hours, the polymer was ground to a fine powder.

2.2.1.3 Synthesis of PMAS-PAni-MWNT composites

PMAS-PAni-MWNT composites were prepared by first dispersing CVD MWNTs (Nanocyl, Belgium) in 1.7 % w/v PMAS solution using ultrasonic conditions as outlined later. Various concentrations of MWNTs were employed to achieve different loading fractions in the final composite. From this point, the composite synthesis is based on the method for synthesising PMAS-PAni composites, by Masdarolomoor and co-workers.⁵ 100 μL 1 M APS in 1 M HCl was added rapidly to the PMAS-MWNT dispersion, which also had 0.8 M An monomer added to it. This was stirred for 5 hours, before the resulting dispersions underwent a cycle of washing (with Milli-Q water) and centrifuging three times, to purify the composite. This work was carried out at the IPRI, Wollongong, Australia.

2.2.2 Dispersion preparation

All dispersions have been prepared through ultrasonication, using a Branson Digital Sonifier Model 450 with a tip of 5 mm diameter.

2.2.2.1 Preparation of CNT dispersions

SDS-CNT dispersions: CNTs (0.7 mg) were added to 3.0 mL SDS solution (0.05 - 1.00 % w/v) and exposed to ultrasound for 3 minutes with pulses of 0.5 s on, 0.5 s off. The sonifier operated at 20 % amplitude, delivering up to 16 W. The samples were placed in cold water baths to prevent excessive heating of the dispersion. Centrifugation of the SDS-CNT dispersions was achieved with an Eppendorf Mini-spin centrifuge, operating at 6000 rpm for 30 minutes.

Gellan gum-CNT dispersions: These were prepared using the same sonicating procedure as for SDS-CNT dispersions, but with various concentrations of CNTs and gellan, described in the relevant chapter. Centrifugation was achieved as described for the SDS-CNT dispersions. Gellan gum-CNT dispersions for inkjet printing were filtered prior to printing, first through glass wool under vacuum, and then through a Millex-LS

polytetrafluoroethylene (PTFE) inline syringe filter (Millipore Corporation) with a pore size of 5 μm .

PMAS-CNT dispersions: These were prepared at various concentrations of CNTs and PMAS, described in the relevant chapter. Dispersions were exposed to ultrasound for 3 minutes with pulses of 2 s on, 1 s off. The sonifier operated at 20 % amplitude, delivering up to 16 W. PMAS-CNT dispersions for inkjet printing were filtered as described for the gellan gum-CNT dispersions.

2.2.2.2 Preparation of Ag NW dispersions

Agarose solutions (0.25 - 1.25 % w/v) were first prepared by heating to 70 °C on a hotplate, with constant stirring. Ag NW's (0.10 - 1.00 % w/v) were dispersed in the hot agarose solutions for 3 minutes with pulses of 0.5 s on, 0.5 s off. The sonifier operated at 20 % amplitude, delivering up to 16 W. The samples were placed in hot water baths, to prevent the agarose from gelling. Dispersions were briefly degassed in an ultrasonic bath for several seconds, before returning to a hot plate to prevent the dispersion from gelling.

2.2.2.3 Yeast cell dispersions

Yeast cells were dispersed in water at a concentration of 2.0 % w/v. Samples were exposed to ultrasound for 30 s with pulses of 0.5 s on, 0.5 s off. The sonifier operated at 10 W. The samples were placed in cold water baths to prevent excessive heating of the dispersion.

After their dispersion in water, yeast cells were then coated in PAH and CMCell using the layer-by-layer (LbL) technique. First, the yeast cells were centrifuged (2 minutes at 2000 rpm) and the supernatant was replaced with Milli-Q water, a process that was repeated three times to wash the cells. The aqueous supernatant was then replaced with PAH solution (0.4 % w/v in 0.5 M NaCl), and the yeast cells were incubated with shaking over 20 minutes. The cells were then washed and centrifuged, following the same procedure as described earlier. Incubation of the cells then took place with CMCell (0.4 % w/v in 0.5 M NaCl) for 20 minutes with shaking, followed by the same washing procedure. Finally, the coated yeast cells were suspended in a warm agarose solution (~ 45 °C), and diluted to a concentration of 0.20 % w/v for dielectrophoresis (DEP).

2.2.3 *Drop deposition*

Drop deposition was carried out with a Deerac Fluidics Equator single-tip liquid handling system, dispensing drops of 100 nL from a reservoir containing freshly prepared solutions or dispersions. Drops were deposited onto untreated silicon, glass, copper sputtered silicon and OTS-treated silicon wafers.

2.2.4 *Inkjet printing*

2.2.4.1 *Inkjet printing gellan gum-CNT and PMAS-CNT dispersions*

Filtered gellan gum-CNT and PMAS-CNT dispersions were printed with a HP Deskjet 690C printer. Cartridges holding the black ink (HP 51629A) for this printer were emptied and flushed several times with Milli-Q water, before filling with the composite dispersions and re-sealing. Patterns to be printed were designed using Microsoft Word and PowerPoint, and printed onto paper and PET substrates.

2.2.4.2 *Inkjet printing PMAS-PAni-MWNT dispersions*

PMAS-PAni-MWNT composites were printed, as-prepared, with a Dimatix materials deposition system (Fujifilm Dimatix). Composites were loaded into Dimatix materials cartridges, which have a capacity of 1.5 mL and do not require any cleaning or preparation. Some of the patterns that were printed were taken from the Dimatix software, others were converted from files such as jpegs and tifs into Dimatix-compatible monochrome bitmap files. Printing was performed onto glossy photopaper, PET substrates and Au-PVDF. This work was carried out at the IPRI, University of Wollongong, Australia.

2.2.5 *Dielectrophoretic assembly in agarose solutions*

2.2.5.1 *DEP cell*

DEP cells were constructed from a glass microscope slide (Thermo Scientific), to which four copper electrodes (0.22 mm thick) were adhered. A photograph and schematic of the cell can be found in Chapter 6.

2.2.5.2 *Dielectrophoretic assembly of Ag NWs in agarose solution*

In the dielectrophoretic assembly of Ag NWs in agarose solution, the DEP cell was placed on a microscope heating stage and heated to 55 °C. Several drops of the hot agarose/NW suspension were then placed between the four electrodes, and covered with

a warm glass microscope cover slip. The depth of the sample within the cell was approximately 0.40 mm. Two of the parallel electrodes on the cell were connected to an Agilent 33220A Waveform Generator, which was in turn connected to an amplifier (Trek model 601C). An alternating current (AC) electric field was applied to the sample, at a frequency of 5 kHz and with a voltage (peak-to-peak) of 50 V cm^{-1} (after amplification). The voltage was ramped in 50 V cm^{-1} increments, until either dielectrophoretic assembly between the electrodes was observed under a microscope, or the field became so large that a flow of solution at the electrodes started to occur, preventing any assembly. Once dielectrophoretic assembly had taken place, the voltage was lowered to 50 V cm^{-1} while the sample was cooled to $\sim 20 \text{ }^\circ\text{C}$ to set the gel. A schematic representation of the dielectrophoretic assembly of Ag NWs is shown in Chapter 6.

2.2.5.3 Dielectrophoretic assembly of yeast cells in agarose solution

In the dielectrophoretic alignment of yeast cells in agarose solution, the DEP cell was placed on a microscope heating stage and heated to $45 \text{ }^\circ\text{C}$. Several drops of the warm yeast/agarose suspension were then placed between the four electrodes, and covered with a glass microscope cover slip. The depth of the sample within the cell was approximately 0.40 mm. Dielectrophoretic assembly was achieved with the same experimental set-up as described for the assembly of Ag NWs and using the same protocol, but the frequency of the field here was 20 kHz. Once dielectrophoretic assembly had taken place, the voltage was lowered to 100 V cm^{-1} while the sample was cooled to $\sim 10 \text{ }^\circ\text{C}$ to set the gel. A schematic representation of the dielectrophoretic assembly of yeast cells is shown in Chapter 6.

2.3 Characterisation

2.3.1 Characterisation of solutions and dispersions

2.3.1.1 UV-visible spectroscopy

UV-visible spectra of all SDS-CNT, PMAS-CNT, PAni-CNT and gellan gum-CNT dispersions were recorded with a Perkin-Elmer Unicam UV3 spectrometer, in quartz cuvettes of 1 cm path length. A scan speed of 120 nm min^{-1} was typically employed. UV-visible spectra of the PMAS-PAni-MWNT composites were recorded with a Shimadzu UV-1601 Spectrophotometer. This was carried out at the IPRI,

University of Wollongong, Australia. Baseline measurements were recorded of the solvent (water, organic solvent) without any added dispersant or dispersant-CNT added.

2.3.1.2 Contact angle analysis

Contact angle analysis of SDS-CNT dispersions was carried out *in situ* at the Deerac Fluidics Equator, augmented with a digital camera and light source, shown in Figure 2.1. Images of the drops were captured every 10 s after deposition until evaporation was complete. Contact angles were determined from the resulting images, where an uncertainty of 1 - 3 degrees was calculated from error analysis.

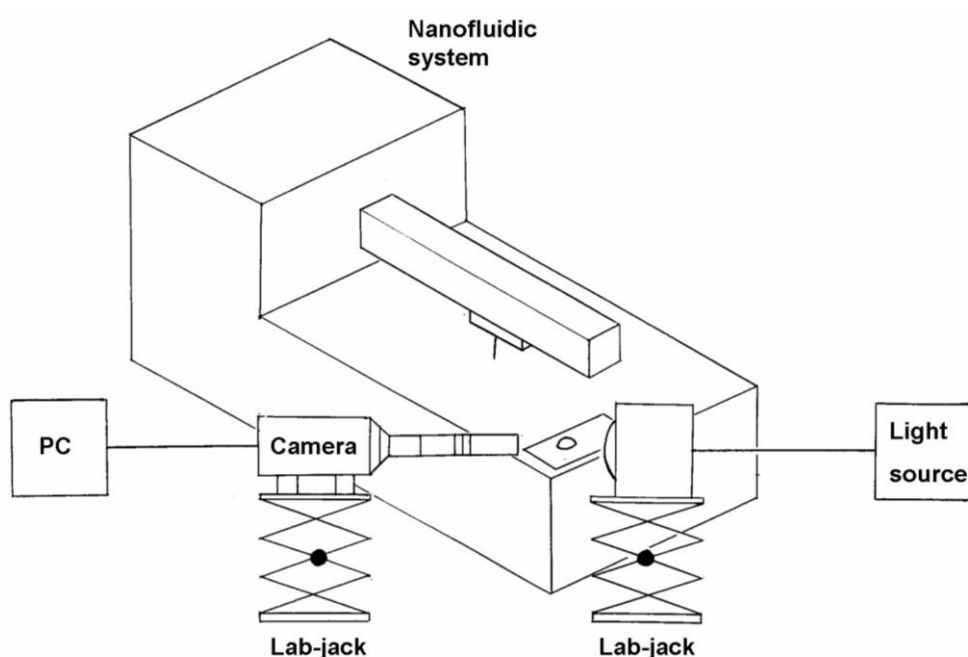


Figure 2.1 Experimental set-up for the measurement of contact angles of sessile drops at the Deerac nanofluidic system.

2.3.1.3 Rheology

Rheology was used to determine the relative viscosities of PMAS-PAni-MWNT dispersions for inkjet printing, and agarose dispersions for dielectrophoresis.

PMAS-PAni-MWNT dispersions: The viscosity of PMAS-PAni-MWNT dispersions was measured using an Anton Paar Physica MCR301 Rheometer, using the parallel plate geometry. Gap spacing 0.5 mm, sample volume 200 μL , shear rate

increased from 0.1 - 100 s⁻¹, temperature 25 °C. This work was carried out at the Department of Engineering, University of Wollongong, Australia.

Agarose dispersions: The viscosity of agarose solutions was measured using a Bohlin Instruments CV0 120 High Resolution Rheometer, using the cone and plate geometry. Gap spacing 150 µm, sample volume 1.40 ml, shear rate increased from 10 - 1000 s⁻¹, temperature 45 °C (SeaPrep agarose) and 55 °C (D5 agarose).

2.3.1.4 Surface tension

The surface tension of PMAS-PAni-MWNT composites was measured via the pendant drop method using a Drop Shape Analyser by Krüss Instruments, model DSA100. The surface tension was given directly by the DSA software, and an average surface tension is quoted from 25 measurements for each composite. This work was carried out at the IPRI, University of Wollongong, Australia.

2.3.1.5 Gas phase chromatography

Molecular weight measurements of PMAS in solution were made using a Waters Aqueous gas phase chromatography system. This work was carried out by Fatemeh Masdarolomoor of the IPRI, University of Wollongong, Australia.

2.3.1.6 Circular dichroism

Circular dichroism spectra of PAni and PAni-CNT dispersions were recorded using a Jasco J810 circular dichromator. This work was carried out at the Department of Biology, University of York, UK.

2.3.2 Characterisation of supported, free-standing and printed films

2.3.2.1 UV-visible spectroscopy

UV-visible spectra of gellan gum-CNT and PMAS-CNT films printed onto PET substrates were recorded with a Perkin-Elmer Unicam UV3 spectrometer. Spectra of PMAS-PAni-MWNT printed films on PET substrates were recorded with a Shimadzu UV-1601 Spectrophotometer (carried out at the IPRI, University of Wollongong, Australia). Baseline measurements of the bare PET substrate were recorded as a reference.

2.3.2.2 *Circular dichroism*

Circular dichroism spectra of supported PANi-CNT films on glass slides were recorded using a Jasco J810 circular dichromator. This work was carried out at the Department of Biology, University of York, UK.

2.3.2.3 *Raman spectroscopy*

Raman spectra were collected with a Jobin Yvon Horiba high-resolution LabRam Raman inverted spectroscopic microscope spectrometer, with a 632.8 nm laser excitation line.

2.3.2.4 *Thermogravimetric analysis (TGA)*

TGA analysis of the PANi-MWNT composites was carried out with a Setaram TG-DTA 92 thermobalance, burning 10 - 12 mg of powder material in air, at a flow rate of 100 mL min⁻¹. The temperature was ramped at 3 °C min⁻¹ up to 1250 °C.

TGA of the PMAS-PANi-MWNT composites was carried out with a TA Instruments TGA Q500 thermogravimetric analyzer, burning approximately 1 mg of free-standing film in air at a flow rate of 60 mL min⁻¹. The temperature was ramped at 10 °C min⁻¹ up to 800 °C. This work was carried out at the IPRI, University of Wollongong, Australia.

2.3.2.5 *Optical microscopy*

Optical microscopy images were obtained with an Olympus BX51 optical microscope fitted with an Olympus DP50 digital camera. For images of films on glass slides and PET substrates, transmitted light was used. For drops deposited onto opaque substrates, such as the silicon wafers, the microscope was operated in reflected light mode. For the reflected light, a white light source was supplied by a mercury arc lamp. In video capture mode for the analysis of contact angles and the observations of film formation for SDS-CNT films, images were captured at intervals of 1 s.

2.3.2.6 *Transmission electron microscopy (TEM)*

TEM images of the PANi-MWNT composites were obtained on a JEOL 2011 TEM, by Mrs Janice Halder, University of Hull. Diluted composite solutions were first evaporated onto Cu 300 mesh grids.

TEM images of the PMAS-PAni-MWNT composites were obtained by Dr Carol Lynam (IPRI, University of Wollongong, Australia) using a Hitachi H7000 TEM at the University of Sydney, Australia.

2.3.2.7 Scanning electron microscopy (SEM)

Scanning electron microscopy (SEM) of the films from evaporated drops was performed by Dr Joachim Loos of the Eindhoven University of Technology, Eindhoven, Netherlands, using an XL30 ESEM-FEG (FEI Company). The SEM was equipped with a field emission electron source. High vacuum conditions were applied, and a secondary electron detector was used for image acquisition. The SEM was operated in either conventional high or low voltage mode. No additional sample treatment of the films was necessary. Standard acquisition conditions for charge-contrast imaging were as follows: working distance of ~ 5 mm for low voltage mode and ~ 10 mm for high voltage mode, slow scan imaging with approximately 2 min/frame.

2.3.2.8 Cyclic voltammetry

Cyclic voltammetry was carried out in a three electrode cell using a glassy carbon working electrode with platinum mesh auxiliary and Ag/AgCl (0.1 M HCl) reference electrodes using an E-Corder 401 interface and Potentiostat (EDAQ). PMAS-PAni-MWNT composite films were cast onto the glassy electrodes, and a scan rate of 50 mV s^{-1} on the forward and reverse sweeps was employed.

Cyclic voltammetry of the PMAS-PAni-MWNT printed films (on Au-PVDF substrates) was carried out using the same set up as for the cast films, but in 1 M HCl and at a scan rate of 500 mV s^{-1} . All cyclic voltammetry was carried out by Fatemeh Masdarolomoor at the IPRI, University of Wollongong, Australia. Videos of the films were captured with a video camera.

2.3.2.9 Topographical analysis

For the study of the topography of thin SDS-SWNT films deposited onto substrates, a replica of the films was first produced from polydimethylsiloxane (PDMS) using a Sylgard 184 Silicone Elastomer kit. 10 parts of the polymer 'base' were vigorously mixed with 1 part of the curing agent, and degassed before pouring over the substrates. Curing was allowed to occur at room temperature (~ 20 °C) for 48 hours. As this gave an 'inverted' replica of the film on the substrate, true replicas could be

produced by preparing a second mould of the inverted replica using PDMS in the same way. A schematic of this process is shown in Chapter 3.

Topographical analysis of the PDMS replicas of the deposited films was carried out using a scanning white light interferometer (Veeco, Wyko NT1100). Quantitative information of the surface roughness/height of the deposit was obtained using the interferometer software. This work was carried out by Dr Chris Walton, Department of Physics, University of Hull.

2.3.2.10 *Electrical characterisation*

Electrical characterisation of free-standing and printed PMAS-PAni-MWNT, and printed PMAS-SNWT composites was performed with a JANDEL four-point probe resistivity system (model RM2). This method of electrical characterisation is believed to be advantageous, as the measurement errors caused by probe resistance, contact resistance between the probe and the film, and the spreading resistance under each probe are eliminated. Film thickness measurements for free-standing films were made with digital callipers.

Current-voltage (*I-V*) characteristics of printed gellan gum-NT and PMAS-NT films were investigated using an Agilent 33220A waveform generator and a Thurlby Thandar Instruments 1906 Computing Multimeter. The voltage was scanned between two potentials, while the current was measured by the multimeter and recorded directly onto a desktop computer.

Electrical characterisation of the agarose gels with dielectrophoretically aligned Ag NWs was carried out with a Thurlby Thandar Instruments 1906 Computing Multimeter. Humid environments were created by storing the gels in a petri dish lined with damp tissue paper, which was refreshed with Milli-Q water periodically to keep it moist.

2.3.3 *Sensing studies*

Sensing studies on printed gellan gum-CNT and PMAS-CNT printed films were made by recording the electrical responses of the printed films as they were subjected to a range of analytes in a controlled environment. A DC voltage of 10 V was applied to the films with an Agilent 33220A waveform generator, and the current measured with a

Thurlby Thandar 1906 Computing Multimeter, connected to a PC to log the data over time. Sensing studies were carried out in two different ways, under *static* and *dynamic* conditions, defined as follows:

Static conditions: the film was placed in a sealed chamber, into which different volumes of the analyte were introduced and allowed to evaporate at ambient conditions. This is shown schematically in Figure 2.2.

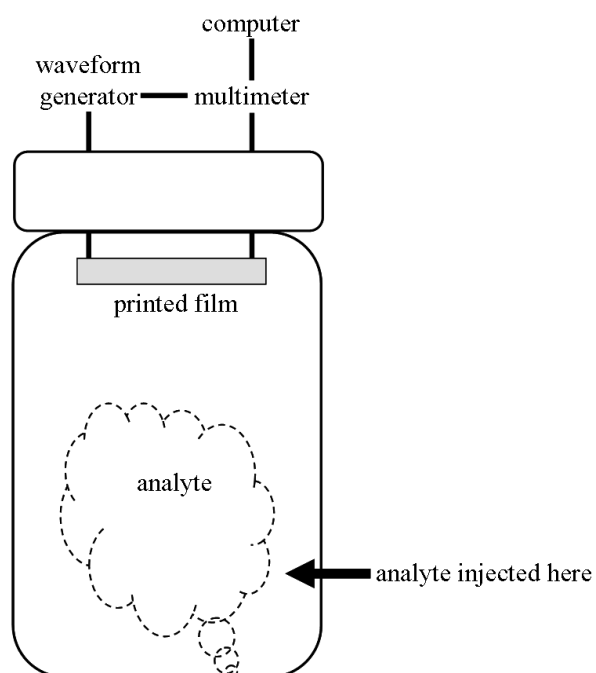


Figure 2.2 Schematic of the experimental set-up for printed film sensing studies under static conditions.

Dynamic conditions: the film was placed in a chamber which was fitted with an inlet and an outlet. The inlet was connected to a glass vessel placed upon a hotplate, into which different volumes of the analyte were introduced where they evaporated within 1 - 2 s. This vessel was also connected to a nitrogen cylinder, which provided the carrier gas, with the gas flow carrying the analyte vapour from the glass vessel to the film in the sensing chamber. The outlet on the sensing chamber was connected to a flow meter (pre-calibrated) to determine the flow rate through the system. This is shown schematically in Figure 2.3.

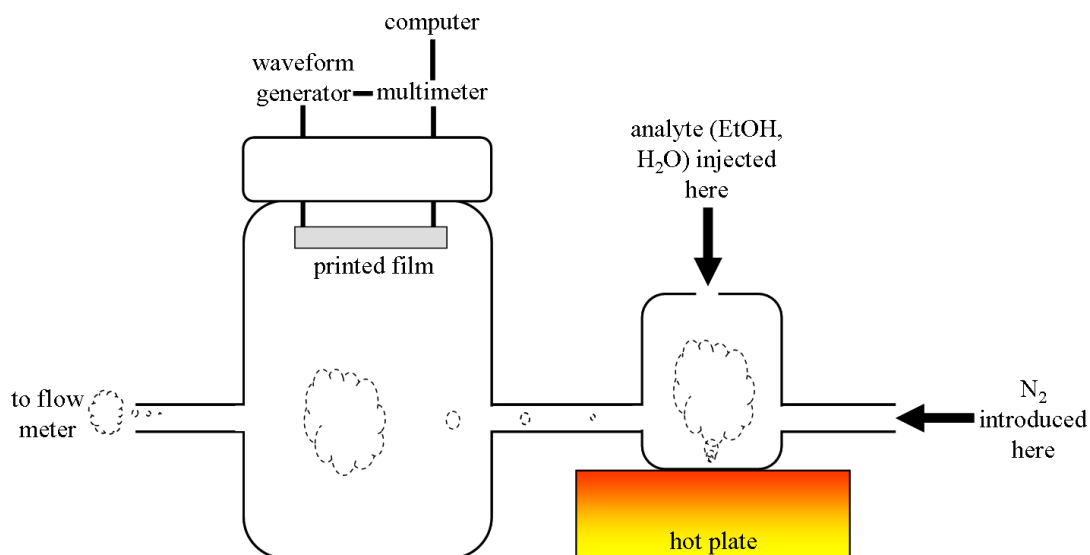


Figure 2.3 Schematic of the experimental set-up for printed film sensing studies under dynamic conditions.

2.3.4 Treatment of living yeast cell strings

2.3.4.1 Fixing yeast cell strings

After dielectrophoretic assembly of the living yeast cells into strings, the agarose gel was incubated in a PAH solution (0.4 % w/v in 0.5 M NaCl) for three hours. The gel was then washed with Milli-Q water, and heated to 45 °C to re-melt the gel, freeing the strings from the gel. The agarose solution/yeast cell strings were collected, diluted with Milli-Q water and then centrifuged and washed with water three times, before the yeast cell strings were suspended in water.

2.3.4.2 Imaging yeast cell strings

For cell imaging, a stock solution of FDA was first prepared in acetone at a concentration of 10 mg mL⁻¹, and stored in the freezer. 20 µL of this FDA solution was added to 1 mL of the yeast cell strings in water, and incubated with shaking for 20 minutes. The cells were then centrifuged and washed with water three times, to remove excess FDA from the supernatant solution. Finally, the cells were suspended in water before placing a small drop of the suspension on a microscope slide and covering with a cover slip. Fluorescence microscopy was carried out with an Olympus BX51 optical microscope fitted with an Olympus DP50 digital camera. A mercury arc lamp was

passed through a fluorescein isothiocyanate filter set (U-MWIBA2), with filters for excitation wavelengths of 470 - 490 nm and emission wavelengths of 510 - 540 nm.

2.4 References

- 1 Pérez-Mendoza, M., Vallés, C., Maser, W. K., Martinez, M. T. and Benito, A. M., *Nanotechnology*, 2005, **16**, S224.
- 2 Lafuente, E., Piñol, M., Oriol, L., Muñoz, E., Benito, A. M., Maser, W. K., Dalton, A. B., Serrano, J. L. and Martinez, M. T., *Mater. & Sci. Eng. C*, 2006, **26**, 1198.
- 3 Kane-Maguire, L. A. P., MacDiarmid, A. G., Norris, I. D., Wallace, G. G. and Zheng, W., *Synth. Met.*, 1999, **106**, 171.
- 4 Shimizu, S., Saitoh, T., Uzawa, M., Yuasa, M., Yano, K., Maruyama, T. and Watanabe, K., *Synth. Met.*, 1997, **85**, 1337.
- 5 Masdarolomoor, F., Innis, P. C., Ashraf, S., Kaner, R. B. and Wallace, G. G., *Macromol. Rapid. Commun.*, 2006, **27**, 1995.

CHAPTER 3

CARBON NANOTUBE NETWORK FORMATION FROM AN EVAPORATING SESSILE DROP

3.1 Introduction

This chapter is devoted to the fabrication of thin carbon nanotube-containing films, formed from the evaporation of a sessile drop of a nanotube dispersion deposited onto a substrate. This represents one of the simplest methods to process a carbon nanotube dispersion into thin films. We examine the factors controlling the film formation, and discuss their morphology and properties. The mechanism of film formation is studied through video microscopy and contact angle analysis, while film morphology is analysed using scanning electron microscopy, Raman spectroscopy and white light interferometry. This chapter focuses on two important parameters affecting film formation: dispersion treatment and substrate hydrophobicity. We discuss the interactions between carbon nanotubes and surfactants, and the process of evaporation of carbon nanotube dispersions on solid substrates in relation to the formation of carbon nanotube films.

3.1.1 *Interactions between carbon nanotubes and surfactants*

Carbon nanotubes (CNTs) have very high van der Waals attraction energies, in the region of $500 \text{ eV } \mu\text{m}^{-1}$ of tube-tube contact,¹ which makes them difficult to unbundle from one another. They are also extremely hydrophobic, and readily aggregate into ropes and bundles when dispersed in water and other solvents. For the non-covalent functionalisation of CNTs, surfactants are a system widely recognised for their ability to disperse insoluble matter in aqueous dispersions, as they do in detergents and cleaning products. They are therefore a logical choice for studying the dispersion of CNTs. Surfactants, through their amphiphilic nature, are able to self-assemble on the surface of the nanotube, providing steric and/or electrostatic repulsion. The literature regarding the interactions between CNTs and surfactants is supplemented by various studies on

surfactant adsorption at planar graphite interfaces, which due to the similarities between graphite and CNTs, are also discussed here.

The surfactant that has perhaps been most studied in relation to its adsorption onto CNTs and their subsequent dispersions, is sodium dodecyl sulphate (SDS). Several groups have attempted an estimation of the concentrations of SDS and CNTs for optimum dispersions. Vigolo and co-workers suggest that the optimum concentrations are 0.35 % w/v nanotubes in 1.00 % w/v SDS, as at lower surfactant concentrations it is suggested that there is insufficient SDS present to give a stable dispersion (the nanotubes sediment within a few minutes). At higher concentrations it is reported that depletion flocculation, due to an increased concentration of SDS micelles, causes the nanotubes to aggregate and fall out of solution.² However, another study states that the optimum concentrations for stable dispersions are 0.50 % w/v nanotubes and 2.00 % w/v SDS.³ The difference in optimum concentrations quoted by these two reports may be attributed to subtly different mixing protocols, or different types of nanotubes with various diameters used in the studies.

Dispersions with CNTs typically consist of small bundles of nanotubes, but one study reports the isolation of individual SWNTs encased within cylindrical SDS micelles.⁴ This was achieved through a high-speed mixing, sonication and centrifugation regime, which separates higher density nanotube bundles from lower density individual nanotubes.⁴ Through this method, dispersions of nanotubes at concentrations as high as 2.00 % w/v in solutions containing around 1.00 % w/v SDS were prepared. They had good stability, avoiding flocculation at temperatures up to 70 °C, sodium chloride concentrations of up to 200 mM and magnesium chloride concentrations up to 10 mM.

On planar graphite interfaces, SDS has been observed as forming hemicylindrical aggregates at concentrations below the critical micelle concentration (CMC).^{5, 6} The CMC is the concentration at which a surfactant is present in sufficient concentration to assemble into organised structures. These hemicylindrical assemblies formed parallel to each other, and their size and spacing could be controlled through the concentrations of the surfactant and additional salt, with a minimum spacing between structures obtained at approximately twice the CMC. The nature of the adsorption of SDS onto the surfaces of CNTs has been the focus of other groups. For example, it has been observed that the surfactant forms hemicylinders on the surface of the CNTs at concentrations above the CMC, but not below this concentration.⁷ This was verified by

transmission electron microscopy, where the size of the hemicylinders was in good agreement with theoretical predictions for structures of this type. Interestingly, the hemicylinders did not form parallel to the axis of the nanotube, instead forming either perpendicularly or in single or double helices at angles of 2° to 30° relative to the nanotube axis. As no cylinders were observed at angles greater than 30° , this would suggest that the hemicylindrical formation might follow the graphitic network dictated by the chiral vector of the nanotube. However to confirm this, samples of pure zigzag, armchair or chiral nanotubes with known vectors would have to be produced and analysed. The presence of hemicylinders has not been observed by all authors however. Moore and co-workers observe a uniform monolayer of SDS on the surfaces of SWNTs,⁸ while a small-angle neutron scattering study by Yurekli and co-workers concludes that actually a structureless and random adsorption of the surfactant occurs.⁹ This study also suggested that the assembly may take different forms on nanotubes with different diameters, as the high curvature on the smallest SWNTs would make hemimicelle structures energetically and sterically unfavourable. Figure 3.1 shows schematic representations of how SDS might adsorb onto a nanotube.

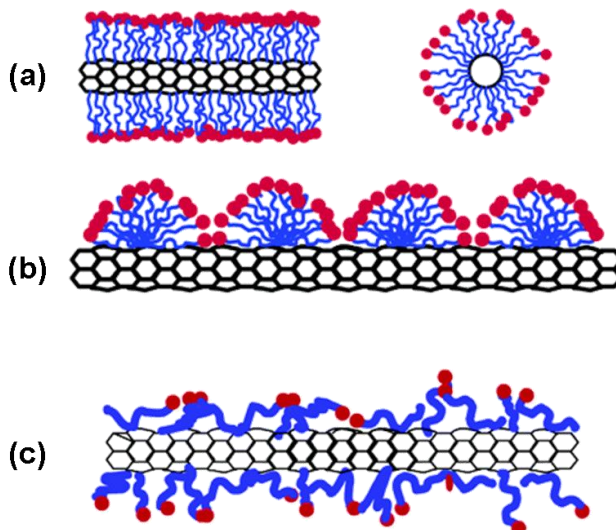


Figure 3.1 Schematic representations of the mechanisms by which SDS might adsorb to CNTs. (a) Uniform monolayer/cylindrical micelle, (b) hemimicelles and (c) random arrangement. Image taken from reference 9.

The anionic surfactant sodium dodecylbenzenesulfonate (SDBS) has also been used to produce stable dispersions of CNTs.¹⁰ A recent report by Bergin and co-workers describes a dilution technique for the separation of individually dispersed SWNTs from bundles stabilised with SDBS, without the need for high speed centrifugation.¹¹ Islam and co-workers suggest that this surfactant forms hemimicelle structures on the surface of the nanotubes, giving particularly stable dispersions compared to those obtained with SDS.¹² The reason for the excellent stability is attributed to the interactions that SDS and SDBS molecules have with the surface of the nanotube when they are lying parallel with the tube axis. As SDBS contains an aromatic ring, it is believed that there is favourable π -stacking where the molecular orbitals overlap with the graphite-like surface of the nanotube. SDS does not have such a ring, and therefore does not enjoy this close interaction with CNTs, leading to lower stability of the surfactant-nanotube complex. This is illustrated in Figure 3.2.

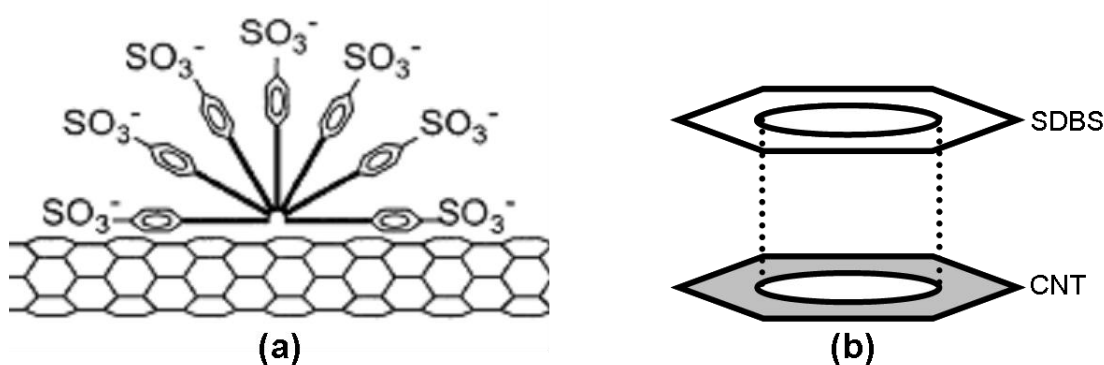


Figure 3.2 Schematic of proposed SDBS adsorption to a CNT. (a) SDBS hemimicelles (image taken from reference 12). (b) π -stacking of the benzene ring in SDBS stacking with the conjugated ring structure of the nanotube wall.

SDBS sitting parallel with the surface of the nanotube is also reported by Matarredona and co-workers, though they do not predict that this will be as part of a hemimicelle configuration.¹³ Instead, they suggest that the surfactant SDBS sitting parallel with the nanotube surface is the configuration most likely at low concentrations, as this would give the greatest surface coverage. When the concentration of surfactant is

increased, it is proposed that the SDBS molecules ‘stand up’ on the surface of the nanotube, forming a monolayer.

3.1.2 Sessile drop evaporation on a substrate

The evaporation of a sessile drop on a substrate appears at first to be a simple system, yet this process has been and continues to be the focus of many researchers.¹⁴ Several terms relating to sessile drops will be referred to throughout this chapter, and are defined here in Figure 3.3. The *contact angle* θ is the angle at which the liquid/vapour interface meets the solid substrate. The *contact line* is the outer perimeter or circumference of the sessile drop where it meets the substrate. The *contact area* is the area of liquid that is in contact with the solid substrate within the *contact line*. The *baseline diameter* is the diameter of the drop.

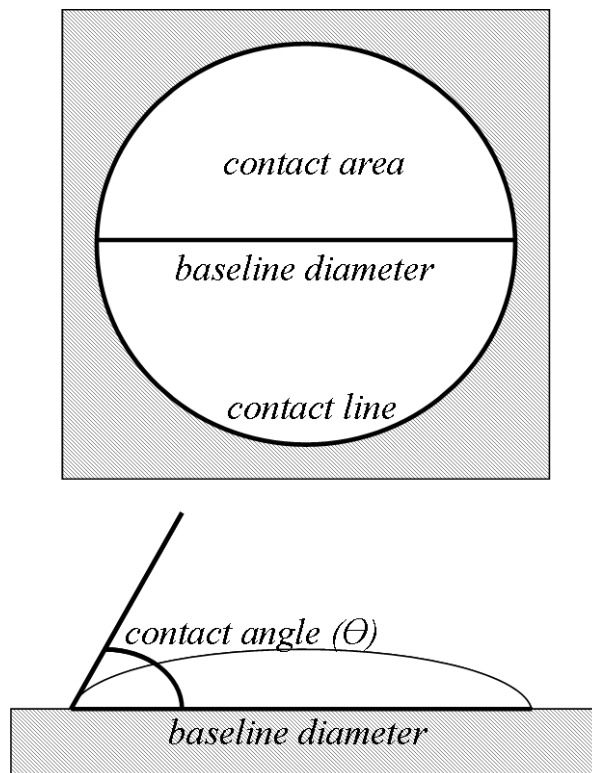


Figure 3.3 Schematic of a sessile drop on a solid substrate.

Evaporation of a sessile drop is thought to proceed through one of two principle mechanisms; constant *contact angle* or constant *contact area*, however the two mechanisms are not necessarily exclusive and the same drop may exhibit both

mechanisms during its lifetime.¹⁵ The lifetime of the drop is defined here as the length of time between drop deposition and evaporation of all solvent from the drop. In the constant contact angle mechanism, the contact angle remains constant as the drop loses mass while the baseline diameter, contact area and contact line decrease. In the constant contact area mechanism however, the baseline diameter, contact area and contact line remain constant, and the contact angle decreases to satisfy the loss in mass from the drop.

The evaporation of a sessile drop on a substrate is further complicated by the presence of solid particles dispersed within the drop, an area that has been studied particularly by Deegan and co-workers. They cite ‘coffee-stain’ rings as commonly observed examples of the effects that solid particles can have on the drying behaviour of an evaporating drop.¹⁶ The explanation for the formation of the ring is that the solid particles, once pressed by the meniscus towards the solid substrate, ‘pin’ the contact line, preventing it from moving over the substrate. As evaporation takes place, liquid from the interior of the drop is transported to the contact line, which results in even more particles being transported and deposited at the drop perimeter.¹⁷ The mechanism of depinning is believed to involve the formation of a ‘dry spot’ next to the contact line, where the liquid film becomes so thin that the contact line is forced to remove itself from the pinning site.¹⁸

3.2 Surfactant drops on silicon substrates

For CNTs to be assembled by a surfactant in an evaporating sessile drop, it seems reasonable that the surfactant itself must possess some self-assembling character. In solutions of a surfactant such as SDS this is commonly observed at elevated concentrations, close to the CMC (approximately 0.17 – 0.25 % w/v).¹⁹ In Figure 3.4 we show the effect of varying the concentration of SDS, from 0.05 to 1.00 % w/v, on the films from evaporated sessile drops on untreated silicon substrates.

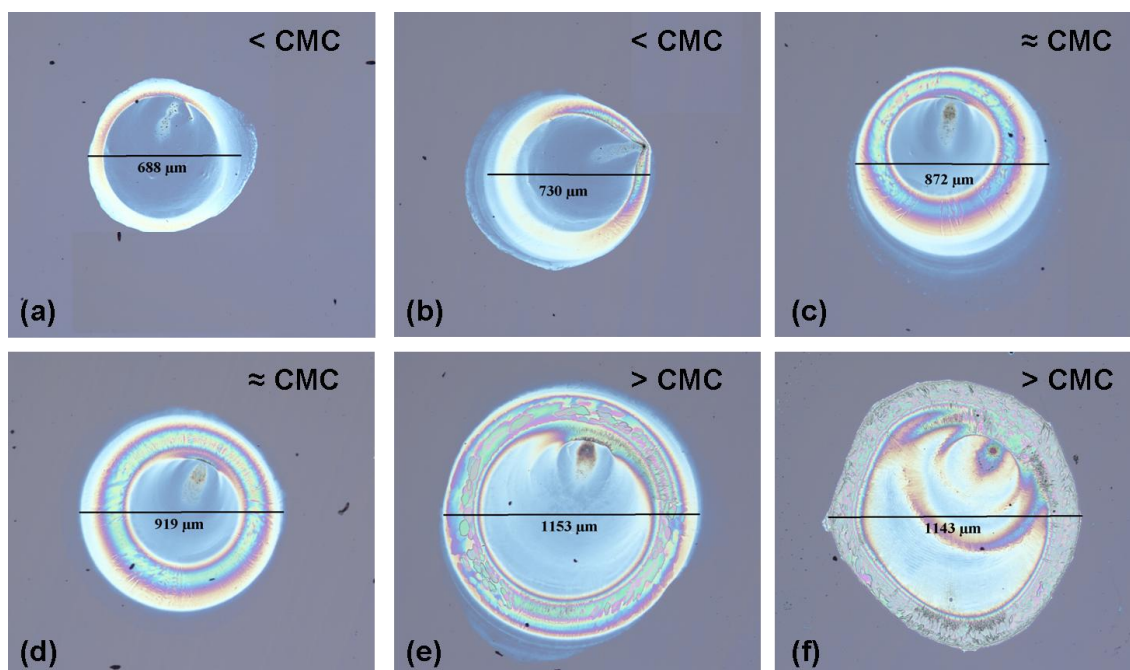


Figure 3.4 Optical microscopy images of evaporated drops deposited from 100 nL SDS solutions on untreated silicon wafers at concentrations (in weight per volume): (a) 0.05 %, (b) 0.10 %, (c) 0.20 %, (d) 0.25 %, (e) 0.50 % and (f) 1.00 %.

In our experiments, we show that with increasing surfactant concentration, the diameter of the film increased from approximately 688 μm (at 0.05 % w/v SDS) to 1143 μm (at 1.00 % w/v SDS). This is consistent with a lowering in the surface tension of the solution by the surfactant, allowing better spreading of the drop. The films exhibit ordered and complex structures for concentrations at and above the CMC (≥ 0.20 % w/v, Figure 3.4c-f). Figure 3.5 shows some examples of this structure in the films from the drop at 0.50 % w/v SDS concentration. This structure appears to comprise of two main types; a non-linear structure such as that seen in the perimeter of the film in Figure 3.5a, and a structure with linear organisation such as that seen in the interior of the drop in Figure 3.5b. It is known from binary phase diagrams that at high concentrations SDS can form lyotropic liquid crystals,²⁰ so perhaps the structure observed here is indicative of assembly into some of these organised phases.

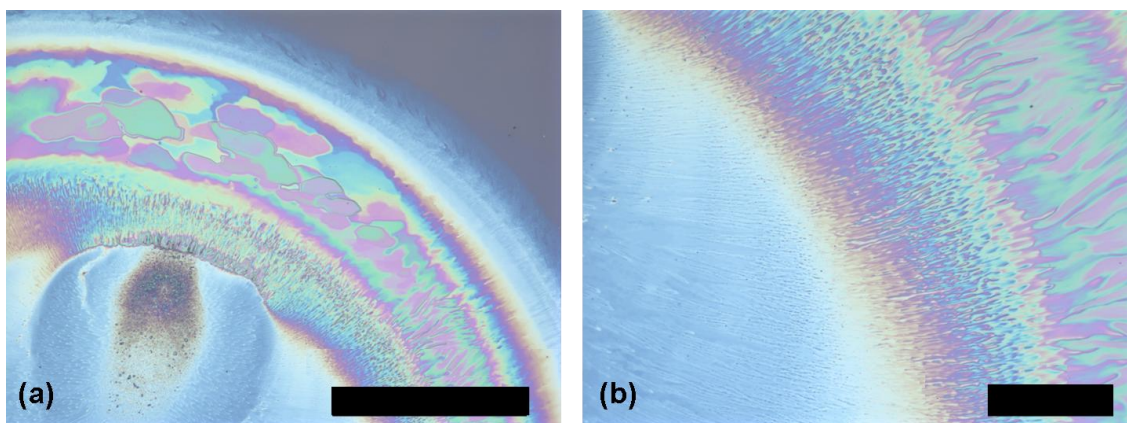


Figure 3.5 High magnification optical microscopy images of the films obtained from 100 nL SDS drops at a concentration (in weight per volume) of 0.50 %, deposited onto untreated silicon wafers. Scale bars (a) 200 μm and (b) 50 μm .

Evidence to support the liquid crystalline nature of this material is presented in Figure 3.6. Drops deposited onto glass microscope slides were viewed between cross polarisers, a technique commonly employed in the characterisation of liquid crystal phases due to their ability to rotate plane polarised light. When viewed through cross polarisers the images show coloured regions and linear assembly, similar in appearance to those regions observed in Figure 3.5 on untreated silicon wafers.

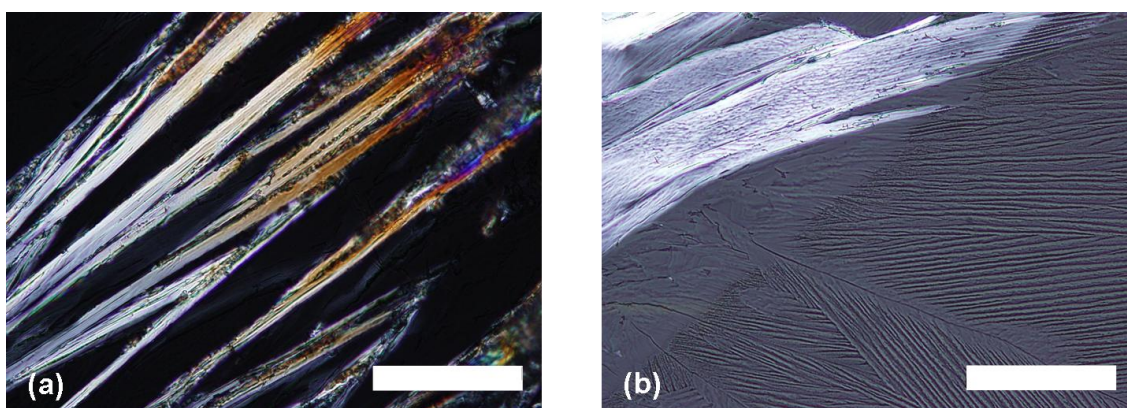


Figure 3.6 High magnification optical microscopy images of the CNT films obtained from 100 nL SDS drops at a concentration (in weight per volume) of 0.25 %, deposited onto glass microscope slides. Scale bars 100 μm in both images.

The highly ordered structures that are observed in the films from evaporated sessile drops at SDS concentrations at and above the CMC range may be of interest in the assembly of CNTs. Due to their assembly at this concentration, all other work in this chapter will describe the solutions and dispersions of SDS and CNTs at an SDS concentration of 0.25 % w/v, unless stated otherwise.

3.3 Surfactant-CNT drops on substrates

3.3.1 SDS-SWNT dispersions

It is well known that the centrifugation of an SDS-SWNT dispersion can result in the removal of large aggregates and bundles of nanotubes. In cases where the centrifugation is sufficient, it is even possible to isolate individually dispersed carbon nanotubes encased within cylindrical micelles.⁴ For this study it would be of interest to investigate the assembly of both small and large bundles of nanotubes, to see if they are assembled differently by the surfactant. Figure 3.7 shows the effect of centrifugation on SDS-SWNT dispersions, with regard to their optical absorption properties.

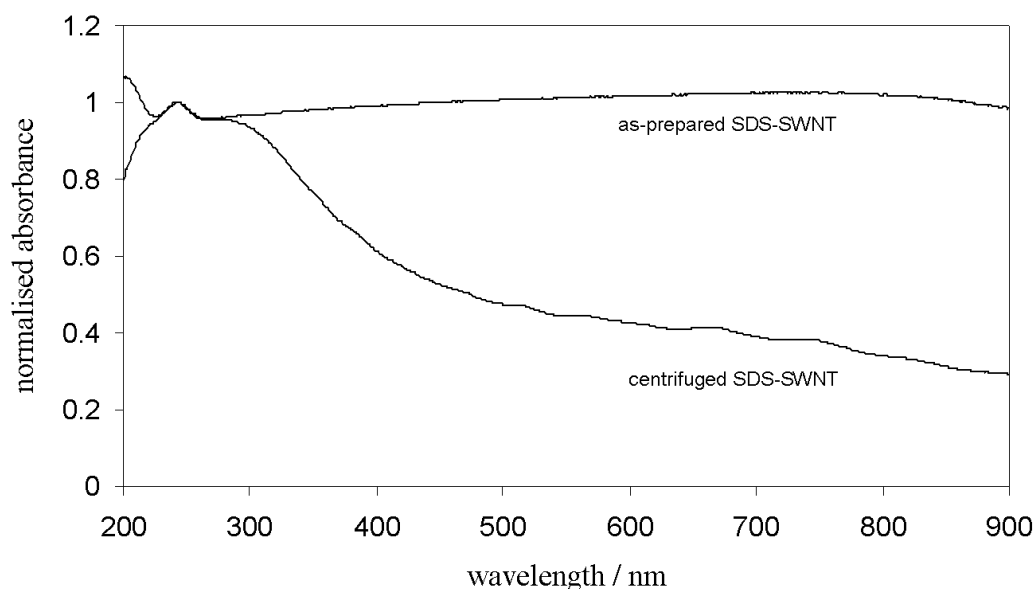


Figure 3.7 UV-vis absorbance spectra of as-prepared and centrifuged SDS-SWNT dispersions. Data normalised by the absorbance band at 242 nm.

Dispersing SWNTs in SDS solutions gave dense, black dispersions, and the relatively featureless spectrum observed in Fig. 3.7 is characteristic of these dispersions. On centrifugation however, some solid material was removed from the supernatant, and the absorbance was lowered. This revealed a series of bands at wavelengths associated with so-called van Hove singularities (see reference 4 for more details). Smalley and co-workers have shown that these bands are well defined for dispersions containing individual SWNTs, but are absent or poorly defined when aggregates are present. Their presence here is an indication that some of the larger bundles have been removed from the dispersion. It was also observed that SDS-SWNT dispersions with SDS concentrations at and above 0.20 % w/v appeared to stabilise significantly more of the CNT material than those dispersions with SDS concentrations lower than 0.20 % w/v. This is further evidence to support the continuation of this work with surfactant concentrations above 0.20 % w/v.

3.3.2 *Optical microscopy*

Sessile drops of as-prepared and centrifuged SDS-SWNT dispersions were deposited onto a variety of substrates, in volumes of 100 nL. When considering applications it will be important to understand both the wetting of the drop and the assembly on different types of surfaces. In this study, untreated silicon wafers, glass microscope slides, silicon wafers sputtered with a layer of copper and octadecyltrichlorosilane (OTS) treated silicon wafers have been investigated as substrates, as they offer different hydrophobicities and surface properties. Figure 3.8 shows the deposits and films from these dispersions on each of the substrates.

There are a number of interesting observations to be made from the images in Figure 3.8. Firstly, it is clear that the sizes of the drops immediately after deposition are not the same on each of the substrates. The largest drop is on the untreated silicon wafer, while the smallest drop is on the OTS-treated silicon wafer, with baseline diameters of 2.20 and 0.79 mm respectively. This indicates that, of the four substrates, these appear to have the lowest (untreated) and highest (OTS-treated) hydrophobicity. The baseline diameters of the drops on the glass slide and the copper wafer indicate that the hydrophobicities of these substrates are intermediate between the two silicon substrates.

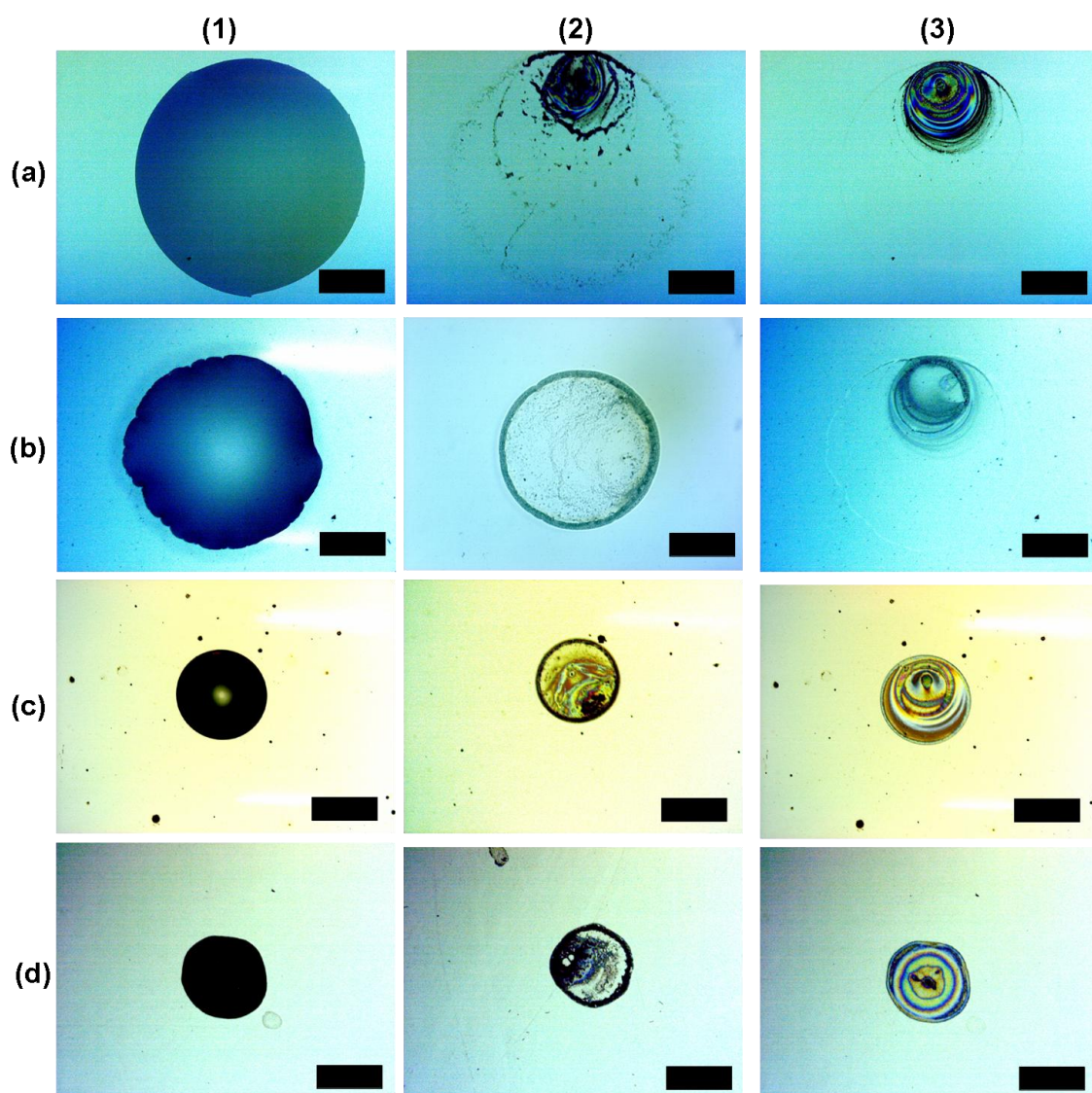


Figure 3.8 Optical microscopy images of drops and evaporated films obtained from 100 nL SDS-SWNT dispersions with SDS at a concentration (in weight per volume) of 0.25 %. Columns: (1) immediately after deposition (centrifuged dispersions), (2) evaporated films from as-prepared dispersions and (3) evaporated films from centrifuged dispersions. Rows show drops deposited onto (a) an untreated silicon wafer, (b) glass microscope slide, (c) copper wafer and (d) OTS-treated silicon wafer. Scale bars 500 μm in all images.

Baseline diameters and contact angles of the drops, measured immediately after their deposition, are reported in Table 3.1. The contact angle was measured from images

captured of the profile of the drop immediately after deposition, using the experimental set up detailed in Chapter 2.

Substrate	Baseline diameter / mm	Mean contact angle / °
Untreated silicon	2.20	3
Glass microscope slide	1.80	8
Copper wafer	0.87	50
OTS-treated silicon	0.79	80

Table 3.1 Geometrical parameters of 100 nL drops from SDS-SWNT dispersions on different substrates.

Also interesting to note are the deposits remaining from the drops of the as-prepared dispersions (Figure 3.8, column 2). These deposits are unlike the films that formed from the drops of SDS solution (Figure 3.4), instead they appear to consist of a heavy, outer ring with further deposits within this perimeter, also known as the ‘coffee-stain’ effect. On each of the substrates, these outer deposits appear to be consistent in size with that of the initial drop diameter. This is in contrast with the deposits from the centrifuged dispersions however, where the size of the films are similar on each of the four substrates, and appear to be independent of the size of the initial drop. The films from the centrifuged dispersions also appear to be more like those from drops of SDS solution, and do not have any ring-like deposits of aggregates. There are, however, some differences between the films from the centrifuged dispersions on the different substrates, mainly in the appearance of the film. On the untreated silicon, glass and copper substrates, the films have a ‘lop-sided’ appearance, while on the OTS-treated silicon substrate, the drop appears to be more symmetrical.

3.3.3 Contact angle analysis

The reasons for the differences in the deposits from as-prepared and centrifuged SDS-SWNT dispersions on the substrates can be further understood by considering the evaporation mechanism of the sessile drops. An insight into these mechanisms can be gained by studying the contact angles and baseline diameters of the drops. The contact angles of the drops were primarily obtained by capturing profile images of the drops,

and measuring the contact angle and baseline diameter from the images. For the drops with very low contact angles ($< 10^\circ$), a second method based on the interference of incident light was adopted, to verify the manual measurements findings.

A profile of how the geometry of a drop from an as-prepared SDS-SWNT dispersion changes as it evaporates is shown in Figure 3.9. The contact angle of the drop immediately after deposition is approximately 5° , while the baseline diameter is 2.20 mm, indicating the flat nature of the drop on this hydrophilic substrate. As the drop starts to evaporate, the baseline diameter remains constant over the first 30 s while the contact angle decreases, before there is a sharp rise in the contact angle and fall in the diameter. After this point the baseline diameter gradually recedes, though not quite at a constant rate, while the contact angle remains quite steady to within a few degrees. This behaviour of the drop is attributed mainly to the presence of aggregates in the as-prepared dispersion, and the pinning of the drop contact line when they are pressed by the meniscus. After the drop has been deposited, aggregates at the contact line pin the drop and prevent the contact line from moving. This pinning of the contact line leads to a flow of solution towards the edge of the drop during evaporation. This leads to the build-up of aggregates observed at the perimeter (as observed during video microscopy resulting in the formation of ring-like deposits in Figure 3.8)

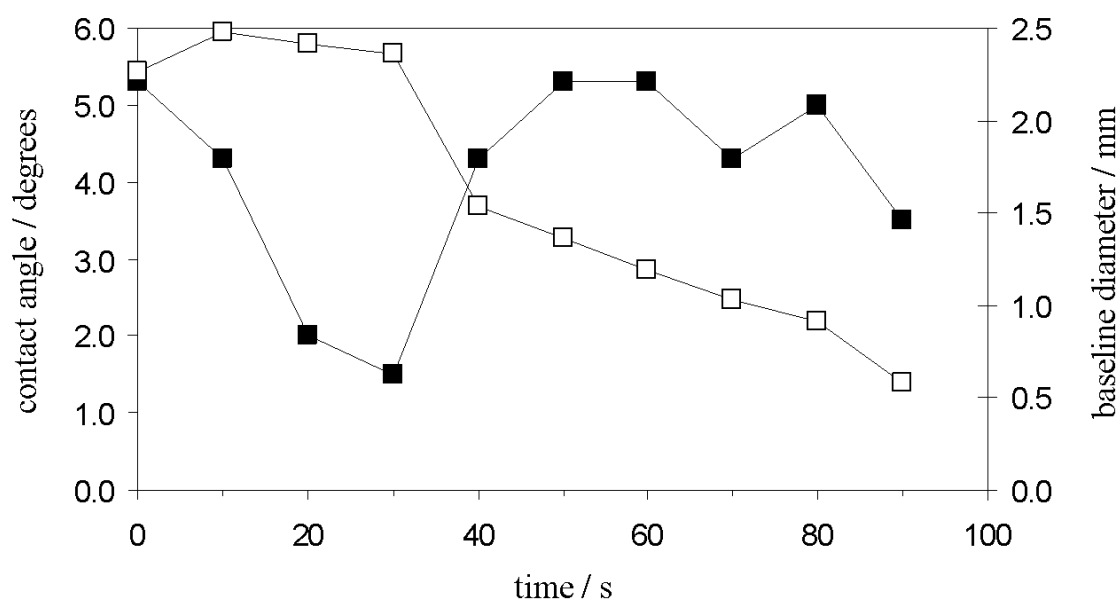


Figure 3.9 Mean contact angle (filled squares) and baseline diameter (empty squares) of a 100 nL drop from an as-prepared SDS-SWNT dispersion deposited onto an untreated silicon wafer.

At some critically low value of the contact angle (apparently around $1^\circ - 2^\circ$ in this case), ‘dry spots’ start to appear at parts of the contact line, and depinning occurs. This results in the large step-wise decrease in the baseline diameter after 30 s as it recedes over the substrate, and the contact angle increases back to almost 5° . From this point, further pinning and depinning events occur, as indicated by the observed rise and fall in the contact angle, leaving smaller ring-like deposits of aggregates on the substrate. This behaviour is similar to that explained by Deegan, in an investigation of how coffee stains form.¹⁷

The behaviour of a drop from an as-prepared dispersion on the most hydrophobic substrate, OTS-treated silicon, is somewhat different and is represented in Figure 3.10. Immediately after deposition of the drop, the contact angle is around 80° and the baseline diameter is approximately 0.79 mm. The drop then evaporates through a ‘constant contact area’ mechanism, where the baseline diameter changes very little while the contact angle decreases. This is the case until the later stages in the evaporation, when the baseline diameter sharply decreases. Although the mechanism of evaporation appears quite different from that observed on untreated silicon, there are some similarities.

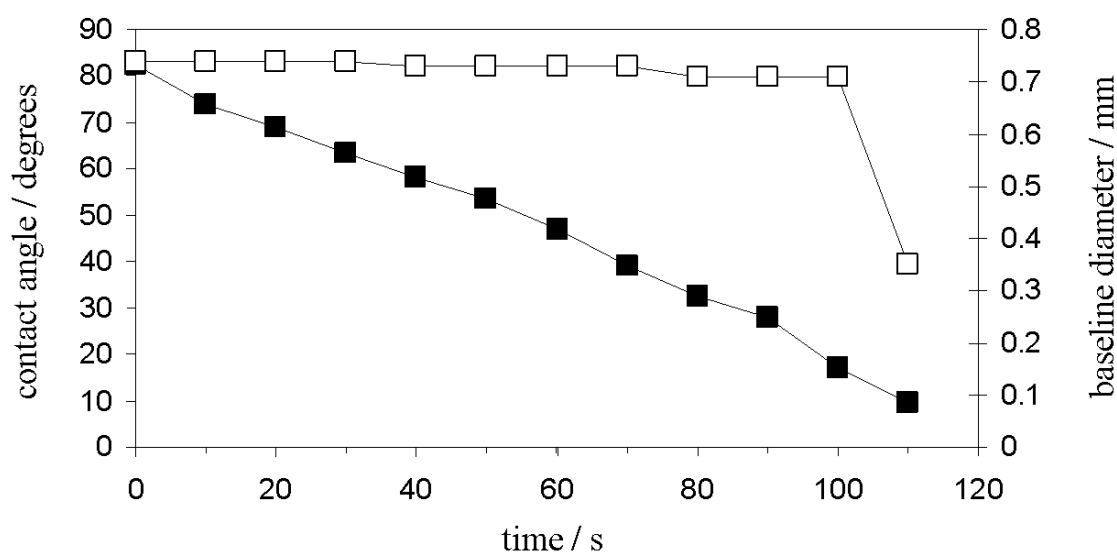


Figure 3.10 Mean contact angle (filled squares) and baseline diameter (empty squares) of a 100 nL drop from an as-prepared SDS-SWNT dispersion deposited onto an OTS-treated silicon wafer.

Aggregates in the dispersion still pin the contact line, and a flow within the drop carries more aggregates to the contact line as the drop evaporates. However, due to the large initial contact angle, the critical point for depinning is not reached until the final stages of drop evaporation (~ 100 s). This results in a ring with a higher density of aggregates compared to the density of the ring on the untreated silicon substrate. In addition, the supplementary deposits within the outer ring are fewer and less dense on the OTS-treated silicon substrate.

For centrifuged dispersions on untreated silicon substrates, the evaporation behaviour of the drop is different again (Figure 3.11). The initial baseline diameter and contact angle of the drop are similar to those from drops of as-prepared dispersions, but as there are no large CNT aggregates to pin the contact line then the baseline diameter immediately starts to recede as it evaporates. This movement of the contact line appears to occur at a steady rate, until all of the solvent has evaporated. However the contact angle does not remain constant, but increases slightly during evaporation. This trend is unexpected, but was observed repeatedly for this sample.

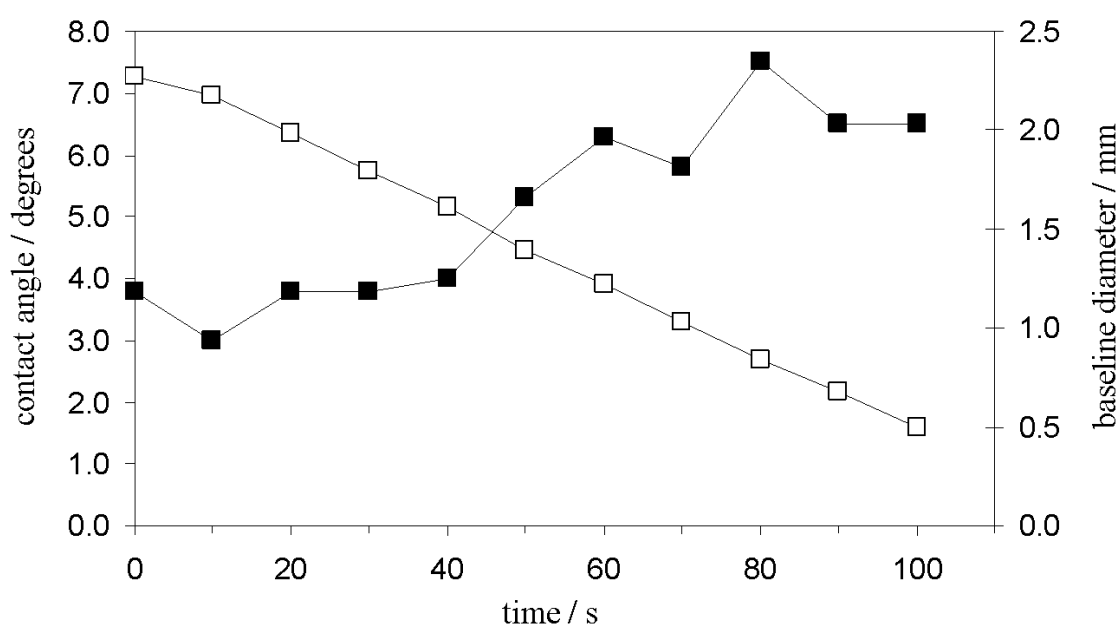


Figure 3.11 Mean contact angle (filled squares) and baseline diameter (empty squares) of a 100 nL drop from a centrifuged SDS-SWNT dispersion deposited onto an untreated silicon wafer.

While it has been observed that surfactants can assemble on substrates ahead of a moving contact line resulting in changes in the contact angle, this is more commonly observed in cases where the surfactant head group is electrostatically attracted to a substrate of opposite charge, resulting in the hydrocarbon chain pointing towards the aqueous bulk of the drop. Such assembly has been noted in systems containing the cationic surfactant cetyltrimethyl ammonium bromide (CTAB) on silicon,²¹ but not SDS on silicon, and this therefore is unlikely to be the explanation here. One other explanation here may be that the initial drop is too large and flat to be considered a spherical cap, and its behaviour does not fit with the classical observations for spherical cap systems.

Drops from a centrifuged dispersion on an OTS-treated silicon substrate display similar behaviour to drops from an as-prepared dispersion, as shown in Figure 3.12. The drop evaporates via a constant contact area mechanism. The contact angle decreases, while the baseline diameter remains constant up to the final stages of evaporation (~ 110 s). As there are no aggregates to pin the contact line, we do not observe any ring-like deposits.

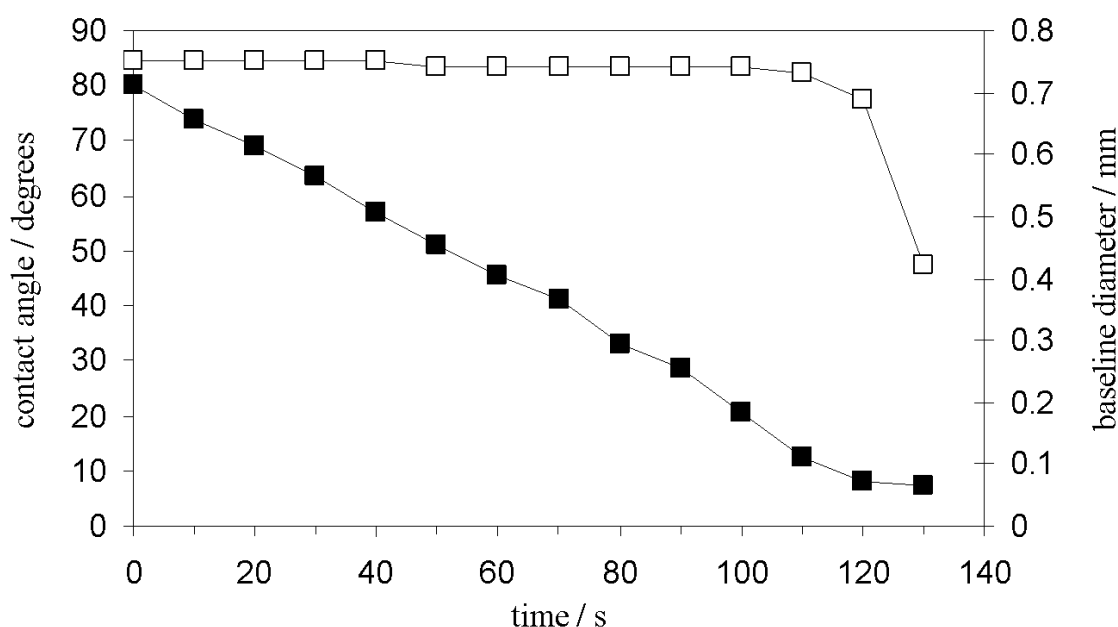


Figure 3.12 Mean contact angle (filled squares) and baseline diameter (empty squares) of a 100 nL drop from a centrifuged SDS-SWNT dispersion deposited onto an OTS-treated silicon wafer.

3.3.4 SDS-SWNT film formation

The differences between the deposits from as-prepared and centrifuged dispersions, and the formation of the CNT ‘coffee-stains’, has been better understood by considering the contact angles of the drops as they evaporate on the substrates. For the films obtained from centrifuged dispersions however, a number of points remain unclear. For example, the films are all of approximately equal diameter on each of the substrates despite the initial drop diameters being different, and some films also appear to have a ‘lop sided’ appearance while others are more symmetric. A combination of video microscopy and images showing the side profile of the drops were used in compiling Figure 3.13, where the baseline diameter of centrifuged dispersions on each of the substrates is plotted over time. Here we define the onset of film formation as the point at which a film *starts* to form at the contact line.

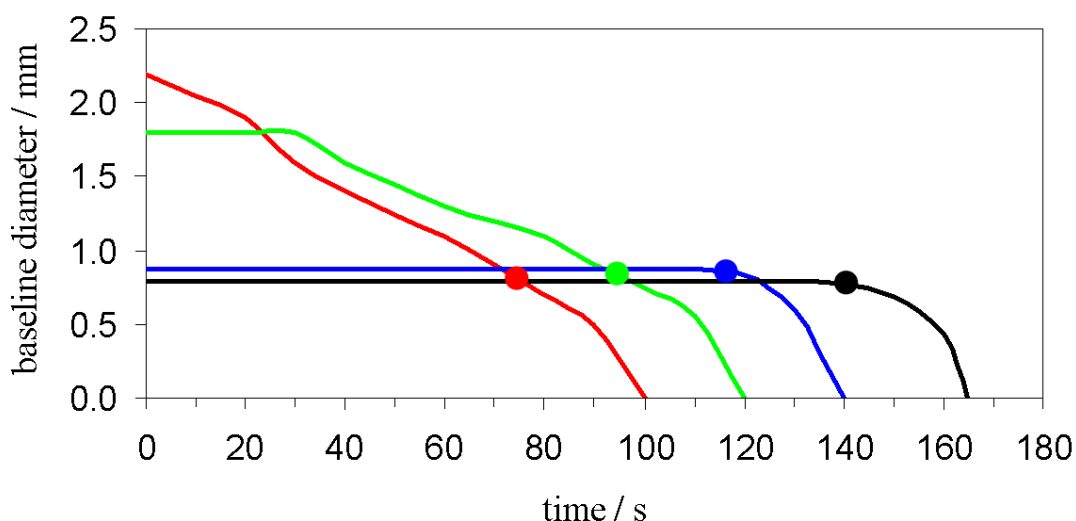


Figure 3.13 Baseline diameter over time for centrifuged SDS-SWNT dispersions on an untreated silicon (red line), glass (green line), copper (blue) and OTS-treated silicon (black line) substrate. Coloured circles represent the point at which the film was first observed on the substrates.

We note that the drops on hydrophobic substrates take longer to evaporate than those on more hydrophilic substrates. This is attributed to the surface area of the drop decreasing with increasing hydrophobicity, at a constant amount of bulk material. As

evaporation occurs at the surface of the drop, particularly around the contact line, then drops on hydrophilic substrates (with a large surface area) would be expected to evaporate faster than those on hydrophobic substrates (with a smaller surface area). It was also observed that, despite the differences in sizes of the initial drops and the mechanisms of drying, at the onset of film formation there are many similarities between the drops. Firstly, the diameters of the drops at the onset of film formation are very similar (0.79 – 0.87 mm) on each of the substrates. After this onset, the contact line recedes over the substrate, shown by the decrease in baseline diameter. This is true for the drops on *all* of the substrates, whether or not the contact line was already in motion. Finally, the time taken from the onset of film formation to the evaporation of the drop is similar on all of the substrates. This information might suggest that, as the baseline diameters are similar at the onset of film formation and the drops then take the same length of time to evaporate, the volumes of the drops are the same on each of the substrates when the film starts to form.

Further evidence to support this assumption can be found by analysing the contact angles of the drops when the film starts to form. This cannot be performed by studying the profile of the drop, as the films are too thin and cannot be seen. Instead, the contact angles of drops from centrifuged dispersions on untreated and OTS-treated silicon substrates at the point of film formation were determined through an interferometry technique. This technique, commonly used to determine the contact angles of sessile drops,²² is made possible due to the periodic destructive and constructive interference of light when it passes through a thin film and is reflected from a surface. This results in a concentric series of light and dark rings around the outside of the drop, also known as interference fringes or ‘Newton’s Rings’.²³ Figure 3.14 shows these fringes for centrifuged SDS-SWNT dispersions on untreated and OTS treated silicon substrates at the onset of film formation. The series of light and dark rings indicating interference are clearly visible in both drops, as are the films that are being left behind by the contact line.

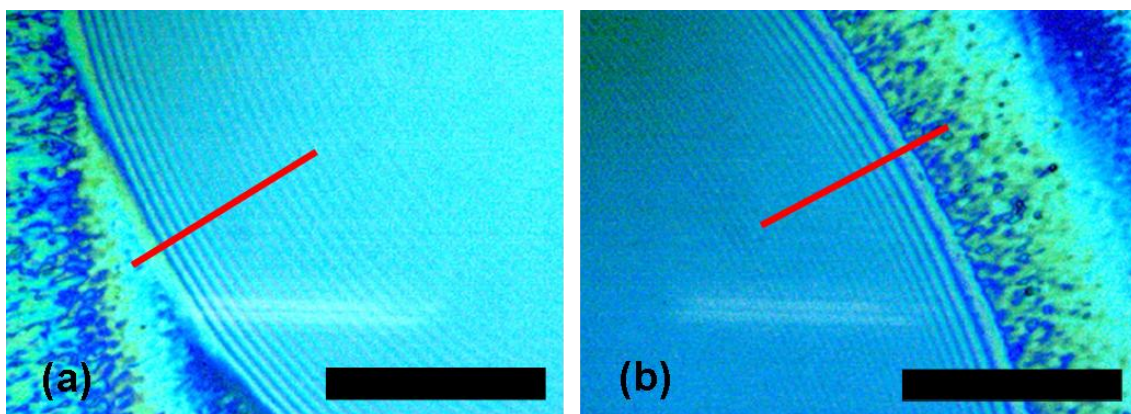


Figure 3.14 Optical microscopy images of centrifuged SDS-SWNT dispersions just after the onset of film formation on (a) untreated and (b) OTS-treated silicon substrates. Scale bars 50 μm in both images. Red lines show where line intensity profiles were obtained.

The red lines show where line intensity profiles were obtained for each drop, with the microscopy software plotting the intensity of the light as a function of distance along the line. This information was used to determine the contact angle, and an example of such an intensity profile is plotted in Figure 3.15. The darker fringes are represented by a drop in the intensity, and the lighter fringes by an increase in the intensity.

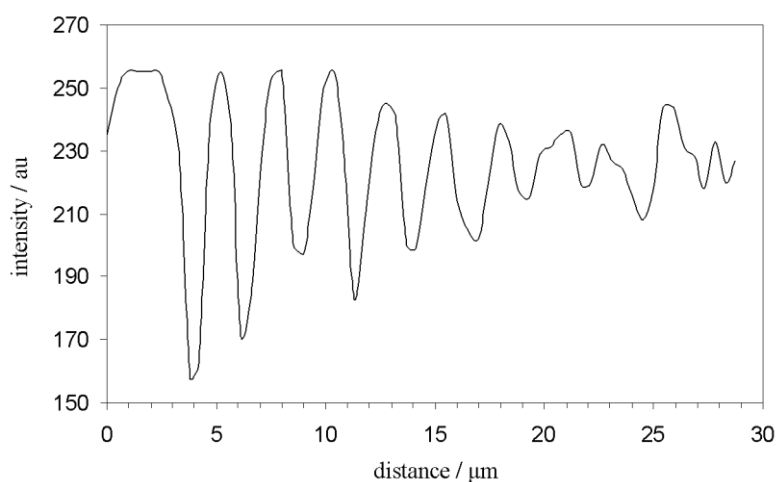


Figure 3.15 Profile of the light intensity along a line perpendicular to the contact line of a centrifuged SDS-SWNT dispersion on an untreated silicon substrate during film formation.

As the thickness of the drops at the perimeter are believed to be much smaller than the diameter of the drop, the curvature of the film is neglected and instead a wedge-shaped film is assumed at the edge. In this case, the dark fringes are caused by destructive interference, when

$$2dn = i\lambda \quad [3.1]$$

where d is the film thickness, n is the refractive index of the solution, i is the fringe number (an integer) and λ is the wavelength of the incident light.²³ Rearranging gives the film thickness,

$$d = \frac{i\lambda}{2n}. \quad [3.2]$$

The film thickness can also be obtained from

$$d = s \tan\theta, \quad [3.3]$$

where s is the distance between fringes and θ is the contact angle. Combining equations 3.2 and 3.3

$$s \tan\theta = \frac{i\lambda}{2n}, \quad [3.4]$$

which can be rearranged to

$$\theta = \tan^{-1} \frac{i\lambda}{2ns}. \quad [3.5]$$

Thus, the contact angles of the drops during film formation can be estimated using equation 3.5. For simplification, a number of assumptions have been made. These are that the refractive index of the solution has not been altered by the presence of surfactant or CNTs, and is equal to that of water. It is also assumed that the incident light is monochromatic ($\lambda = 406$ nm), is normal to the substrate and that there is no stray light. As we are interested in comparing the contact angles for the drops on each substrate, rather than knowing the exact contact angles, it is reasonable to make these assumptions as long as they are the same for each substrate, and the contact angle then becomes proportional to the fringe spacing. On untreated silicon during film formation, for a fringe spacing of $2.4 \mu\text{m}$, the contact angle θ was calculated to be $3.6^\circ \pm 1.3^\circ$. On OTS-treated silicon during film formation, for a fringe spacing of $2.7 \mu\text{m}$, θ was calculated to be $3.2^\circ \pm 1.1^\circ$. We can therefore say that the contact angles for the drops on each substrate are almost identical, within the estimated error. As the baseline diameter of the drops and the contact angles are now known to be similar, this suggests that at the point of film formation the volumes of the drops are also the same.

The relevance of the drops having the same volume on each of the substrates at the onset of film formation is that the factor governing this process can now be explained. As the drop evaporates, it loses mass. If this mass loss is due solely to evaporation of the solvent and not the surfactant, then the concentration of the surfactant will gradually increase within the drop. As the drops all have the same mass immediately after deposition, and also at the point of film formation, then it can be predicted that the concentration of the surfactant within the drop is the same on each substrate, and this is the factor controlling film formation. This assumption is supported by considering the diameters of the films from the surfactant only drops, in Figure 3.4. The size of the films increases with increasing surfactant concentration, even though the sizes of the initial drops should be the same after the concentration reaches the CMC range (as no further lowering in the surface tension would be expected). If there is a threshold concentration of surfactant that must be attained for film formation, then this will be reached earlier in drops with higher surfactant concentrations, thus giving them larger films, as observed in Figure 3.4. This is further evidence that the size of the film is governed not by the size of the initial drop or how it evaporates, but by the surfactant concentration.

Hence, there appears to be a threshold, or critical, concentration of surfactant within the drop that triggers the formation of a film. Calculations of the mass of the drops on each substrate suggest that at the point of film formation,^{*} the concentration of surfactant within the drop has risen to approximately 4 % w/v. This raises an interesting issue concerning the higher ordered assemblies that have been observed in the films (Figures 3.4 and 3.5). The type of structures that SDS can form depends on the concentration of SDS and the temperature, according to the binary phase diagram for an SDS-water system.²⁰ At a concentration of 4 % w/v, we might expect the presence of micelles, but it would require the concentration of SDS to reach approximately 40 % w/v (with the drop having to reduce to below 1 % of its original mass) for the formation of hexagonal or lamellar liquid crystalline regions to occur. The optical microscopy suggested that these films are actually formed *at* the contact line, and looking through the drop onto the substrate ahead of the contact line has shown no assembly. This therefore suggests that the concentration of surfactant is not uniform throughout the

^{*} The volume of the drop at the point of film formation was calculated based on a spherical cap, with cap dimensions measured from optical microscopy and video images of the side of the drop. This was then used, with the density of the dispersion, to obtain the mass.

drop, and that there could be concentration gradients with regions of very high surfactant concentration at the contact line.

The factors affecting film formation and why the films are of equal size on each substrate, regardless of their initial size, are now thought to be understood. However, one final aspect remains unclear - the reasons why the films on hydrophilic and hydrophobic substrates have different appearances regarding their symmetry. As has already been mentioned, the films on hydrophilic substrates, such as untreated silicon, have lop-sided, unsymmetrical appearances, while the films on hydrophobic substrates, such as OTS-treated silicon, are more symmetrical in appearance. This is shown in Figure 3.16. The surfactant rings in the film on the untreated silicon substrate are not totally concentric, instead appearing to lean preferentially towards one part of the drop, unlike the rings in the film on the OTS-treated silicon wafer which are much more concentric. There is also a dark feature in the films, which from studying the drops as they evaporate is known to be formed by the final part of the drop. In the film on the untreated silicon wafer, this feature is not at the centre of the film, instead it is located towards one side of the film. On the OTS-treated silicon wafer however, this feature is found precisely in the middle of the film.

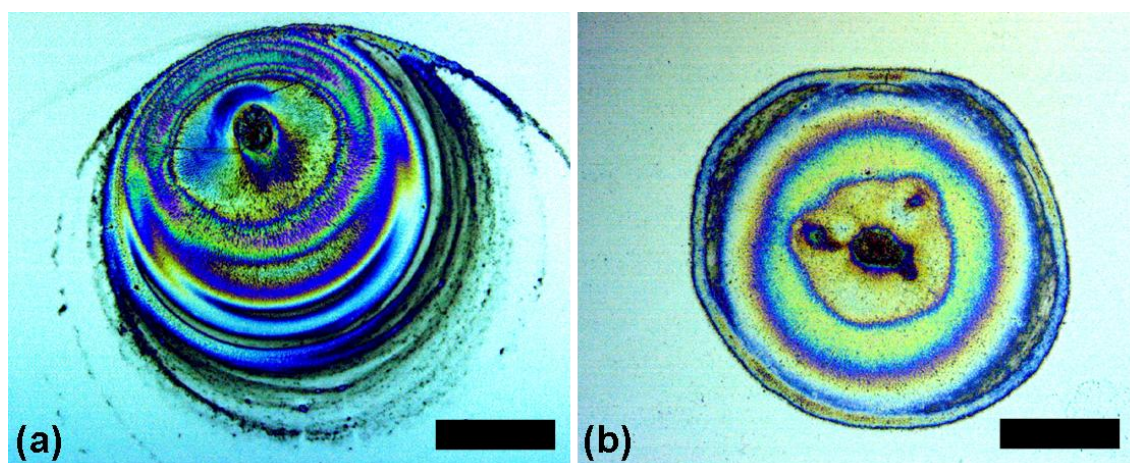


Figure 3.16 Optical microscopy images of films obtained from centrifuged SDS-SWNT dispersions on (a) untreated and (b) OTS-treated silicon substrates. Scale bars represent 250 μm in both images.

The differences in the appearances of the films can be understood by studying the behaviour of the drops during the film forming process (Figure 3.17). On the untreated silicon substrate the contact line does not de-pin equally from all around the drop. Rather, the contact line at the top of the drop in the images remains stationary until approximately 15 s after film formation begins, while the contact line around the rest of the drop de-pins, forming the film. This unequal movement of the contact line is what results in the lop-sided appearance of the film, and also the position of the final drying feature towards one side of the drop. On the OTS-treated silicon substrate however, the contact line de-pins equally all around the drop from the beginning of the film forming process to the end. This gives the symmetric, concentric appearance of the rings in the film, and the presence of the final drying feature at the centre of the film, rather than towards one side.

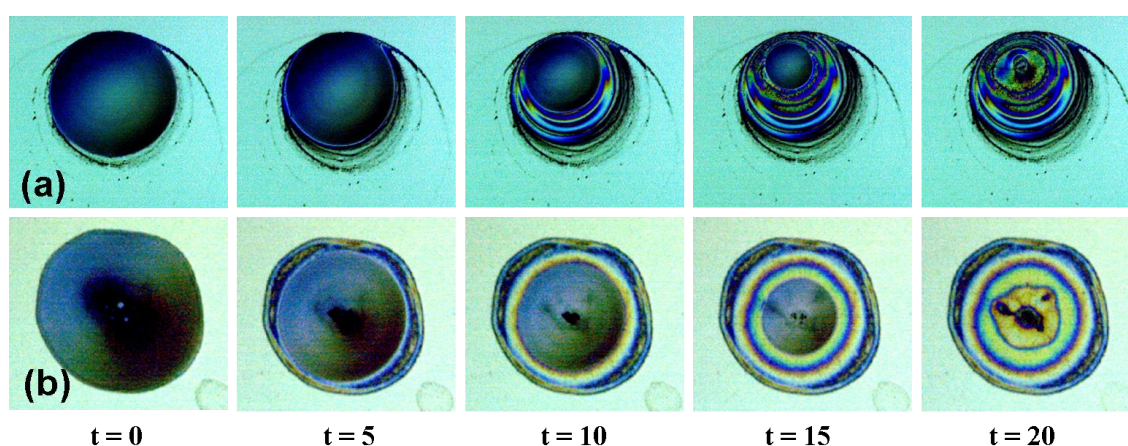


Figure 3.17 Optical microscopy images of drops from centrifuged SDS-SWNT dispersions as they form films on (a) untreated and (b) OTS-treated silicon substrates. Times below images refer to the time, in seconds, after film formation has commenced.

The presence of multiple pinning sites in the drops from as-prepared dispersions results in the formation of ring-like collections of nanotube aggregates, and prevents the formation of a surfactant film. However drops from centrifuged dispersions on untreated silicon substrates resulted in a single pinning site, causing the film to be deposited in an inhomogeneous manner. One explanation for this may be that there are small numbers of particles on the substrate, or remaining aggregates within the drop.

This results in contact line pinning at a single site and prevents it from moving at this point, while the rest of the contact line can still recede over the substrate during evaporation, forming a film.

This does not, however, explain why there is such uniform de-pinning of the drops on the OTS-treated silicon, where the same single-particle pinning sites may be present. One explanation may be that, due to the larger contact angle of the drop on the OTS-treated silicon substrate, the meniscus of the evaporating drop cannot effectively trap the pinning particle at the contact line, and it therefore stays in the bulk of the drop until the later stages of evaporation. Another explanation is postulated by considering what happens when a single pinning site is encountered on a substrate. Figure 3.18 shows schematic representations of pinning sites on an untreated and an OTS-treated silicon substrate. A pinning site on a substrate represents a barrier that must be overcome if the contact line is to pass over it. Based on our experimental observations, when this pinning site is met there appear to be two competing interactions. (i) the drop carries fluid to the contact line and the pinning site to maintain the pinning site, and (ii) the substrate, depending on its hydrophobicity, tries to minimise the surface area with the drop, with the contact line receding over the substrate. If we assume here that the pinning site and the dispersion are the same on each substrate, then we can conclude that the first interaction is equal for both substrates. The second interaction, based on the minimisation of the surface area of the drop on the substrate, would therefore be the dominant interaction. On the hydrophilic substrate (untreated silicon), the initial baseline diameter of the drop would suggest that the substrate and the dispersion enjoy a large surface area (see Figure 3.8). When the pinning site is encountered, the affinity between the substrate and the dispersion appears to be sufficient for the contact line to remain at the pinning site, which is what we observe experimentally. On the hydrophobic substrate (OTS-treated silicon) however, the initial baseline diameter is much smaller, indicating less affinity between the dispersion and the substrate. As the pinning site is encountered, it would appear from our observations that this low affinity is the driving force behind the contact line passing over the pinning site, as the drop retains its spherical shape at the contact area.

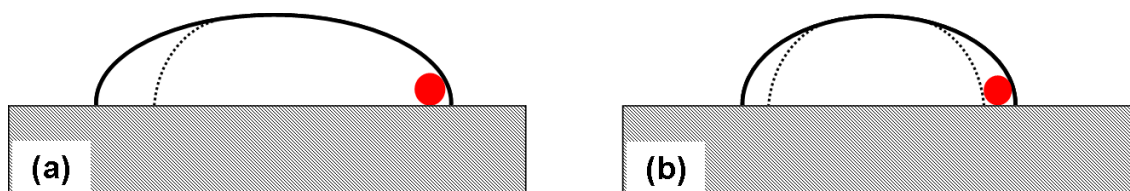


Figure 3.18 Schematic representation when the contact line of a drop from a centrifuged SDS-SWNT dispersion meets a pinning site (red circle) on an (a) untreated and (b) OTS-treated silicon substrate. Dashed lines represent movement of the contact line after the pinning site is encountered.

3.3.5 Raman spectroscopy

The distribution of CNTs in films prepared by evaporative casting SDS-SWNT dispersions was studied through Raman spectroscopy. Raman spectroscopy is a powerful tool for the characterisation of CNTs, and is used to detect the presence of CNTs in the films. A typical Raman spectrum for SWNTs is presented in Figure 3.19, showing the three characteristic regions: the so-called radial breathing modes (RBM), D-band and the G-band, which are observed at approximately $200 - 300 \text{ cm}^{-1}$, 1330 cm^{-1} and 1600 cm^{-1} , respectively.²⁴

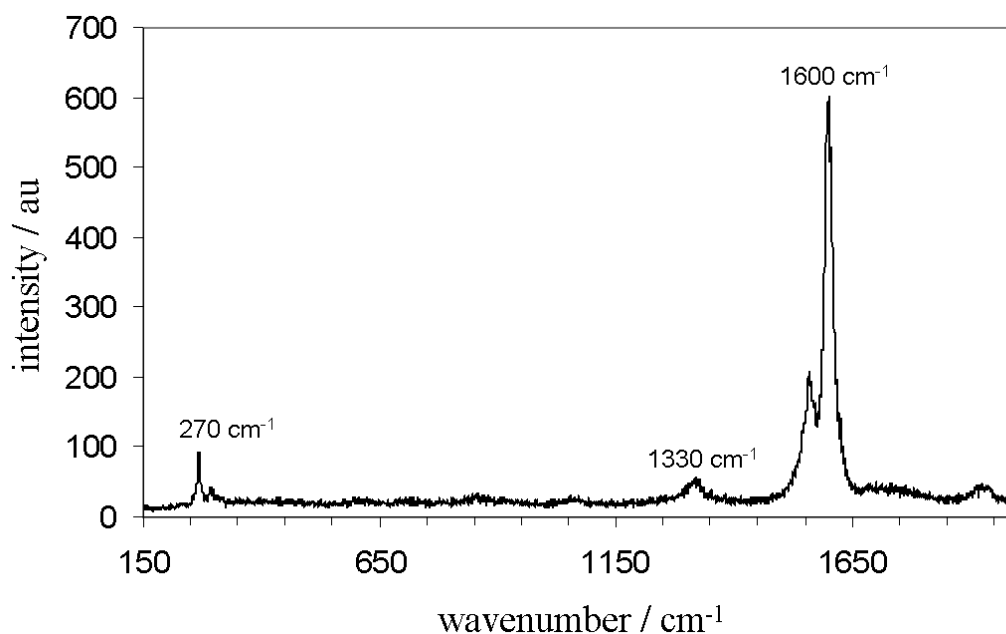


Figure 3.19 Typical Raman spectrum of SWNT. The RBM, D-band and G-band are at approximately 270 , 1330 and 1660 cm^{-1} , respectively.

The distribution of CNTs in films on untreated silicon substrates was determined by recording spectra in the G-band region at various locations over the film area (Figure 3.20). The G-band was selected as this gives the largest intensity.

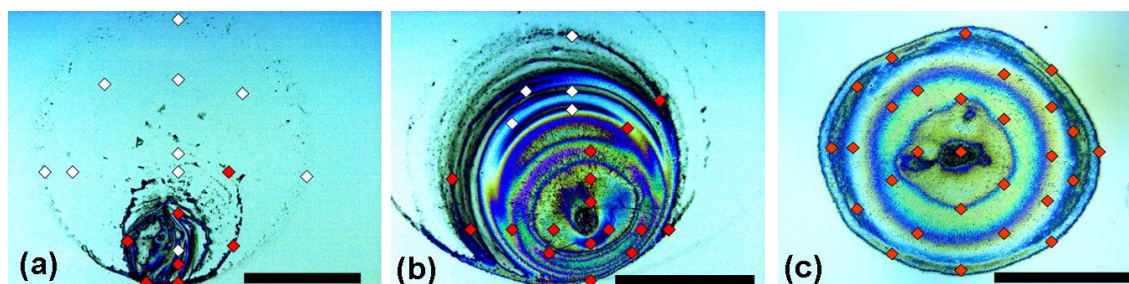


Figure 3.20 Optical microscopy images of films and deposits from SDS-SWNT dispersions. (a) As-prepared dispersion on untreated silicon (scale bar 1 mm), and centrifuged dispersions on (b) untreated and (c) OTS-treated silicon substrates (scale bars 0.5 mm). Diamonds represent sites where Raman spectra were collected; white diamonds - no nanotubes present, red diamonds - nanotubes present.

Raman spectroscopy revealed that the CNTs are located mainly within the aggregate-rings of the deposits formed from as-prepared dispersions (Figure 3.20a). A centrifuged dispersion deposited onto untreated silicon (Figure 3.20b) shows a far wider distribution of CNTs, which appear to cover most of the film area. There were some regions however where CNTs were not observed, in the region of the film opposite to the part that became pinned during the film forming process. This pinning may have led to a higher concentration of nanotubes deposited in the film close to this pinning site. On the OTS-treated silicon substrate (Figure 3.20c) however, the distribution of CNTs appeared to be uniform over the entire film area, with none of the analysed sites giving a negative response for nanotubes.

3.3.6 Scanning electron microscopy

Scanning electron microscopy (SEM) images of the deposits and films from as-prepared and centrifuged dispersions on untreated silicon wafers are shown in Figure 3.21. The image of the deposit from the as-prepared dispersion (Figure 3.21a) was taken

from one of the ring deposits, and shows the nanotubes in a dense, randomly orientated network. Analysis over other parts of the deposit supported the Raman spectroscopy findings that the nanotubes were largely confined to these ring-like regions. In the films from the centrifuged dispersions, a series of parallel, evenly spaced cylindrical structures were observed. These structures measured approximately 0.5 μm in diameter and were several microns in length, although if they are the same linear assemblies observed during optical microscopy then they extend over several hundred microns. As these structures were also observed in the films from the drops of surfactant-only solutions, it is likely that they are surfactant features.

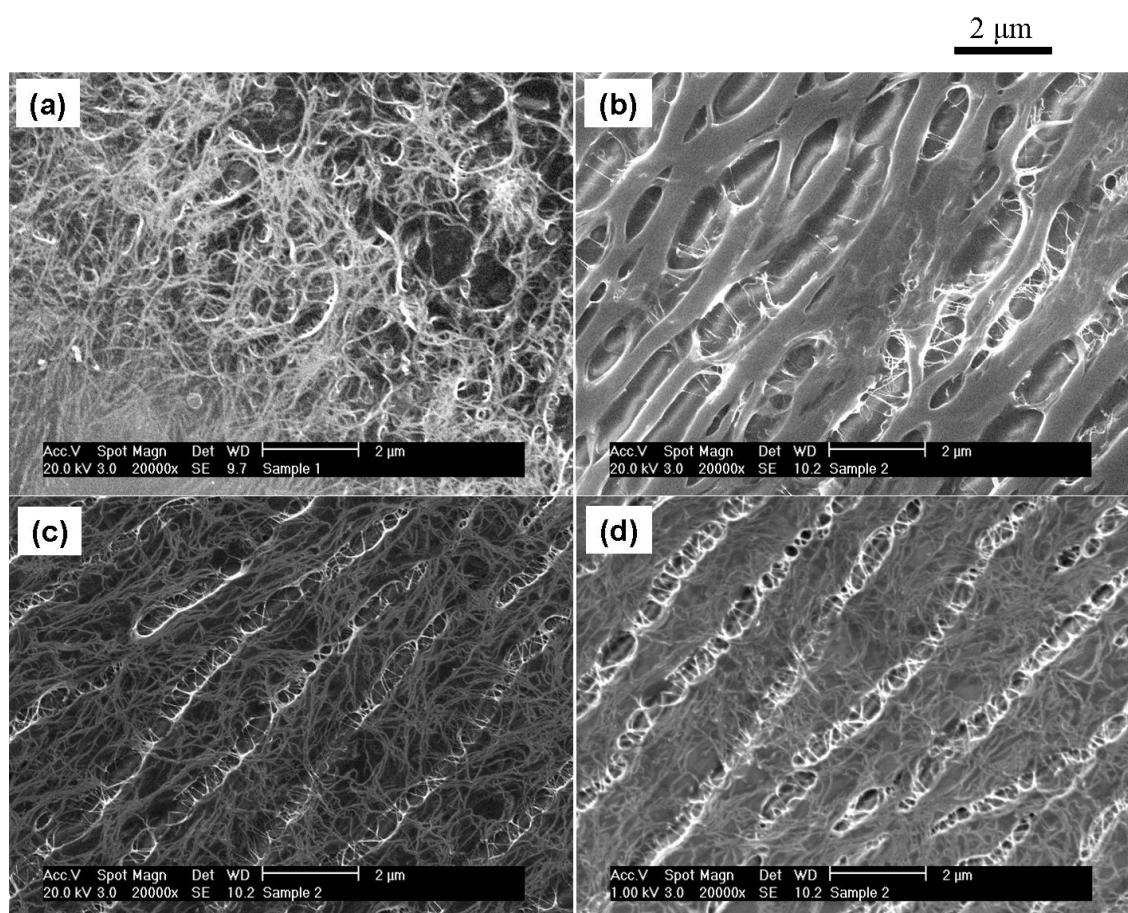


Figure 3.21 Scanning electron microscopy (SEM) images of the deposits and films from SDS-SWNT dispersions deposited onto untreated silicon wafers. (a) As-prepared dispersions and (b), (c) and (d) centrifuged dispersions. Images (c) and (d) are charge-contrast images at acceleration voltages of 20 kV and 1 kV respectively. (Images taken by Dr J. Loos, Eindhoven University of Technology, Netherlands.)

The CNTs have formed a randomly orientated network that spans these assemblies, covering most of the area of the film. Charge contrast imaging allows the analysis of the film at different depths,²⁵ revealing nanotubes distributed throughout the film and not just confined to the surface. SEM analysis was carried out by Dr J. Loos, at the Eindhoven University of Technology, Netherlands.

3.3.7 *Optical profiling*

Further information regarding the topography of the films and distribution of material was obtained by scanning white light interferometry. In this technique, a single beam of white light is split into reference and sample beams, which are then recombined to produce light and dark fringes corresponding to the topography of the sample.²⁶ Direct analysis of the films suggested that the film height was in some places lower than the substrate, which is not physically possible. This is most likely due to organised surfactant phases reflecting the light differently to the rest of the sample, resulting in these anomalous results. In order to remove this effect, it was necessary to make the films on the substrates appear to the interferometer as a bulk material with uniform properties in terms of refractive index. Sputtering with a thin layer of gold was employed initially, but this method proved destructive to the sample, preventing any additional analysis. A less destructive route was to produce a polydimethyl siloxane (PDMS) replica of the film on the substrate, following a procedure shown in Figure 3.22. This allowed us to produce an accurate replica of the original film, from which the profile of the film on the substrate could be obtained by inverting the height profile. In addition, the height profile of a mould of the initial replica was in good agreement with the height profile of the initial replica.

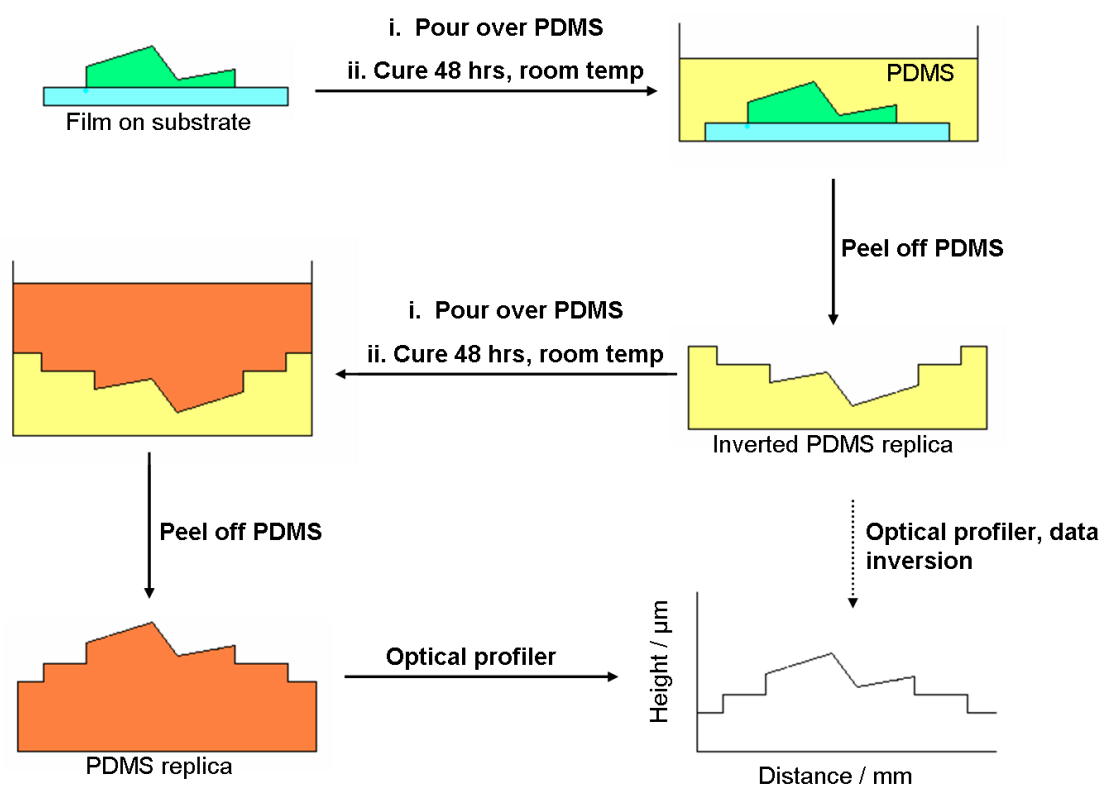


Figure 3.22 Scheme to show how the films and deposits on substrates are replicated with PDMS.

Figure 3.23 shows the typical height profile of a deposit from a drop of an as-prepared SDS-SWNT dispersion on an OTS-treated silicon substrate. These images are generated by the optical profiler software, which plots the height of the film as a function of the x and y coordinates. In the images from the optical profiler (Figure 3.23b and c), the regions in blue represent the substrate and the lowest points, through to regions in red being the highest points. The data in the height profile suggests that at the highest points the deposit is approximately $1\ \mu\text{m}$ thick, but that the spread of material over the substrate is not very uniform. The presence of an outer ring-like deposit, observed through optical microscopy and Raman spectroscopy, is also confirmed here.

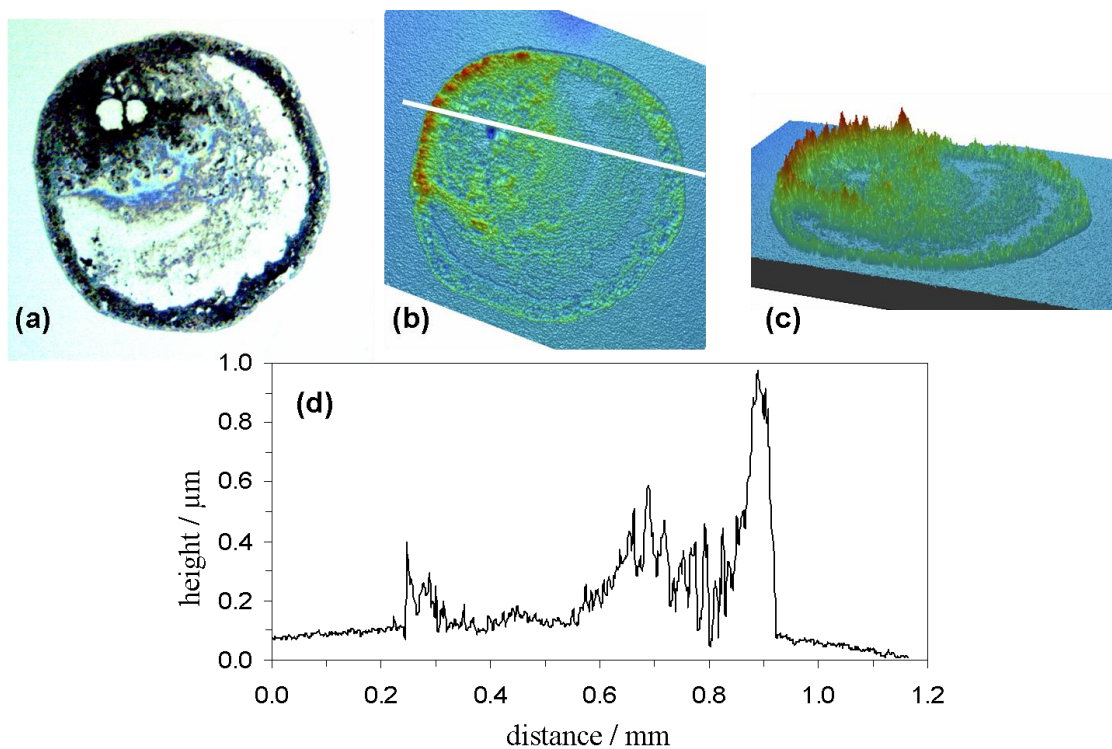


Figure 3.23 (a) Optical microscopy and (b) and (c) optical profiling images of the deposit from an as-prepared SDS-SWNT dispersion on an OTS-treated silicon substrate. (d) Height profile of the deposit taken over the white line in (b).

The profiles of a film from a centrifuged SDS-SWNT dispersion on an untreated silicon substrate are shown in Figure 3.24. The film is not uniform, with some regions almost a micron in thickness, while it appears other regions are devoid of material. This evidence supports the Raman spectroscopy results indicating a non-uniform distribution of CNTs. It also suggests that most of the material is in the region where the contact line became pinned during the evaporation.

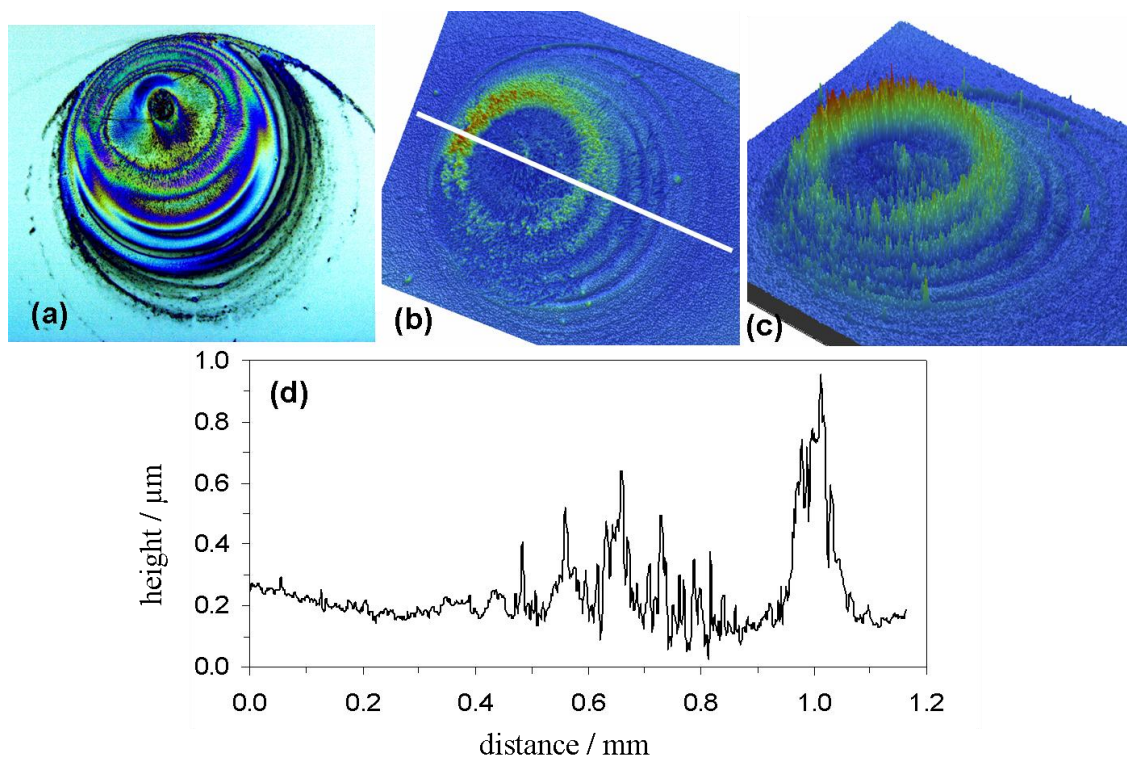


Figure 3.24 (a) Optical microscopy and (b) and (c) optical profiling images of the deposit from a centrifuged SDS-SWNT dispersion on an untreated silicon substrate. (d) Height profile of the deposit taken over the white line in (b).

On an OTS-treated silicon substrate, the deposition of material is far more symmetrical compared to that observed on the untreated silicon substrate. Figure 3.25 shows that the film thickness varies from $0.3 \mu\text{m}$ at the perimeter of the film, to $0.7 \mu\text{m}$ at the centre of the film and the final evaporation point. Unlike the film on untreated silicon and the deposit from the as-prepared dispersion, there appear to be no areas devoid of material, supporting the excellent spread of nanotubes observed in Raman spectroscopy.

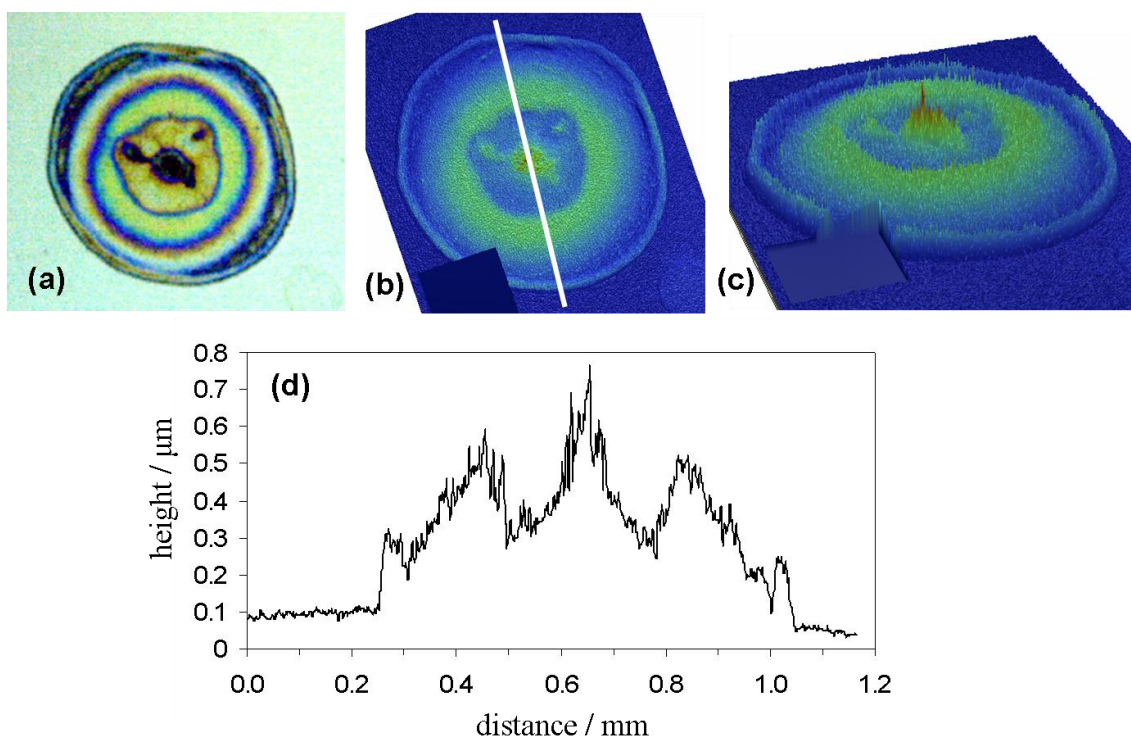


Figure 3.25 (a) Optical microscopy and (b) and (c) optical profiling images of the deposit from a centrifuged SDS-SWNT dispersion on an OTS-treated silicon substrate. (d) Height profile of the deposit taken over the white line in (b).

3.4 Conclusions

We have fabricated and characterised SDS-SWNT films, deposited onto different substrates. It has been found that the state of the SDS-SWNT dispersion affects the type of deposit remaining when a sessile drop evaporates on a substrate. Aggregates in as-prepared dispersions pin the contact line, resulting in a ‘coffee-stain’ like deposit. Removal of the aggregates through centrifugation allows the contact line to recede freely, and a film is formed. The hydrophobicity of the substrate also greatly affects both the size and nature of the deposits remaining, due to the different drop sizes formed initially and the subsequent drying mechanisms.

Films from centrifuged dispersions on hydrophilic substrates have an uneven distribution of material, including SWNTs, and appear to be susceptible to gravity-induced pinning, or pinning by a single aggregate. Films on hydrophobic substrates exhibit a more even distribution of material, due to the uniform motion of the contact

line during evaporation of the drop, and appear to be less susceptible to aggregate-induced pinning.²⁷

3.5 References

- 1 Thess, A., Lee, R., Nikolaev, P., Dai, H., Petit, P., Robert, J., Xu, C., Hee Lee, Y., Kim, S. G., Rinzler, A. G., Colbert, D. T., Scuseria, G. E., Tománek, D., Fischer, J. E. and Smalley, R. E., *Science*, 1996, **273**, 483.
- 2 Vigolo, B., Pénicaud, A., Coulon, C., Sauder, C., Pailler, R., Journet, C., Bernier, P. and Poulin, P., *Science*, 2000, **290**, 1331.
- 3 Jiang, L., Gao, L. and Sun, J., *J. Coll. Int. Sci.*, 2003, **260**, 89.
- 4 O'Connell, M. J., Bachilo, S. M., Huffman, C. B., Moore, V. C., Strano, M. S., Haroz, E. H., Rialon, K. L., Boul, P. J., Noon, W. H., Kittrell, C., Ma, J., Hauge, R. H., Weisman, R. B. and Smalley, R. E., *Science*, 2002, **297**, 593.
- 5 Wanless, E. J. and Ducker, W. A., *J. Phys. Chem.*, 1996, **100**, 3207.
- 6 Wanless, E. J. and Ducker, W. A., *Langmuir*, 1997, **13**, 1463.
- 7 Richard, C., Balavoine, F., Schultz, P., Ebbesen, T. W. and Mioskowski, C., *Science*, 2003, **300**, 775.
- 8 Moore, V. C., Strano, M. S., Haroz, E. H., Hauge, R. H. and Smalley, R. E., *Nano Lett.*, 2003, **3**, 1379.
- 9 Yurekli, K., Mitchell, C. A. and Krishnamoorti, R., *J. Am. Chem. Soc.*, 2004, **126**, 9902.
- 10 Priya, B. R. and Byrne, H. J., *J. Phys. Chem. C*, 2008, **112**, 332.
- 11 Bergin, S. D., Nicolosi, V., Cathcart, H., Lotya, M., Rickard, D., Sun, Z. Y., Blau, W. J. and Coleman, J. N., *J. Phys. Chem. C*, 2008, **112**, 972.
- 12 Islam, M. F., Rojas, E., Bergey, D. M., Johnson, A. T. and Yodh, A. G., *Nano Lett.*, 2003, **3**, 269.
- 13 Matarradona, O., Rhoads, H., Li, Z., Harwell, J. H., Balzano, L. and Resasco, D. E., *J. Phys. Chem. B*, 2003, **107**, 13357.
- 14 Guena, G., Poulard, C., Voue, M., De Connick, J. and Cazabat, A. M., *Coll. Surf. A*, 2006, **291**, 191.
- 15 Picknett, R. G. and Bexon, R., *J. Coll. & Int. Sci.*, 1977, **61**, 336.
- 16 Deegan, R. D., Bakajin, O., Dupont, T. F., Huber, G., Nagel, S. R. and Witten, T. A., *Nature*, 1997, **389**, 827.
- 17 Deegan, R. D., Bakajin, O., Dupont, T. F., Huber, G., Nagel, S. R. and Witten, T. A., *Phys. Rev. E*, 2000, **62**, 756.
- 18 Deegan, R. D., *Phys. Rev. E*, 2000, **61**, 475.

-
- 19 Porter, M. R., *Handbook of Surfactants*, Blackie Academic and Professional, London, 1994.
- 20 Kékicheff, P., Grabielle-Madelmont, C. and Ollivon, M., *J. Coll. Int. Sci.*, 1989, **131**, 112.
- 21 Frank, S. and Garoff, S., *Coll. & Surf. A: Physicochem. & Eng. Aspects*, 1996, **116**, 31.
- 22 Stöckelhuber, K.W., Radoev, B. and Schulze, H.J., *Coll. Surf. A*, 1999, **156**, 323.
- 23 Middleton, L.R., *A Textbook of Light*, G.Bell and Sons Ltd., London, 1958.
- 24 Dresselhaus, M. S., Dresselhaus, G., Jorio, A., Filho, A. G. S. and Saito, R., *Carbon*, 2002, **40**, 2043.
- 25 Loos, J., Alexeev, A., Grossiord, N., Koning, C. E. and Regev, O., *Ultramicroscopy*, 2005, **104**, 160.
- 26 www.veeco.com, checked 25th April 2009.
- 27 Small, W. R., Walton, C. D., Loos, J. and in het Panhuis, M., *J. Phys. Chem. B*, 2006, **110**, 13029.

CHAPTER 4

PREPARATION AND CHARACTERISATION OF CARBON NANOTUBE COMPOSITES IN AQUEOUS AND ORGANIC SOLVENTS

4.1 Introduction

This chapter will describe the preparation and characterisation of CNT composites using conducting polymers as dispersants. The conditions required to achieve dispersions of CNTs with these dispersants will be discussed, and the properties of the dispersions will be characterised. In the case of the CNT composite with two conducting polymers as dispersants, the composites have been processed into thin films, which have also been characterised.

4.1.1 *Conducting polymers*

Traditionally, polymers are thought of as insulating materials, ideal for protecting us from the conducting wires that provide our homes and appliances with electricity. There are, however, some polymers that can possess conductivities similar to those of metals. More amazingly, they can also be finely tuned so that the same polymer can undergo a ten order of magnitude change in conductivity, converting it from being an insulator to a conductor by changing the chemistry of the polymer.¹ These polymers are known as inherently conducting polymers, and they have over the past 30 years become the subject of much research due to their expected use in intelligent materials.²

The first reports of polymers that had high conductivities were by Shirakawa and co-workers in 1977,^{*} who observed that polyacetylene films oxidised (doped) with iodine became shiny, and increased in conductivity by nine orders of magnitude.³ This was followed by similar findings for the polymers polypyrrole,⁴ polyaniline⁵ and polythiophene.⁶ Since then, developments have been made exploring the synthesis,

^{*} Hideki Shirakawa, with co-workers Alan Heeger and Alan MacDiarmid would later win the Nobel Prize in Chemistry, 2000, for their discovery and development of electrically conductive polymers.

processing and doping of these polymers, so that they might find applications as sensors,⁷ actuators⁸ and electrochromic devices,⁹ to name just a few.

4.1.2 *Conductivity of conducting polymers*

When Shirakawa and co-workers first converted polyacetylene into a conducting film through exposure to iodine vapour, they made the first advances in understanding the mechanisms of polymer conduction.³ Later, they would observe similar behaviour when exposing the films to chlorine and bromine vapour, finding that the rise in conductivity followed a trend down the periodic table - the highest conductivity was obtained with iodine, the smallest with chlorine.¹⁰ This effect that the halogen vapours had on the polyacetylene films was termed ‘doping’, by analogy with the doping of semiconductor materials. In a semiconductor, conductivity can be achieved by either introducing dopants that are rich in electrons (n-doping) or holes (p-doping) into a system, increasing the number of charge carriers present. For conducting polymers, the term ‘doping’ is slightly misleading, though one that has become popular and therefore will be a term used throughout this thesis.

A more appropriate term to describe the interaction occurring between polyacetylene and the halogen vapours would be that of a ‘redox reaction’.¹¹ This is because the role of the ‘dopant’ is to either add or remove an electron from the polymer, itself becoming oxidised or reduced accordingly. The ‘dopant’ can therefore be thought of as a reducing or oxidising agent, and in the case of the halogens acting on polyacetylene, they act as oxidising agents, removing an electron from the polymer to give two new species. These are a polymer that becomes positively charged - a radical cation, also known as a ‘polaron’, and the halogen that becomes negatively charged in its reduced form. One of the properties of conducting polymers that makes them susceptible to undergo such redox reactions is that they have an extended conjugated nature, giving them small ionization potentials and/or large electron affinities, allowing the easy removal or injection of electrons into their system.¹¹ When an electron is removed, as in the case of polyacetylene with halogen vapour, the radical cation (polaron) that is formed on the polymer becomes partially localised due to attraction to the counterion (the reduced halogen). If the counterion is not particularly mobile, then the polaron cannot migrate very far along the polymer chain when an electric field is applied. For this reason, polymers must be sufficiently ‘doped’, so that there is a high enough concentration of counterions along the polymer chain for the polaron to be able

to migrate from one to the other, thus giving the polymer conductivity. With additional doping, further polarons can also form, which either act singularly or pair up, to become a ‘bipolaron’. It is the migration of these polarons and bipolarons, not just along individual chains but between adjacent polymer chains, that account for the conductivity in many conducting polymers.

4.1.3 Polyaniline

Since their discovery, one of the most studied conducting polymers is polyaniline (PAni), based on repeat units of aniline that polymerise in a ‘head to tail’ configuration. PAni exists in various oxidation states, which can be described based on a four ring-repeating unit, shown in Figure 4.1.

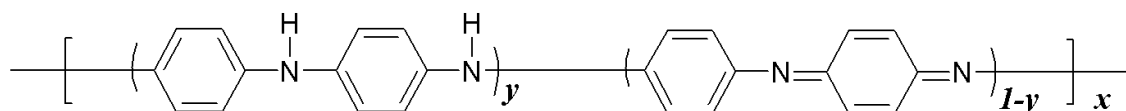


Figure 4.1 General structure of polyaniline. y (0, 0.5 or 1) determines the oxidation state of the polymer. x is the number of repeat units.

The fully reduced form of PAni, leucoemeraldine base ($y = 1$, Figure 4.1), is transparent and has poor conductivity. The half oxidised form, emeraldine ($y = 0.5$, Figure 4.1), exists in two states: emeraldine base (blue, insulating) and emeraldine salt (green, conducting). The base form can be converted to the salt either by doping with an acid, or through electrochemical manipulation of the polymer.¹² The fully oxidised form, pernigraniline ($y = 0$, Figure 4.1), is purple and has poor conductivity.¹³ PAni in its leucoemeraldine form is readily oxidised, and the pernigraniline form is also easily degraded.

There are two general routes towards the synthesis of PAni.

(i) Electrochemical polymerisation, which typically employs a three-electrode set-up comprising a working electrode on to which the polymer is deposited, a counter electrode and a reference electrode. There are three variables: galvanostatic polymerisation (under constant current) potentiostatic polymerisation (under constant potential), and potentiodynamic polymerisation, (variation of current and potential).¹⁴ The polymerisation is usually carried out in an acidic electrolyte, which serves to

solubilise the monomer and results in the emeraldine salt form of the polymer being formed. Employing this method of polymerisation, it is possible to direct the growth of the PANi onto working electrodes such as indium tin oxide (ITO) glass¹⁵ and platinum,¹⁶ while the thickness of the polymer film and the amount of doping can be controlled via the electrode potential.¹⁷

(ii) Chemical polymerisation, which requires three main components. These are the aniline monomer, an acidic medium, again to solubilise the monomer and ensure the PANi is synthesised in its emeraldine salt form, and an oxidant to oxidise the monomer.¹⁸ Typical oxidants include ammonium persulphate (APS),^{19, 20} potassium dichromate and hydrogen peroxide,²¹ though APS is the most commonly used. Other variables that can affect the molecular weight, morphology and conductivity of PANi are reaction temperature,²² pH,²³ reaction time, monomer/oxidant ratio²⁴ and rate of oxidant addition.²⁵ By positioning a substrate in the reaction vessel, the polymer can be grown directly onto this substrate.

Of the different oxidation states of PANi, it is the emeraldine salt form that is of most interest, for its conductivity and ability to become optically active upon interaction with chiral dopants. The introduction of the optical activity has been attributed to the polymer forming a helical screw, maintained by the chiral dopant anions via electrostatic and hydrogen bonding with the polymer backbone.²⁶ Such optical activity has been achieved with a number of different chiral acids,²⁷ though camphorsulfonic acid (CSA) is the most widely employed. Optical activity with this acid has been induced by doping the emeraldine base form of PANi with CSA,²⁸ as well as synthesising the polymer in the presence of CSA, using both chemical²⁰ and electrochemical^{29, 30} methods of polymerisation. It is envisaged that chiral PANi might find applications in chiral separations, where single enantiomers from a racemic mixture are selectively captured on a membrane, allowing the other enantiomer to pass through.³¹

4.1.4 *Water soluble polyaniline*

The stability, conductivity and potential for the inducement of optical activity in PANi make it a candidate for many applications, such as actuators, chiral separation membranes and thin conducting films. As its solubility is limited to organic solvents however, efforts have been made to synthesise a water-soluble version of this polymer. One route that has been employed has been to use a water-soluble polyelectrolyte,

poly(acrylic acid), as a template for the growth of PANi, forming a composite that is bound by electrostatic interactions and is soluble in water.³² Other methods include reacting PANi with fuming sulphuric³³ or chlorosulfuric acid,³⁴ resulting in the rings of PANi becoming functionalised with sulfonic acid groups which enhance the water solubility of the polymer. Finally, the polymerisation of sulfonated aniline monomers has been achieved through chemical oxidation, resulting in the polymer poly(2-methoxyaniline-5-sulfonic acid) (PMAS).^{35,36} Where the PANi chain is functionalised with sulfonic acid groups to achieve solubility in water, it is believed that the polymerisation of sulfonated monomers rather than reaction of the backbone with sulfonic acid results in the more thermally stable polymers, due to lower steric strain in the chains.³⁷

4.1.5 Conducting polymer-CNT composites

As discussed in Chapter 1, one of the main challenges facing researchers working with CNTs is how to convert them from an as-produced bulk material, where their unique and outstanding properties are hidden, into a useful material that exploits these properties. One route that is being explored as a potential solution to this problem is to incorporate CNTs into composites, with polymers acting as a host matrix and dispersant for the nanotubes.² In particular, conducting polymers are seen as an excellent composite material for CNTs, with the CNTs adding enhanced conductivity and mechanical strength to the composite, and the polymer ideal for processing the nanotubes and providing an interface that is sensitive to external stimuli.

Composite synthesis with conducting polymers and CNTs has been achieved through methods including direct mixing,³⁸ covalent³⁹ and non-covalent⁴⁰ functionalisation, and *in situ* polymerisation, where the polymer is synthesised in the presence of the nanotubes.⁴¹ Much of this work has focused on the conducting polymer PANi, with Ramamurthy and co-workers adding MWNTs to PANi emeraldine base through mixing, and processing the dispersions into films that could then be doped to the emeraldine salt form with exposure to HCl.⁴² Where PANi is synthesised with the CNTs present *in situ*, it is believed that the nanotubes act as molecular templates for the polymer growth.⁴³ This is believed to arise through efficient π - π interactions, or stacking of the aniline rings on the surface of the nanotubes, leading to a close interaction between the polymer and the nanotubes. This mechanism of 'ring stacking' has also been suggested for CNT composites with phenylenevinylene⁴⁴ and PMAS.⁴⁵

CNT composite powders with polyaniline in the emeraldine base form have been processed into supported⁴³ and free-standing films,⁴⁶ which can then be doped into the emeraldine salt form through exposure to acid vapour. Several reports have found that the electrical and mechanical properties of composites with CNTs are improved when compared to the properties of the polymer alone.⁴⁷

4.2 PANi-CNT composites

4.2.1 PANi-MWNT composite dispersions in DMSO

Non-aqueous composites of MWNTs with PANi were prepared through an *in situ* polymerisation route, as described in Chapter 2. Two types of MWNTs were used in this study, produced by the Arc-discharge and CVD processes. Figure 4.2 shows the UV-vis absorption spectra of these composites and polymer in DMSO, at a concentration of 0.5 mg mL^{-1} .

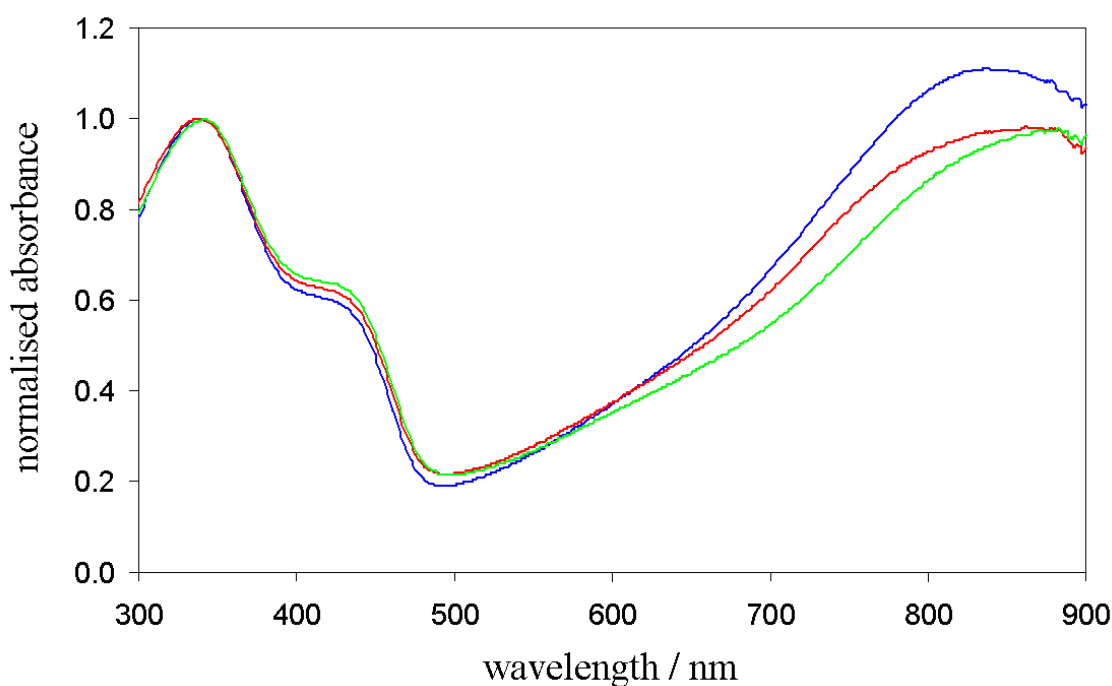


Figure 4.2 UV-vis spectra (normalised at 340 nm) for PANi (blue line), and PANi-CNT composites with Arc MWNTs (red line) and CVD MWNTs (green line) in DMSO at a concentration of 0.5 mg mL^{-1} .

The spectra for PANi and the composites with both types of nanotube all show the same characteristic features commonly observed for PANi emeraldine salt. These features are bands at approximately 340, 430 and 860 nm, which have previously been assigned as the $\pi - \pi^*$, polaron - π^* and π - polaron transitions, respectively.⁴⁸ The presence of the localised band at 860 nm indicates that the polymer is in the ‘compact coil’ conformation where the polymer chains are tightly coiled, rather than the ‘extended coil’ conformation.¹³ The presence of nanotubes does not appear to effect this conformation, as the position of the characteristic bands is unchanged.

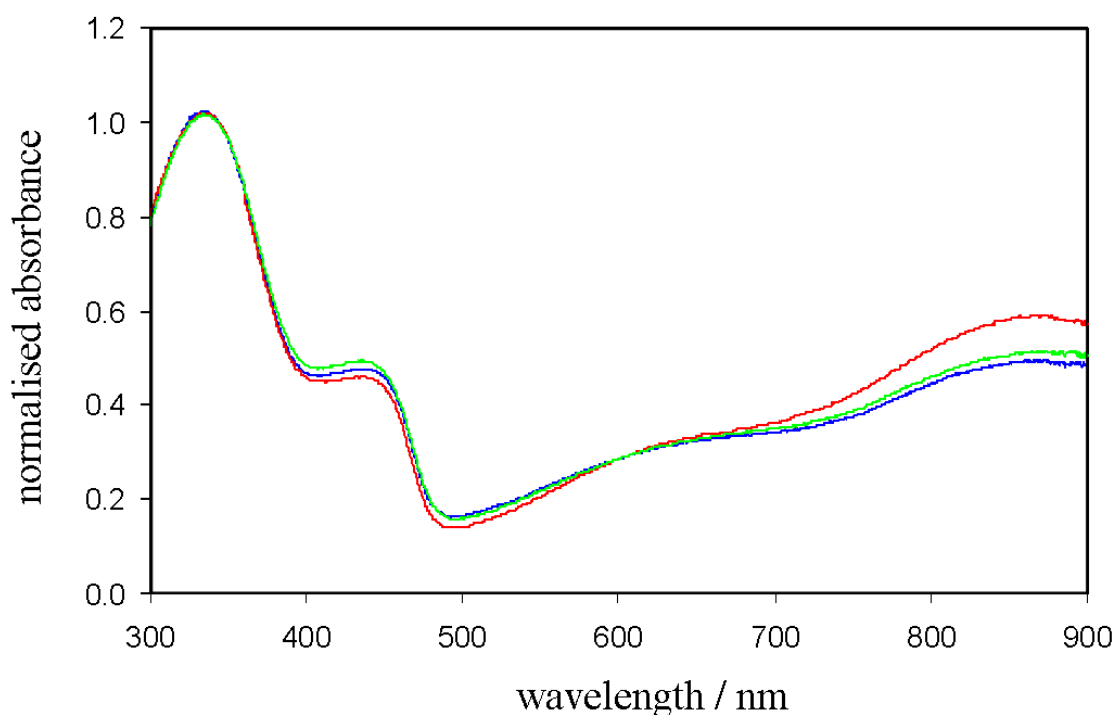


Figure 4.3 UV-vis spectra (normalised at 340 nm) for PANi (blue line), and PANi-CNT composites with Arc MWNTs (red line) and CVD MWNTs (green line) in DMSO at a concentration of 0.1 mg mL⁻¹.

Diluting the composites to 0.1 mg mL⁻¹ results in the following changes in the spectra; a new band appears at approximately 620 nm, while the relative intensity of the $\pi - \pi^*$ and polaron bands change. This new band has been attributed to a localised polaron band, and is a result of solvent induced deprotonation.²⁰ The extent of the deprotonation is only partial however, as a band is still observed 860 nm – when the polymer is fully deprotonated, as in Pani emeraldine base, this peak disappears entirely.

Figure 4.4 shows the UV-vis spectra of PANi and the PANi composite with Arc MWNTs in the solvent *m*-cresol. This solvent has previously been described as acting as a ‘secondary dopant’ for Pani, converting it from the ‘compact coil’ to ‘extended coil’ form through interactions between the solvent and the polymer. This results in the localised band at 860 nm becoming delocalised into the near infra red region, and is believed to occur as the ring in *m*-cresol and its phenolic group act to straighten out the polymer through van der Waals interactions.⁴⁹⁻⁵¹

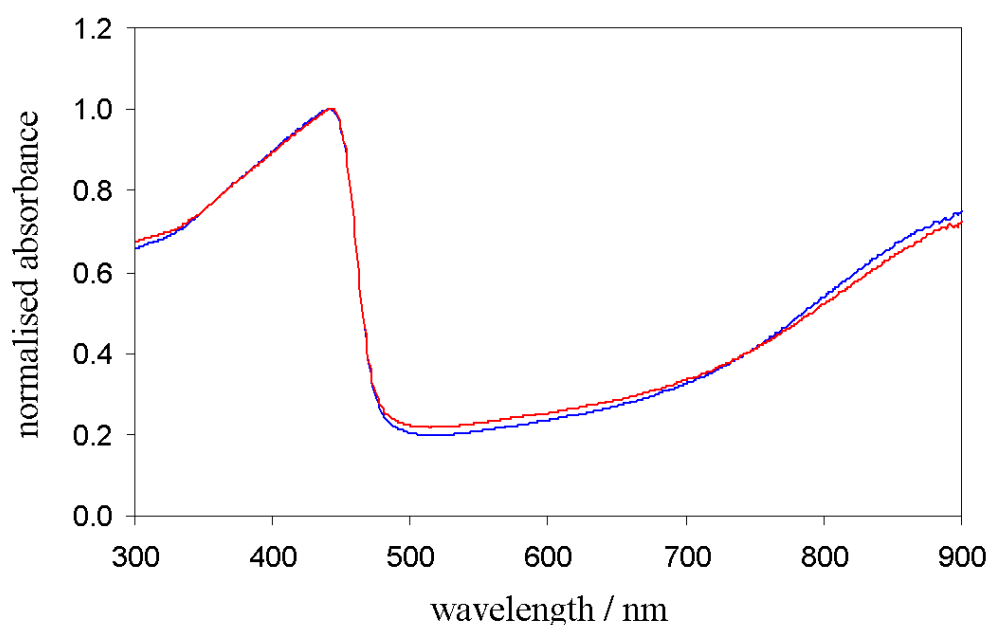


Figure 4.4 UV-vis spectra (normalised at 440 nm) for PANi (blue line) and the PANi-CNT composite with Arc MWNTs (red line) in *m*-cresol at a concentration of 0.5 mg mL⁻¹.

4.2.2 Transmission electron microscopy of PANi-MWNT composites

Transmission electron microscopy (TEM) images of the composites with Arc and CVD MWNTs are shown in Figure 4.5. From the image in Figure 4.5a we can count the number of walls of the nanotube - this particular nanotube appears to be made up of 9 carbon cylinders. The wetting of the nanotubes by the polymer is also evident, particularly in Figure 4.5b where the nanotube appears to be coated by the polymer all along its axis. Good wetting of the nanotubes by the polymer is important for two reasons. (i) we expect that nanotubes with their entire surface coated in polymer will be less likely to aggregate and sediment from their dispersion than nanotubes with some of

their surfaces exposed. (ii) a good polymer-nanotube interaction is expected to be advantageous for sensing applications, where a change in the electrical properties of the polymer may be felt by the nanotubes.

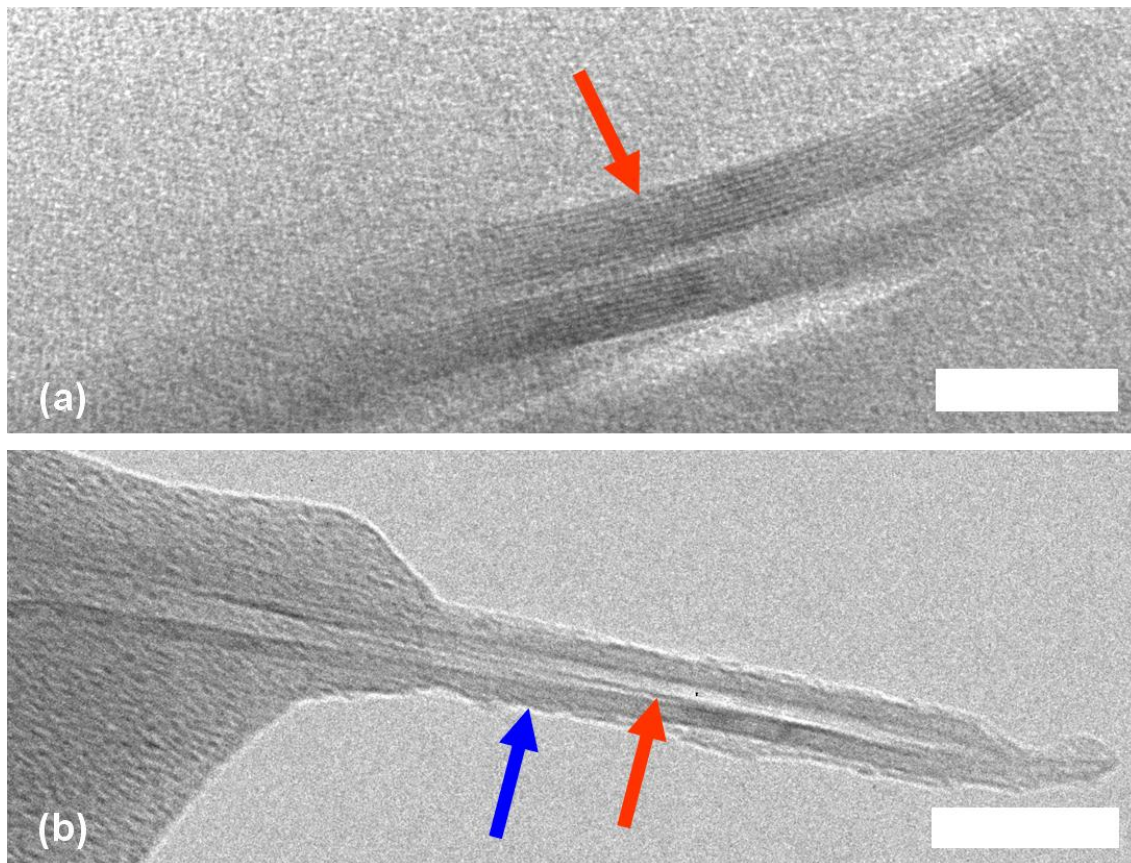


Figure 4.5 TEM images of PANi-CNT composites with (a) Arc MWNTs (scale bar 25 nm) and (b) CVD MWNTs (scale bar 50 nm). Red arrows show MWNTs, blue arrow shows PANi wetting the nanotubes. Images taken by Mrs Janice Haller, University of Hull.

4.2.3 Thermogravimetric analysis of PANi-MWNT composites

Figure 4.6 shows the thermogravimetric analysis (TGA) spectra of Pani emeraldine salt, the two PANi-MWNT composites and the two different types of nanotubes used to make the composites.

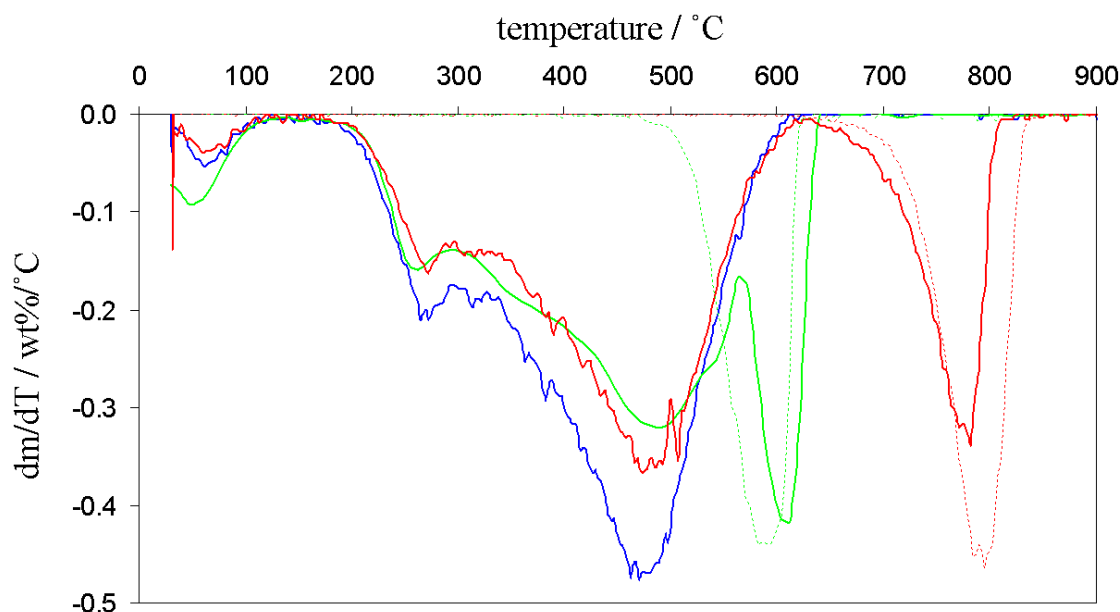


Figure 4.6 TGA derivative spectra of PANi (blue line), the composite with Arc MWNTs (red line) and the composite with CVD MWNTs (green line). The dashed lines indicate the spectra for the Arc MWNTs (dashed red line) and CVD MWNTs (dashed green line) alone.

The CVD and Arc MWNTs show single decomposition features centred at 590 and 790 °C, respectively. The higher decomposition temperature of the Arc MWNTs is attributed to their higher level of graphitisation, which makes them more thermally stable than CVD MWNTs. Graphitisation is the ratio of sp^2 hybridised carbon to sp^3 hybridised carbon, which is higher for these Arc MWNTs than it is for the CVD MWNTs. The spectra for PANi comprises of three main regions; loss of water (up to 100 °C), decomposition of the dopant anion (at around 270 °C) and degradation of the polymer backbone (280 - 630 °C).⁵² The composites exhibited four features, attributed to the polymer and nanotubes. The polyaniline backbone decomposition features have shifted to higher temperature. This suggests that the presence of the nanotubes enhances thermal stability within the composite, preventing the polymer from decomposing until higher temperatures are reached. The feature attributed to decomposition of the nanotubes are shifted to lower temperature for the Arc MWNT composite (red line), and to higher temperature for the CVD MWNT composite. This effect for the Arc MWNT composite where the polymer peak is shifted to higher temperature and the nanotube

peak is shifted to lower temperature has previously been attributed to the formation of a new PANi-nanotube phase.⁵³

4.2.4 *Optical activity of PANi-MWNT composites*

4.2.4.1 *Optical activity and circular dichroism*

Molecules that cannot be superimposed on their mirror images are said to be chiral, with each of the mirror images termed enantiomers.⁵⁴ These enantiomers share identical physical properties to each other, and interact similarly with achiral substances; however they react differently with other chiral molecules. This difference in the interactions between two types of chiral molecule is a very important factor in drug development, as many of the enzymes and amino acids in the body are chiral, and so chiral drugs must be of the correct chirality to have the desired effect on the body. To this end, chiral separation, to remove one enantiomer from a racemic (both enantiomers) mixture, is an important process .

One way to measure whether a molecule is chiral or not is to measure its optical activity - based upon studying the interactions of the molecule with polarised light. Chiral molecules can rotate plane polarised light either to the left or the right, depending on the enantiomer of the molecule, and they can also preferentially absorb circularly polarised light that corresponds with the chirality of the molecule. In the technique known as circular dichroism (CD), the difference between the amount of left and right circularly polarised light that a sample absorbs is measured, and plotted as a function of wavelength. Non-chiral molecules or racemic mixtures with equal amounts of each enantiomer would give CD spectra with no net difference in the adsorption of either handedness of the light. However if only one of the enantiomers is present in the sample or it is present in sufficient excess, then a spectra will be recorded that is characteristic of that enantiomer. The spectrum of the other enantiomer of that chiral molecule would give a spectrum that is identical to the first enantiomer, but as a mirror image, or inverted about the x axis.

4.2.4.2 *Circular dichroism of PANi-MWNT composites*

Conducting polymers can display optical activity, either inherently through covalent attachment of chiral substituents to their backbone, or through doping with a chiral dopant molecule. In the doping mechanism, it is believed that the dopant interacts with the polymer through electrostatic interactions and hydrogen bonding, causing the

polymer backbone to adopt a helical screw.²⁶ The helicity/direction of this screw depends on the chirality of the dopant.

In this work, the dopant camphorsulfonic acid acts not only to convert the polymer into its emeraldine salt form, but also to induce chirality. Figure 4.7 shows the CD spectra of PANi and the two MWNT composites, in DMSO at a concentration of 0.5 mg mL⁻¹.

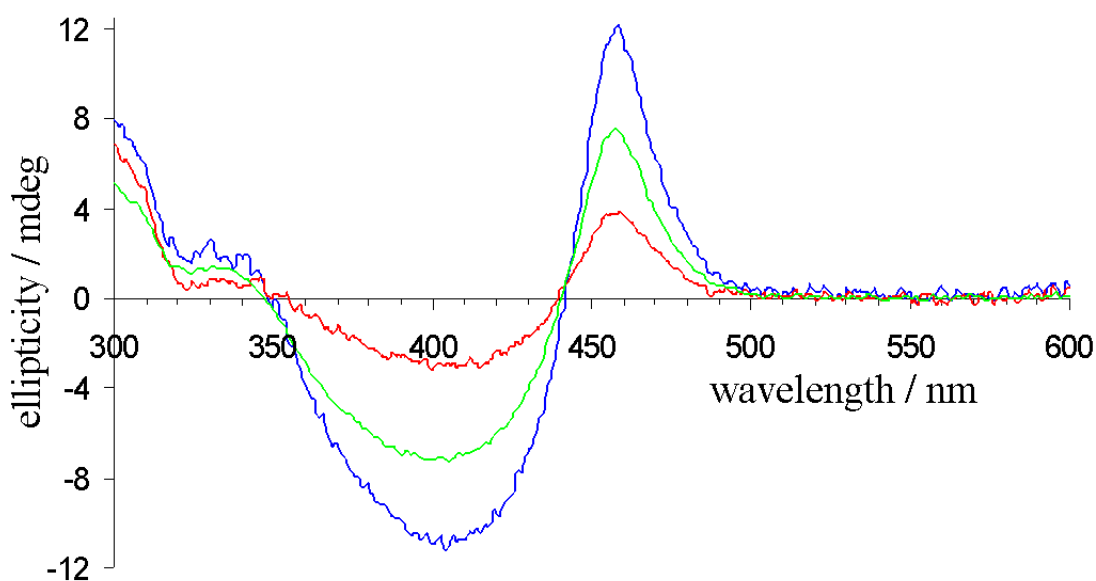


Figure 4.7 Circular dichroism spectra of PANi (blue line) and the composites with Arc MWNTs (red line) and CVD MWNTs (green line). Samples dispersed in DMSO at a concentration of 0.5 mg mL⁻¹.

The spectrum for PANi doped with camphorsulfonic acid corresponds with that observed by other workers, where the optical activity was induced through doping of the polymer after it had been synthesised. The bisignate (positive and negative) bands observed here, known as the ‘cotton effect’, at approximately 400 and 450 nm are attributed to low wavelength polaron and $\pi - \pi^*$ absorption transitions.^{28, 30} These same peaks are also observed in each of the spectra for the PANi-MWNT composites, though they are somewhat reduced in intensity, especially for the composite with the Arc MWNTs. Although CNTs themselves are chiral, a random mixture of nanotubes of different chiralities would not be expected to contribute to the CD spectra, so we

assume that the observed optical activity is attributed to the polymer.² The reduction in intensity for the composites may be due to the observation (in TEM and TGA analysis) that the polymer interacts with the nanotubes, forming a polymer-nanotube phase. This may therefore suggest that the polymer adsorbed to the nanotube surface does not contribute to the optical activity of the composite, with the optical activity only caused by ‘free’ polymer in the composite. Another explanation may be that the chirality of the polymer adsorbed to the nanotubes is influenced by and follows the chirality of the nanotubes, which would therefore cancel out, as a mixture of nanotubes of differing chirality would have no *net* chirality. Further evidence to support this arises from the lower intensity of the peaks in the Arc MWNT composite than in the CVD MWNT composite, where the Arc MWNTs are better graphitised than the CVD and so more efficient polymer stacking onto the Arc MWNT might be expected due to the higher ratio of sp^2 hybridised carbon. This would leave more ‘free’ polyaniline in the CVD composite than in the Arc composite, and account for the larger optical activity in the CVD composite.

Earlier, the effects of solvent induced deprotonation of the PANi in DMSO at low concentrations were discussed. Here, the effect that this de-doping has on the optical activity is shown in Figure 4.8.

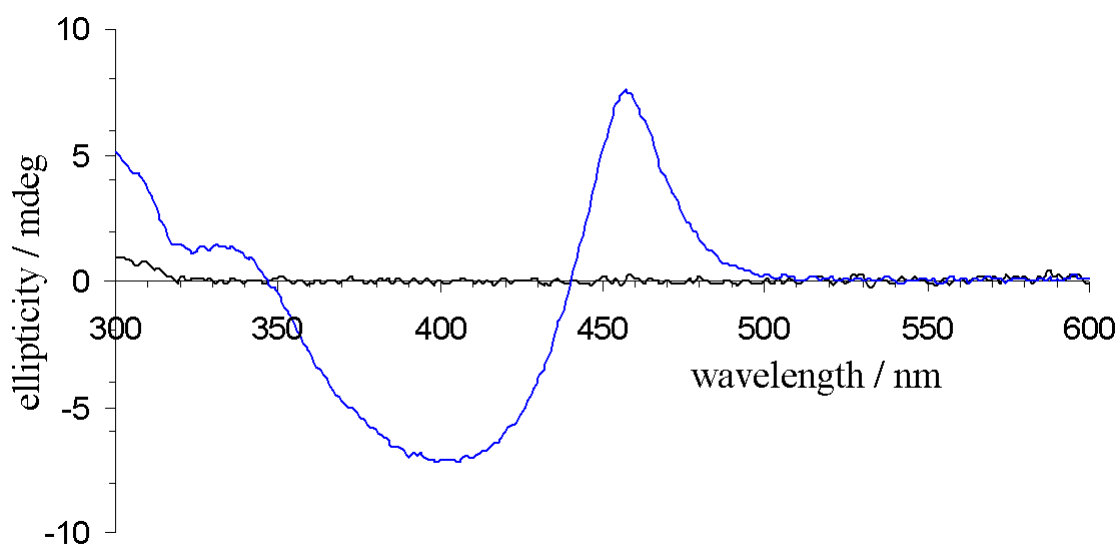


Figure 4.8 Circular dichroism spectra of commercial PANi emeraldine salt in DMSO at concentrations of 0.5 mg mL^{-1} (blue line) and 0.1 mg mL^{-1} (black line).

At the higher concentration of 0.5 mg mL^{-1} , the polymer shows the characteristic bisignate spectrum, suggesting that the polymer is optically active. At the lower concentration however, of 0.1 mg mL^{-1} , no peaks are observed. This provides further evidence that the solvent DMSO de-dopes PANi at low concentrations, and as the dopant here is a *chiral* acid, this therefore results in a loss of optical activity in the polymer.

Figure 4.9 shows the spectra of PANi and the composite with Arc MWNTs in another organic solvent, *m*-cresol, at a concentration of 0.5 mg mL^{-1} .

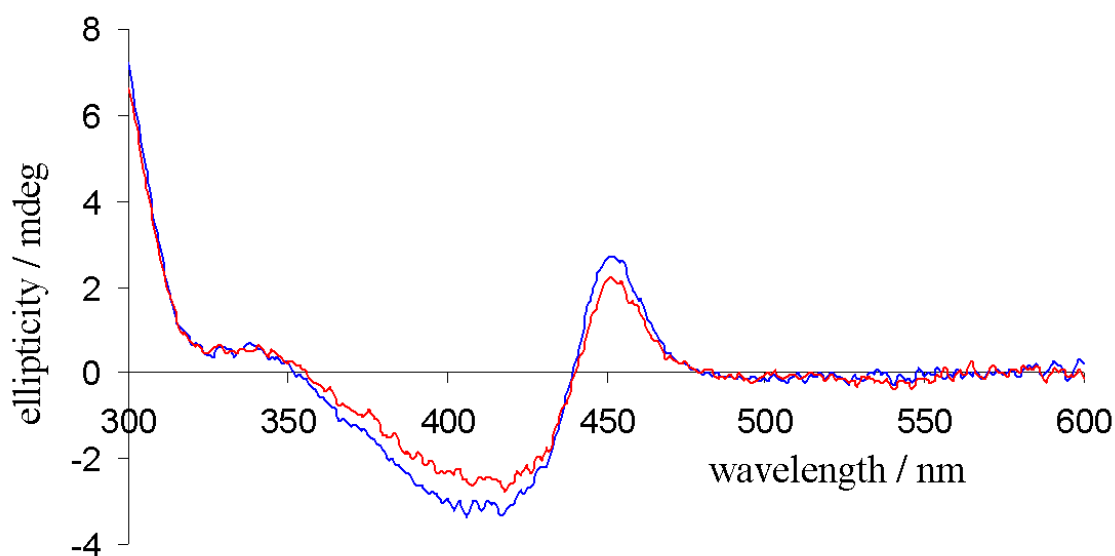


Figure 4.9 Circular dichroism spectra of PANi (blue line) and the composite with Arc MWNTs (red line) in *m*-cresol at a concentration of 0.5 mg mL^{-1} .

In *m*-cresol, the intensity of the optical activity is reduced compared to the optical activity in DMSO, though there is not the same further reduction for the composite with Arc MWNTs. It has been explained that *m*-cresol interacts strongly with the polymer, acting as a secondary dopant, and the reduced intensity of the optical activity in this solvent might therefore be attributed to the increased interactions between the polymer and the solvent.

Films of PANi and the composite with Arc MWNTs in *m*-cresol, at a concentration of 0.5 mg mL^{-1} , were cast onto glass slides. As Figure 4.10 shows, the optical activity of the composites is retained when the dispersions are cast into films.

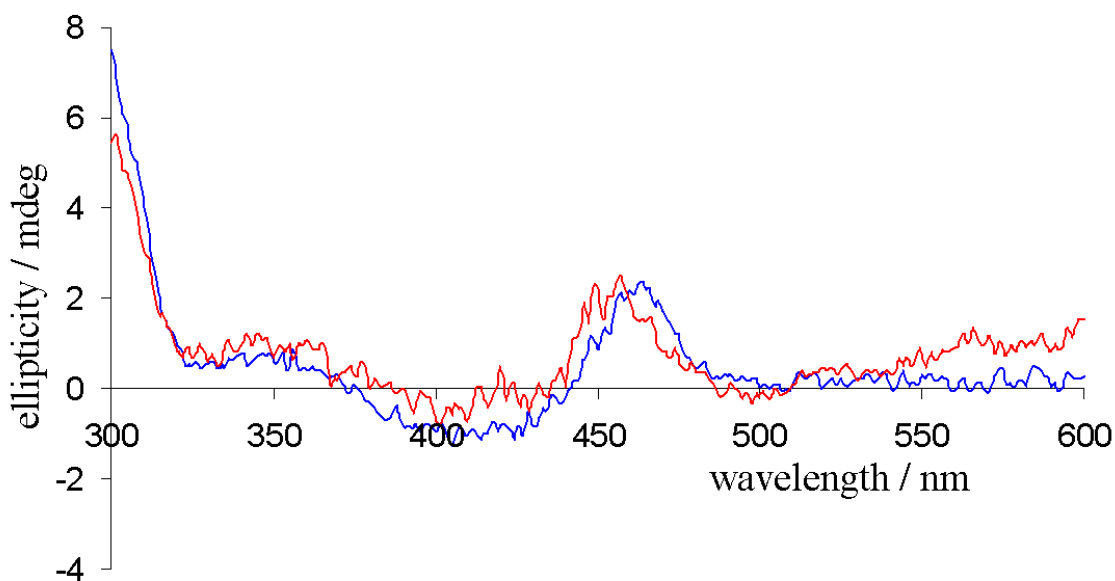


Figure 4.10 Circular dichroism spectra of supported films from PANi (blue line) and the composite with Arc MWNTs (red line). Films cast from *m*-cresol at a concentration of 0.5 mg mL⁻¹.

In summary, we have successfully synthesised PANi-CNT composites where the optical activity is induced *during* the polymerisation by the presence a chiral acid, rather than doping the polymer after it has been synthesised.⁵⁵ These composites are soluble in the organic solvents DMSO and *m*-cresol, and show optical activity both in solution and in dried films.

4.3 PMAS-CNT composites

Studying the interactions between a range of different CNTs and a dispersant is of great interest, as we consider the suitability of dispersions for processing methods such as drop deposition and inkjet printing. For example, what is the least amount of mixing required for nanotube dispersions, what are the conditions that lead to dispersions with the highest loading fractions of nanotubes and which dispersions are most stable against aggregation of the nanotubes over time? Here we will consider some of these issues, trying to relate these properties of the dispersions to the inherent

properties of the nanotubes, such as their size (number of walls, length and diameter/curvature), orientation (straight or bent/curved) and graphitisation.

4.3.1 Effects of sonicating time on the molecular weight of PMAS

An important factor when considering the dispersion of CNTs with conducting polymers is that of sonication time. Sonicating CNTs can not only be detrimental to the nanotubes in terms of shortening their length,⁵⁶ but also to the polymer, as an investigation of the effects of sonicating time on the molecular weight (Mw) of PMAS shows in Figure 4.11. PMAS solution was prepared at a concentration of 1.0 mg mL^{-1} , and sonicated at a power of 20 W with pulses of 2 s on, 1 s off for 60 minutes. At regular intervals, a small portion of the sample was removed and the molecular weight was measured with gas phase chromatography (GPC).

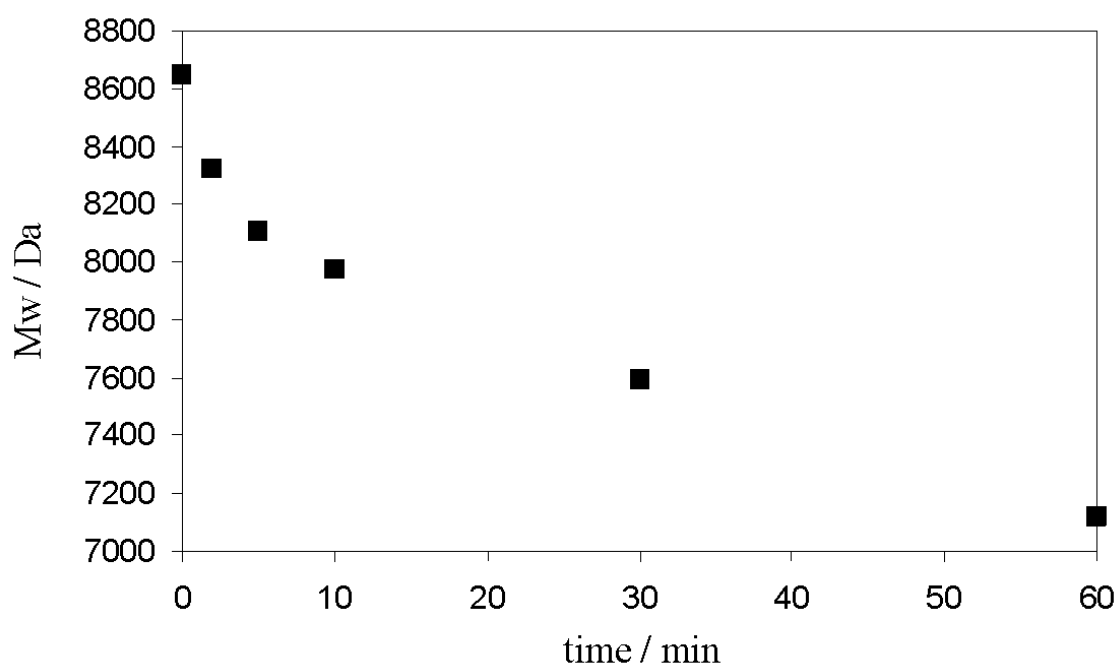


Figure 4.11 Effects of sonicating time on the molecular weight of PMAS. PMAS solution prepared at 1.0 mg mL^{-1} , and sonicated at a power of 20 W with pulses of 2 s on, 1 s off. Molecular weight data obtained by GPC analysis.

The molecular weight of the polymer before sonicating is approximately 8600 Da, but even with two minutes sonicating this drops significantly, to around 8300 Da.

This decrease in the molecular weight is attributed to a shortening in the chain length caused by the harsh mixing. After sixty minutes of sonicating, the molecular weight of the polymer had decreased to approximately 7100 Da, a reduction of almost 20 %. Clearly, the length of time that nanotubes are dispersed in a conducting polymer should be as short as possible, to avoid this reduction in polymer chain length.

4.3.2 Investigating PMAS-CNT interactions

A number of different types of nanotubes (at a concentration of 1 mg mL⁻¹) have been dispersed in PMAS (at a concentration of 5 mg mL⁻¹) with sonication, over a 24 minute period. The dispersions were sonicated at approximately 20 W, with pulses of 2 s on, 1 s off. After 6, 12, 18 and 24 minutes, a small portion was removed from the dispersion and diluted to a total solids concentration of 0.1 mg mL⁻¹ for UV-vis spectroscopy. The spectra in each of the following figures are normalised to the lowest wavelength peak. Figure 4.12 shows the UV-vis spectra of PMAS and PMAS-SWNT dispersions, prepared using HiPco SWNTs (lot PØ185, Carbon Nanotechnologies Inc., Houston, TX). These nanotubes have a diameter distribution of 0.7 – 1.3 nm,⁵⁷ are well graphitised and have a bent/curved orientation (see Chapter 3, Figure 22).

The spectrum for PMAS has been described by other authors, and comprises two main regions.⁵⁸ These regions are a band at 280 - 400 nm representing a $\pi - \pi^*$ transition, and a sharp peak at approximately 474 nm representing a low wavelength polaron band. With the addition of SWNT, three main changes to the spectra are observed. These are a shift to lower wavelength of the $\pi - \pi^*$ transition band, a decrease in intensity of the low wavelength polaron peak at 474 nm, and an increase in intensity in the spectra from around 500 nm onwards.⁴⁵ The shift and lowering in intensity of the two peaks is attributed to a change in conformation of the polymer upon interaction with the nanotubes, and similar effects have been described for PANi-nanotube interactions.⁵⁹ The increase in intensity at longer wavelengths is attributed to the presence of the nanotubes, and the visible van Hove singularities indicate that the SWNTs have been dispersed into small bundles or individual nanotubes by the polymer.

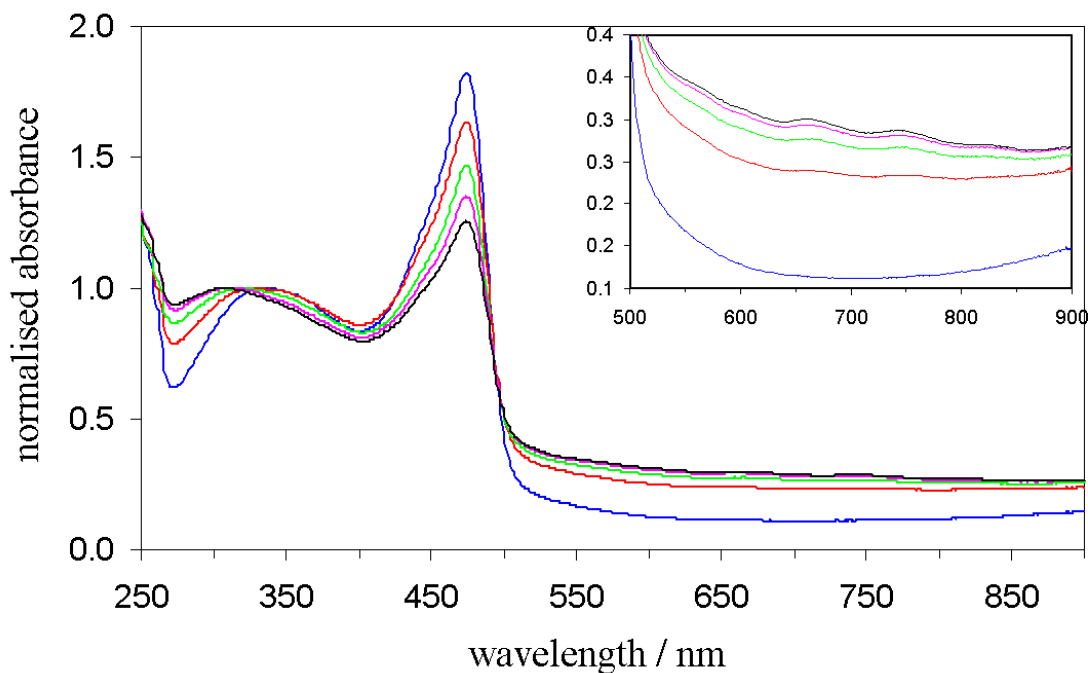


Figure 4.12 UV-vis spectra of PMAS (blue line) and PMAS-SWNT dispersions sonicated 6 minutes (red line), 12 minutes (green line), 18 minutes (pink line) and 24 minutes (black line). Inset is an enlargement of the van Hove singularities, observed between 500 and 900 nm.

The effects that have been observed appear to be dependant on the length of sonicating time, with larger shifts and higher/lower intensities observed for longer sonicating times. This is interesting, as it suggests that these nanotubes undergo gradual incorporation into the polymer - some mixing takes place at short sonicating times, but for extra nanotube solubilisation, longer times are required. This is in contrast to the case of PMAS-CVD MWNT dispersions, shown in Figure 4.13.

The CVD MWNTs (Batch no. NFL 60, Nanocyl, Belgium) are larger in diameter than the SWNTs and are not as well graphitised, but they are also bent/curved in orientation. As Figure 4.13 shows, the changes in the spectra on the addition of CVD MWNTs are the same as those observed for SWNTs (without the presence of the van Hove singularities), but there is not the same dependence of degree of change in the spectra on the length of sonicating time. With the CVD MWNTs, the spectrum after 24 minutes sonicating is no different to that obtained after 6 minutes sonicating, which suggests that the incorporation of CVD MWNTs has reached a limit after just 6 minutes

of mixing. With the SWNTs, nanotubes were still being incorporated after 24 minutes of mixing.

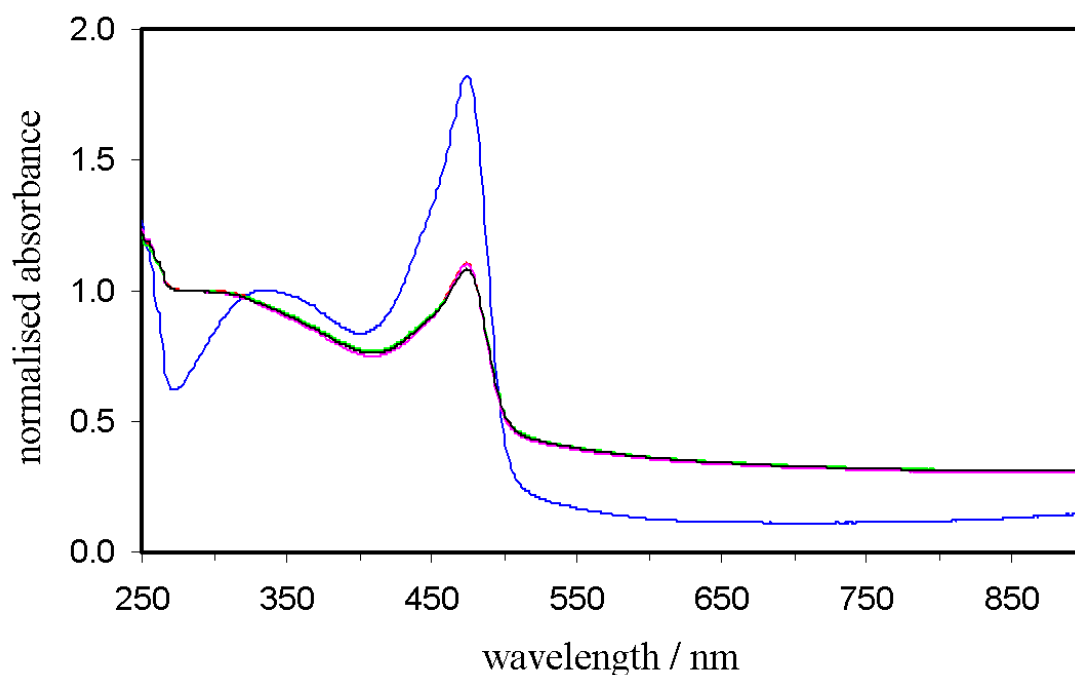


Figure 4.13 UV-vis spectra of PMAS (blue line) and PMAS-CVD MWNT dispersions sonicated 6 minutes (red line), 12 minutes (green line), 18 minutes (pink line) and 24 minutes (black line).

Figure 4.14 shows the UV-vis spectrum for PMAS-DWNT dispersions, with the DWNTs (Nanocyl, Belgium) also formed through the CVD technique. These nanotubes are intermediate in diameter between the SWNTs and the MWNTs.

The changes in the UV-vis spectra for these PMAS-DWNT composites are greater than for the SWNT composite, but not as large as for the MWNT composite. The changes in the spectra increase with sonication time, as seen for SWNTs, but the peak shifts and intensity changes are similar to those observed for the MWNTs. This suggests that the MWNTs are most easily and rapidly dispersed, followed by the DWNTs and then the SWNTs.

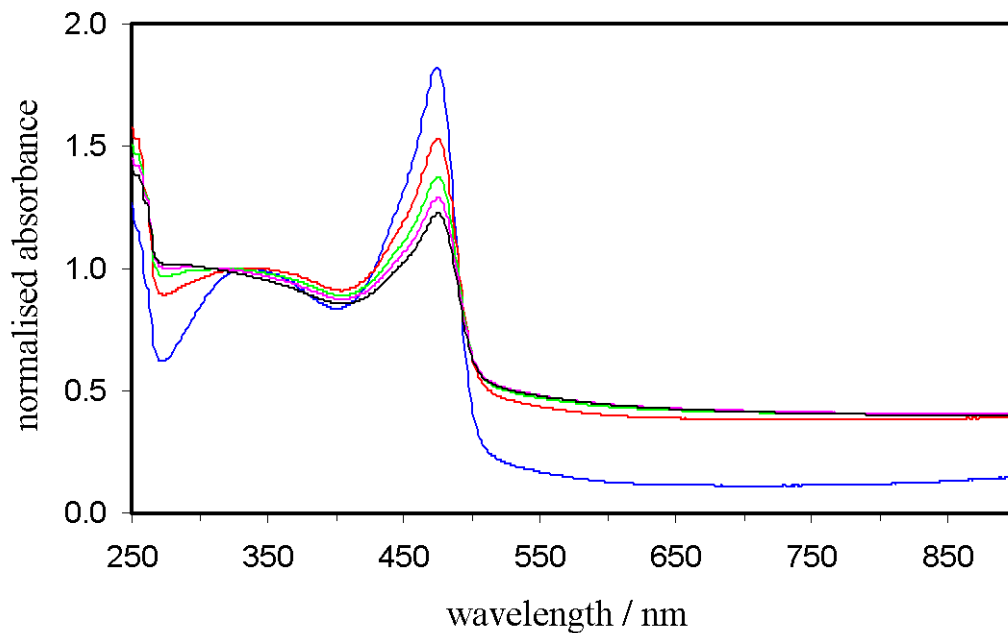


Figure 4.14 UV-vis spectra of PMAS (blue line) and PMAS-DWNT dispersions sonicated 6 minutes (red line), 12 minutes (green line), 18 minutes (pink line) and 24 minutes (black line).

Arc MWNT (supplied by the Instituto de Carboquímica, Zaragoza, Spain) were also dispersed in PMAS.

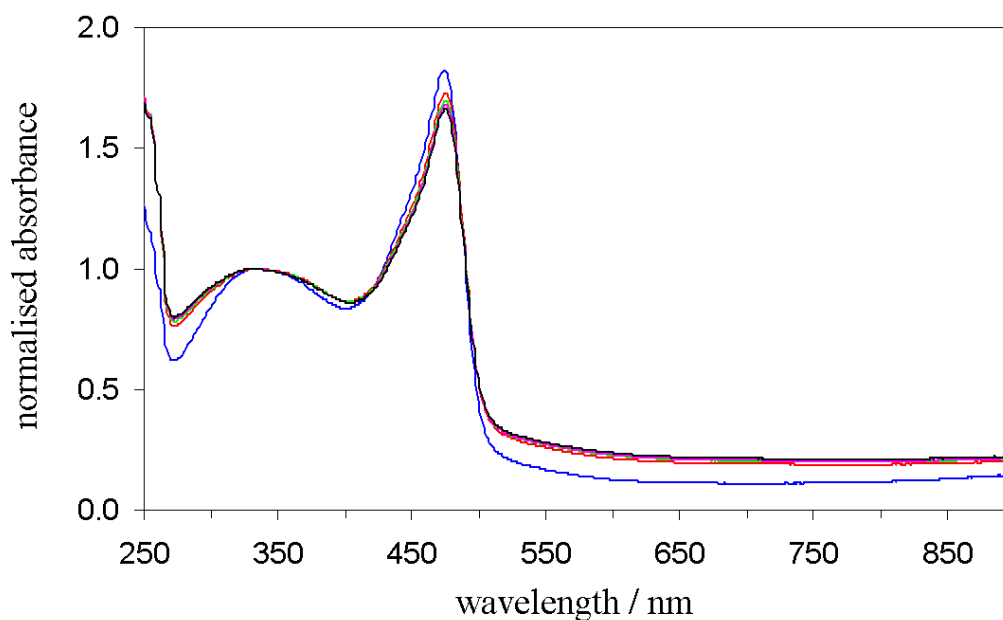


Figure 4.15 UV-vis spectra of PMAS (blue line) and PMAS-Arc MWNT dispersions sonicated 6 minutes (red line), 12 minutes (green line), 18 minutes (pink line) and 24 minutes (black line).

The stabilisation in solution of these nanotubes by the polymer does not appear to improve significantly after 6 minutes sonicating, shown by only the very small changes in the spectra that occur with sonicating up to 24 minutes.

To examine the stability of dispersions of different CNTs in PMAS, dispersions with SWNTs and CVD MWNTs were left for 6 weeks (hereafter referred to as 'aged'), prior to measuring the UV-vis spectrum to investigate the effects of aging. The spectra recorded for these composites, and an aged PMAS solution, are shown in Figure 4.16.

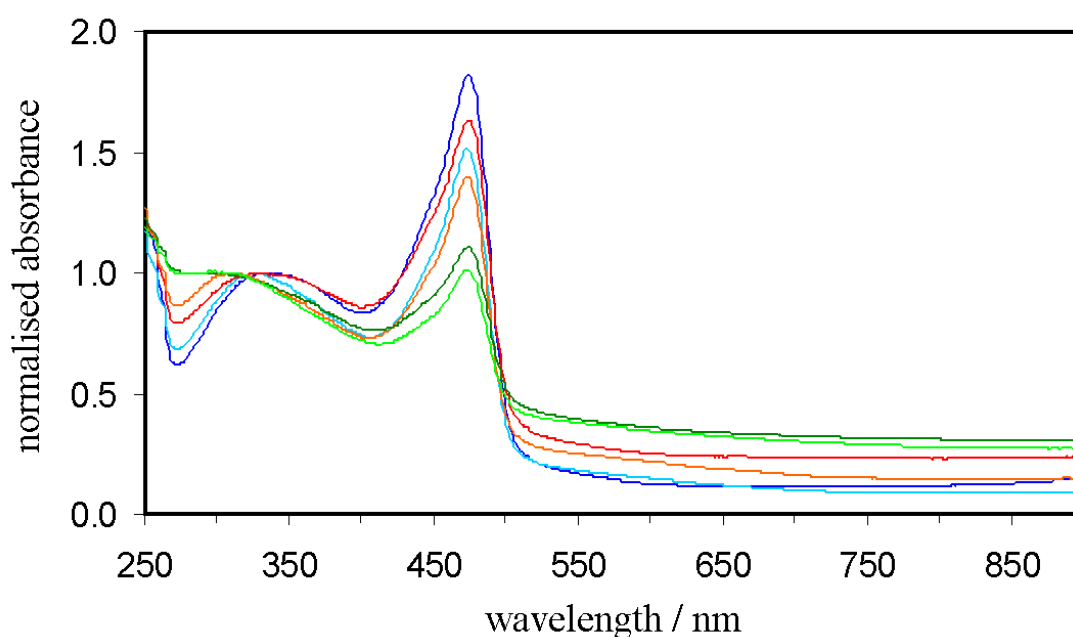


Figure 4.16 UV-vis spectra of PMAS fresh (blue line) and aged 6 weeks (light blue line, PMAS-SWNT fresh (red line) and aged 6 weeks (orange line) and PMAS-MWNT fresh (green line) and aged 6 weeks (lime green line). Dispersions sonicated for 24 minutes originally.

After 6 weeks, the spectrum for PMAS shows the following changes; the band centred at 280 - 410 nm has shifted to a lower wavelength and there is also quite a large decrease in the intensity of the peak at 474 nm. Both of the composite dispersions also show these aging effects, though they are less pronounced for the CVD MWNT composite, as significant changes due to interactions with the nanotubes were observed in the 'fresh' spectra, immediately after their preparation. The differences between the composites are visible for wavelengths > 500 nm onwards, and are related to the

presence of nanotubes in the dispersion. For the SWNT dispersion, the UV-vis intensity in this region has decreased upon aging. Visual inspection of the sample revealed a black sediment at the bottom of the sample. This suggests that nanotubes have settled out of the dispersion due to aggregation. In contrast, for the CVD MWNT dispersion the intensity in the region from 500 nm onwards has not changed as significantly, and no black sediment was observed in the sample. This provides further evidence that the interaction between PMAS and the CVD MWNTs is more favourable compared to that with SWNTs, as the stability of the dispersion can be considered as some indication of the interaction between the polymer and the nanotubes.

4.4 Characterisation of PMAS-PAni-MWNT composites

A number of different strategies were employed to synthesise a water soluble composite of PAni and CNTs, based on polymerisation of the sulfonated aniline monomer, 2-methoxyaniline-5-sulfonic acid (MAS) in the presence of CNTs. This follows the finding that dispersing CNTs in a polymer solution with sonicating can lead to a decrease in the polymer molecular weight, and so a more facile method of composite production is desired. The strategies that were employed, not discussed in detail here, included direct incorporation of CNTs (CVD MWNTs, HiPco SWNTs, Arc MWNTs), addition of chirality inducing agents (1-phenylethylamine, L-arginine), use of functionalised nanotubes (MWNT-NH₂) and addition of surfactant (cetyl trimethyl ammonium bromide) during the polymerisation reaction. None of these strategies, after studying UV-vis spectra or SEM images of the composites, appeared to have resulted in the successful synthesis of a composite. However, a recent paper published after these attempted composite syntheses discussed the synthesis of a water soluble composite of PMAS and PAni, where the PMAS acts as both a stabiliser and dopant for the PAni.⁶⁰ Having already produced a composite of PAni and CNTs through *in situ* polymerisation (see section 4.2), a small modification to the reported method for the synthesis of a PMAS-PAni composite was made to incorporate MWNTs. The synthesis procedure is described in Chapter 2, and took place, with the characterisation that follows here, at the IPRI, University of Wollongong, Australia.

4.4.1 PMAS-PAni-MWNT solution properties

The loading fractions of MWNTs in the final composites are estimated from the amounts of the starting materials, and also the expected conversion percentage of aniline to PAni, which from previous studies is believed to be about 70 %.⁶⁰ Based on this, composites with 3.4, 6.6, 12.4, 17.5 and 32.0 % w/w CVD MWNTs were successfully synthesised, and were also found to be stable in solution over a number of days. Composites with higher loading fractions of CNTs were synthesised, but these were unstable and nanotube material sedimented out from the dispersions. Figure 4.17 shows a photograph of the dispersions (at a concentration of 0.1 mg mL^{-1}) with MWNT loading fractions up to 32.0 % w/w.

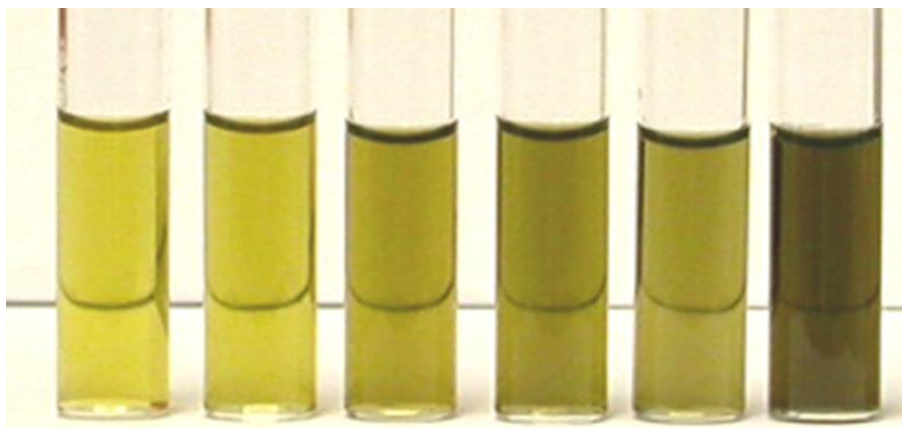


Figure 4.17 Photograph of PMAS-PAni-MWNT dispersions in water at a concentration of 0.1 mg mL^{-1} . Nanotube loading fraction increases from left to right, starting at 0.0, 3.4, 6.6, 12.4, 17.5 and 32.0 % w/w MWNT.

The dispersions appear to become darker with increasing MWNT loading fraction. These observations are examined in more detail in the UV-vis spectra of the composite dispersions, shown in Figure 4.18. The spectra have been normalised with respect to the intensity at 385 nm.

The spectra of the PMAS-PAni material is dominated by the PMAS, with a broad band between 300 - 375 nm and a peak at 474 nm, attributed to a $\pi - \pi^*$ transition and a low wavelength polaron band respectively.⁶⁰ None of the features associated with PAni are observed, though shoulders in the $\pi - \pi^*$ transition and low wavelength polaron bands are observed, perhaps suggesting the presence of another polymer besides PMAS.

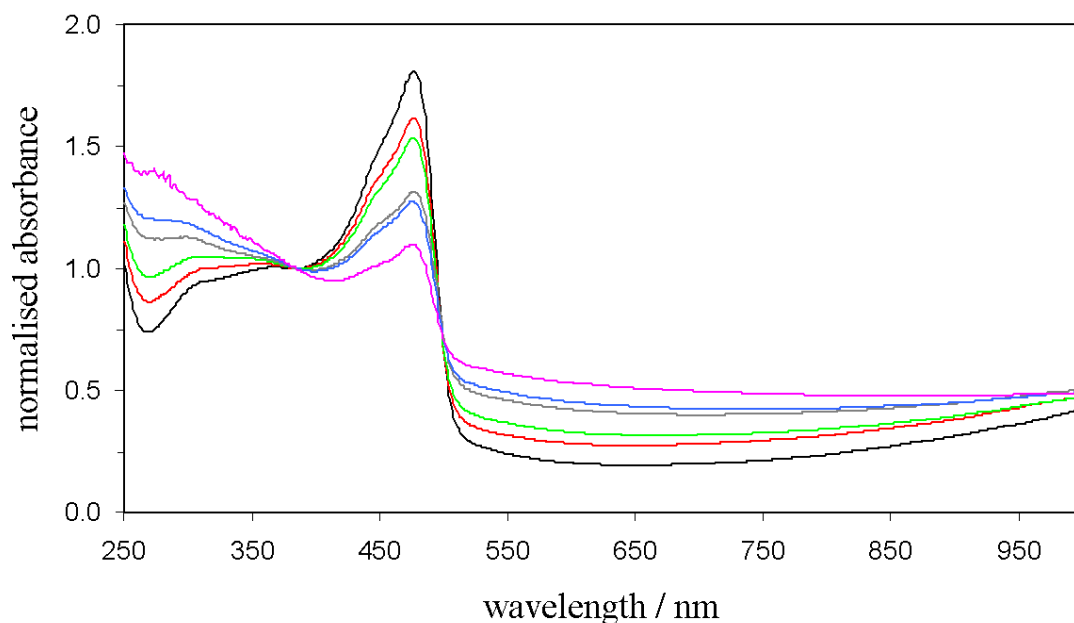


Figure 4.18 UV-vis spectra (normalised) of PMAS-PAni-MWNT composites in solution (0.1 mg mL^{-1}) with 0.0 % (black line), 3.4 % (red line), 6.6 % (green line), 12.4 % (grey line), 17.5 % (blue line) and 32.0 % (pink line) w/w MWNT.

With the addition of nanotubes to the composite, changes in the spectra are observed that become more pronounced with increasing nanotube concentration. The band at 300 - 375 nm shifts to lower wavelength, while the peak at 474 nm decreases in intensity. In addition, intensity of the spectra increases $> 500 \text{ nm}$. These changes are consistent with those previously observed for PMAS when it is employed as a dispersant for nanotubes.⁴⁵

A dispersion of the PMAS-PAni-MWNT composite with 17.5 % w/w MWNT was deposited onto a copper grid for TEM analysis, shown in Figure 4.19. In the TEM images, the CNTs are clearly visible. The polymer can be seen wetting the nanotubes, and it appears that good surface coverage of the nanotubes has been obtained. The high loading fractions of nanotubes in the composites and stability of these dispersions can be attributed to the excellent wetting of the nanotubes by the polymer, as we could not see any nanotubes with their surfaces exposed, which might lead to aggregation.

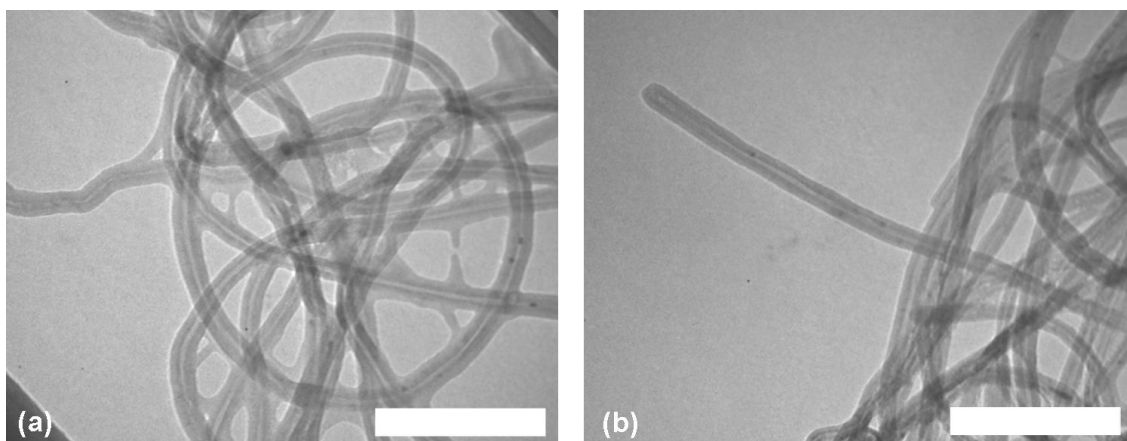


Figure 4.19 TEM images of the PMAS-PAni-MWNT composite with 17.5 % w/w MWNTs. Scale bars 200 nm. Images taken by Dr Carol Lynam, at the University of Sydney.

4.4.2 TGA of PMAS-PAni-MWNT

The thermal stability of the composites, and the CVD MWNTs, was examined through TGA, shown in Figure 4.20.

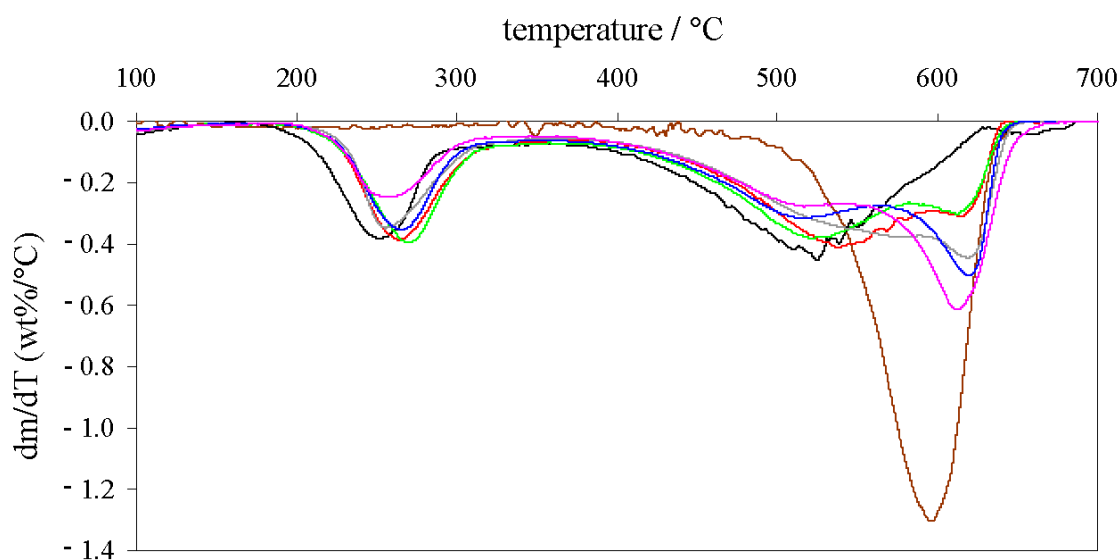


Figure 4.20 TGA derivative spectra of PMAS-PAni composites with 0.0 % (black line), 3.4 % (red line), 6.6 % (green line), 12.4 % (grey line), 17.5 % (blue line) and 32.0 % (pink line) w/w MWNT. Also shown is the spectra for the CVD MWNTs (brown line).

The TGA spectrum of the PMAS-PAni material shows a peak at approximately 250 °C, followed by a broad band culminating in a peak centred at around 520 °C. These features are attributed to the loss of the PMAS side groups (sulfonic acid and methoxy groups), followed by degradation of the polymer backbone. With the introduction of nanotubes into the composite, a number of changes in the spectra are observed, and as with the UV-vis spectra in Figure 4.18 these changes become more apparent with increasing nanotube loading fraction. The changes in the spectra are a shift of the polymer degradation peaks from 250 °C and 520 °C to higher temperature, and the presence of an additional peak at 630 °C. The nanotube material exhibits a single degradation peak at 600 °C, so this new peak at higher temperature in the composites might be attributed to a more thermally stable polymer-nanotube phase, similar to that observed for the PAni-MWNT composites with CVD MWNTs (see section 4.2.3).

4.4.3 *Electrical properties of PMAS-PAni-MWNT free-standing films*

Four point probe measurements were performed on free-standing films of uniform thickness cast from the composites. For thin films such as those produced in this study, the sheet resistance, R_s , can be calculated from

$$R_s = \frac{Vk}{I} \quad [4.1]$$

where V is the voltage measured, k is a constant dependant on the probe spacing, and I is the applied current. The sheet resistance is then given in the units of ohms per unit square ($\Omega \square^{-1}$), describing the resistance of a sample between two electrodes on opposite sides of a theoretical square, where the size of the square is unimportant.⁶¹ From the sheet resistance, the resistivity, ρ , can be calculated if the thickness of the film is known,

$$\rho = R_s t \quad [4.2]$$

where t is the thickness of the film. Note that the true resistance of the uniform thin film is directly proportional to the sheet resistance, with the proportionality constant being given by the ratio of the length of the sample to its cross-sectional width. As the units of

resistivity are commonly given in $\Omega \text{ cm}$, the thickness of the film is therefore usually measured in cm. From the resistivity, the conductivity, σ , of the film can easily be determined,

$$\sigma = \frac{1}{\rho} \quad [4.3]$$

giving the conductivity in units of S cm^{-1} . Sheet resistance does not apply to the sample when the thickness of the film exceeds 0.1 times the spacing between adjacent needles of the probe, in which case the bulk resistivity would be calculated.

The sheet resistances of these films are shown in Figure 4.21.

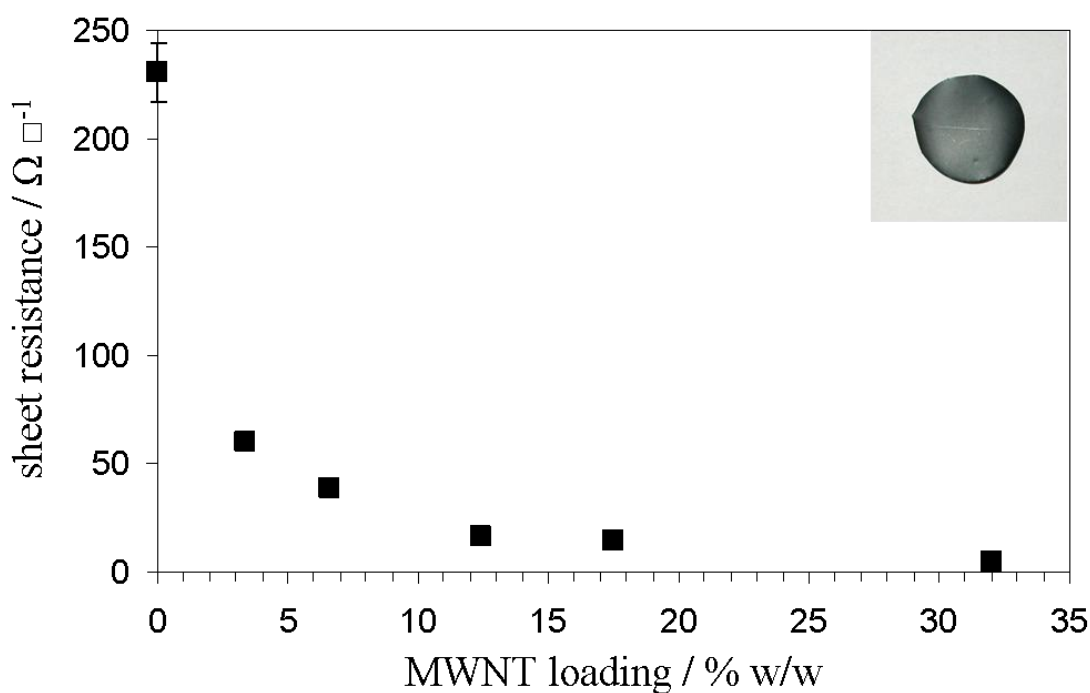


Figure 4.21 Sheet resistance as a function of MWNT loading fraction in the composite. Inset is an image showing one of the freestanding films.

Increasing the amount of MWNTs in the composite increases the number of conducting pathways in the network, with a percolating network forming at low (several % w/w) concentrations.⁶² The sheet resistance decreases by almost two orders of magnitude from $230 \Omega \square^{-1}$ for the PMAS-PA_ni material, to $5.0 \Omega \square^{-1}$ for the composite with 32.0 % w/w MWNT. It is interesting to note that there is a large fall in the sheet resistance by adding just 3.4 % MWNT to the composite ($R_s = 60.4 \Omega \square^{-1}$), but

increasing the nanotube loading fraction further, to as much as 32.0 % w/w MWNT, has a lesser effect on the sheet resistance. This demonstrates the percolation threshold being approached at a low loading fraction of CNTs, which is one of their main advantages over other conducting fillers.

4.4.4 Electrochromic behaviour of PMAS-PAni-MWNT composites

4.4.4.1 Cyclic voltammetry

In voltammetry, the current at a working electrode is monitored as a function of the applied potential. This is a useful and widely employed technique to determine the nature of electrochemical processes, such as the reduction and oxidation of conducting polymers. Linear voltammetry involves the sweeping of the potential between two values, but in cyclic voltammetry, the potential is then swept back again. This process can be carried out at different rates, depending on the rate at which the reactions take place, and can also be repeated many times. From cyclic voltammetry, we can determine the electrochemical processes that are occurring for a polymer system, whether the processes are reversible, and the rates at which they occur.⁶³

4.4.4.2 Electrochromic properties of PMAS-PAni-MWNT composites

Composite films were cast onto glassy electrodes for cyclic voltammetry, to investigate any electroactive behaviour that the composites might show. A typical cyclic voltammogram for the composite with 17.5 % w/w MWNT is shown in Figure 4.22.

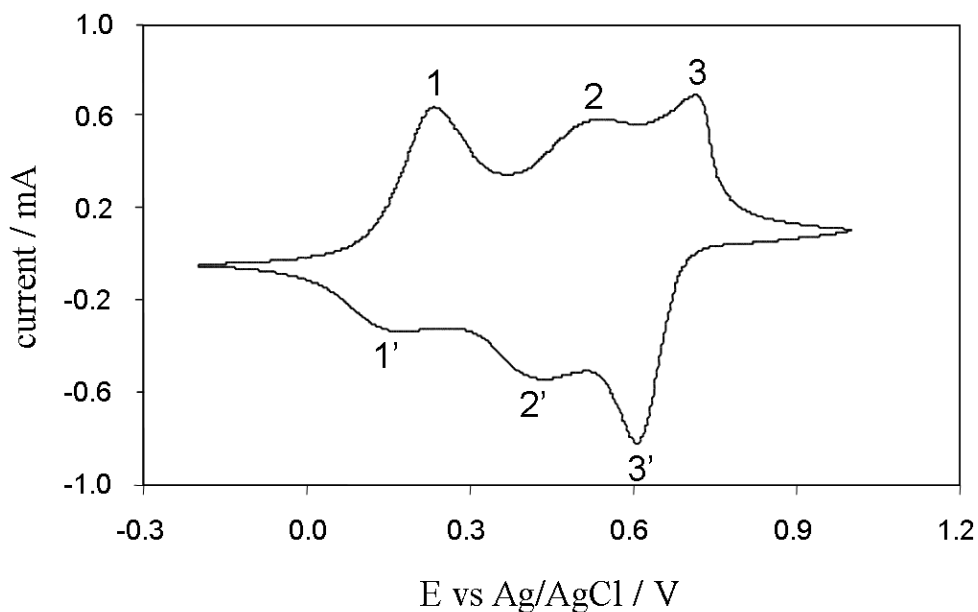


Figure 4.22 Cyclic voltammogram of a PMAS-PAni-MWNT composite film (17.5 % w/w MWNT) drop cast onto a glassy electrode (film density 0.535 mg cm^{-3}). Sweep carried out in 0.1 M HCl at a scan rate of 50 mV s^{-1} . Data acquired by Fatemeh Masdarolomoor, IPRI, University of Wollongong, Australia.

The cyclic voltammogram in Figure 4.22 shows that the PMAS-PAni-MWNT composite exhibits three redox couples, which have previously been assigned as follows. At negative potential, PMAS and PAni exist in their leucoemeraldine state (fully reduced), but as the potential becomes positive the polymers undergo oxidation, forming their half oxidised form (peak 1), and then the fully oxidised forms of pernigraniline for PMAS (peak 2) and PAni (peak 3). Decreasing the potential thus reduces the polymers following the same route - peak 3' is the PAni pernigraniline to emeraldine transition, peak 2' is the PMAS pernigraniline to emeraldine transition and peak 1' is the PMAS and PAni emeraldine to leucoemeraldine transition.⁶⁰ As the peaks in the cyclic voltammogram of the composite with nanotubes are in the same positions as the composite without nanotubes, it seems therefore that the presence of nanotubes does not appear to impede upon the electroactive properties of the composite. We did not observe any electrochromic behaviour (change in colour at different potentials) for the composite with 17.5 % w/w MWNTs, due to the presence of a high nanotube

loading fraction. However at lower loading fraction, 3.4 % w/w MWNTs, electrochromic behaviour was observed.

4.5 Conclusions

Dispersions of CNTs with conducting polymers have been prepared, using both mixing and *in situ* polymerisation routes. Optically active PANi-CNT composites have been prepared through polymerisation of aniline monomer in the presence of CNTs and a chiral dopant. This resulted in composite materials with enhanced thermal stability due to the presence of nanotubes. These materials retained their optical activity in solutions as well as supported films. Water soluble composites of CNTs with the conducting polymer PMAS were also produced through mixing, in a study looking at the effects that the mixing time and type of nanotube had on the quality of the dispersion. It was found that, of the nanotubes studied, CVD MWNTs with their low curvature/large diameter and comparatively poor graphitisation gave dispersions with the largest observed nanotube uptake in the shortest mixing time. This understanding is important, as the mixing strategies involved are detrimental to the chain length and thus conductivity of the polymer, so reducing the amount of mixing lessens this effect on the dispersant. Finally, composites comprising both PANi and PMAS were synthesised, employing a combination of mixing and *in situ* polymerisation methods to give water soluble composites with MWNT loading fractions as high as 32.0 % w/v. These composites showed enhanced thermal stability and conductivity due to the presence of the nanotubes, and retained the electroactive behaviour of the polymers.

4.6 References

- 1 MacDiarmid, A. G. and Heeger, A. J., *Synth. Met.*, 1979/80, **1**, 101.
- 2 in het Panhuis, M., *J. Mater. Chem.*, 2006, **16**, 3598.
- 3 Shirakawa, H., Louis, E. J., MacDiarmid, A. G., Chiang, C. K. and Heeger, A. J., *J. Chem. Soc. Chem. Comm.*, 1977, 579.
- 4 Diaz, A. F., Kanazawa, K. K. and Gardini, G. P., *J. Chem. Soc. Chem. Comm.*, 1979, 635.
- 5 Diaz, A. F. and Logan, J. A., *J. Electroanal. Chem.*, 1980, **111**, 111.
- 6 Yamamoto, T., Sanechika, K. and Yamamoto, A., *J. Polym. Sci., Polym. Lett. Ed.*, 1980, **18**, 9.
- 7 Barisci, J. N., Conn, C. and Wallace, G. G., *Trend Polym Sci.*, 1996, **4**, 307.
- 8 Baughman, R. H., *Synth. Met.*, 1996, **78**, 339.
- 9 Genies, E. M., Lapkowski, M., Santier, C. and Vieil, E., *Synth. Met.*, 1987, **18**, 631.
- 10 Chiang, C. K., Fincher, C. R., Park, Y. W., Heeger, A. J., Shirakawa, H., Louis, E. J., Gau, S. C. and MacDiarmid, A. G., *Phys. Rev. Lett.*, 1977, **39**, 1098.
- 11 Brédas, J. L. and Street, G. B., *Acc. Chem. Res.*, 1985, **18**, 309.
- 12 Skotheim, T. A., *Handbook of Conducting Polymers, 1 & 2*, Marcel Dekker, New York, 1986.
- 13 Macdiarmid, A. G. and Epstein, A. J., *Synth. Met.*, 1995, **69**, 85.
- 14 Nicholas-Debarnot, D. and Poncin-Epaillard, F., *Anal. Chim. Acta.*, 2003, **475**, 1.
- 15 Brett, C. M. A., Brett, A. M. C. F. O., Pereira, J. L. C. and Rebelo, C., *J. Appl. Electrochem.*, 1993, **23**, 332.
- 16 Genies, E. M. and Tsintavis, C., *J. Electroanal. Chem.*, 1986, **200**, 127.
- 17 Abrantes, L. M., Correia, J. P., Savic, M. and Jin, G., *Electrochim. Acta.*, 2001, **46**, 3181.
- 18 MacDiarmid, A. G., Chiang, J. C., Halpern, M., Huang, W. S., Mu, S. L., Somasiri, N. L. D., Wu, W. and Yaniger, S. I., *Mol. Cryst.*, 1985, **121**, 173.
- 19 Genies, E. M., Tsintavis, C. and Syed, A. A., *Mol. Cryst., Liq. Cryst.*, 1985, **121**, 181.
- 20 Kane-Maguire, L. A. P., MacDiarmid, A. G., Norris, I. D., Wallace, G. G. and Zheng, W., *Synth. Met.*, 1999, **106**, 171.

-
- 21 Pron, A., Genoud, F., Menardo, C. and Nechtschein, M., *Synth. Met.*, 1988, **24**, 193.
- 22 Mattoso, L. H. C., MacDiarmid, A. G. and Epstein, A. J., *Synth. Met.*, 1994, **68**, 1.
- 23 Venancio, E. C., Wang, P.-C. and MacDiarmid, A. G., *Synth. Met.*, 2006, **156**, 357.
- 24 Armes, S. P. and Miller, J. F., *Synth. Met.*, 1988, **22**, 385.
- 25 Huang, J. X. and Kaner, R. B., *J. Am. Chem. Soc.*, 2006, **128**, 968.
- 26 Majidi, M. R., Ashraf, S. A., Kane-Maguire, L. A. P., Norris, I. D. and Wallace, G. G., *Synth. Met.*, 1997, **84**, 115.
- 27 Syed, A. A., Kane-Maguire, L. A. P., Majidi, M. R., Pyne, S. G. and Wallace, G. G., *Polymer*, 1997, **38**, 2627.
- 28 Majidi, M. R., Kane-Maguire, L. A. P. and Wallace, G. G., *Polymer*, 1995, **36**, 3597.
- 29 Innis, P. C., Norris, I. D., Kane-Maguire, L. A. P. and Wallace, G. G., *Macromolecules*, 1998, **31**, 6521.
- 30 Majidi, M. R., Kane-Maguire, L. A. P. and Wallace, G. G., *Polymer*, 1994, **35**, 3113.
- 31 Maruyama, T., Adachi, N., Takatsuki, T., Torri, M., Sanui, K. and Ogata, N., *Macromolecules*, 1990, **23**, 2748.
- 32 McCarthy, P. A., Huang, J., Yang, S.-C. and Wang, H.-L., *Langmuir*, 2002, **18**, 259.
- 33 Yue, J. and Epstein, A. J., *J. Am. Chem. Soc.*, 1990, **112**, 2800.
- 34 Ito, S., Murata, K., Teshima, S., Aizawa, R., Asako, Y., Takahashi, K. and Hoffman, B. M., *Synth. Met.*, 1998, **96**, 161.
- 35 Shimizu, S., Saitoh, T., Uzawa, M., Yuasa, M., Yano, K., Maruyama, T. and Watanabe, K., *Synth. Met.*, 1997, **85**, 1337.
- 36 Masdarolomoor, F. M., Innis, P. C., Ashraf, S. and Wallace, G. G., *Synth. Met.*, 2005, **153**, 181.
- 37 Neoh, K. G., Kang, E. T. and Tan, K. L., *Polym. Deg. & Stab.*, 1994, **43**, 141.
- 38 Sandler, J. K. W., Kirk, J. E., Kinloch, I. A., Schaffer, M. S. P. and Windle, A. H., *Polymer*, 2003, **44**, 5893.

-
- 39 Qu, L., Veca, L. M., Lin, Y., Kitaygorodskiy, A., Chen, B., McCall, A. M.,
Connell, J. W. and Sun, Y. P., *Macromolecules*, 2005, **38**, 1850.
- 40 McCarthy, B., Coleman, J. N., Czerw, R., Dalton, A. B., in het Panhuis, M.,
Maiti, A., Drury, A., Bernier, P., Nagy, J. B., Byrne, H. J., Carroll, D. L. and
Blau, W. J., *J. Phys. Chem. B*, 2002, **106**, 2210.
- 41 Cochet, M., Maser, W. K., Benito, A. M., Callejas, M. A., Martinez, M. T.,
Benoit, J.-M., Schreiber, J. and Chauvet, O., *Chem. Comm.*, 2001, **16**, 1450.
- 42 Ramamurthy, P. C., Malshe, A. M., Harrell, W. R., Gregory, R. V., McGuire, K.
and Rao, A. M., *Solid-State Electron.*, 2004, **48**, 2019.
- 43 Sainz, R., Benito, A. M., Martinez, M. T., Galindo, J. F., Sotres, J., Baró, A. M.,
Corraze, B., Chauvet, O. and Maser, W. K., *Adv. Mater.*, 2005, **17**, 278.
- 44 in het Panhuis, M., Maiti, M., Dalton, A. B., van den Noort, A, Coleman, J. N.,
McCarthy, B. and Blau, W. J., *J. Phys. Chem. B*, 2003, **107**, 478.
- 45 in het Panhuis, M., Kane-Maguire, L. A. P., Moulton, S. E., Innis, P. C. and
Wallace, G. G., *J. Nanosci. & Nanotech.*, 2004, **4**, 976.
- 46 Sainz, R., Benito, A. M., Martinez, M. T., Galindo, J. F., Sotres, J., Baró, A. M.,
Corraze, B., Chauvet, O., Dalton, A. B., Baughman, R. H. and Maser, W. K.,
Nanotechnology, 2005, **16**, S150.
- 47 Harris, P. J., *Int. Mater. Rev.*, 2004, **49**, 31, and references therein.
- 48 Xia, Y., Wiesinger, J. M., MacDiarmid, A. G. and Epstein, A. J., *Chem. Mater.*,
1995, **7**, 443.
- 49 MacDiarmid, A. G. and Epstein, A. J., *Synth. Met.*, 1994, **65**, 103.
- 50 Xia, Y., Wiesinger, J. M., MacDiarmid, A. G. and Epstein, A. J., *Chem. Mater.*,
1995, **7**, 443.
- 51 Tigelaar, D. M., Lee, W., Bates, K. A., Saprigin, A., Prigodin, V. N., Cao, X.,
Nafie, A., Platz, M. S. and Epstein, A. J., *Chem. Mater.*, 2002, **14**, 1430.
- 52 Kulkarni, M. V. and Viswanath, A. K., *J. Macromol. Sci., Pure Appl. Chem.*,
2004, **41**, 1173.
- 53 Sainz, R., Benito, A. M., Martinez, M. T., Galindo, J. F., Sotres, J., Baro, A. M.,
Corraze, B., Chauvert, O. and Maser, W. K., *Adv. Mater.*, 2005, **17**, 278.
- 54 Ege, S., *Organic Chemistry: Structure and Reactivity*, 3rd edition, **1994**, (D.C.
Heath and Company: Lexington).

-
- 55 Sainz, R., Small, W. R., Young, N. A., Vallés, C., Benito, A. M., Maser, W. K. and in het Panhuis, M., *Macromolecules*, 2006, **39**, 7324.
- 56 Tung, S., Rokadia, H. and Li, W. J., *Sensor. Actuat. A-Phys.*, 2007, **133**, 431.
- 57 Chiang, I. W., Brinson, B. E., Huang, A. Y., Willis, P. A., Bronikowski, M. J., Margrave, J. L., Smalley, R. E. and Hague, R. H., *J. Phys. Chem. B.*, 2001, **105**, 8297.
- 58 Strounina, E. V., Kane-Maguire, L. A. P. and Wallace, G. G., *Synth. Met.*, 1999, **106**, 129.
- 59 in het Panhuis, M., Sainz, R., Innis, P. C., Kane-Maguire, L. A. P., Benito, A. M., Martínez, M. T., Moulton, S. E., Wallace, G. G. and Maser, W. K., *J. Phys. Chem. B*, 2005, **109**, 22725.
- 60 Masdarolomoor, F., Innis, P. C., Ashraf, S., Kaner, R. B. and Wallace, G. G., *Macromol. Rapid Commun.*, 2006, **27**, 1995.
- 61 <http://www.jandel.com/faq.htm>, checked 25th April 2009.
- 62 Du, F., Fischer, J. E. and Winey, K. I., *Phys. Rev. B*, 2005, **72**, 121404.
- 63 Atkins, A. and de Paula, J., *Atkins' Physical Chemistry 7th Edition*, Oxford University Press, Oxford, 2002.

CHAPTER 5

INKJET PRINTING FUNCTIONAL CARBON NANOTUBE COMPOSITES

5.1 Introduction

Inkjet printing is a technique that is becoming increasingly popular for the deposition of both aqueous and non-aqueous solutions and dispersions.¹ This is mainly due to the ability of this technique to accurately and reproducibly deposit not only very small volumes (10^{-12} L) onto a substrate, but also to deposit such solutions and dispersions over larger areas as well. Amongst the potential applications that this technique is expected to contribute to are radio-frequency identification tags, organic light emitting diodes (OLEDs), thin film transistors, chemical and biological sensors and miniature printed circuits. In this chapter we study films of CNT networks that have been fabricated by inkjet printing CNT dispersions, and assess their potential use as sensing materials.

5.1.1 Inkjet printing and fluid properties

Inkjet printers can be split into two main categories, according to the technology that is used to produce and eject a drop from the printer. These are *thermal* inkjet printers and *piezoelectric* inkjet printers. Thermal inkjet printers have small heated chambers through which a current can be passed when a drop of ink is required. This current causes a steam explosion in the chamber, forcing a drop of ink out of the chamber through a nozzle and onto the substrate. The ejected ink is then replaced in the chamber through a combination of surface tension effects and contraction of the vapour bubble.² In piezoelectric inkjet printers, a piezoelectric material takes the place of the heating plate in the chamber. When a voltage is applied, this piezoelectric crystal changes shape or size, creating a 'pressure pulse' which forces a drop of ink to be expelled from the printer, with more ink from the reservoir taking its place. The piezoelectric and thermal methods of drop formation are therefore similar in principle,

relying on a pressure pulse to eject a drop of ink from a nozzle, but they employ different ways to exert this pressure on the ink. Because the thermal inkjet printer uses a temperature increase to produce steam, this method of printing appears to be limited to aqueous systems. The piezoelectric inkjet printers on the other hand are more versatile, allowing the printing of non-aqueous systems, and thus much of the literature concerning recent developments in this field focuses on piezoelectric printers for this reason.

Typical nozzle diameters in inkjet printers range from 20 - 30 μm , and they are capable of ejecting ink drops with volumes of approximately 1 - 20 pL at velocities of several meters per second. For continuous inkjet printing, the chamber must also be able to be refilled in around 100 μs , and while the ink should not drip from underneath the nozzle, it must not ‘clog’ the nozzle either.² To meet these demands, it has been necessary to formulate inks that have well-defined physical properties, and this has been achieved through adding humectants, solvents, surfactants, thickeners and defoamers, amongst others, to the inks. Amongst the most important properties of an ink are the surface tension and viscosity, which are two vitally important parameters determining how the ink flows into the chamber, how the drop breaks up as it leaves the nozzle, and how the ink spreads over the substrate. An estimate of how well a material can be printed is given by Fromm, taking into account the surface tension, γ , viscosity, η , and density, ρ , of the fluid, as well as the nozzle aperture, d , to give the dimensionless Z number.³

$$Z = \frac{\rho \gamma d^3}{\eta^2} \quad [5.1]$$

Fromm predicted that only materials with a Z number of greater than 2 could be printed, and that the drop diameter would increase with Z . However a number of further studies⁴ have shown that fluids with Z numbers of 1 - 10, and even up to 91 can still be printed.⁵ Other factors cited as being influential as to whether a material can be successfully printed are whether or not the small ‘satellite’ drops that form will join up with the main drop, and the vapour pressure of the solvent. Printing is not therefore a straightforward task for processing materials, with many factors to be considered.

5.1.2 *Inkjet printing polymers and other materials*

Inkjet printing has been used both as an additive and as a subtractive technique for device fabrication. In additive printing, the material that is of interest is printed directly onto the substrate in the desired pattern. Subtractive printing however involves printing a mask or etchant onto the substrate, in areas where the material is not wanted, before applying the material of interest to the whole of the substrate. The mask or etchant is then removed, leaving a pattern of the material that is defined by the printed lines that have been removed.⁶ Although the additive printing method would appear to be quicker and with fewer steps involved, the subtractive method is useful for patterning materials that cannot themselves be printed, and can also be used to create channels into which the material can flow by tuning the surface properties of the etchant, substrate and ink.

Amongst the materials that have already been inkjet printed, polymers and in particular conducting polymers, are perhaps of most interest as they are expected to be useful components in light-weight, low cost, easy to process, flexible displays. An important breakthrough in this area was made by Sirringhaus and co-workers, who used a combination of photolithography, spin coating and inkjet printing to create all-polymer transistor circuits.⁷ They printed poly(3,4-ethylenedioxythiophene) doped with polystyrene sulfonic acid as the source, drain and gate electrodes, with poly-vinylphenol as the semi-conducting layer achieved through spin coating. The issue of large line width associated with inkjet printing was solved through creating narrow hydrophilic channels by photolithography, into which the printed polymer could flow, giving channel widths of 5 μm . In more recent work, a lithography-free approach has been developed relying solely on inkjet printing to pattern the source and drain electrodes, improving the channel widths to dimensions less than 100 nm.⁸ The use of spin coating has also now been removed from the fabrication step by another group, to give all-inkjet printed polymer field effect transistors.⁹ However channel widths of not less than 100 μm could be obtained, and it remains a challenge to fabricate such devices entirely through inkjet printing that have channel widths, and therefore performances, comparable with those produced via the more expensive lithographic route. Other studies have utilised inkjet printing polymers and organic molecules as a tool in the fabrication of OLEDs and photovoltaic devices,^{10 - 12} electrochromic displays^{13, 14} and sensors.^{15, 16}

In some cases, the printing of dispersions that contain solid particles is either beneficial or a necessity, and there are several studies reporting the inkjet printing of such dispersions. Tekin and co-workers describe the printing of cadmium telluride quantum dots dispersed in a poly(vinyl alcohol) (PVA) matrix, studying the luminescence as a function of the quantum dot size and loading fraction within the PVA.¹⁷ For printed features that offer the best possible conductivity, metal films would be the logical option, and several groups have made progress in this area. Hong and co-workers for example have printed copper hexanoate onto glass substrates, which when cured with UV-light gives printed metal tracks with resistivities of the order $8 \mu\Omega \text{ cm}$.¹⁸ Elsewhere, gold nanoparticles encapsulated with hexane thiol in different solvents have been printed onto polyester substrates, followed by sintering of the metal at $190 \text{ }^\circ\text{C}$ to form continuous tracks. The conductivity of the printed tracks was found to depend on the choice of solvent, with films from α -terpineol having conductivities of approximately 17 MS m^{-1} , while films from toluene had a conductivity of 34 MS m^{-1} .¹⁹ Of most interest in this area however has been the inkjet printing of silver tracks onto substrates, and conductivities close to that of bulk silver have been achieved in some instances. Two approaches have been taken, printing either solutions of silver or suspensions of silver particles, with both methods requiring sintering through heat or microwave radiation²⁰ to form continuous tracks. Smith and co-workers have printed an organometallic silver solution onto glass, polyimide and epoxy substrates, giving films with resistivities of approximately $2 - 3 \mu\Omega \text{ cm}$.²¹ Films from silver nanoparticles have given resistivities of $6 \mu\Omega \text{ cm}$ (particle diameter 7 nm),²² and $16 \mu\Omega \text{ cm}$ (particle diameter 50 nm).²³

One other type of material that has been inkjet printed is biological materials, such as cells, deoxyribonucleic acid (DNA) and proteins. One study by Sumerel and co-workers describes the printing of the protein streptavidin, DNA from salmon sperm and sinapinic acid onto a range of substrates.²⁴ Bietsch and co-workers also report inkjet printing thiolated DNA onto gold substrates, achieving layers free of defects and with good surface homogeneity.²⁵ The accurate deposition of cells is a particularly attractive possibility, with recent studies reporting the printing of human fibroblast²⁶ and neural cells,²⁷ with good cell vitality retained.

5.1.3 Inkjet printing carbon nanotubes

The inkjet printing of CNTs is an area that has attracted little attention so far, probably due to the difficulties encountered experimentally in preparation of CNT containing inks. One of the first reports in this area was by Kordás and co-workers, who printed covalently functionalised MWNTs onto transparent substrates.²⁸ The concentration of nanotubes in their ‘inks’ was approximately 0.25 mg mL^{-1} , but they required a build up of 30 printed layers to achieve a sheet resistance of less than $1 \text{ M}\Omega \square^{-1}$, and 90 printed layers for a sheet resistance of $40 \text{ k}\Omega \square^{-1}$. This high sheet resistance could be attributed to the low concentration of nanotubes in the ink, or the fact that the nanotubes have been functionalised covalently to allow their dispersion in water. Another study by Sumerel and co-workers also reports the inkjet printing of MWNTs dispersed by salmon sperm DNA, though they did not study the printed films in any great detail.²⁴ It remains a challenge however to print single walled carbon nanotubes (SWNTs), and due to their excellent electrical properties it should be possible to reduce the sheet resistance of such printed films by several orders of magnitude, compared to the sheet resistance of the dispersant, while retaining good optical transparency.

5.1.4 Gellan gum - a naturally occurring polysaccharide

Polysaccharides are polymers made up of many monosaccharide (sugar) building blocks, such as glucose or fructose. Polysaccharides with building blocks all of the same type are known as homopolysaccharides, while those with a mixture are known as heteropolysaccharides. Gellan gum is one such naturally occurring polysaccharide, secreted by the microorganism *Pseudomonas elodea*, and based on the repeat unit shown in Figure 5.1.

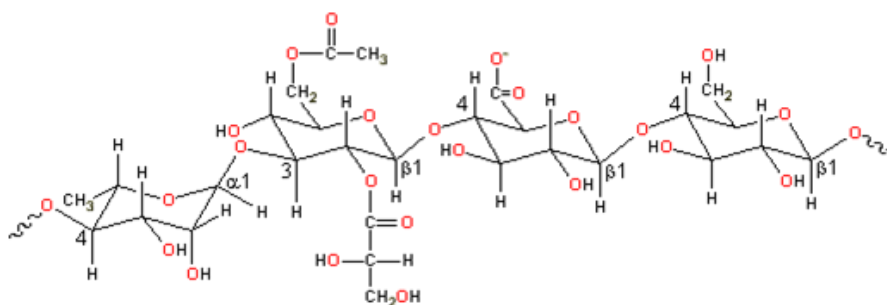


Figure 5.1 Four ring repeating unit of gellan gum, based on alternating glucose, rhamnose and glucuronic acid sub-units. Image reproduced from reference 29.

The repeat unit of gellan gum is based on four monosaccharides: one rhamnose, one glucuronic acid and two glucose residues.³⁰ When a solution of gellan in water cools from high temperature, the polysaccharide chains undergo a transition from random coils to double helices. This is then followed by the aggregation of these double helices into three-dimensional networks, through complexation with cations and hydrogen bonding with water.^{31,32}

This chapter will discuss the inkjet printing of a number of different carbon nanotube composites, previously characterised in Chapter 4. We also introduce the characterisation and inkjet printing of CNTs dispersed with gellan gum (GG). This will give an insight as to which dispersants and which printing methods are best suited to inkjet printing carbon nanotubes. The properties of the composite films will be characterised, with particular attention paid to any functional behaviour that the films show, such as sensitivity to humidity and concentrations of volatile substances, or electroactive properties.

5.2 Gellan gum-CNT composites

5.2.1 Characterisation of gellan gum-CNT dispersions

5.2.1.1 Comparison of gellan gum-SWNT dispersions with SDS-SWNT dispersions

Aqueous composites of CNTs dispersed by gellan gum were prepared as described in Chapter 2. The dispersing ability of gellan gum was compared to that of SDS, by dispersing the same amount of CNTs with two concentrations of each dispersant. The amount of CNTs dispersed in solution was determined qualitatively from UV-vis spectroscopy, as shown in Figure 5.2.

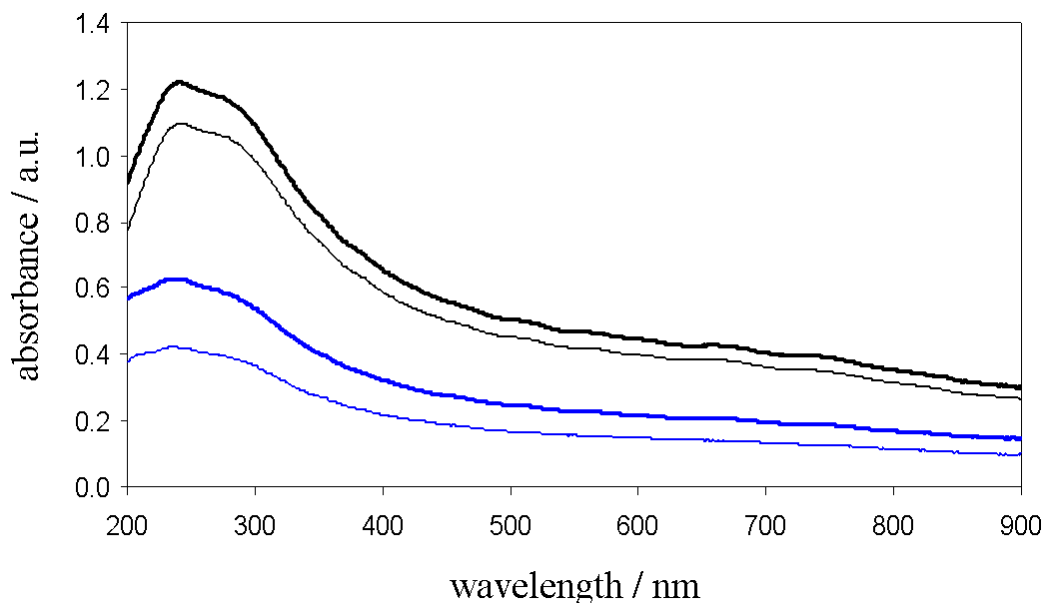


Figure 5.2 UV-vis spectra of aqueous SWNT dispersions dispersed with gellan gum (black lines) and SDS (blue lines). Dispersants at concentrations of 0.010 (heavy lines) and 0.005 % w/v (thin lines).

The amount of nanotubes dispersed is indicated by the intensity of the absorbance across the spectrum - a larger intensity suggests a greater amount of CNTs in the dispersion. The van Hove singularities are also evident in the spectra, confirming in each sample that it is SWNTs that have been dispersed. For each of the dispersants, more nanotubes have been dispersed at the higher concentration of dispersant (0.010 % w/v) than at the lower concentration (0.005 % w/v). This is to be expected, as the nanotubes are known to have very large surface areas, and thus lower concentrations of dispersant may not be able to adsorb to a sufficiently large part of the nanotube surface to prevent aggregation of the nanotubes. When comparing the two dispersants at equal concentration however, it is clear from Figure 5.2 that gellan gum has stabilised a greater amount of SWNTs in solution than SDS. In fact, the spectra show that even at the lower concentration of 0.005 % w/v, gellan gum dispersed a greater amount of CNTs than SDS at the higher concentration of 0.010 % w/v. One possible explanation for this observation might be attributed to the mechanisms by which the nanotubes are stabilised against aggregation by the dispersants. It is known that SDS forms monolayers on the surfaces of the nanotubes, probably with the molecules adopting a ‘heads up’ orientation and with the molecules packed quite closely together. This dense

packing of the surfactant on the surfaces of the nanotubes most likely means that a high concentration of the dispersant would be required to ensure sufficient coverage over the surface of the nanotubes and prevent their aggregation. Gellan gum however is known to disperse and suspend particles in solution without significantly increasing the viscosity of the surrounding medium, as it can form an extended network through the solution. Such a network formed at low concentrations may be sufficient to prevent the nanotubes aggregating together, without completely covering the surfaces of the nanotubes.

5.2.1.2 Effect of pH on gellan gum-SWNT dispersions

As gellan gum is anionic in nature, a factor which partly accounts for its ability to disperse CNTs, manipulating the amount of charge in the system could play a part in further stabilising or destabilising the dispersion.^{33,34} Aqueous dispersions of SWNTs with 0.01 % w/v gellan gum were prepared at varying pH, through the addition of HCl or NaOH prior to dispersing the nanotubes. The effects of this pH manipulation on the dispersions are shown in Figure 5.3.

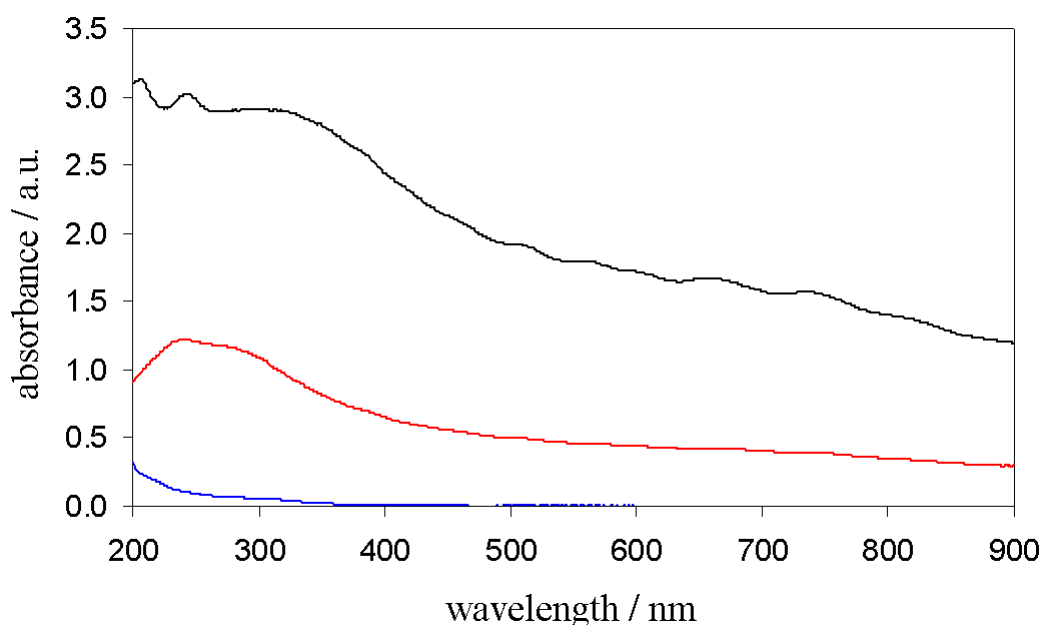


Figure 5.3 UV-vis spectra of aqueous gellan gum-SWNT dispersions (0.01 % w/v gellan gum) at pH 3.2 (blue line), 7.3 (red line) and 10.3 (black line).

The addition of HCl to the gellan gum solution, lowering the pH to 3.2, resulted in dispersions with seemingly very low amounts of nanotubes stabilised within them. This is indicated by the absorbance of this dispersion being close to zero in the region where the van Hove singularities are normally observed. The addition of NaOH to the gellan gum solution however, raising the pH to 10.3, resulted in dispersions that appeared to have significantly more nanotubes dispersed within them compared to those dispersions where no alteration to the pH had been made.

These differences in the dispersions of the nanotubes can be explained by considering the effect that the change in pH is having on the anionic gellan gum. Two mechanisms of destabilisation are perhaps possible when the pH is lowered. The first mechanism is shielding of the anionic carboxylic acid groups by H^+ resulting in decreased electrostatic repulsion between the gellan chains, which has also been observed in the presence of monovalent metal cations.³⁵ The second mechanism proposed is one of the pH controlling the amount of carboxylic acid groups that are dissociated, and therefore changing the degree of anionic nature of the polysaccharide. In a study by Horinaka and co-workers, it was concluded that the second mechanism, where pH controls the degree of dissociation within the gellan gum, was responsible for the aggregation behaviour.³⁶ Such aggregation of gellan gum in these low pH systems with CNTs might therefore result in a loss of the structural network separating the nanotubes, leading to the observed aggregation and failure to disperse the nanotubes.

The observed improvement in the dispersing ability of gellan gum for CNTs when the pH is raised with NaOH was not expected, however. This stabilisation might be explained though by similar mechanisms but with the opposite effect to those proposed for the destabilising effect at lower pH. Where it was proposed that H^+ may shield the electrostatic repulsive forces between carboxyl groups, it is possible that the hydroxyl anions of NaOH may actually increase the amount of electrostatic repulsion. Or in the other mechanism, where the increased concentration of H^+ prevents the dissociation of carboxylic acid groups, the hydroxyl anions would lead to dissociation of more of the carboxylic acid groups. Either of these mechanisms could lead to gellan networks with more electrostatic repulsion, perhaps enabling the nanotubes to be better separated and therefore dispersed throughout the dispersion, as has been observed.

5.2.1.3 Effect of NaCl on gellan gum-SWNT dispersions

As the amount of nanotubes that can be dispersed in gellan gum appears to be somewhat dependant on the pH of the surrounding medium, it may also be possible to manipulate the quality of these dispersions with salt. Gellan gum-SWNT dispersions at pH 10.3 were prepared with added NaCl at concentrations from 0.0001 to 0.1 M, with the spectra shown in Figure 5.4.

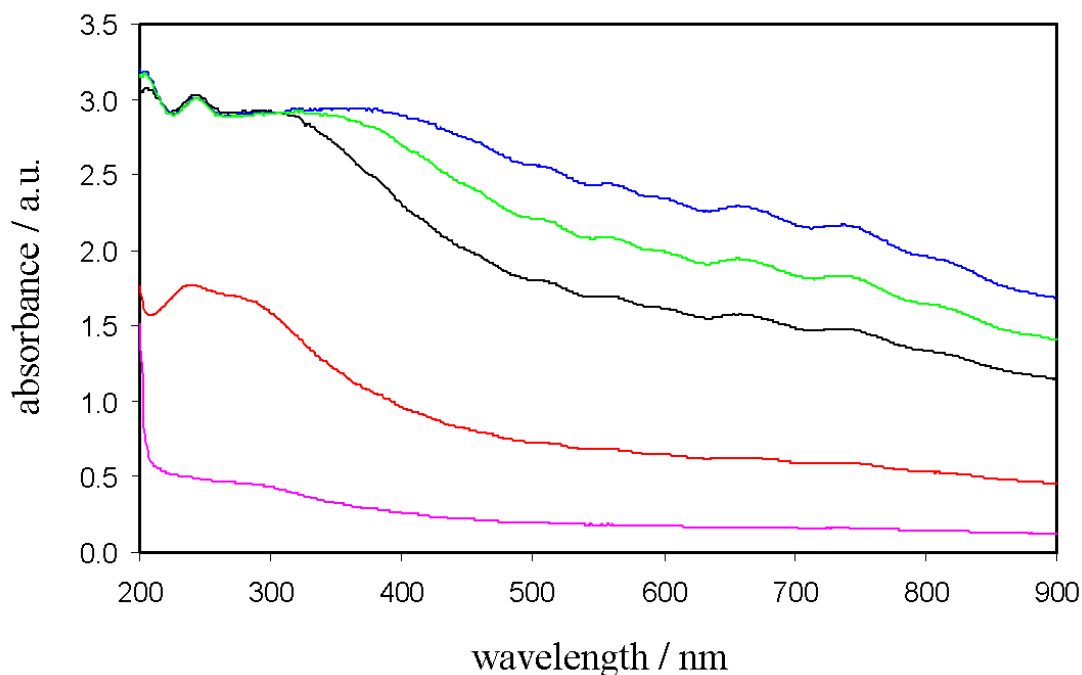


Figure 5.4 UV-vis spectra of aqueous gellan gum-SWNT dispersions at pH 10.3, without salt (black line) and with NaCl at a concentration of 0.0001 M (blue line), 0.001 M (green line), 0.01 M (red line) and 0.1 M (pink line).

At high concentrations of NaCl (0.1 and 0.01 M), the dispersions do not have as high concentrations of CNTs stabilised within them compared to the dispersion with no added salt. This is attributed to the high salt concentrations shielding the electrostatic repulsion between gellan chains, allowing aggregation and thus there is no extended network formation, leading to sedimentation of the nanotubes. Surprisingly, at low concentrations of NaCl (0.001 and 0.0001 M) the concentration of nanotubes in the dispersion increases when compared to the dispersion with no added salt. This suggests that low levels of salt may enhance the stability of the gellan gum-SWNT dispersions,

perhaps by shielding the charges on the chains enough to encourage the chains to interact with each other and form a stronger network, but without causing them to fully aggregate together.

This study has revealed that gellan gum is a significantly more efficient dispersant for CNTs than the surfactant SDS, most likely due to the way in which gellan disperses CNTs without needing to form a dense monolayer on their surface. By exploiting the anionic nature of gellan gum, it has also been shown that by tuning the pH and salt concentrations, dispersions with a higher nanotube content can be obtained.

5.2.2 Inkjet printing gellan gum-CNT composites

5.2.2.1 Optical transmittance

Dispersions of SWNTs and MWNTs in gellan gum for printing were prepared, using ultrasound, at concentrations of 0.10 % w/v gellan gum and 0.10 % w/v CNTs. A gellan gum dispersion for printing was prepared at a concentration of 0.10 % w/v. Prior to loading the dispersion into the emptied ink cartridges, the dispersions were filtered through glass wool under vacuum, and then through an in-line syringe filter with a 5 μm pore size, to remove aggregates. Figure 5.5 shows the transmittance spectra of a single layer of the films, printed onto transparent polyethylene terephthalate (PET) sheets.

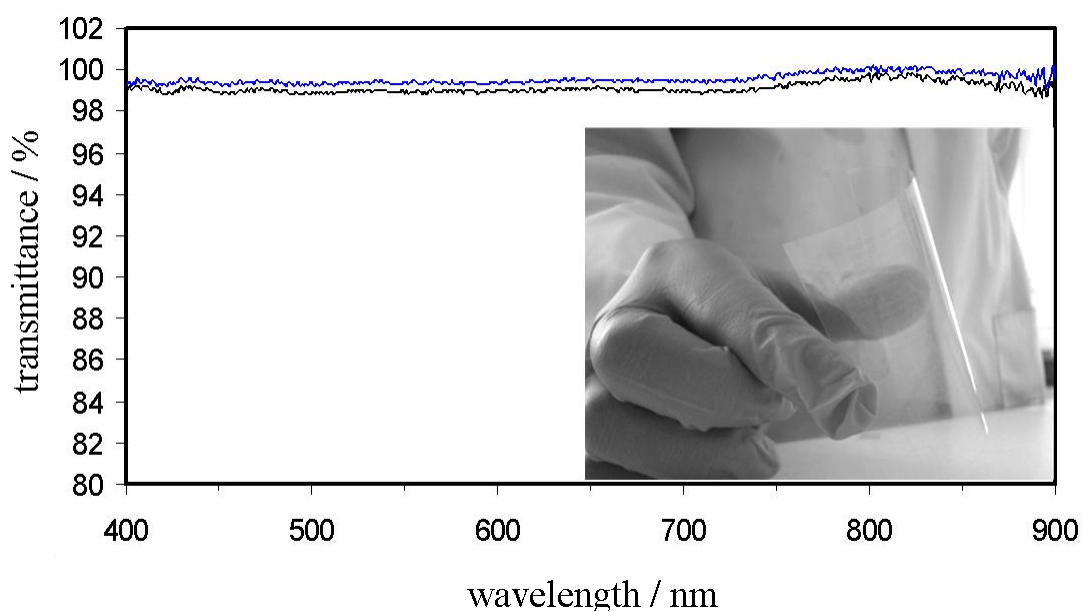


Figure 5.5 UV-vis transmittance spectra of gellan gum (blue line) and gellan gum-SWNT (black line) films printed onto transparent sheets. Inset is a photograph of one such gellan gum-SWNT film.

The transmittance of the films is approximately 99 % even with the incorporated carbon nanotubes, indicating the promise of these materials for use in transparent, conducting materials. The photograph inset into Figure 5.5 also demonstrates the transparency of the composite film, as well as the flexibility of these printed films.

5.2.2.2 Electrical and sensing properties

When the electrical properties of the films were characterised under ambient conditions (room temperature of $\sim 20\text{ }^{\circ}\text{C}$ and humidity $\sim 25 - 35\%$), the resistances of the films were in the region of $350\text{ M}\Omega$ and $12\text{ M}\Omega$ for gellan gum and gellan gum-SWNT films, respectively.

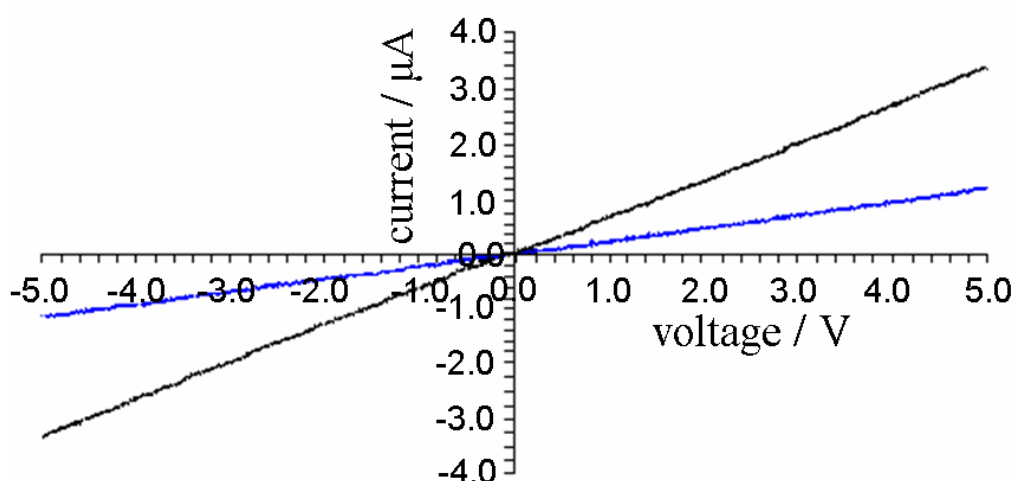


Figure 5.6 Typical current-voltage (I - V) characteristics of a gellan gum (blue line) and a gellan gum-SWNT film (black line) printed onto PET sheets. Measurements made in a sealed chamber saturated with water vapour.

Typically the introduction to an insulating matrix of CNTs at concentrations at and above the percolation threshold can result in a lowering of the resistance of the material by up to nine orders of magnitude.³⁷ Clearly this is not observed here, with the resistance only being lowered by one order of magnitude. This may suggest that the concentration of CNTs in the filtered dispersion is not sufficiently high for a percolating network to be formed in the printed film. However, other studies of the printed films suggest that perhaps there is another effect influencing the films. During the initial

stages of the sensing experiments before the films are exposed to any analytes, a nitrogen carrier gas is flowed over the film, with the result usually being that no change in the resistance of the film is observed, hence justifying the use of nitrogen as an inert carrier gas in these experiments. For the gellan gum and gellan gum-SWNT films however, exposure to nitrogen gas resulted in the current through the film falling to below the detection limit of our experiment, indicating an increase in the resistance. On removal of the carrier gas however, a measurable current was once more observed, indicating that the resistance of the film had returned. When the films were exposed to water vapour in the carrier gas, the current rose significantly, suggesting that the increase in resistance on exposure to a flow of nitrogen gas may be attributable to a drying effect on the atmosphere surrounding the films. Figure 5.7 shows the responses of several films to water vapour at varying concentrations, using the dynamic sensing conditions described in Chapter 2.

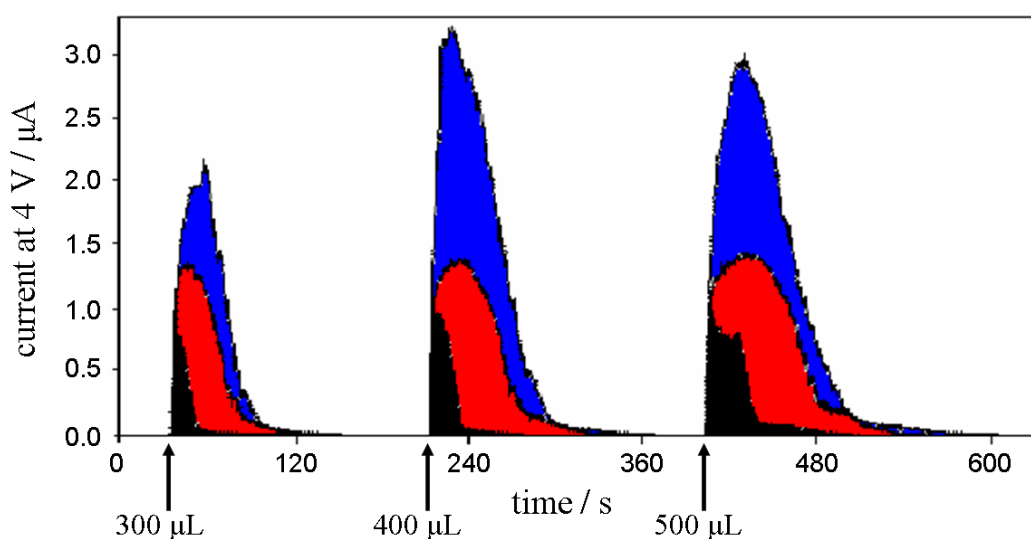


Figure 5.7 Response of gellan gum (black regions), gellan gum-MWNT (red regions) and gellan gum-SWNT (blue regions) films to water vapour under a nitrogen gas flow at 7 mL s^{-1} . Volumes of water injected into the system and their time of introduction are indicated in the figure.

The response of all three films upon exposure to water vapour was almost instantaneous, with a rapid rise in the current observed. After some time, the current fell back down to immeasurable levels for each of the films, indicating that the water had

once more been removed from the system. For exposure to the same amount of water vapour, the extent of this rise in current followed the order gellan gum (least rise), gellan gum-MWNT and gellan gum-SWNT (largest rise). It also appeared that for the composite films, the magnitude of the response was similar, and did not increase with increasing water concentration. The total response of the films however did show a dependence on the amount of water that they were exposed to, as shown in Figure 5.8. The total responses of the films were obtained from calculating the areas under the curves.

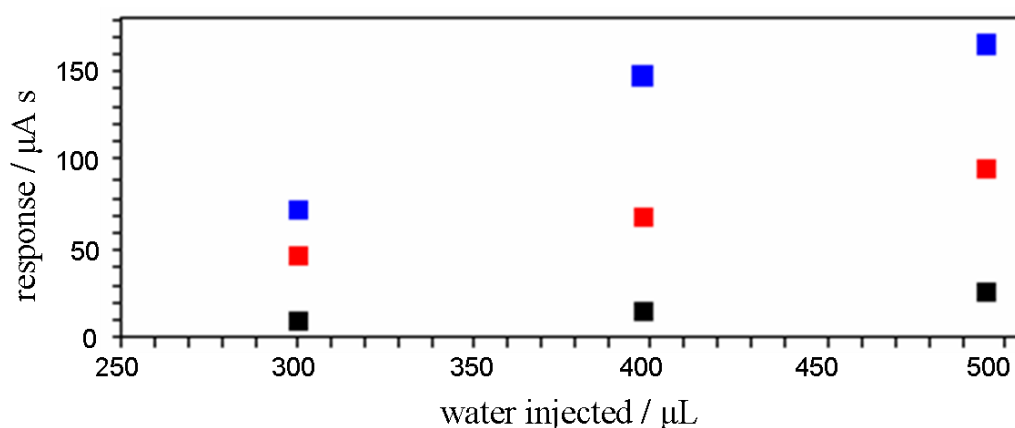


Figure 5.8 Total response of the films as a function of volume of water that they were exposed to. Gellan gum (black squares), gellan gum-MWNT (red squares) and gellan gum-SWNT (blue squares).

The gellan gum films gave the lowest total responses upon exposure to increasing amounts of water vapour, as shown in Figure 5.8. The gellan gum-SWNT films gave the largest total responses to the water vapour. It is therefore clear that the presence of at least a small amount of water vapour is required to enable electrical conduction through both the gum and the composite films. One possible explanation for the dependence of film resistance on the presence of water vapour might be that the electrical pathways in the composite films are dominated by nanotube-gum-nanotube junctions. Here the gum in the absence of water would act as a tunnelling barrier between nanotube junctions, and water is therefore required for the junctions to become more conducting. Another possible explanation is that the nanotubes, not in sufficient number for the percolation threshold to have been reached, have a low mobility in the

gellan gum films. The presence of water may then cause the gellan to swell, allowing greater mobility of nanotubes through the film and an increased number of electrically conducting nanotube-nanotube junctions to appear, giving a decrease in the resistance of the film. This explanation may account for the different total responses observed for the gellan gum films with MWNTs and SWNTs. Due to the thinner diameter of SWNTs, there are likely to be a greater number of these nanotubes as opposed to MWNTs for the same nanotube weight fraction in the films, ensuring a greater number of nanotube-nanotube junctions forming and therefore giving the films with the lowest resistance.

The response of a gellan gum-MWNT film to several other analytes was investigated in a similar manner, by evaporating the analytes at high temperature (~ 200 °C) and using a flow of nitrogen gas to carry them to the films. Volumes of 70 μL were evaporated and exposed to the films, as shown in Figure 5.9.

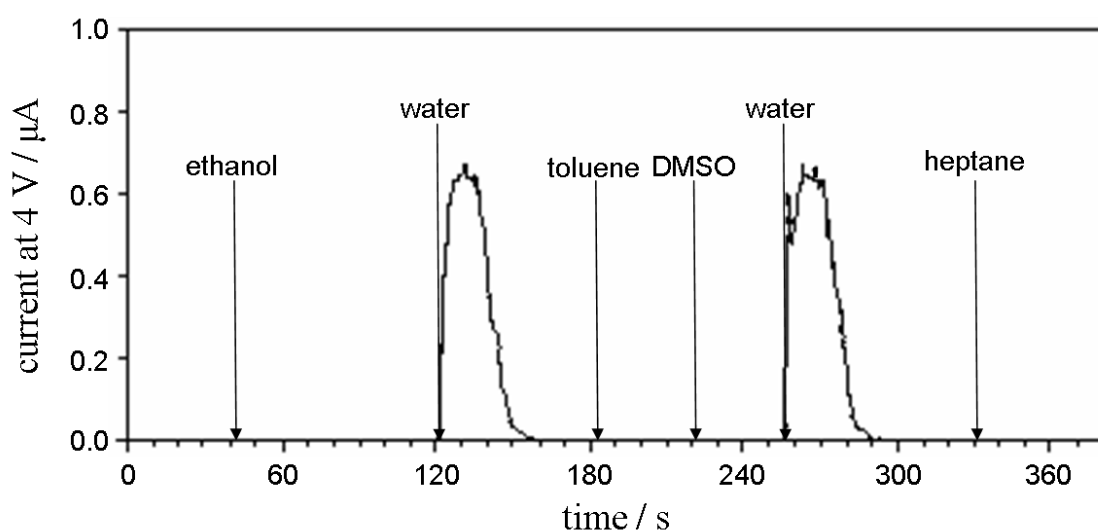


Figure 5.9 Response of a gellan gum-MWNT film to various analytes, introduced in volumes of 70 μL at a nitrogen flow rate of 7 mL s^{-1} .

The results in Figure 5.9 show that the sensitivity of the composite films is highly selective, with measurable responses observed for exposure to water vapour only. When exposed to ethanol, toluene, DMSO and heptane, the composite films showed no measurable response. Even after exposure to some of these analytes, re-exposure to water vapour (shown at approximately 260 s) elicited a similar response to

that observed earlier (at 120 s), showing that the ability of the film to respond to water vapour is not impaired by other analytes.

5.3 PMAS-CNT composites

5.3.1 UV-vis spectroscopy of composite inks and films

Dispersions of PMAS, PMAS-MWNT and PMAS-SWNT were prepared for printing at concentrations of 1.00 % w/v PMAS and 0.10 % w/v CNTs. Before loading into the emptied ink cartridges, the dispersions were filtered as described earlier for gellan gum-CNT dispersions. Figure 5.10 shows the UV-vis absorbance spectra of the filtered inks.

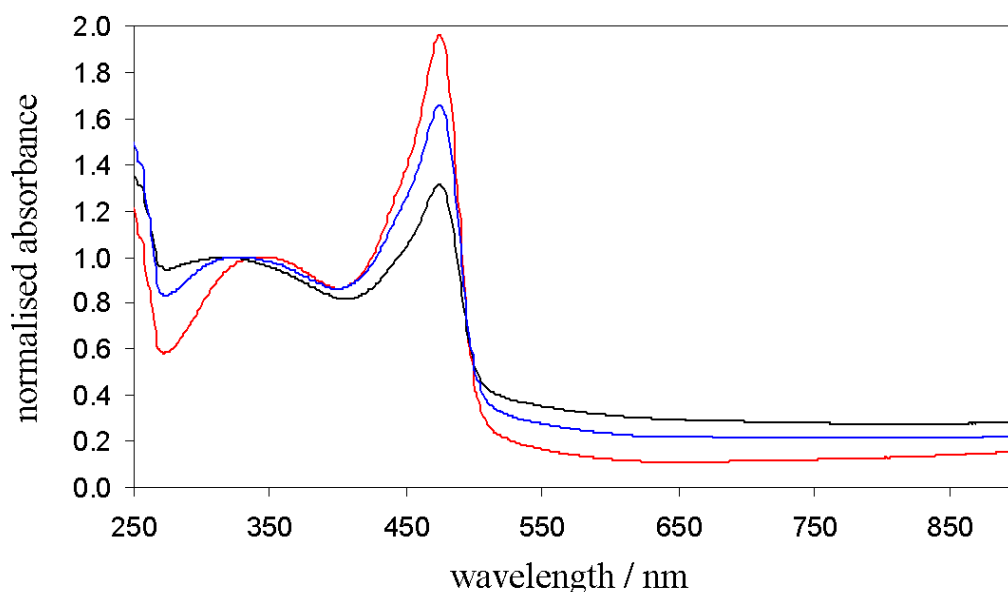


Figure 5.10 UV-vis absorbance spectra of PMAS (red line), PMAS-SWNT (blue line) and PMAS-MWNT (black line) dispersions, filtered for printing. Spectra normalised to the π - π^* transition band (~ 340 nm).

The absorbance spectra of the filtered inks reveal the same spectral changes to the polymer, PMAS, observed in the interaction studies described in Chapter 4. Briefly, these are a shift of the π - π^* transition peak to lower wavelength, a decrease in absorbance of the low wavelength polaron band and an increase in absorbance after 500 nm for nanotube containing inks. The PMAS-SWNT ink also shows the characteristic

van Hove singularities associated with individually dispersed and small bundles of SWNT in solution.³⁸ These observations in the spectra are a good indication that, despite the filtering process that removes an unknown quantity of the nanotubes, some nanotubes have been sufficiently well dispersed to pass through the filter and remain dispersed in the ‘ink’.

The inks were then loaded into empty, cleaned ink cartridges and printed in single layers onto PET substrates. Figure 5.11 shows the UV-vis transmittance spectra of the printed layers.

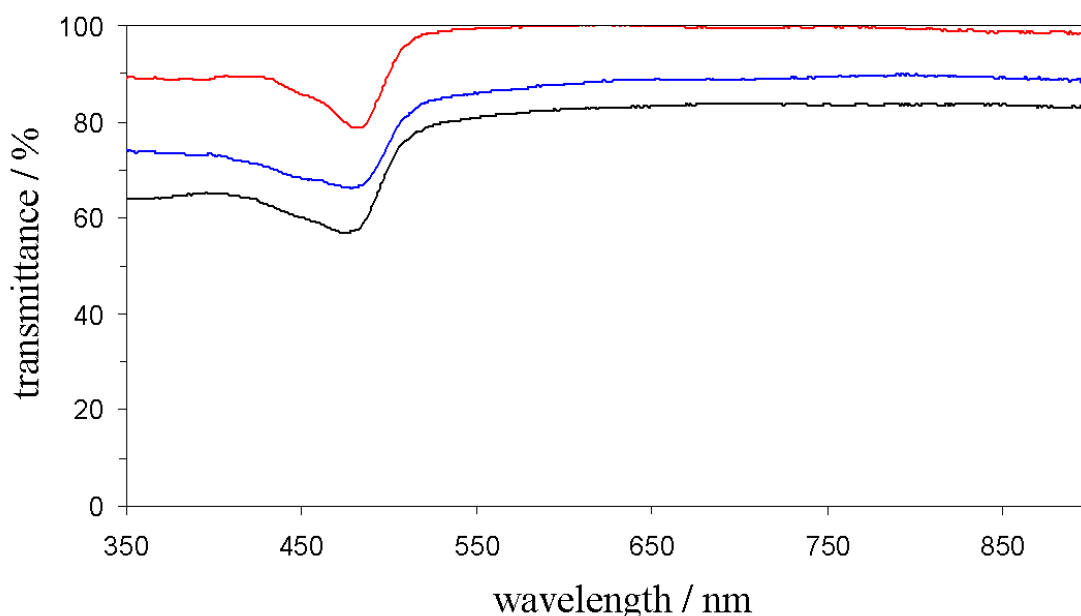


Figure 5.11 UV-vis transmittance spectra of PMAS (red line), PMAS-SWNT (blue line) and PMAS-MWNT (black line) films printed onto transparent sheets.

The transmittance spectra show that the film with the highest transmittance is that of PMAS, with a transmittance of better than 80 % for a wavelength $\lambda < 550$ nm and ~ 100 % for $\lambda > 550$ nm. The printed films with CNTs had slightly lower transmittances, as had been expected from the absorbance spectra of these inks. This is due to the presence of CNTs in the composite films, which absorb over this region. The PMAS-MWNT film had the lowest transmittance of approximately 55 % at 475 nm, however across other parts of the visible spectrum the transmittance was almost 80 %. Many potential applications of thin, flexible and conducting films that CNTs are

expected to be of use in will require the transmittance through the film to be as low as possible. The spectra here would suggest that SWNTs may be superior to MWNTs in this respect. Figure 5.12 shows photographs of some of the printed PMAS-SWNT films on transparent sheets, demonstrating their flexibility and the complexity of the patterns attainable.

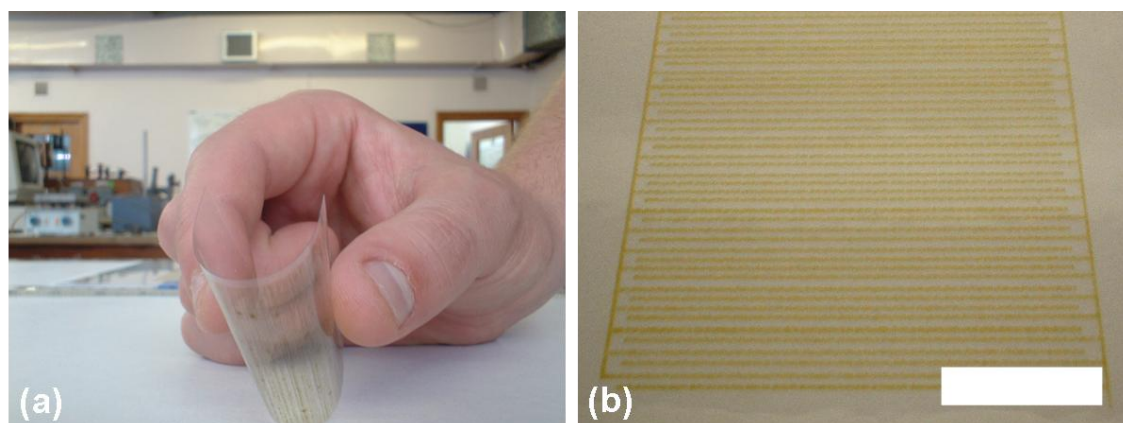


Figure 5.12 Photographs of printed PMAS-SWNT films on transparent sheets. (a) Rectangular pattern being bent almost in double and (b) interdigitated electrode pattern (scale bar 1 mm).

5.3.2 Raman spectroscopy of printed films

The lower transmittance of the composite films with CNTs as opposed to the film of the polymer is an initial indication that nanotubes have successfully passed through the printer, and have been deposited onto the transparent substrate. Further evidence to support this observation is shown in Figure 5.13, showing the Raman spectrum of a printed PMAS-SWNT film. This provides firm evidence of the presence of CNTs in the composite film, as the Raman spectrum acts as a fingerprint for CNTs.

The spectrum of the HiPco SWNTs clearly shows three distinct regions. These regions are the so-called radial breathing modes (RBM), D-line and the G-line, which are observed at approximately $200 - 300 \text{ cm}^{-1}$, 1330 cm^{-1} and 1600 cm^{-1} , respectively.³⁹ These three characteristic features also dominate the spectrum of the printed PMAS-SWNT film, and are therefore evidence that nanotubes have become sufficiently stabilised against aggregation by the polymer to pass through the print head of the ink cartridge and onto the substrate.

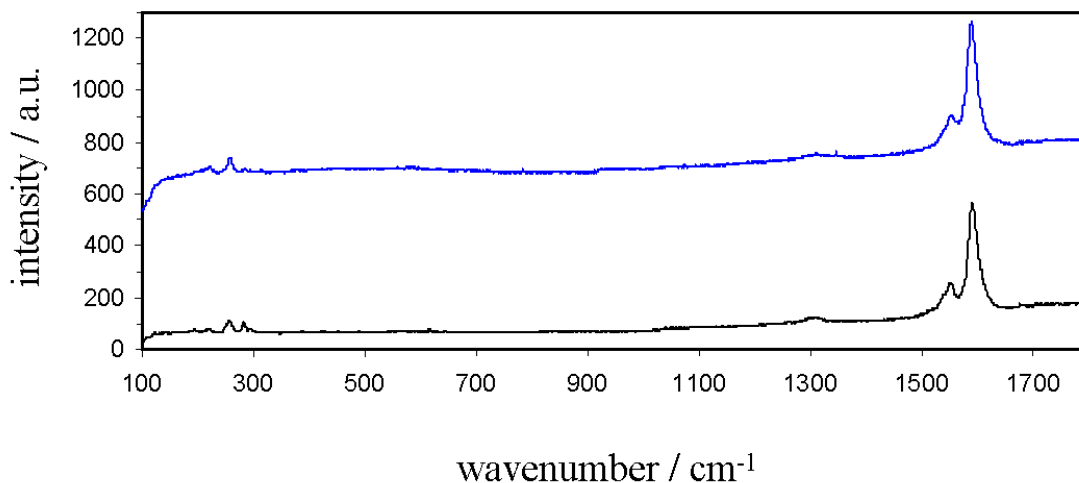


Figure 5.13 Raman spectra of HiPco SWNTs (black line) and a printed PMAS-SWNT film (blue line). Spectra offset for clarity.

5.3.3 Electrical and sensing properties of printed films

The resistances of the printed materials were obtained from I - V plots, shown in Figure 5.14. The printed PMAS films had a resistance in the region of 30 M Ω , while the PMAS-SWNT films had a resistance in the region of 60 k Ω , measured over a path length of 40 mm and a film area of 800 mm². This represents a lowering in the resistance of 3 orders of magnitude with the presence of nanotubes, due to the presence of a percolating network through the polymer film.

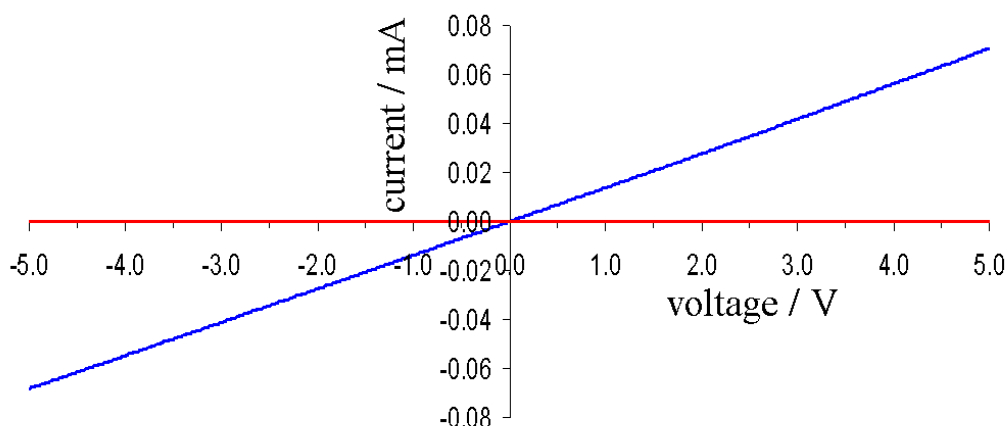


Figure 5.14 Typical I - V characteristics of a PMAS (red line) and a PMAS-SWNT film (blue line) printed onto PET sheets.

A room temperature four-point probe conductivity measurement of the PMAS-SWNT film also yielded a direct current (DC) conductivity of $0.75 \pm 0.14 \text{ S cm}^{-1}$, and a sheet resistance of $130 \pm 24.0 \text{ k}\Omega \square^{-1}$. Significantly, this is the sheet resistance of a single printed layer of the PMAS-SWNT composite - a previous study²⁸ on inkjet printing functionalised MWNT found that it required a minimum of 30 printed layers to achieve sheet resistances below $1 \text{ M}\Omega \square^{-1}$.

The resistance of the printed layers was measured parallel and perpendicular to the direction of print head motion over the substrates. This was performed after optical microscopy of the printed layers revealed that the films appeared to have better continuity in the direction of the print head motion, while perpendicular to the motion the films had gaps in between the lines of print (Figure 5.15).

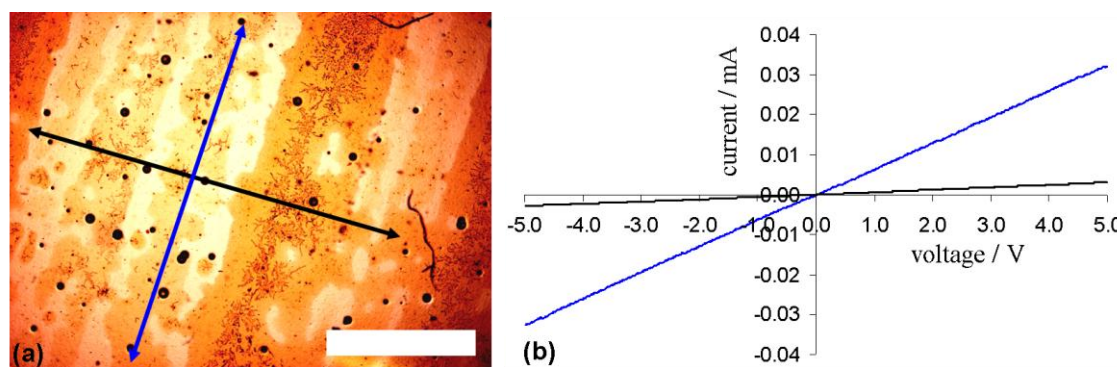


Figure 5.15 (a) Optical microscopy image of a printed PMAS-SWNT film on a PET substrate (scale bar 1 mm). The blue arrow is parallel with the print head motion over the substrate, and the black arrow is perpendicular to the motion. (b) *I-V* characteristics of the PMAS-SWNT film, measured parallel to (blue line) and perpendicular to (black line) the direction of the print head motion over the substrate. Measurements made over a film area of 800 mm^2 , at a temperature of $20 \text{ }^\circ\text{C}$ and 25 – 35 % relative humidity.

The resistance of the film measured parallel to the direction of the print head motion over the substrate was $153 \text{ k}\Omega$, while the resistance of the film perpendicular to the motion of the print head, over the same path length, was $1.6 \text{ M}\Omega$. The printed PMAS film showed a similar dependence of resistance to the direction of print head

motion, yielding a resistance of 11.1 M Ω parallel with the print, and an immeasurable resistance perpendicular to the direction of the print. This dependence of the resistance of the films on the orientation of the printed layers illustrates the imperfect wetting of the polymer and composite 'inks' on to the PET substrates. Ideally, the inks should form a continuous layer in two dimensions - parallel *and* perpendicular to the direction of the print head motion over the substrate. To form more continuous layers with the polymer and composite inks, several options might be available.

1. The surface tension of the 'inks' could be lowered through the addition of surfactant, to allow better spreading onto the substrates. This may lead to problems in dispensing the ink from the cartridge however, and might require further additives (such as a defoamer) to allow printing.
2. The substrate could be treated to render its surface more hydrophilic, and therefore allow better spreading of the ink.
3. The spacing between the adjacent printed lines could be reduced, to the point where the adjacent lines are close enough to become continuous on the substrate.
4. Multiple layers could be printed by passing the substrate through the printer again and again. The layers could either be printed directly on top of each other, or at 90° to each other.

Printing multiple layers of the PMAS-SWNT composite was carried out, to assess the viability of this route towards films with lower and more uniform resistances across the film area. A rectangular pattern was printed onto one PET sheet, and after it had dried the sheet was rotated by 90° and a second layer was printed over the first. The resistance of the film, over a 2 cm path length, was 161 k Ω in parallel to the first printed layer, and 2 M Ω in parallel to the second printed layer, at 90° to the first layer. Thus the printing of two layers at 90° to one another had not lowered the resistance at all. Multiple layers were then printed over each other, without rotating the substrate, so that the layers directly overlaid each other. The dependence of the transmittance of the films on the number of printed layers is shown in Figure 5.16. The transmittance of the films generally shows a decrease with increasing the number of layers deposited. This indicates that more material is being deposited, and therefore a decrease in the resistance might also be expected due to the greater number of CNTs in the films that comprise multiple printed layers.

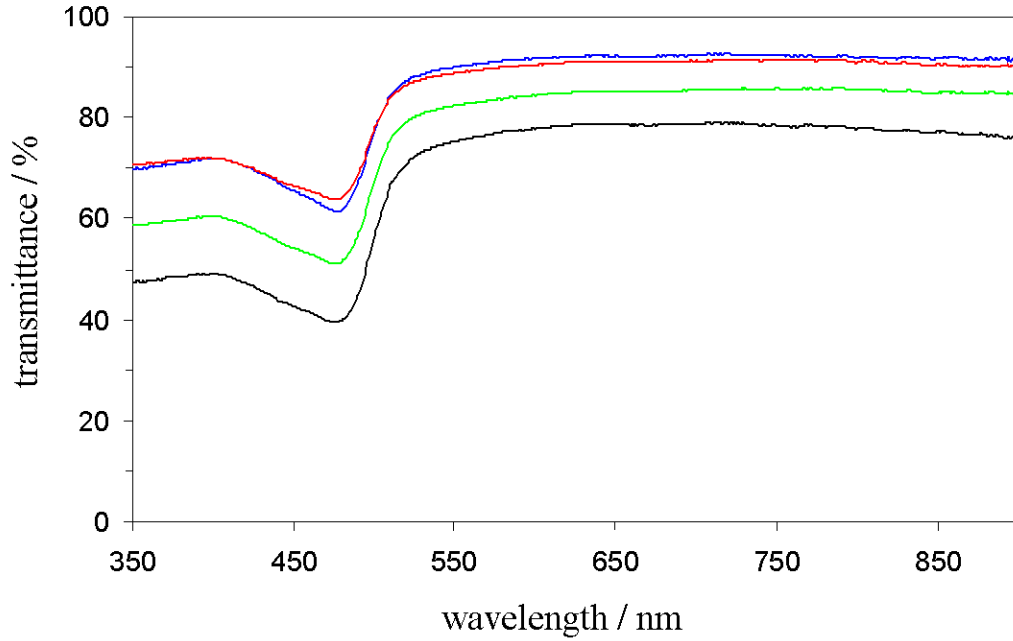


Figure 5.16 UV-vis transmittance spectra of PMAS-SWNT films printed onto transparent sheets. Films consist of one (blue line), two (red line), three (green line) and four (black line) printed layers.

As the film resistances in Table 5.1 show however, no trend in the film resistance with increasing number of printed layers was observed.

Number of printed layers	Resistance / $k\Omega$
1	153
2	immeasurable
3	135
4	83

Table 5.1 Summary of the film resistances (measured over a path length of 20 mm, film area 800 mm^2) for PMAS-SWNT films with multiple printed layers, measured from *I-V* characteristics.

For the film with two printed layers, no *I-V* plot could be obtained, and even for the film with three printed layers the decrease in resistance is relatively small. The reason for this lack of dependency of the film resistance on the number of layers was

discovered from optical microscopy images of the films. It has already been discussed that the continuity of the film in the direction of the print head motion over the substrate is very good, and is where the resistance of the films here has been recorded. However the films with multiple layers showed a number of periodic cracks at 90° to these continuous print lines, breaking the continuity of the printed features. It is these cracks that appear to lead to a decrease in the resistance of the films despite the increasing number of layers. The cause of the cracks is thought to arise from the mechanical process of feeding the substrate through the printer, as part of the printer mechanism scratches the substrate, and is therefore a drawback of the printing process using a commercial inkjet printer.

The photograph shown back in Figure 5.12a showed the film being bent almost in half, which is made possible due to the flexibility of the underlying substrate. Figure 5.17 shows the resistance of a PMAS-SWNT film as it undergoes a repeated cycle of bending followed by relaxation.

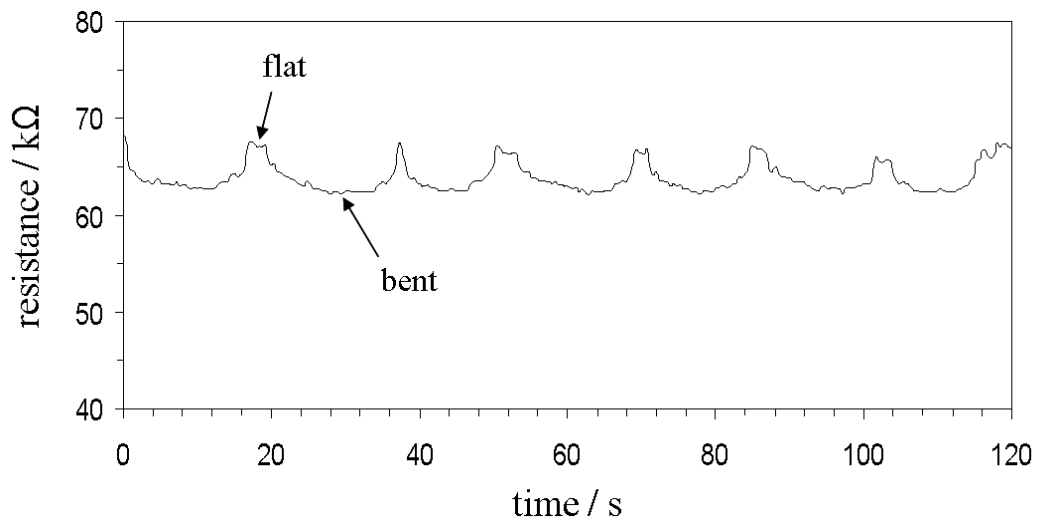


Figure 5.17 Resistance of a PMAS-SWNT film (measured over a path length of 4 cm) as it is periodically bent and released.

We can see that although the resistance is lowered slightly when the film is bent, this is a reversible process where the resistance returns to the original value when the film is released. This demonstrates the robust nature of the films, where the percolative CNT network does not appear to be damaged by bending the films.

The potential for these films to be used as sensors was assessed in a similar manner to those of the gellan gum-CNT films, using both static and dynamic methods of carrying out the sensing experiments (see Chapter 2). In the static sensing experiments, a PMAS-SWNT film was loaded into a sensing chamber, and an aliquot of ethanol was then introduced and allowed to evaporate. The current through the film was measured at a constant voltage over time (thereby giving the resistance), until the current reached a constant value, which indicated the maximum response of the film. The chamber was then opened to allow rapid removal of the ethanol from the system. Figure 5.18 plots the maximum response of one such PMAS-SWNT film as it is exposed to increasing concentrations of ethanol. The maximum response is given as the percentage change in the resistance, $\% \Delta R/R_0$, where ΔR is the change in resistance ($R - R_0$), R is the resistance of the film at its maximum response and R_0 is the initial resistance of the film.

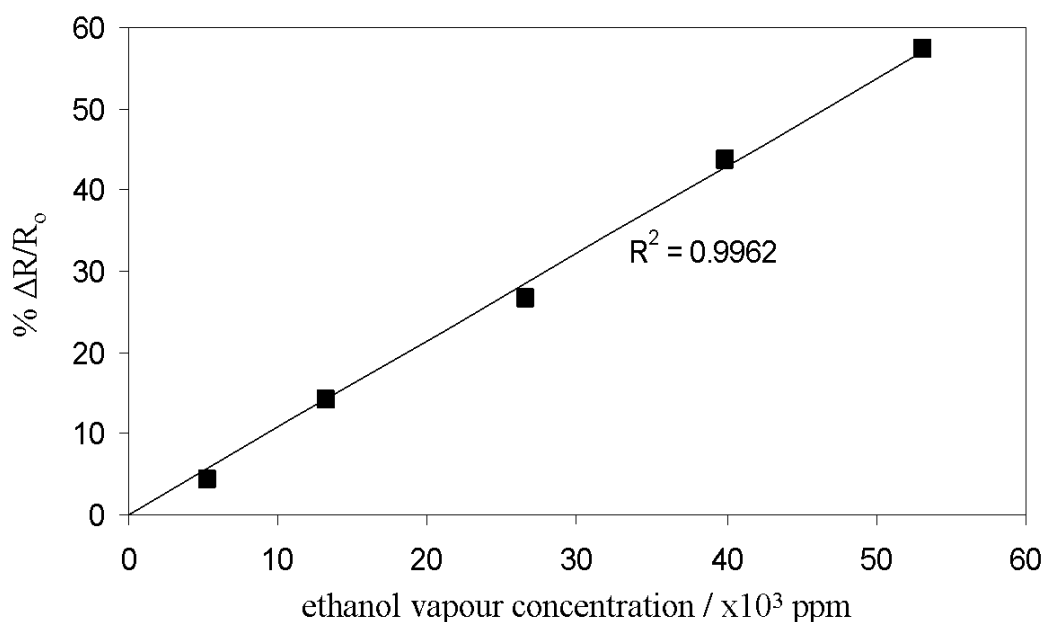


Figure 5.18 Maximum responses recorded for a PMAS-SWNT film exposed to ethanol vapour. Room temperature and humidity (20 °C, 25 – 35 %), film area 800 mm².

When ethanol was introduced to the PMAS-SWNT films, the current through the films gradually started to fall, indicating an increase in the resistance. At some time after this exposure to ethanol, the current reached a constant value which indicated that

the film had reached its maximum response. It was observed that the time taken for the film to start showing a response, and also the time taken for the film to reach its maximum response increased with increasing ethanol content in the chamber. This has been attributed to the longer time required for larger volumes of ethanol to evaporate at ambient conditions. The maximum response exhibited by the films, as shown in Figure 5.18, also shows that the magnitude of the response depends on the concentration of ethanol in the chamber, with a linear dependence observed. This demonstrates that the films could be used as sensors to determine an unknown concentration of ethanol in an environment, based on a calibration plot such as this, by measuring the electrical response of the film. As the response of the films to ethanol showed a linear trend with concentration, the limits of detection could be calculated. Analysis gave the limits of detection of the films as approximately 150 ppm.

Removal of the chamber and exposure of the film to ambient air resulted in a rapid rise in the current back to the original value, suggesting that the films could be re-used over and over again. This phenomenon also revealed that the interaction between the PMAS-SWNT films and ethanol was reversible, and that no permanent alteration to the film had taken place. To gain further understanding into the sensing mechanism, the films were exposed to the vapours from a number of other aromatic and alcohol compounds. The responses are given in Table 5.2.

Vapour	% $\Delta R/R_0$	Dielectric constant
Methanol	56.5	33
Ethanol	31.3	24
2-propanol	10.9	20.1
Butan-1-ol	6.7	17.8
Chloroform	0	4.8
Toluene	0	2.4

Table 5.2 Maximum responses of a printed PMAS-SWNT film exposed to various alcoholic and aromatic compounds at 20 °C. Film area 800 mm². Vapour concentration 30,000 ppm.

The films showed a rise in the resistance when exposed to the vapours from alcohols, with the magnitude of the response increasing with the dielectric constant, and therefore the polarity, of the alcohol. Not shown here but commonly observed was the response of the films to water vapour, which gave the largest rise in the resistance of the film - interestingly this is the *opposite* effect to that observed for the gellan gum composite films, where the resistance of the films fell with exposure to water vapour. The observed rise in the resistance here is attributed to swelling of the polymer, which leads to breaking of nanotube-nanotube conducting pathways. The films did not exhibit any measurable response to the aromatic compounds chloroform and toluene, which had the lowest dielectric constants of the compounds studied. This is being investigated further.

The times taken for the films to show a maximum response to ethanol vapour under static conditions ranged from 10 minutes (at ~ 5000 ppm ethanol) to 55 minutes (at ~ 55000 ppm ethanol). We can improve the sensing time by using dynamic conditions, explained in Chapter 2. Figure 5.19 shows the dynamic responses of PMAS and PMAS-SWNT printed films to ethanol vapour, at a gas flow rate of 1.0 mL s^{-1} and a constant voltage of 10.0 V.

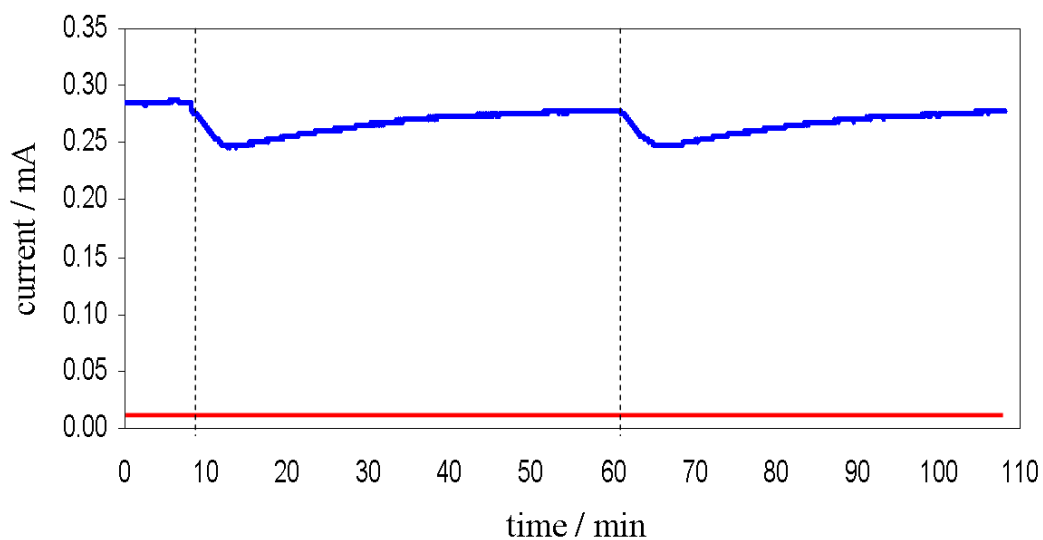


Figure 5.19 Current change over time for PMAS (red line) and PMAS-SWNT (blue line) printed films when exposed to ethanol vapour. Dashed lines indicate the points at which ethanol was introduced to the system. Nitrogen carrier gas flow rate = 1.0 mL s^{-1} . Volume of ethanol injected = $80 \text{ }\mu\text{L}$. Film area 800 mm^2 .

The PMAS films, with resistances higher than those of the PMAS-SWNT films by around 3 orders of magnitude, did not show a measurable response at 10 V that could be differentiated from baseline noise. However the PMAS-SWNT film clearly shows a measurable response, with the current falling after ethanol is introduced to the system. This illustrates one of the advantages of having CNTs in the films, as even if they do not act as the sensing element, they lower the resistance of the film and can allow sensing to be carried out at lower voltages. The PMAS films did show measurable responses to ethanol vapour under the same vapour conditions, but only with voltages significantly in excess of 10.0 V applied to the film.

The initial current fall, and therefore response, of the PMAS-SWNT film to ethanol vapour is observed after only a few seconds, with the maximum response after approximately five minutes. The current then rises gradually back to the original value as the ethanol is flushed from the sensing chamber by the carrier gas. It is assumed that the response time of the film is much faster than the recovery time due to the short time that it takes to transport the ethanol into the sensing chamber. Once the ethanol is in the sensing chamber however, the chamber volume is much larger and therefore if the ethanol distributes itself evenly then it will take longer to remove all of the ethanol from the system. This is further investigated and shown in Figure 5.20.

The response curves to ethanol vapour in Figure 5.20 reveal a number of interesting pieces of information.

1. The time taken for the film to show a maximum response is shorter for the higher carrier gas flow rate, and longer at the lower carrier gas flow rate.
2. The time taken for the film to show complete recovery (return of the resistance to the initial value) is also shorter for the higher carrier gas flow rate and longer at the lower carrier gas flow rate.
3. The magnitude of the maximum response of the film to ethanol vapour is smaller at the higher carrier gas flow rate than it is at the lower carrier gas flow rate, despite the volume of ethanol introduced being the same in each case.

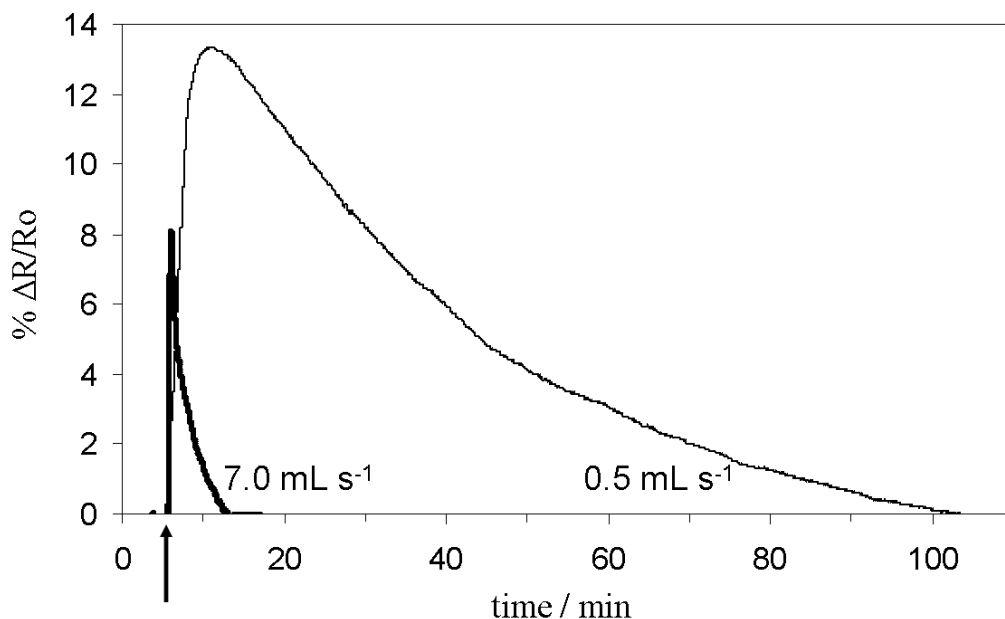


Figure 5.20 Response ($\% \Delta R/R_0$) of a PMAS-SWNT film (area 800 mm^2) exposed to ethanol vapour (from $80 \text{ }\mu\text{L}$ injected) at two different flow rates of the carrier gas. Arrow indicates time of ethanol introduction.

The difference in times taken for the film to show a response and recovery after exposure to ethanol vapour can be better understood by considering the flow of ethanol through the sensing chamber. An estimate of the concentration of ethanol in the sensing chamber over time at the two different flow rates has been calculated, with a number of assumptions made. These are:

1. The volume of the vessel into which the ethanol is injected is estimated to be approximately 85 mL .
2. Standard pressure and temperature are assumed.
3. There is no adsorption of ethanol onto any part of the sensing apparatus, and all of the ethanol in the system is 'free'.

As the conditions and apparatus set-up have been kept constant throughout the experiments, then any errors on the part of the first two assumptions will be the same for each of the flow rates. The third point however, assuming that all of the ethanol in the system is 'free', may depend on the flow rates as any adsorption/desorption may be affected by the carrier gas flow rate. The concentration of ethanol in the sensing

chamber, and thus the amount of ethanol that the film is exposed to, is calculated from the amount of ethanol already in the chamber, the amount flowing into the chamber and the amount flowing out of the chamber every second, as follows:

$$C_t = \frac{V_{sens,t-1} + V_{in,t} - V_{out,t-1}}{V_C}, \quad [5.2]$$

where C_t is the total concentration of ethanol in the sensing chamber at any time t , $V_{sens,t-1}$ is the volume of ethanol already in the sensing chamber at time $t-1$ second, $V_{in,t}$ is the volume of ethanol flowing into the sensing chamber at time t , $V_{out,t-1}$ is the volume of ethanol that has left the system at time $t-1$ second and V_C is the volume of the sensing chamber. A plot of this data over time for each of the carrier gas flow rates is shown below in Figure 5.21.

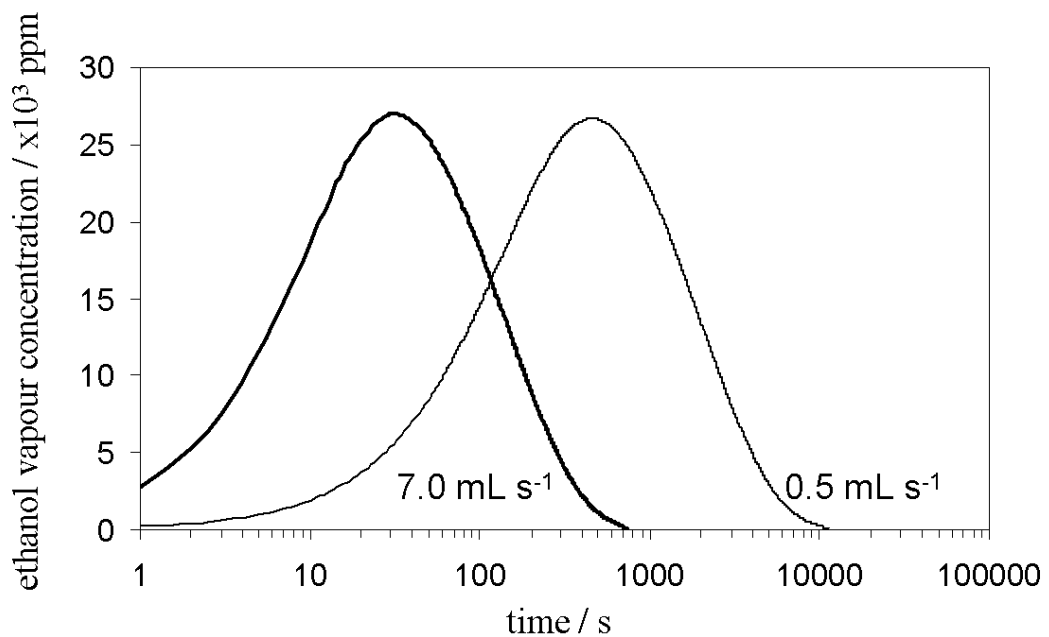


Figure 5.21 Theoretical estimation (from equation 5.2) of the ethanol vapour concentration in the sensing chamber at two flow rates of the carrier gas.

At the higher carrier gas flow rate of 7.0 mL s^{-1} , it is clear that the ethanol is being transported into and then out of the sensing chamber faster than it is at the lower flow rate of 0.5 mL s^{-1} . It is also clear that the concentration of ethanol in the chamber peaks, or reaches a maximum, faster at the higher flow rate than it does at the lower flow rate. This would explain why the response time and recovery time of the film at the higher flow rate are faster than they are at the lower flow rate. What is not yet clear however is the reason why the magnitude of the response should be different for the two different flow rates. The data in Figure 5.21 suggests that, despite the different rates of ethanol transport into and then out of the sensing chamber, the concentration actually peaks at the same amount for each flow rate, at approximately 27000 ppm. It is known from the static sensing measurements that the response of the film is dependant on the concentration of ethanol that the film is exposed to, and so there must be another effect taking place here to explain the discrepancy in the response magnitude at the different flow rates. We can see from Figure 5.21 that at the flow rate of 7 mL s^{-1} , the time from initial exposure to the peak concentration of ethanol is just 12 s, and the total exposure time is approximately 800 s. At the flow rate of 0.5 mL s^{-1} however, the time from initial exposure to the peak concentration of ethanol is approximately 700 s, and the total exposure time is over 10000 s. The film therefore has far more time to interact with the ethanol at the lower flow rate, particularly in the period of time from vapour introduction to the peak concentration, than it does at the lower flow rate. This would suggest that, despite the concentration peaking at the same amount at each flow rate, it is the length of interaction time that is the dominant factor for response magnitude.

Figure 5.22 plots the response times and the magnitudes of a PMAS-SWNT film to ethanol vapour at several different flow rates.

The spectrum of the HiPco SWNTs clearly shows three distinct regions. These regions are the so-called radial breathing modes (RBM), D-line and the G-line, which are observed at approximately $200 - 300 \text{ cm}^{-1}$, 1330 cm^{-1} and 1600 cm^{-1} , respectively.⁴⁰ These three characteristic features also dominate the spectrum of the printed PMAS-SWNT film, and are therefore evidence that nanotubes have become sufficiently stabilised against aggregation by the polymer to pass through the print head of the ink cartridge and onto the substrate.

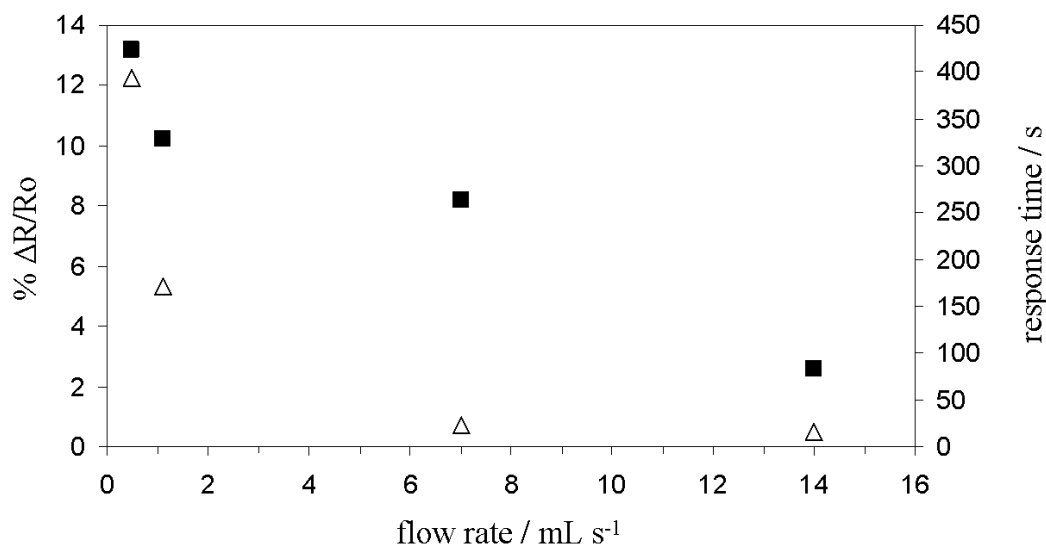


Figure 5.22 Maximum response (filled squares) and response time (empty triangles) of PMAS-SWNT films to ethanol vapour (fixed concentration) as a function of carrier gas flow rate.

5.3.4 Sensing mechanism of PMAS-SWNT films

The printed PMAS-SWNT films have shown sensitivity to ethanol and other alcohol vapours, with the magnitude of the film response increasing with the dielectric constant of the alcohol. Interestingly, the response of the film is an increase in the resistance of the composite, whereas with the gellan gum-nanotube films, the response was a decrease in the resistance with exposure to water vapour. This would suggest that different sensing mechanisms are at work in each case.

Possible sensing mechanisms that might account for the rise in resistance observed for the PMAS-SWNT films include a physical swelling of the film, where the swelling might cause existing nanotube-nanotube junctions to be broken. Other authors have also reported that the sensing mechanism might be due to a charge transfer interaction between the analyte and the conducting polymer,⁴¹ or between the analyte and the CNTs themselves.⁴² This might also account for the dependence of the response magnitude on the dielectric constant of the analyte. As a response was observed with the PMAS films without nanotubes, though at higher applied voltages, it would seem that it is the conducting polymer that is key to the sensing mechanism. The main function of the CNTs in the films therefore would be as a conducting filler, lowering the resistance of the film to allow sensing at low voltages. That is not to say however that the nanotubes play no part in the sensing mechanism, as supplementary interactions

between the vapour and the nanotubes or charge transfer between the polymer and the nanotubes may also be taking place.

5.4 PMAS-PAni-MWNT composites

This work was undertaken at the IPRI, University of Wollongong, Wollongong, Australia.

5.4.1 Suitability of the composites for printing

It has already been discussed that the commercial inks used in inkjet printing are highly formulated, giving them properties that allow them to be printed under a very precise set of conditions. Amongst the two most important properties of the inks are their viscosity and surface tension, which for commercial inkjet printer inks should be approximately 2 cPs and 35 mN m⁻¹ respectively.² However for the Dimatix printer used in this part of the study, these ideal values of the viscosity and surface tension are in the region of 10 - 12 cPs and 28 - 33 mN m⁻¹ respectively.⁴³ The viscosities of the as-prepared composite dispersions were between 40 - 100 cPs, but could be lowered to the more 'ideal' region of 9 - 12 cPs simply by diluting the composites to 1.0 % w/v total solids. The surface tensions of the PMAS-PAni-MWNT composite inks were measured, and found to be in the region of 67 - 72 mN m⁻¹ (Figure 5.23).

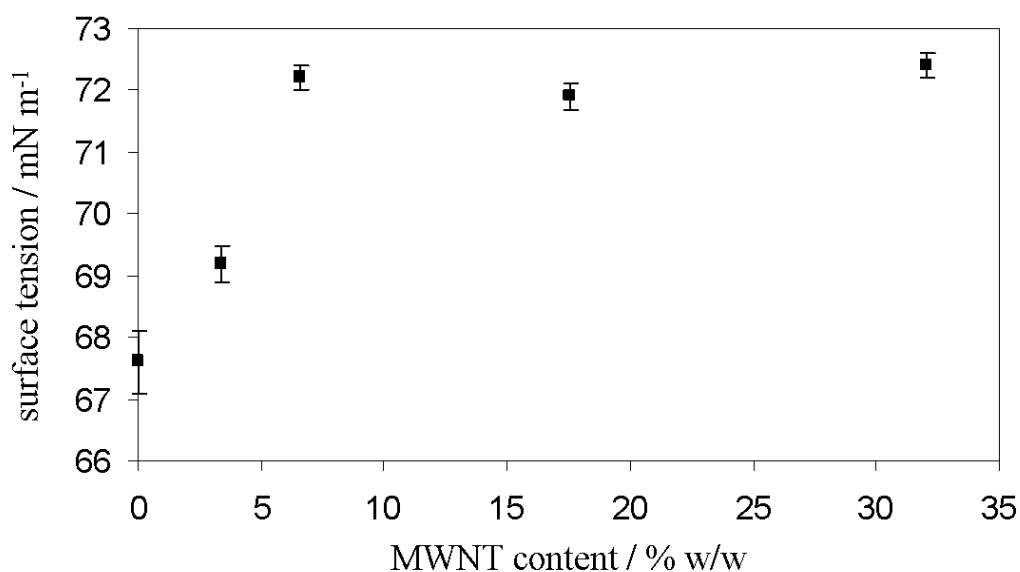


Figure 5.23 Surface tension of PMAS-PAni-MWNT composite 'inks' at a total solids concentration of 1.0 % w/v.

The composite ink without nanotubes had the lowest surface tension, with the addition of nanotubes resulting in a slight rise in the surface tension with increasing nanotube content before reaching a plateau. It has been observed by Xue and co-workers that CNTs can cause the surface tension of water-based dispersions to rise above the surface tension of pure water,⁴⁴ though the rise here is not observed to that extent, with the surface tension reaching a plateau at approximately 72 mN m^{-1} . The reason for the increase in surface tension with the presence of nanotubes might be due to a lowering in the concentration of the polymers, which are known to lower the surface tension here (the surface tension of the PMAS-Pani composite with no nanotubes was 67.5 mN m^{-1}). As the total solids content of the dispersion was maintained at 1.0 % w/v, then as the concentration of nanotubes increases, the concentration of polymers must therefore decrease. This theory is supported by a surface tension of 71.7 mN m^{-1} measured for a PMAS-PAni composite at the lower concentration of 0.5 % w/v. The increasing concentration of CNTs may not then cause the surface tension to rise significantly above the plateau value, as it has already been shown that the nanotubes are well coated by the polymers.

One of the composite inks was prepared with 0.25 % w/v SDS, resulting in a lowering of the surface tension to approximately 31 mN m^{-1} , which is within the ideal region for the Dimatix inkjet deposition system. When this ink was printed however, after several drops had been printed the ink started to foam and wet around the print head, presumably caused by the lowering in the surface tension, resulting in a pool of ink forming that prevented further drops being fired from the printer and onto the substrate. Eventually this pool of ink reached a critical point, and a large drop of the ink fell onto the substrate. Clearly, this is a case where in solving one problem, another problem presents itself, and is one of the reasons why commercial inks for printing are so heavily formulated. One solution to this problem may have been to add a defoamer or dewetting agent, to stop the ink from wetting around the print head, however this involves further additions to the composite ink, which is undesirable.

Despite not being in the region that is deemed most suitable for inkjet printing, an attempt was made to print the PMAS-PAni-MWNT composite without altering the surface tension. After several passes over the substrate, the composite ink appeared to aggregate around the print head, and stopped being printed onto the substrate. One of the features of the Dimatix materials printer, however, is that it possesses the capability

to undergo a cleaning cycle during the printing. This cycle can consist of the printhead 'blotting' itself on a clean sponge, 'purging' a large amount of ink from the cartridge or 'spitting' a small volume of ink from the cartridge, in any combination of actions and at any interval during the printing that is desired. It was found after several trials that by applying a cleaning cycle of 'spit, purge, spit, blot' to the print head after every five passes over the substrate, aggregation of ink around the print head could be prevented. This method of printing with the included cleaning cycle resulted in the quality of the printed features being comparable with those from the Dimatix model fluid, and was used in all the printing studies that follow.

Finally, the issue of nanotube aggregates in the composite ink is addressed. With gellan gum and PMAS composite inks, and where the nanotubes were mixed together with the aqueous dispersant, aggregates have been observed in the composite ink which can clog up the ink cartridge. This prevents printing, and effectively destroys the ink cartridge as the blockage cannot then be removed. Here however, with the PMAS-PAni-MWNT composites, the composite inks could be printed without the need for any filtering of the dispersion prior to printing, despite the extremely high loading fractions used. One explanation for this could be that polymerisation in the presence of the nanotubes might be ensuring better dispersion of the nanotubes, preventing them from aggregating together. Evidence for this has already been shown in the TEM images of the composites (Chapter 4), where the coverage of the polymers over the nanotubes appeared to be excellent. A second explanation as to why these composites can be printed without the need for filtering may be that the printing process is helped by the cleaning cycle, which is designed to keep ink flowing through and stop any aggregation of material around the print head. Not needing to filter the composite inks is extremely advantageous, as this process has been a major reason for the loss of nanotubes in the other work reported here. As long as nanotubes do not sediment within the ink cartridge, then it is hoped that the concentration of nanotubes in the printed films should be approximately equal to the initial concentrations in the composites.

5.4.2 Optical and electrical characterisation of the printed films

The composite inks were diluted to a total solids concentration of 1.0 % w/v for printing, and printed at a drop spacing of either 15 or 20 μm .^{*} They were then printed onto a range of substrates including glossy photopaper, transparent PET substrates, ITO glass and gold coated polyvinylidene fluoride (Au-PVDF). Figure 15.24 shows the UV-vis transmittance spectra for a single layer of the composite with 17.5 % w/w MWNTs, printed onto a PET substrate.

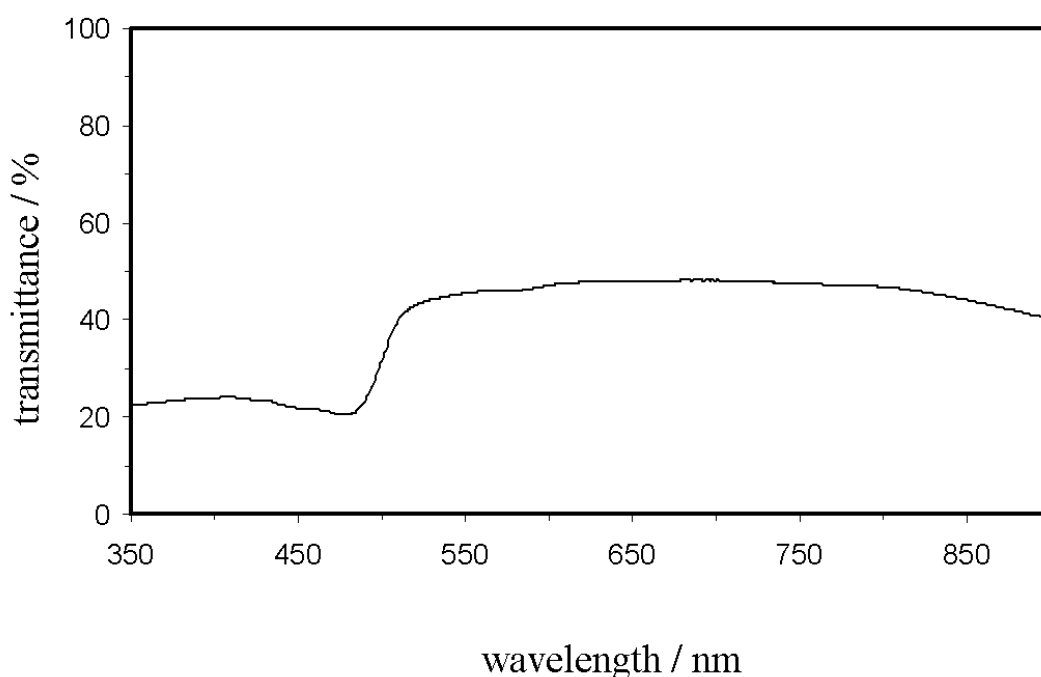


Figure 5.24 UV-vis transmittance spectra of a PMAS-PAni-MWNT film (17.5 % w/w MWNT) printed onto a PET substrate. Drop spacing 15 μm .

The spectra is similar to that observed for the PMAS-nanotube films, and is dominated by the spectra of the PMAS (from 350 to approximately 500 nm) and CNTs (from 500 nm onwards). Due to the high concentration of CNTs in the composite, the transmittance of the film is quite low, with the highest transmittance at approximately 50 %.

^{*} The drop spacing is the distance, in both the x and y dimensions, between the centres of drops on adjacent lines and columns. Where the drop spacing is less than the drop diameter, overlapping will occur and a continuous film will be formed. Where the drop spacing is larger than the drop diameter however, the drops will remain discrete.

Figure 5.25 shows photographs of some of the images printed onto glossy photopaper and transparent PET substrates. The colour of the printed films is yellow, supporting both the absorbance and transmittance UV-vis spectra of the composites where the main features observed are those of PMAS. When printed onto photopaper, the resolution of the printed images was excellent, and comparable with identical images printed with the model Dimatix ink.

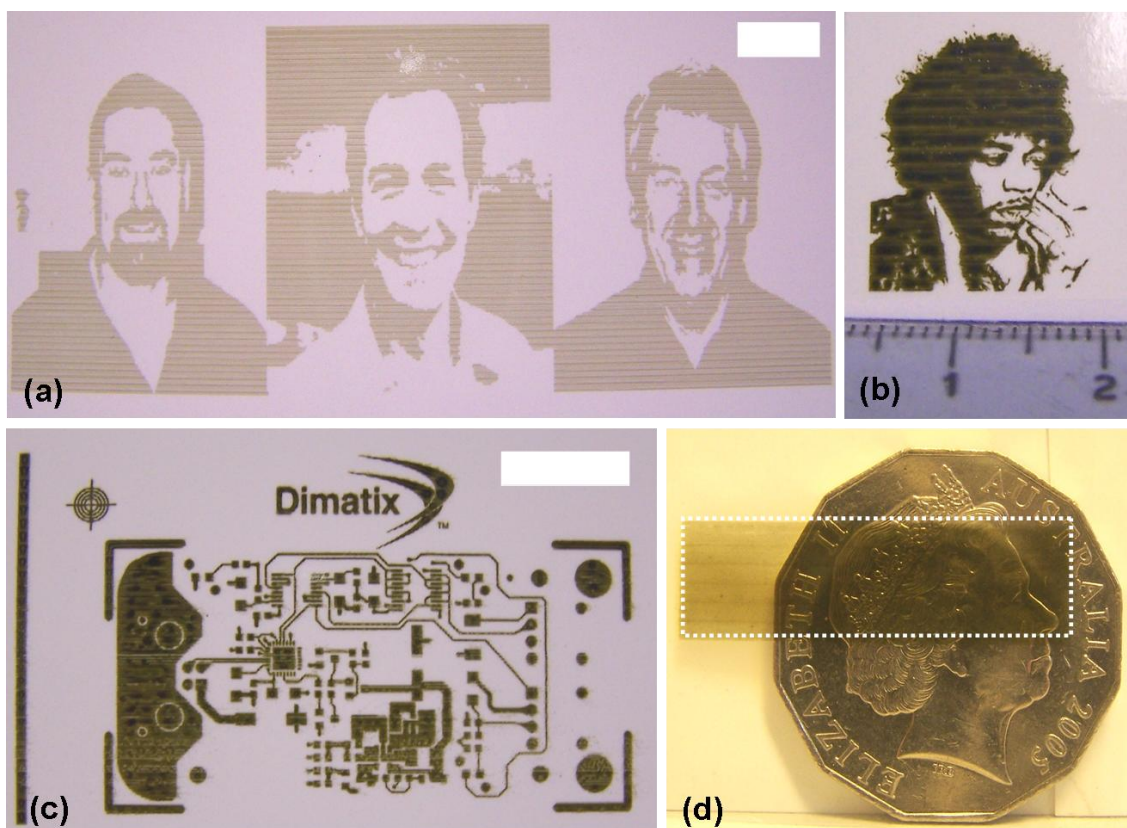


Figure 5.25 Photographs of printed PMAS-PAni-MWNT films (17.5 % w/w MWNT) printed onto glossy photopaper (a-c) and a PET substrate (d). Images of (a) Professors Innis, Spinks and Kane-Maguire from the University of Wollongong (left to right), scale bar 1 cm. (b) Jimi Hendrix and (c) Dimatix ‘circuit’ design, scale bar 1 cm.

The printed ‘circuit’ in Figure 5.25c is from an image that is part of the Dimatix software, however the other printed images (Figure 5.25a and 5.25b) were converted from photographic images into the necessary type of file for printing using the Dimatix

software. This demonstrates the potential of this printing system to be used to print virtually any type of image or design desired by the user.

The film printed onto the transparent PET substrate, a simple rectangle, shows improved continuity compared to those films of the PMAS-SWNT composites printed by the Hewlett-Packard deskjet printer (see Figures 5.12a and 5.15a). This can be achieved simply by reducing the drop spacing using the Dimatix printer, resulting in the ink drops being deposited closer together and allowing a more continuous film to form. The excellent continuity of the film was demonstrated by four-point probe electrical characterisation of the films, where the orientation of the probe in relation to the print direction had no effect on the sheet resistance of the films, printed onto either the PET substrates or the glossy photopaper.

Typical sheet resistances for the films printed onto glossy photopaper are shown in Table 5.3.

MWNT % w/w	Drop spacing / μm	Sheet resistance / $\text{k}\Omega \square^{-1}$
17.5	15	2.68 ± 0.07
32.0	15	0.50 ± 0.16

Table 5.3 Sheet resistances of PMAS-PAni-MWNT films printed (1 layer) onto glossy photopaper.

As with the drop cast composite films, reported in Chapter 4, a higher loading fraction of carbon nanotubes in the composite film results in a lower sheet resistance. The sheet resistance of the printed films is higher than that of the drop cast films by around 1 - 2 orders of magnitude, though this is attributed to the different thicknesses of the drop cast (tens of μm) compared to the printed (expected to be hundreds of nm) films. As the conductivity is proportional to the film thickness, we expect the conductivity of the printed and drop cast films to be of the same order of magnitude. The sheet resistance of the film with 32.0 % w/w MWNT is believed to be the lowest sheet resistance for a printed carbon nanotube film to date.

When printed onto the transparent PET substrates, the sheet resistance of the films was higher than on the glossy photopaper. Figure 5.26 shows how the number of printed layers influences the transmittance and sheet resistance of the films.

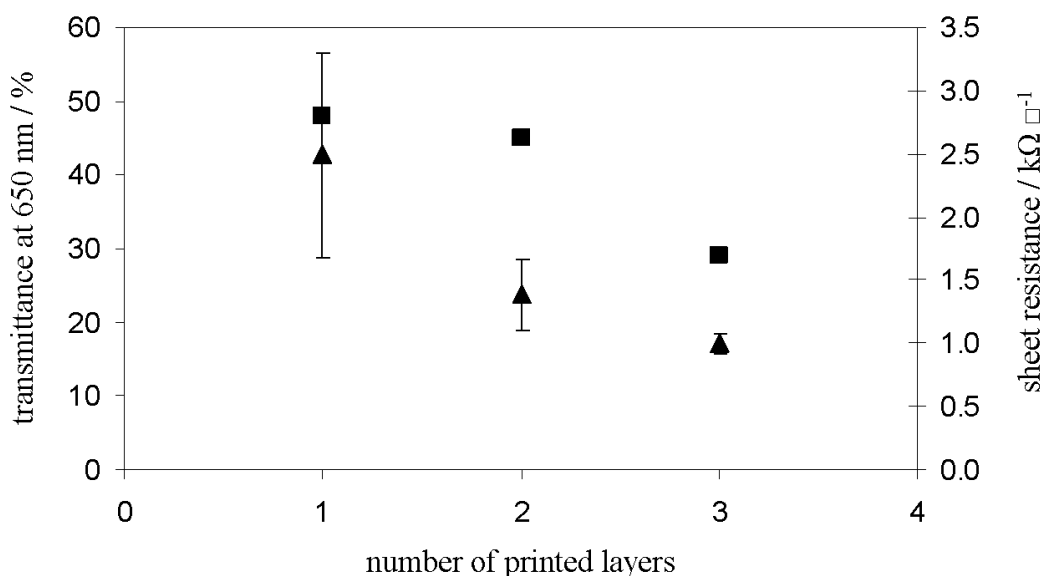


Figure 5.26 Sheet resistance (triangles) and transmittance (squares) as a function of number of printed layers of a PMAS-PAni-MWNT (17.5 % w/w MWNT) composite printed onto PET substrates.

As observed for the printed PMAS-SWNT films (Figure 5.11), the transmittance with increasing number of printed layers decreases, due to the greater concentration of nanotubes being deposited. However there is also a decrease in the sheet resistance of the films with an increasing number of layers, which was not observed with the PMAS-SWNT films. This is likely to be a result of the improved continuity of the films due to the non-contact printing method used in the Dimatix system, which does not result in any breaks or scratches in the film that occur with the ‘desktop’ printer used earlier. The film with the lowest sheet resistance was that with 3 printed layers, with $R_s = 1.00 \pm 0.08 \text{ k}\Omega \square^{-1}$, although the transmittance (at 650 nm) was just 29 %.

The influence of changing the drop spacing on the transmittance and sheet resistance was investigated with the composite with 32.0 % w/w MWNT, and is summarised in Table 5.4.

Drop spacing / μm	Transmittance at 650 nm / %	Sheet resistance / $k\Omega \square^{-1}$
15	37	2.01 ± 0.08
20	68	5.03 ± 0.39

Table 5.4 Sheet resistance and transmittance of PMAS-PAni-MWNT (32.0 % w/w MWNT) films printed onto PET substrates.

The data in Table 5.4 shows that the film printed with the smaller drop spacing has the lower transmittance and sheet resistance. This is attributed to the composite material being deposited over a smaller area, leading to a thicker film with more densely packed carbon nanotubes. By comparing data for the films (1 layer, 15 μm drop spacing) with 17.5 and 32.0 % w/w MWNT, it is also observed that the composite film with the higher nanotube content has the lower transmittance and sheet resistance. This shows that the transmittance and sheet resistance of PMAS-PAni-MWNT films can be controlled by three factors - the drop spacing, nanotube loading fraction and number of printed layers, all resulting in an increased amount of nanotubes deposited.

5.4.3 *Electrochromic behaviour of PMAS-PAni-MWNT films*

It has been shown in an earlier chapter that the PMAS-PAni-MWNT composite films show electrochromic behaviour, where the colour of the film can be manipulated. This manipulation is achieved through controlling the oxidation state of the polymers through electrochemical means. Here, we have looked at the electroactivity of the printed films, to see if any electrochromic behaviour is again observed. As conducting electrodes are necessary for this technique, the films were printed onto ITO coated glass and Au-PVDF. A typical cyclic voltammogram is shown in Figure 5.27.

The cyclic voltammogram of the printed film on Au-PVDF displays similar characteristics to those observed for the cast films in chapter 4. These features are the three redox couples that have been assigned previously for the PMAS-PAni composite without carbon nanotubes.⁴⁵ The photographs in Figure 5.27 show the colours of the film at each end of the voltammogram. The film is yellow in colour, representing the leucoemeraldine (fully reduced) forms of PMAS and PAni, at negative potentials. As the voltage is ramped through to a positive potential, the film becomes blue, indicating that both the polymers are in their pernigraniline (fully oxidised) state. It was observed that the films could withstand repeated cycling between their oxidation states, with no visible degradation of the film. These are thought to be the first reported inkjet-printed CNT films that display such electrochromic behaviour. At higher loading fractions of carbon nanotubes, the colour change in the film could not be observed visually, despite the films retaining their electroactivity.

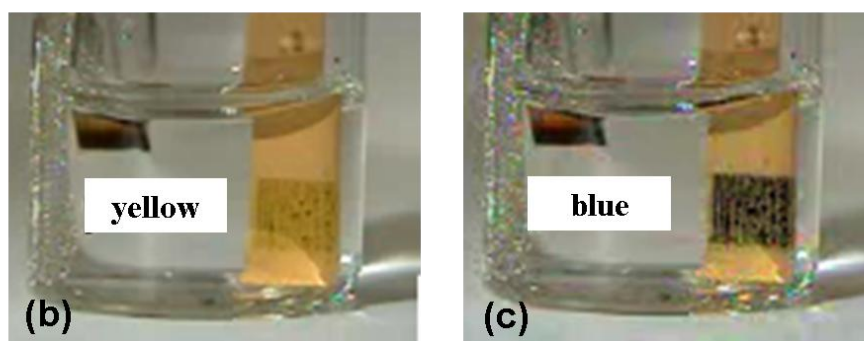
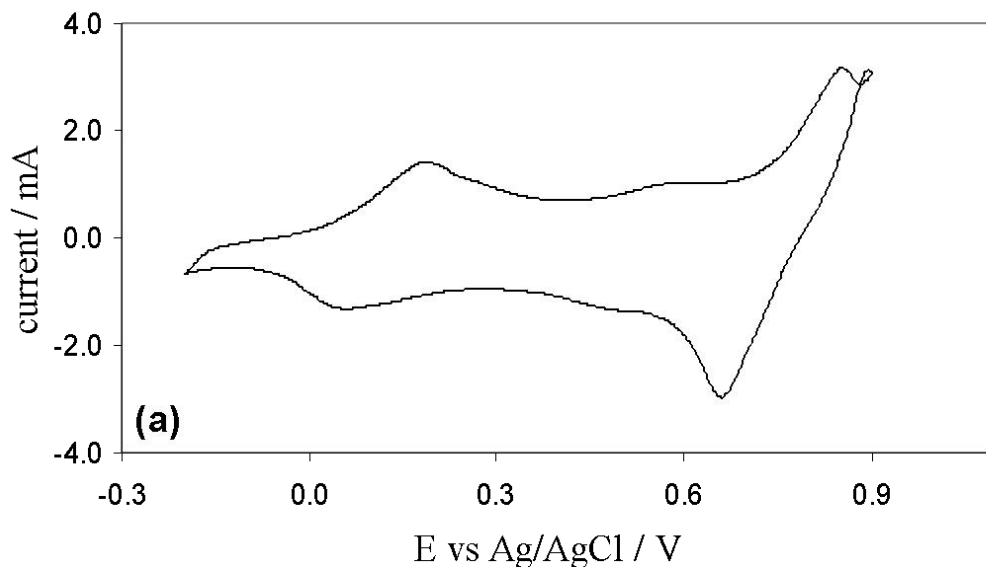


Figure 5.27 (a) Cyclic voltammogram of a PMAS-PAni-MWNT composite film (3.4 % w/w MWNT) printed on to Au-PVDF. Scan rate 500 mV s^{-1} in 1.0 M HCl. (b) and (c), movie images of the films displaying electrochromic behaviour. Results obtained by Fatemeh Masdarolomoor, University of Wollongong.

5.5 Conclusions

We have used the dispersants gellan gum, PAni and PMAS to formulate CNT containing inks that have successfully been printed onto a range of substrates. This includes the printing of SWNT, which had not previously been achieved. Compared to other work in this field, the examples of CNT films printed here have amongst them very low sheet resistances (for single printed layers), high nanotube loading fractions and very high transparency. With the polysaccharide gellan gum, the effects of pH and

salt concentration were found to be important factors determining the initial stability and quality of the dispersions, due to their interaction with the anionic gellan gum. Inkjet printed CNT films with gellan gum show sensitivity to water vapour, though not to other analytes.⁴⁶ They could potentially be used therefore as humidity sensors. CNT films with PMAS show sensitivity to ethanol and other alcoholic vapours.⁴⁷ Their response depends on the concentration of ethanol, and also the length of time that the film is exposed to ethanol for, which can be controlled by the carrier gas flow rate in dynamic sensing conditions. CNT films with both PMAS and PANi are electroactive, and show electrochromic behaviour if the CNT loading fraction in the films is not too high. Furthermore, the PMAS-Pani-MWNT films have the lowest reported sheet resistance to date for an inkjet printed CNT film (to the best of the authors knowledge).⁴⁸

5.6 References

- 1 Tekin, E., Smith, P. J. and Schubert, U. S., *Soft Matter*, 2008, **4**, 703.
- 2 Calvert, P., *Chem. Mater.*, 2001, **13**, 3299.
- 3 Fromm, J. E., *IBM J. Res. Dev.*, 1984, **28**, 322.
- 4 Reis, N., Ainsley, C. and Derby, B., *J. Appl. Phys.*, 2005, **97**, 094903.
- 5 de Gans, B. -J., Kazancioglu, E., Meyer, W. and Schubert, U. S., *Macromol. Rapid Commun.*, 2004, **25**, 292.
- 6 Hohnholz, D. and MacDiarmid, A. G., *Synth. Met.*, 2001, **121**, 1327.
- 7 Sirringhaus, H., Kawase, T., Friend, R. H., Shimoda, T., Inbasekaran, M., Wu, W. and Woo, E. P., *Science*, 2000, **290**, 2123.
- 8 Sele, C. W., von Werne, T., Friend, R. H. and Sirringhaus, H., *Adv. Mater.*, 2005, **17**, 997.
- 9 Liu, Y., Varahramyan, K. and Cui, T., *Macromol. Rapid Commun.*, 2005, **26**, 1955.
- 10 Yoshioka, Y. and Jabbour, G. E., *Adv. Mater.*, 2006, **18**, 1307.
- 11 Xia, Y. and Friend, R. H., *Macromolecules*, 2005, **38**, 6466.
- 12 Yoshioka, Y. and Jabbour, G. E., *Synth. Met.*, 2006, **156**, 779.
- 13 Möller, M., Asaftei, S., Corr, D., Ryan, M. and Walder, L., *Adv. Mater.*, 2004, **16**, 1558.
- 14 Shim, G. H., Han, M. G., Sharp-Norton, J. C., Creager, S. E. and Foulger, S. H., *Soft Matter*, 2008, **18**, 594.
- 15 Mabrook, M. F., Pearson, C. and Petty, M. C., *IEEE Sens. J.*, 2006, **6**, 1435.
- 16 Li, B., Santhanam, S., Schultz, L., Jeffries-EL, M., Iovu, M. C., Sauvé, G., Cooper, J., Zhang, R., Revelli, J. C., Kusne, A. G., Snyder, J. L., Kowalewski, T., Weiss, L. E., McCullough, R. D., Fedder, G. K. and Lambeth, D. N., *Sensor. Acuat. B-Chem*, 2007, **123**, 651.
- 17 Tekin, E., Smith, P. J., Hoepfener, S., van den Berg, A. M. J., Susa, A. S., Rogach, A. L., Feldmann, J. and Schubert, U. S., *Adv. Funct. Mater.*, 2007, **17**, 23.
- 18 Hong, C. M., Gleskova, H. and Wagner, S., *Mater. Res. Soc. Symp. Proc.*, 1997, **471**, 35.
- 19 Redinger, D. R., Molesa, S., Yin, S., Farschi, R. and Subramanian, V., *IEEE Trans. Electron. Devices*, 2004, **51**, 1978.

-
- 20 Perelaer, J., de Gans, B. -J. and Schubert, U. S., *Adv. Mater.*, 2006, **18**, 2101.
- 21 Smith, P. J., Shin, D. -Y., Stringer, J. E., Derby, B. and Reis, N., *J. Mater. Sci.*, 2006, **41**, 4153.
- 22 Lee, K. J., Jun, B. H., Kim, T. H. and Joung, J., *Nanotechnology*, 2006, **17**, 2424.
- 23 Lee, H. -H., Chou, K. -S. and Huang, K. -C., *Nanotechnology*, 2005, **16**, 2436.
- 24 Sumerel, J., Lewis, J., Doraiswamy, A., Deravi, L. F., Sewell, S. L., Gerdon, A. E., Wright, D. W. and Narayan, R. J., *Biotechnol. J.*, 2006, **1**, 976.
- 25 Bietsch, A., Hegner, M., Lang, H. P. and Gerber, C., *Langmuir*, 2004, **20**, 5119.
- 26 Saunders, R. E., Gough, J. E. and Derby, B., *Biomaterials*, 2008, **29**, 193.
- 27 Xu, T., Gregory, C. A., Molnar, P., Cui, X., Jalota, S., Bhaduri, S. B. and Boland, T., *Biomaterials*, 2006, **27**, 3580.
- 28 Kordás, K., Mustonen, T., Tóth, G., Jantunen, H., Lajunen, M., Soldano, C., Talapatra, S., Kar, S., Vajtai, R. and Ajayan, P. M., *Small*, 2006, **2**, 1021.
- 29 www.Isbu.ac.uk, checked 25th April 2009.
- 30 Jansson, P. E., Lindberg, B. and Sandford, P. A., *Carb. Res.*, 1983, **124**, 135.
- 31 Ogawa, E., Matsuzawa, H. and Iwahashi, M., *Food Hydrocoll.*, 2002, **16**, 1.
- 32 Hamcerencu, M., Desbrieres, J., Khoukh, A., Popa, M. and Riess, G., *Carbo. Polymer*, 2008, **71**, 92.
- 33 Nicolosi, V., Cathcart, H., Dalton, A. R., Aherne, D., Dieckmann, G. R. and Coleman, J. N., *Biomacromolecules*, 2008, **9**, 598.
- 34 Sun, Z., Nicolosi, Z., Rickard, D., Bergin, S. D., Aherne, D. and Coleman, J. N., *J. Phys. Chem. C.*, 2009, **112**, 10692.
- 35 Moritaka, H., Nishinari, K., Taki, M. and Fukuba, H., *J. Agric. Food Chem.*, 1995, **43**, 1685.
- 36 Horinaka, J., Kani, K., Hori, Y. and Maeda, S., *Biophys. Chem.*, 2004, **111**, 273.
- 37 Sainz, R., Benito, A. M., Martínez, M. T., Galindo, J. F., Sotres, J., Baró, A. M., Corraze, B., Chauvet, O., Dalton, A. B., Baughman, R. H. and Maser, W. K., *Nanotechnology*, 2005, **16**, S150.
- 38 O'Connell, M. J., Bachilo, S. M., Huffman, C. B., Moore, V. C., Strano, M. S., Haroz, E. H., Rialon, K. L., Boul, P. J., Noon, W. H., Kittrell, C., Ma, J., Hauge, R. H., Weisman, R. B. and Smalley, R. E., *Science*, 2002, **297**, 593.

-
- 39 Chambers, G., Carroll, C., Farrell, G. F., Dalton, A. B., McNamara, M., in het Panhuis, M. and Byrne, H. J., *Nano Lett.*, 2003, **3**, 843.
- 40 Chambers, G., Carroll, C., Farrell, G. F., Dalton, A. B., McNamara, M., in het Panhuis, M. and Byrne, H. J., *Nano Lett.*, 2003, **3**, 843.
- 41 Bissell, R. A., Persaud, K. C. and Travers, P., *Phys. Chem. Chem. Phys.*, 2004, **4**, 3482.
- 42 Someya, T., Small, J., Kim, P., Nuckolls, C. and Yardley, J. T., *Nano Lett.*, 2003, **3**, 877.
- 43 Jettable Fluids Formulation Guidelines, www.Dimatix.com, checked 25th April 2009.
- 44 Xue, H. S., Fan, J. R., Hu, Y. C., Hong, R. H. and Cen, K. F., *J. Appl. Phys.*, 2006, **100**, 104909.
- 45 Masdarolomoor, F. M., Innis, P. C., Ashraf, S., Kaner, R. B. and Wallace, G. G., *Macromol. Rapid. Commun.*, 2006, **27**, 1995.
- 46 in het Panhuis, M., Heurtematte, A., Small, W. R. and Paunov, V. N., *Soft Matter*, 2007, **3**, 840.
- 47 Small, W. R. and in het Panhuis, M., *Small*, 2007, **3**, 1500.
- 48 Small, W. R., Masdarolomoor, F., Wallace, G. G. and in het Panhuis, M., *J. Mater. Chem.*, 2007, **17**, 4359.

CHAPTER 6

ELECTRICALLY ANISOTROPIC GELS AND ORGANISED ASSEMBLIES FORMED BY ARRESTED DIELECTROPHORETIC ASSEMBLY

6.1 Introduction

This chapter describes a general method to produce new structures formed through dielectrophoretic assembly, without the need for functionalising either the substrate or the building blocks. This is achieved by performing dielectrophoresis (DEP) of the building blocks in a solution of a gelling agent above the gelling temperature, and then cooling to gel the solution after the assembly has been achieved and with the field still applied. The cooled gel entraps the assembled structure, preventing its disassembly and allowing further analysis without the presence of the external electric field. In the example demonstrated here, assembling silver nanowires (Ag NWs) into microwires through DEP in agarose gel, the resulting composite gels display anisotropic electrical properties. The building blocks can also be functionalised for sensing applications. We have also adapted this same technique for the fabrication of yeast cell ‘strings’ - linear chains of living yeast cells attached to one another. This was achieved without using any templates.

6.1.1 Theory of dielectrophoresis

While electrophoresis is the motion of charged particles in uniform electric fields, DEP is the migration of matter in *non-uniform* electric fields. This effect was first reported by Pohl in 1951, who observed the “relative motion of suspensoid and medium resulting from polarization forces produced by an inhomogeneous electric field”.¹ Recently, DEP has received considerable attention as it is being recognised as a technique that may be suitable for the manipulation and organisation of objects with sub-micrometre dimensions.

In Figure 6.1, we illustrate the dielectrophoretic force that a spherical particle might experience in a uniform and a non-uniform electric field.

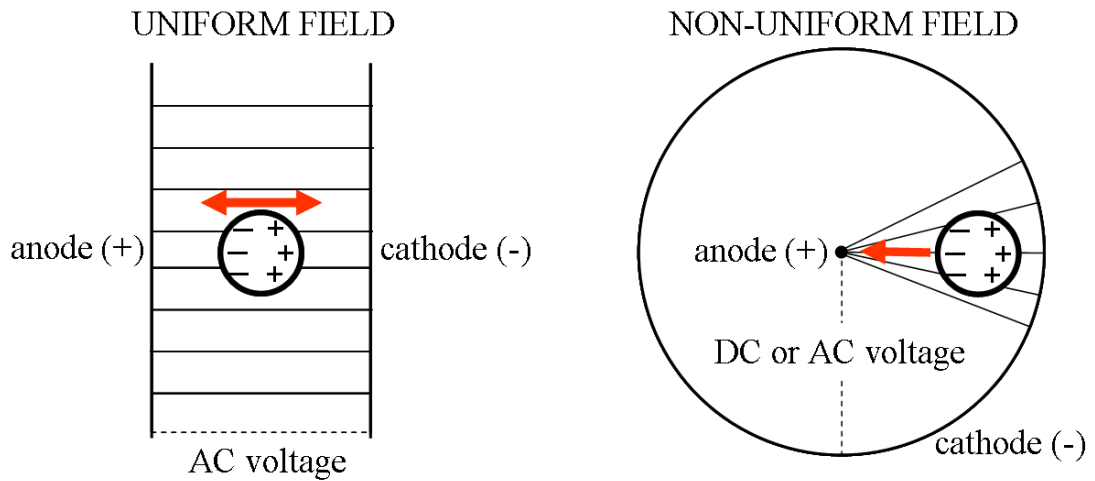


Figure 6.1 Diagram of forces acting on a spherical particle in a uniform and a non-uniform electric field. Red arrow indicates direction of particle motion.

A particle placed in an electric field will undergo polarisation, with the positive and negative electric charges of the particle separating and collecting towards the negative and positive electric fields, respectively. If the field is uniform and the particle has zero net charge, then it can be expected that the particle would be attracted equally to both electrodes. This would result in no net movement of the particle towards either electrode. If the field is non-uniform however, as shown in Figure 6.1, then one end of the dipole will be in a weaker field than the other end.² A net force will then result, pulling the particle towards the region of highest field intensity. It is also possible to use AC as well as DC voltages, as switching the polarity of the electrodes will merely result in a reversing of the particle dipole - the strong and weak regions of the field will remain and thus motion of the particle will continue, rather than move towards the other electrode. This is advantageous, as DEP can require quite large voltages that, if were applied as a DC voltage, could lead to undesired electrophoresis and electrolysis in aqueous dispersions.

The dielectrophoretic force F_{DEP} exerted on a particle with a dipole moment p in a non-uniform electric field E is given by

$$F_{DEP} = p\nabla E \quad [6.1]$$

where ∇ (nabla) is the gradient vector operator, a term signifying that a force is only exerted when the field is non-uniform. In an AC field, the time averaged dielectrophoretic force on a particle is given by³

$$F_{DEP} = \Gamma \varepsilon_m \operatorname{Re}\{K_f\} \nabla |E|^2 \quad [6.2]$$

where Γ is a factor depending on the geometry of the particle, ε_m is the permittivity of the medium and $\operatorname{Re}\{K_f\}$ is the effective polarisability of the particle. In the case of a rod or a cylinder with radius r and length l , the geometrical factor Γ is given as

$$\Gamma = \frac{\pi}{6} r^2 l \quad [6.3]$$

The factor K_f depends on the complex permittivities of the particle ε_p^* and the medium ε_m^*

$$K_f = \frac{\varepsilon_p^* - \varepsilon_m^*}{\varepsilon_m^*} \quad [6.4]$$

where the complex permittivities are calculated from

$$\varepsilon_p^* = \varepsilon_p - i \frac{\sigma_p}{\omega} \quad \varepsilon_m^* = \varepsilon_m - i \frac{\sigma_m}{\omega} \quad [6.5]$$

The complex permittivities take into account the permittivities of the particle ε_p and the medium ε_m , the conductivities of the particle σ_p and the medium σ_m , the

imaginary number i ($-1^{0.5}$) and the angular frequency of the applied electric field ω . The angular frequency is calculated from

$$\omega = 2\pi f \quad [6.6]$$

where f is the frequency of the electric field. Combining these equations, the dielectrophoretic force experienced by a rod or cylinder in a non-uniform electric field is given by

$$F_{DEP} = \frac{\pi}{6} r^2 l \epsilon_m \operatorname{Re} \left(\frac{\epsilon_p^* - \epsilon_m^*}{\epsilon_m^*} \right) \nabla |E|^2 \quad [6.7]$$

The equations show that the dielectrophoretic force depends upon many factors, of which the permittivities of the medium and the particle and the frequency of the field are particularly noteworthy. We can see that the effective polarisability of the particle is dependant upon both of these factors, and can be a positive or negative term depending on the relative magnitudes of these parameters. When the term is positive, we refer to the force acting on the particle as being a *positive* dielectrophoretic force. This occurs when the permittivity of the particle is greater than that of the surrounding medium, and results in motion of the particles towards the regions of high field strength.⁴ When the effective polarisability is negative however, we refer to the force acting on the particle as being a *negative* dielectrophoretic force. This occurs when the permittivity of the surrounding medium is greater than that of the particle, and results in motion of the particles towards the regions of low field strength. Both positive and negative DEP have many practical applications, which will be discussed in more detail in the next section.

6.1.2 Practical applications of dielectrophoresis

As DEP does not require that the building blocks possess any specific property or attribute, it has proved to be a very versatile technique suited to different materials and different purposes. For example, one of the most widely used applications that employs DEP exploits the *negative* dielectrophoretic force, where particles move away from regions of high field strength. This application is known as dielectrophoretic-field-flow-fractionation, a technique used for the sorting and separating of cells.⁵ In this

process, a mixture of different cells are introduced to a long, thin chamber that is lined with electrodes. As an electric field is applied to the electrodes, the cells will experience different negative dielectrophoretic forces, which give them varying displacements from the walls of the chamber. A flow is then established through the chamber, with the cells nearest the chamber walls being eluted slower than the cells towards the centre of the chamber. The cells are thus separated, and can then be collected and counted or further analysed.

There are of course many applications of DEP that utilise the *positive* dielectrophoretic force, where objects are brought closer together for their assembly. This is known as a 'bottom up' approach for fabricating nanostructures. In one important study, Hermanson and co-workers report the dielectrophoretic fabrication of electrically conducting microwires from nanoparticle suspensions.⁶ They evaluate the effects of voltage, frequency, particle size and concentration on the branching, thickness and growth rate of colloidal suspensions of gold nanoparticles assembled into microwires. Barsotti and co-workers also studied the assembly of gold nanoparticles into organised structures between electrodes, showing through theory and experiment that the assembly is dependant upon the applied voltage and electrode gap size.⁷ Other reports on the dielectrophoretic assembly of gold nanoparticles and nanorods study the morphology of the assemblies,⁸ the effects that limit the conductance of the assemblies⁹ and the how the diameter of the formed microwires can be tuned.¹⁰

Other building blocks to be assembled using DEP include silicon nanowires, with Wissner-Gross reporting the disassembly and reconfiguration of silicon interconnects between gold electrodes.¹¹ There are several reports on the dielectrophoretic assembly of CNTs, including a study by Tang and co-workers who show that an aqueous dispersion of SWNTs can be organised into sub-micrometre fibrils.¹² This work was later adapted for the production of SWNT tips for atomic force microscopes, with the authors fabricating tips of controlled diameter and length which they show are particularly well suited for imaging structures with high aspect ratios.¹³ Hydrogen sensors based on dielectrophoretically assembled CNTs have been reported by Suehiro and co-workers. They combine CNTs with either palladium electrodes or nanoparticles in their sensors, which can detect 0.05 % H₂ in air at 90 °C.¹⁴ Papadakis and co-workers have also reported the fabrication of networks and vertically aligned arrays of silver nanowires organised through DEP.¹⁵ They suggest that the solvent, and

field strength and frequency are important parameters which determine the types of assembly obtained.

One application in particular where DEP may provide a useful tool is in the fabrication of anisotropic materials. Materials that possess anisotropic conductivity are expected to find practical applications in fields such as sensing, touch-sensitive displays and conducting adhesives.^{16, 17} A good strategy to achieve such electrical anisotropy within insulating materials is the manipulation and controlled assembly of conducting nanowires and microwires. Several approaches exist to produce such materials, including magnetic¹⁸⁻²⁰ and optical²¹ methods of aligning and organising conducting fillers in an insulating matrix. It would seem though that DEP, where no special property (such as magnetism) of the building blocks is required, is also ideally suited for the production of anisotropic conducting materials.

DEP is however in many cases only a method for temporary assembling of structures, as the dielectrophoretic force which causes the particles to aggregate is lost when the field is switched off. The building blocks may then undergo Brownian motion, electrostatic repulsion or gravity induced sedimentation, depending on the properties of the nanoparticles involved, resulting in disassembly of the structures. Several methods have been proposed to facilitate the preservation of these structures formed by DEP. One such method is reported by Shang and co-workers, who use chemical functionalisation to achieve permanent assemblies.²² They functionalise their electrodes with biotin and then wash with avidin which has multiple binding sites for the biotin molecules. The gold nanorods that they assemble are also functionalised with biotin, and when DEP is performed the rods are pulled into position between the electrodes, with the avidin bound to the substrates also binding to the biotin on the gold rods. This locks the assemblies in place, even when the field is removed. Alternatively, Papadakis and co-workers have reported that the solvent in which the building blocks are dispersed can influence the nature of their assembly.¹⁵ They show that when silver nanowires are dispersed in water, the assemblies break up on removal of the field, but when they are dispersed in ethanol the structures remain. They attribute these findings to the change of solvent affecting the electrostatic, van der Waals and surface tension forces which ultimately determine the adhesion between the nanowires and the substrate. Another route to permanent assemblies of dielectrophoretically assembled structures is presented by Snoswell and co-workers, who fabricate strings of colloidal latex and microgel

particles.²³ These assemblies remain intact due to the use of oppositely charged particles, which are held together through attractive forces.

These methods, although undoubtedly resulting in the fixation of dielectrophoretically assembled structures, do not constitute a generic method for DEP induced assembly. For example, not all particles can be functionalised with biotin or other binding agents, nor will they experience the same adhesive forces when dispersed in ethanol as do silver nanowires. In addition, the use of oppositely charged colloidal particles is suitable only for the fabrication of strings of oppositely charged colloidal particles. There remains therefore no general method to arrest the structures formed through dielectrophoretic assembly, which does not rely on any specific property of the building block, solvent or substrate. This is the issue that we will address in this chapter.

6.1.3 Agarose gel

Agarose is a linear, non-ionic polysaccharide derived from seaweed, consisting of repeat units of agarobiose which itself is a disaccharide based on alternating units of 1,3-linked β -D-galactopyranose and 1,4-linked 3,6-anhydro- α -L-galactopyranose (Figure 6.2).

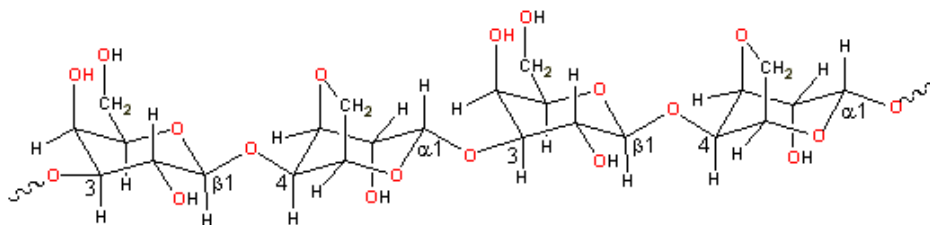


Figure 6.2 Repeating structure of agarose gel, showing two agarobiose units. Image reproduced from reference 24.

Agarose is insoluble in cold water, but readily becomes hydrated in hot water to form random coils. When the solution is cooled down, the agarose chains aggregate together to form double helices, which then further aggregate into a three dimensional network. These double helices and aggregated networks are formed through hydrogen bonding and the hydrophobic interaction, trapping water molecules inside the double helical cavity.²⁵

Agarose has widespread use in the food industry, providing thickening and gelling properties in products such as marshmallows and processed cheese. Perhaps its

most common application though is as a separation medium in agarose gel electrophoresis. This is a technique employed for the separation of proteins and DNA molecules from a mixture, allowing them to be collected and analysed further. Briefly, the process involves moulding a rectangular block of agarose gel, into which small reservoirs are cut at one end. These reservoirs are filled with a DNA sample, and two electrodes are inserted at either end of the gel, with the cathode placed just behind the reservoirs. A DC voltage is then applied, resulting in the migration of the negatively charged DNA molecules through the gel towards the anode. After a pre-determined time, the DC field is switched off, which halts the migration of DNA through the gel, and the sample can then be stained with a dye (such as ethidium bromide) to visualise the specific locations of the DNA. Larger molecules (DNA, proteins) or those with smaller charge will migrate through the gel slower, and thus not as far in the same time, as smaller molecules or those with higher charge. The agarose therefore acts as a molecular sieve, separating the different DNA molecules from each other. The agarose pore size, field strength and length of time that the field is applied for can all influence the migration of DNA through the agarose.

6.2 The effects of an electric field on the gelling transition of agarose

Before attempting the dielectrophoretic assembly of nano-structures within a gel, it was first necessary to determine the effects that an electric field may have on the gelling of agarose solution. It was envisaged that the presence of an AC electric field may induce some alignment of the agarose molecules between the electrodes, perhaps leading to optical anisotropy in the formed gel. This in itself may be an interesting development, but for the purposes of assembling nano-structures, any anisotropy induced in the gel may also be lost on removal of the field, which may contribute to disassembly of any structures formed within the gel. In addition, any change in the way that the agarose molecules interact with each other may have an effect on the gelling point, possibly shifting the temperature at which the system gels either to higher or lower temperature. This would be important to know, particularly if the gelling temperature of agarose were to be shifted to lower temperature, as removing the field before the gel had set might also result in breaking of the assembled structures.

6.2.1 Strategy for measuring the effect of an AC field on agarose gelation

The progress of agarose gelation can be monitored through UV-vis spectroscopy, as clear changes are observed in the spectra of the gel at high and low temperatures (Figure 6.3).

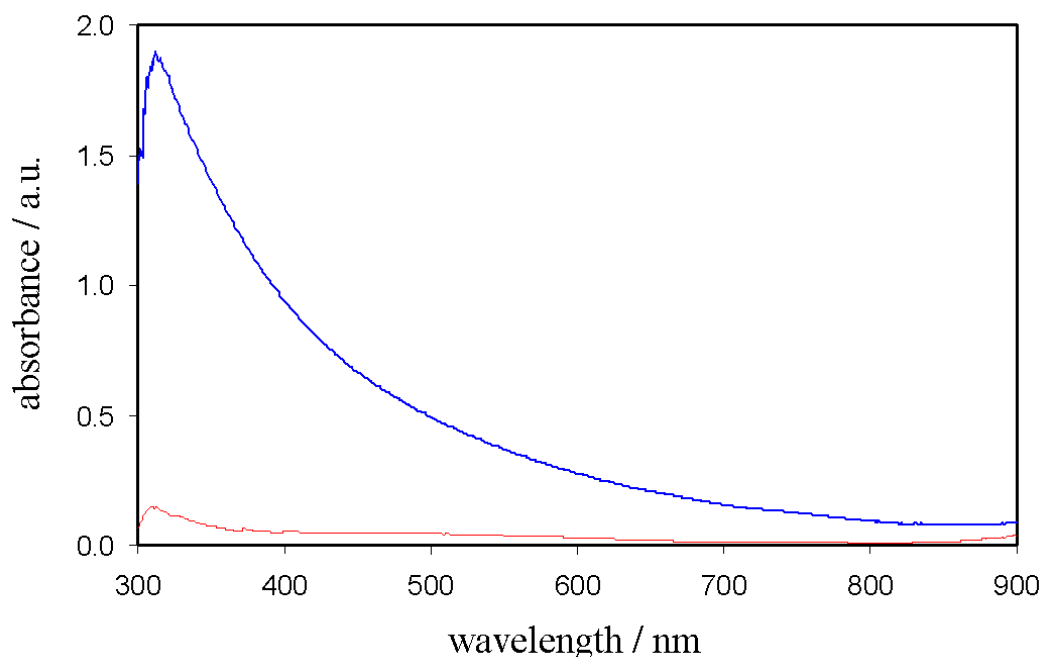


Figure 6.3 UV-vis absorbance spectra of agarose solution at a concentration of 2.0 % w/v at 60 °C (red line), where the solution is still liquid, and 20 °C (blue line), after gelling.

At 60 °C, when the agarose is in a sol state, the UV-vis spectrum reveals few features (red line). On cooling however, there is a gradual increase in the turbidity of the gel until the gel is fully set, giving the spectrum shown in Figure 6.3 at 20 °C (blue line). The rise in the turbidity of the gel has been examined by other groups and has been attributed to the pores within the gel, and the absorbance can be used to give an estimate of the size of the pores within the gel.²⁶

In order to monitor the absorbance while an electric field is applied to the agarose solution, we customised a quartz cuvette with ITO electrodes, shown in Figure 6.4. The electrodes were placed with their ITO coated sides facing towards each other, through the cuvette, and were separated with two small PDMS spacers to maintain the electrode spacing. The cell was fitted with either two or four (in a quartz cell with four

clear walls) ITO electrodes, depending on the property of the gel that was being measured. A thermocouple was positioned in the gel, for accurate temperature measurements during the cooling.

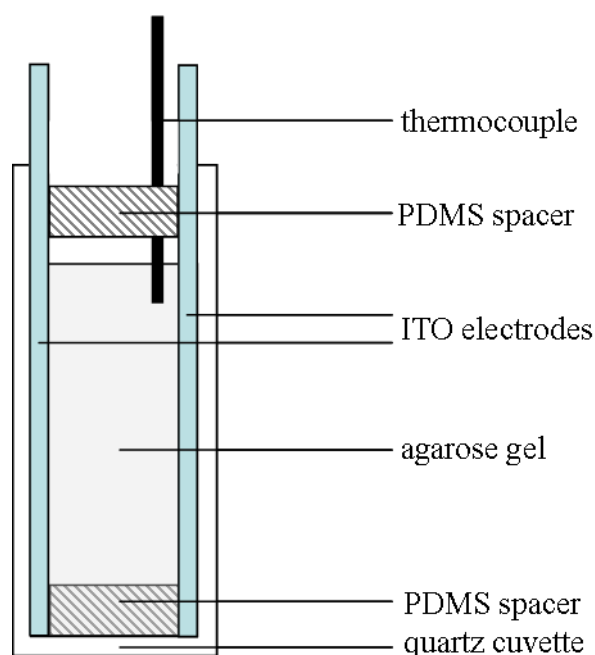


Figure 6.4 Diagram of the cell used for studying the effects of an AC field applied to agarose solution as it cools, through UV-vis spectroscopy.

6.2.2 Effect of an AC field on the gelation of agarose solutions

The effect of an applied electric field on the optical properties of the agarose gel was examined, heating the agarose to 60 °C where it is in a sol state, applying the field and then cooling in the presence of the field to 20 °C. The spectra of the gel measured parallel and perpendicular (at 90 °) to the applied field were then recorded when the gel had reached a temperature of 20 °C (Figure 6.5).

With the field applied to the gel, it appears that the absorbance measured parallel with the direction of the field is slightly higher than the absorbance measured perpendicular to the direction of the field (Figure 6.5). One hour after the removal of the field from the gel however, the absorbances have increased, but are now similar when measured in each direction. This might suggest that the field does have some influence over the gelling behaviour of agarose, perhaps even resulting in some optical anisotropy, but that any anisotropy or structure caused by the field then relaxes to an isotropic state when the field is removed.

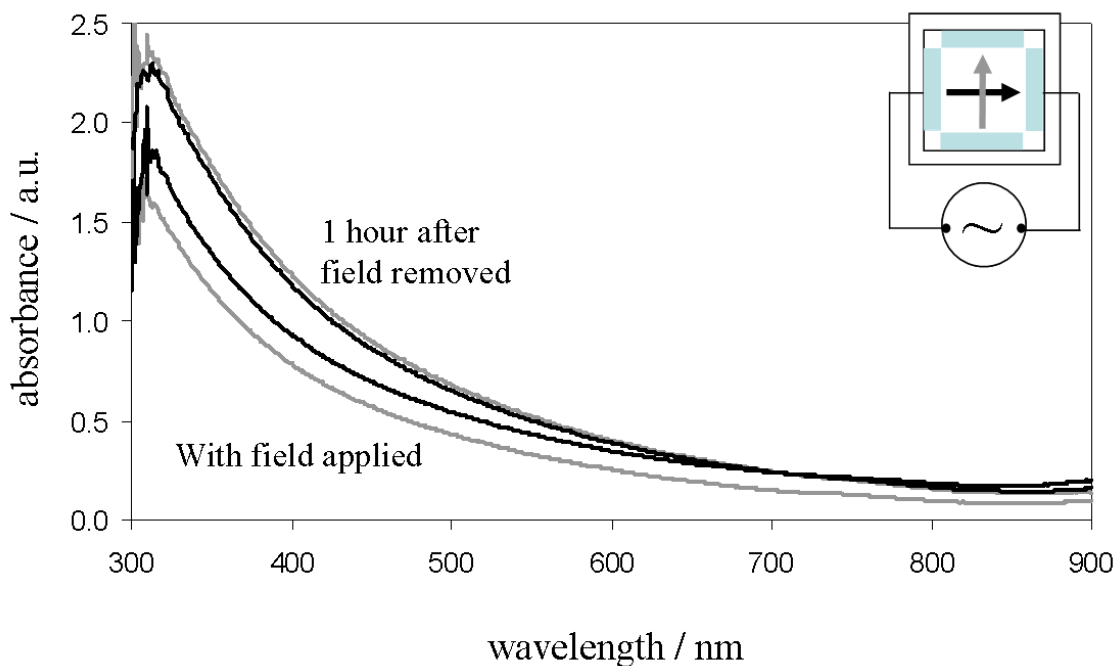


Figure 6.5 UV-vis absorbance spectra of agarose solution (at a concentration of 2.0 % w/v) at 20 °C. Spectra measured parallel (black lines) and perpendicular (grey lines) to the direction of the applied field (5 kHz, 500 V cm⁻¹), and recorded with the field applied, and 1 hour after removal of the field. Inset is a cross section diagram of the cell for clarity.

The gelling transition of agarose gel with and without an applied AC field was also measured through UV-vis spectroscopy, by plotting the absorbance at a fixed wavelength as a function of temperature. As there is a rise in the absorbance upon gelling across the whole of the spectrum, the wavelength could conceivably be fixed at any point, but in keeping with the work of Narayanan and co-workers, here we fix the wavelength at 750 nm.²⁶ Figure 6.6 shows such absorbance versus temperature plots for agarose solutions under a cooling rate of 1.0 °C min⁻¹, with and without an applied electric field.

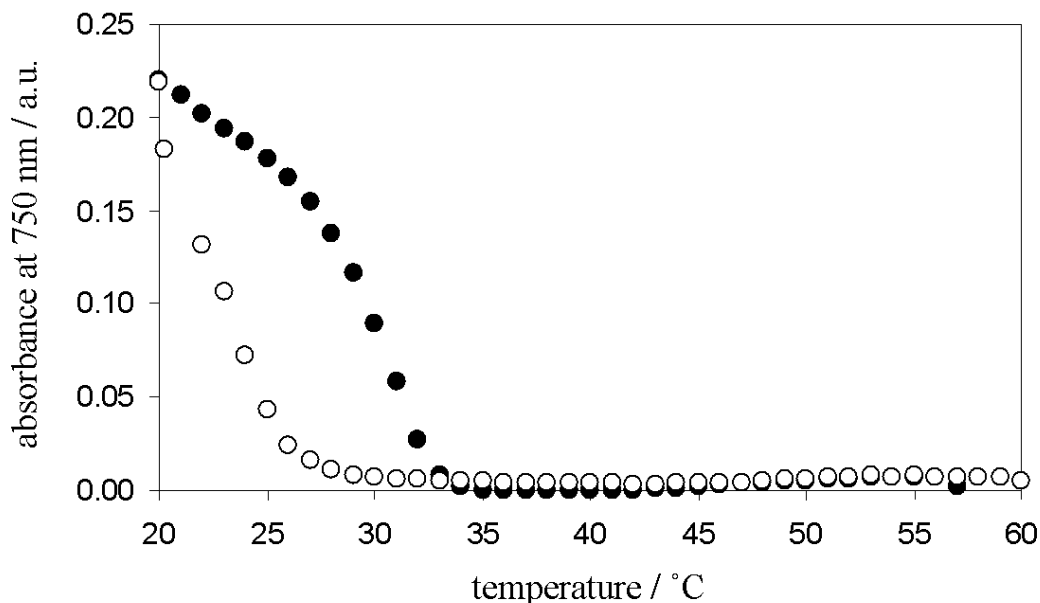


Figure 6.6 Plot showing the absorbance rise of agarose solution (2.0 % w/v) as a function of temperature at a cooling rate of $1.0\text{ }^{\circ}\text{C min}^{-1}$. Plots show cooling transitions without any field applied (filled circles) and with an AC field of 5 kHz and 500 V cm^{-1} (empty circles).

With no field applied to the gel the onset of gelation is observed at approximately $33\text{ }^{\circ}\text{C}$, several degrees lower than the quoted gelling temperature for agarose at this concentration of around $37\text{ }^{\circ}\text{C}$. With an AC field applied, the gelling occurs at significantly lower temperature, with the onset of gelation not observed until approximately $28\text{ }^{\circ}\text{C}$. This might suggest that the presence of an AC field is also having an effect on the gelling temperature of agarose.

To check that this shift on the gelling temperature is not a kinetic effect, the absorbance rise during cooling was re-measured, but at a slower cooling rate. This rate was approximately five times slower than in the initial experiments, cooling the solution by $0.2\text{ }^{\circ}\text{C min}^{-1}$, so that the absorbance could stabilise at each temperature before the temperature was lowered further. The results are shown in Figure 6.7.

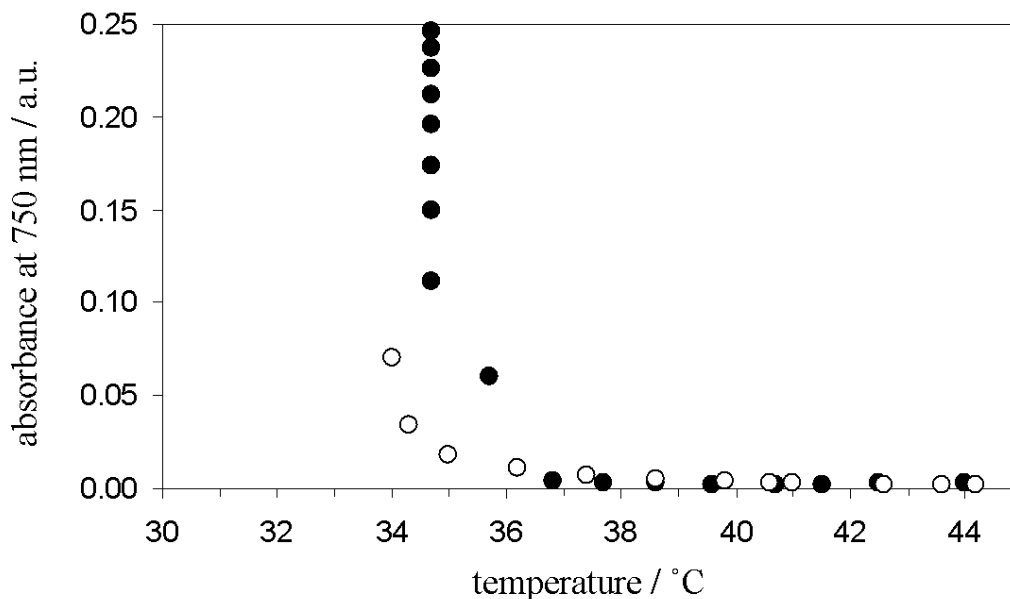


Figure 6.7 Plot showing the absorbance rise of agarose solutions (2.0 % w/v) as a function of temperature under a cooling rate of $0.2 \text{ }^\circ\text{C min}^{-1}$. Plots show cooling transitions without any field applied (filled circles) and with an AC field of 5 kHz and 500 V cm^{-1} (empty circles).

At this slower cooling rate, we do not observe the same shift in the gelling temperature when the field is applied to the solution that was observed at the faster cooling rate. Instead in both cases the absorbance starts to rise, signalling the onset of gelling, at approximately $36 - 37 \text{ }^\circ\text{C}$, which is in the region of the quoted gelling transition for agarose at this concentration. As no real shift in the gelling temperature has been measured, it seems that the presence of an applied electric field is having mainly a kinetic effect on this property of the gel. However, the cooling rate does appear to be an important factor for the observed gelling temperature, as the shift in gelling temperature with no applied field is approximately $3 - 4 \text{ }^\circ\text{C}$, while with the applied field the shift is $8 - 9 \text{ }^\circ\text{C}$ (Figure 6.8).

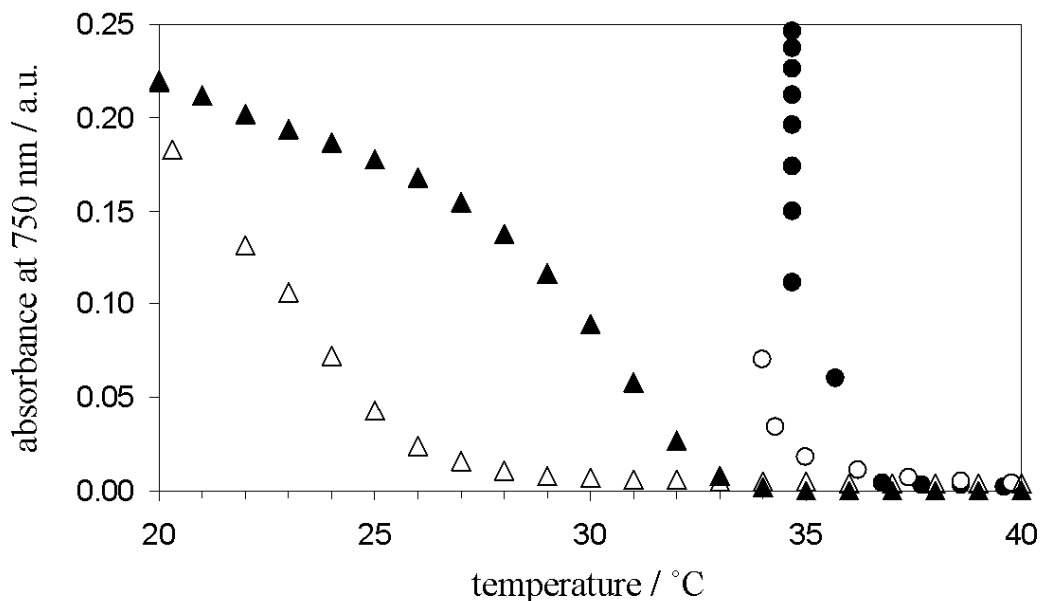


Figure 6.8 Plot showing the onset of gelling for agarose solution (2.0 % w/v) without (filled symbols) and with (empty symbols) the presence of an AC field (5 kHz, 500 V cm^{-1}). Gels cooled at cooling rates of 1.0 °C min^{-1} (triangles) and 0.2 °C min^{-1} (circles).

From Figure 6.8 we can see that, although it appears to be the cooling rate that is influencing the observed shift in the gelling temperature of agarose, the presence of the field results in a more pronounced shift.

6.3 Dielectrophoretic assembly and encapsulation of nanoparticles in a solution

Here we demonstrate a novel technique to ‘arrest’ the structures formed through DEP, which requires no chemical functionalisation of either the building blocks or the substrate. We achieve this by performing the dielectrophoretic assembly in an agarose solution above the gelling temperature, and then cooling the solution in the presence of the field. This results in the gel setting around the formed structures, physically preventing them from breaking apart under gravity or through Brownian motion. We demonstrate this novel technique by assembling microwires from Ag NWs, with diameters from 50 – 200 nm and lengths of 40 – 50 μm , in agarose gel.

6.3.1 New strategy for carrying out dielectrophoretic assembly in a gelling solution

Figure 6.9 depicts the novel method that we have developed for the dielectrophoretic assembly of Ag NWs, and their subsequent entrapment within an agarose gel.

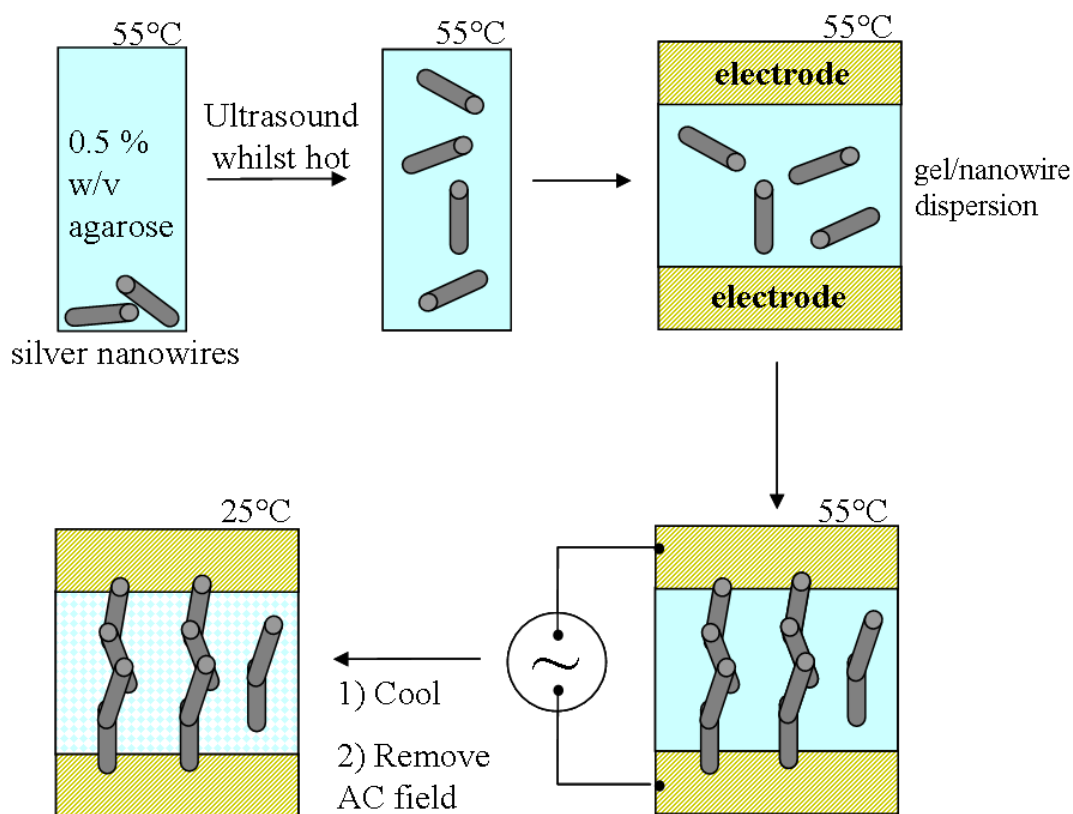


Figure 6.9 Schematic of the preparation of anisotropic agarose gels by dielectrophoretic assembly and encapsulation of Ag NWs.

First we disperse the building blocks, which in this case are Ag NWs, in a hot agarose solution using ultrasound. After degassing in an ultrasonic bath, the dispersion was quickly returned to a hot plate where it is kept warm to prevent the sample from gelling. The experimental cell (specially constructed for DEP, and discussed in more detail later) is placed on a microscope heating stage, and warmed to 55 °C. Several drops of the hot dispersion are then placed on the cell between the electrodes, and covered with a warmed glass cover slip. An AC field is then passed between the two electrodes, resulting in the dielectrophoretic assembly of the NWs into an organised structure. In the presence of the field, the gel is then cooled so that it sets around the

structures, until the temperature of the system is well below that of the agarose gelling transition. At this point, the electric field can then be removed without the organised structures disassembling due to Brownian motion.

The dielectrophoretic assembly cell consisted of a glass microscope slide, to which four copper electrodes were adhered. To study the electrical anisotropy of the gels, the electrodes were positioned on the cell as shown in Figure 6.10. These four electrodes have been labelled A-A and B-B, with the pairs sat opposite and at 90° to each other.

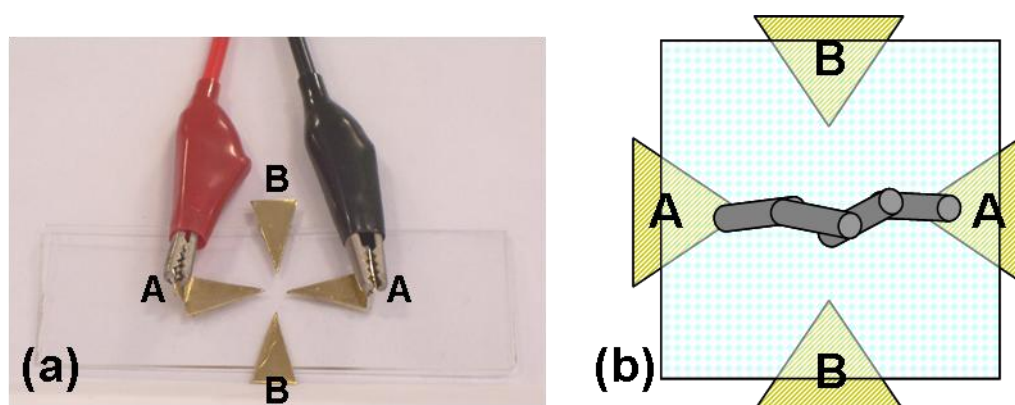


Figure 6.10 (a) Photograph of the experimental cell constructed for dielectrophoresis, with the electrodes labelled into pairs A-A (through which the AC field is applied) and B-B. (b) Schematic of the envisaged preferential assembly between the electrodes A-A.

In preliminary studies where the four electrodes (A-A and B-B) were spaced equally from each other, it was found that in addition to microwires forming between the electrodes A-A, assemblies were also observed between the electrodes A-B. This supplementary assembly was considered undesirable for studying anisotropy, so to prevent it from happening, the electrodes A-A were positioned closer together. The electrodes are thus not equally spaced, with the A-A spacing (4 mm) shorter than the B-B (9 mm) and A-B spacing (~ 4.5 mm).

6.3.2 *Microwire growth diagram of the dielectrophoretic assembly of Ag NWs in agarose gel*

The dielectrophoretic assembly of Ag NWs in agarose solution depends on a number of parameters. These are the temperature of the cell, the concentrations of agarose and Ag NWs, the diameter of the NWs, field frequency and voltage, and the length of time that the field is applied for. Here we have kept the temperature at which DEP takes place constant at 55 °C, and used a constant field frequency of 5 kHz. However the voltages that were required for dielectrophoretic assembly were found by varying the voltage, starting at a voltage of 50 V cm⁻¹ and then rising incrementally in steps of 50 V cm⁻¹. At each voltage the sample was studied visually, to assess whether any assembly had taken place, for around one minute before raising the voltage again. When assembly of a microwire between the electrodes was observed, the field was then lowered to 50 V cm⁻¹ while the sample was cooled. This field strength proved strong enough to maintain the microwire and prevent it from undergoing disassembly while the gel was cooled, but it was not sufficiently strong enough so that further assembly or migration of surrounding nanowires towards the microwire took place.

For each of the NW samples with different diameters (50, 100 and 200 nm), we have studied their dielectrophoretic assembly at a range of NW and agarose concentrations. By studying each diameter NW, at concentrations ranging from 0.10 to 1.00 % w/v, in agarose solutions ranging in concentration from 0.50 to 1.25 % w/v, we have been able to construct a microwire growth diagram for the dielectrophoretic assembly of Ag NWs in agarose solution (Figure 6.11). The lowest concentration of agarose that was studied was 0.50 % w/v, as lower concentrations did not yield gels with sufficient mechanical strength to prevent the formed microwires from undergoing disassembly when the field was removed. The observations of the assemblies formed by DEP have been split into three types, shown as different coloured circles in the microwire growth diagram. For some systems, a microwire assembled between the electrodes at a given field strength (shown as a full black circle), while other systems showed partial assembly of an incomplete microwire (shown as a broken black circle). However for some systems, no assembly was observed even at very high, up to 1250 V cm⁻¹, field strengths (shown as a full red circle).

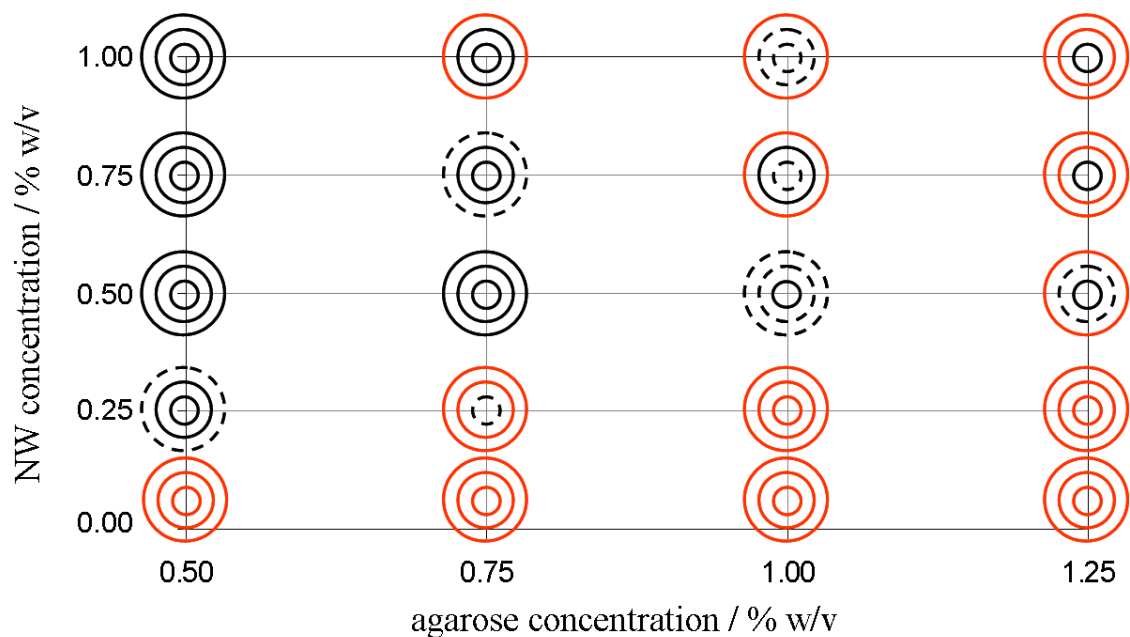


Figure 6.11 Microwire growth diagram for the assembly of Ag NWs in agarose solution at varying field strengths. Small, medium and large circles represent the 50, 100 and 200 nm Ag NWs respectively. Full black lines represent assembly between the electrodes, dashed black lines represent partial assembly, and red lines represent no assembly.

The microwire growth diagram shows that much of the observed assembly of microwires, both complete and incomplete, generally occurs at intermediate concentrations of the agarose and NWs. These concentrations are approximately 0.50 - 1.00 % w/v agarose and 0.50 - 1.00 % w/v Ag NW, though not all combinations of these concentrations resulted in assembly, as shown by this region of assembly being approximately triangular in shape on the diagram. At low concentrations of NWs (≤ 0.25 % w/v), assembly of a microwire is observed only at low concentrations of the agarose (0.50 % w/v). Lowering the NW concentration to 0.10 % w/v or increasing the agarose concentration above 0.50 % w/v results in no assembly being observed. This is attributed to the nanowires not being in sufficient number to reach the percolation threshold under the dielectrophoretic force and form a microwire, particularly when the concentration and viscosity of the agarose is increased.

We can see from the microwire growth diagram that for each concentration of NWs (≥ 0.50 % w/v), as the concentration of the agarose is increased we observe less assembly. Similarly, for each concentration of the agarose (≥ 0.75 % w/v), as the NW

concentration is increased we also start to observe less assembly. The combination of these two observations gives rise to the triangular region of predominantly red circles towards the upper right hand side of the diagram, indicating less assembly at high concentrations of the NW and agarose. The observed fall in assembly when the agarose concentration is increased can be attributed to a rise in the viscosity of the medium, preventing the NWs migrating through the solution to the regions of high field strength, even when large fields are applied. When the concentration of NWs is increased, the observed fall in assembly may also be attributed to an increase in the viscosity, with several groups reporting the increased effective viscosity of suspensions of rod-like particles.^{27, 28} The increased concentration of NWs might however have another, competing effect on the system - their increased number might favour assembly of a microwire due to closer proximity of the NWs. In this case though, it would seem that the effective viscosity increase is the more dominant of the two effects.

These observations have thus far described the general trends in the assembly of Ag NWs in agarose solution, regardless of the diameter of the NWs. Here we will focus on the effects that NW diameter have on the assembly, with regard to the microwire growth diagram in Figure 6.11.

The growth diagram suggests that the assembly of the NWs with the smallest diameter, 50 nm, is more widespread and less affected by NW and agarose concentrations than the larger NWs. For example, even at an agarose concentration of 1.25 % w/v and a NW concentration of 1.00 % w/v, we can see that a complete microwire was formed with the 50 nm NWs, but not for the larger diameter NWs. By fixing the concentration either of the agarose or the NWs and studying the assembly when the concentration of the other is increased, we can see that this is a common trend. For example at a fixed NW concentration of 1.00 % w/v (see the microwire growth diagram) and agarose concentration of 0.50 % w/v, full assembly is observed for each NW diameter. At 0.75 % w/v agarose, no assembly was observed for the 200 nm NWs, while at 1.00 % w/v agarose, only partial assembly was observed for the 50 and 100 nm NWs. Then at 1.25 % w/v agarose, the 50 nm NWs assembled but no assembly was observed for the 100 and 200 nm NWs.

It seems therefore that when considering the prevention of assembly due to a likely viscosity increase caused by either (or both) an increase in agarose or NW concentration, the larger NWs are most affected, while the smaller NWs are least

affected. This might be explained by considering the properties of the system that might be affected by the diameter of the NWs, such as the number of nanowires at a given concentration and their mass. When considering three samples, with different diameter NWs but at the same concentration, then the sample with the wires of 50 nm will contain 4 and 16 times as many NWs as the sample with 100 nm and 200 nm diameter NWs, respectively. So if one of the factors affecting the dielectrophoretic assembly of the nanowires is their number, and perhaps proximity to each other, then this might partly explain the observed assembly of the smaller NWs when larger NWs will not assemble, at the same NW and agarose concentrations. Larger diameter NWs will also have larger volumes, and therefore masses, than those of the smaller diameter NWs. This may increase the sedimentation rate of the larger NWs, resulting in their removal from the area where the dielectrophoretic assembly is taking place.

The microwire growth diagram has revealed that the dielectrophoretic assembly of Ag NWs in agarose solution seems therefore to be affected by a number of competing/contributing factors. These factors are believed to include the viscosity of the system caused by the agarose and the NW concentration, and the number of individual nanowires present in the sample. The results also indicate that the sedimentation of NWs from the sample may play a role in the formation of microwires by DEP. That these different factors might affect the assembly of the microwires to varying extents is reflected in the voltages required for microwire assembly. These ranged from 150 - 700 V cm^{-1} , though there appeared to be no apparent trend, for any diameter NW, of the assembly voltage with either increasing NW or agarose concentration in the system.

6.3.3 *Optical microscopy of dielectrophoretically assembled Ag microwires*

We now look in more detail at the microwires formed through DEP, studying the assemblies formed at agarose and NW concentrations of 0.50 % w/v. Figure 6.12 shows optical microscopy images of the microwires assembled with 50 nm Ag NWs.

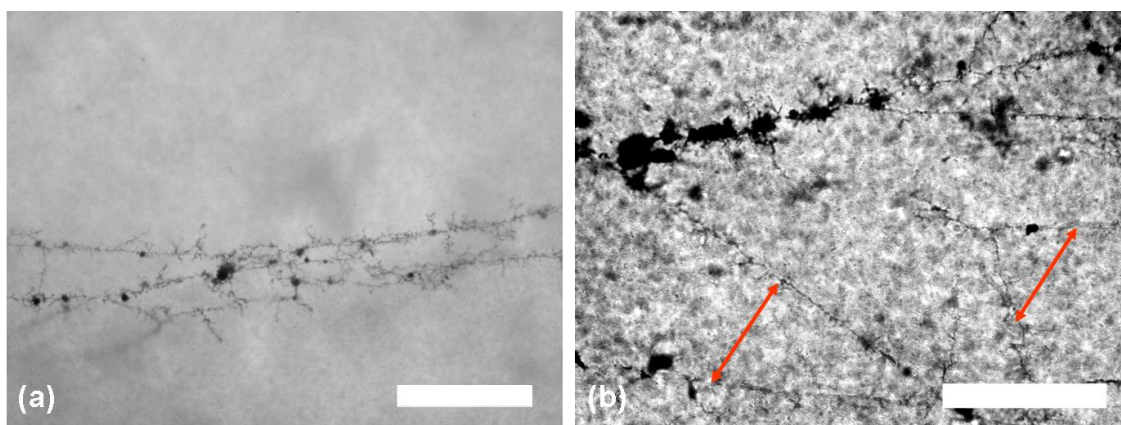


Figure 6.12 Optical microscopy images of dielectrophoretically assembled silver microwires from 50 nm diameter Ag NW (at a concentration of 0.50% w/v) in agarose solution (also at a concentration of 0.50 % w/v). Scale bars represent (a) 200 μm and (b) 100 μm . Red arrows highlight a network of very thin microwires.

The 50 nm diameter NWs assembled to form a single microwire between the electrodes, though significant branching was observed. This gives the microwire assembly the appearance of a ‘web’ (Figure 6.12a), with no central wire present - just an interconnecting network of microwires bridging the inter-electrode gap. The branches appear to stem from large aggregates of NWs, which can be seen in the microscopy images as dense black areas along the microwire. It was not possible to measure the diameter of the microwire accurately, particularly as some regions of the wire appeared to comprise of aggregates of NWs and the wire was therefore not uniform in size. However, visual observations of some sections of the microwires suggested that they were extremely thin in some places, and one goal in the future would be to produce microwires entirely of individual nanowires without the presence of aggregates.

Figure 6.13 shows optical microscopy images of the 100 nm diameter Ag NWs, assembled to form a microwire. In Figure 6.13a, a single microwire between the two electrodes is shown, with this microwire clearly thicker in diameter than that formed by the 50 nm NWs. This microwire does not appear to be branched however, consisting of one single microwire despite the apparent presence of some aggregates of NWs at various points along the assembled wire. Figure 6.13b shows several incomplete microwires between the two electrodes, some of which are connected to one of the electrodes and some which are ‘free-standing’ in the space between the electrodes.

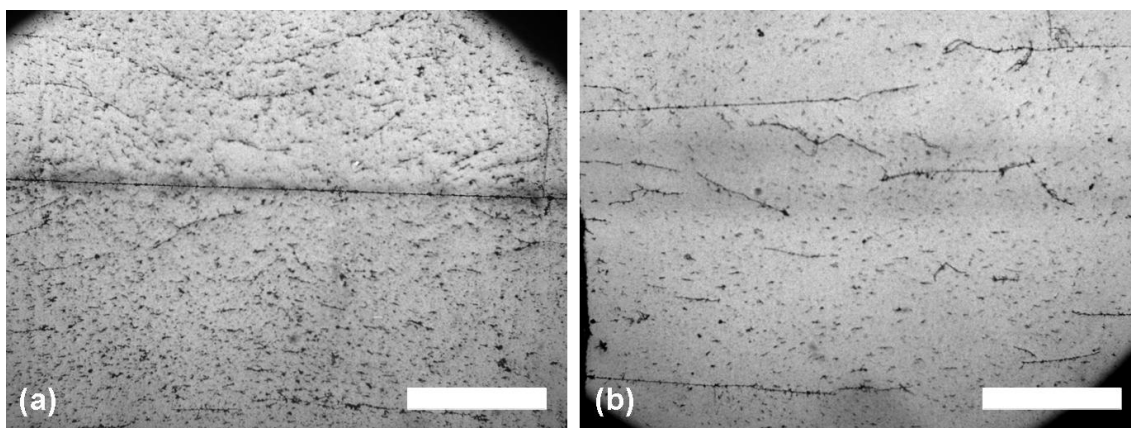


Figure 6.13 Optical microscopy images of dielectrophoretically assembled silver microwires from 100 nm diameter Ag NW (at a concentration of 0.50% w/v) in agarose solution (also at a concentration of 0.50 % w/v). Scale bars represent 1 mm in both images.

Optical microscopy images of the 200 nm diameter Ag NWs are shown in Figure 6.14.

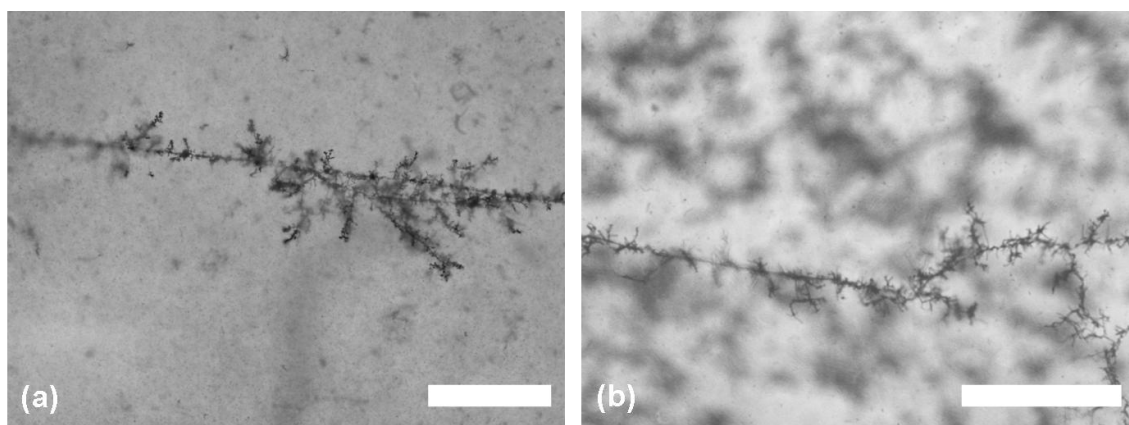


Figure 6.14 Optical microscopy images of dielectrophoretically assembled silver microwires from 200 nm diameter Ag NW (at a concentration of 0.50% w/v) in agarose solution (also at a concentration of 0.50 % w/v). Scale bars represent (a) 200 μm and (b) 100 μm .

The microwire formed by the 200 nm diameter Ag NWs appeared to have characteristics somewhere between those formed by the 50 and 100 nm NWs. The wire

comprised of a single bridging microwire, similar to that observed for the 100 nm NWs, but a degree of branching was also observed similar to that seen for the 50 nm NWs. The branches however did not interconnect to form a ‘web’ of microwires, instead the branches were quite short, not extending more than 300 μm from the main wire.

6.3.4 *Electrical properties of assembled microwires and gels after DEP*

The electrical properties of the gels and assembled microwires were characterised using the electrodes positioned in the cell (labelled A-A and B-B in Figure 6.10). The importance of having these electrodes in the solution before the assembly took place was illustrated by attempts to remove the gel from the cell, which resulted in rupture of the assembled microwire. This also provided us with a very easy way of monitoring the integrity, or structure, of the microwires, by measuring their electrical properties over time. With the formation of a microwire between the two electrodes, we expected to see a drop in the resistance through the gel - if the microwire then broke or became disrupted in any way, then the resistance would be expected to rise again. This method of monitoring the integrity of the structure of the wire is far more sensitive than simple visual evaluation through optical microscopy.

The resistance of the gel without added Ag NWs was of the order $10^6 \Omega \text{ cm}^{-1}$, and even with the addition of NWs, if no dielectrophoretic assembly was performed the resistance remained in this order of magnitude. If dielectrophoretic assembly was performed however, resulting in a microwire being formed between the electrodes A-A, then the resistance of the gel/microwire measured between these electrodes was of the order $10^2 - 10^3 \Omega \text{ cm}^{-1}$. This represents a lowering of the resistance by three to four orders of magnitude, compared to the resistance of the same gel measured through the other electrodes in the sample at 90° (the electrodes B-B). Resistances for the samples with 0.50 % w/v agarose and 0.50 % w/v Ag NWs are summarised in Table 6.1.

NW diameter / nm	$R_{A-A} / \text{k}\Omega \text{ cm}^{-1}$	$R_{B-B} / \text{k}\Omega \text{ cm}^{-1}$
50	4.65 ± 1.15	6470 ± 2490
100	1.15 ± 0.25	4780 ± 575
200	3.15 ± 1.35	6590 ± 1980

Table 6.1 Resistances (per distance between the electrodes) of agarose gels (0.50 % w/v) with Ag NWs (0.50 % w/v) after dielectrophoretic assembly and gelling, measuring through the electrodes A-A (R_{A-A}) and B-B (R_{B-B}).

As the resistances in Table 6.1 show, the formation of a microwire between the electrodes A-A has effectively given the gels anisotropic electrical character, with the resistance of the material lower when measured in this direction than it is when measured at 90° . This is, to our knowledge, the first time gels with anisotropic electrical properties have been fabricated using DEP.²⁹

Interestingly, we did not find any trend in the resistance of the microwire/gel through the electrodes A-A on the diameter of the NWs. The lowest resistances were measured for microwires obtained with 100 nm Ag NWs, which from optical microscopy are believed to be thicker, straighter and less branched than those formed from the 50 and 200 nm NWs. We might expect that if the microwire is formed from only single, individually dispersed NWs with no aggregates or branching, then the resistance should be dependant on the diameter of the NWs, with the lowest resistances obtained for the largest diameter NWs. In these studies so far however, two major factors have been observed that make such a dependence difficult to observe. One factor is that the microwires consist of aggregates of NWs, have variable diameter and contain branches which bridge adjacent microwires. A second factor is that in some cases, supplementary, incomplete microwires have also been formed between the electrodes, which may also contribute to a lowering in the resistance of the gel. In addition, we did not observe an established trend in the microwire resistance on the initial concentration of NWs in the gel.

The majority of the resistance measurements were made using a standard multimeter. To further investigate the properties of the assembled microwires, a current-

voltage (I - V) plot was obtained for the microwire from 50 nm Ag NWs (0.50 % w/v) in agarose gel (0.50 % w/v). This is shown in Figure 6.15.

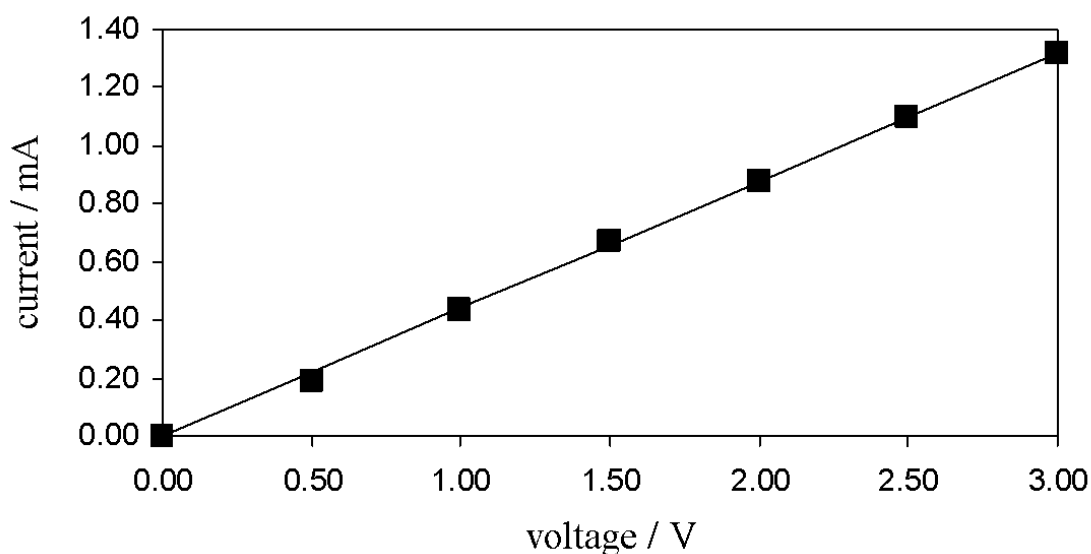


Figure 6.15 Current-voltage characteristics for a microwire from 0.50 % w/v 50 nm Ag NWs in 0.50 % w/v agarose gel.

As the current through the microwire follows a linear trend with increasing voltage, we can conclude that the microwires display simple Ohmic behaviour. From the slope, we measured this particular microwire to have a resistance of $2.27 \text{ k}\Omega \text{ cm}^{-1}$.

To assess the stability of the anisotropic gel and the assembled microwire, we monitored the resistance through the electrodes A-A and B-B periodically over several hours. During this time, the gel was maintained at room conditions, with a temperature of approximately 20 - 25 °C and humidity of 25 - 35 %. The mass of the gel was also measured, and is plotted as a percentage of the initial mass (Figure 6.16)

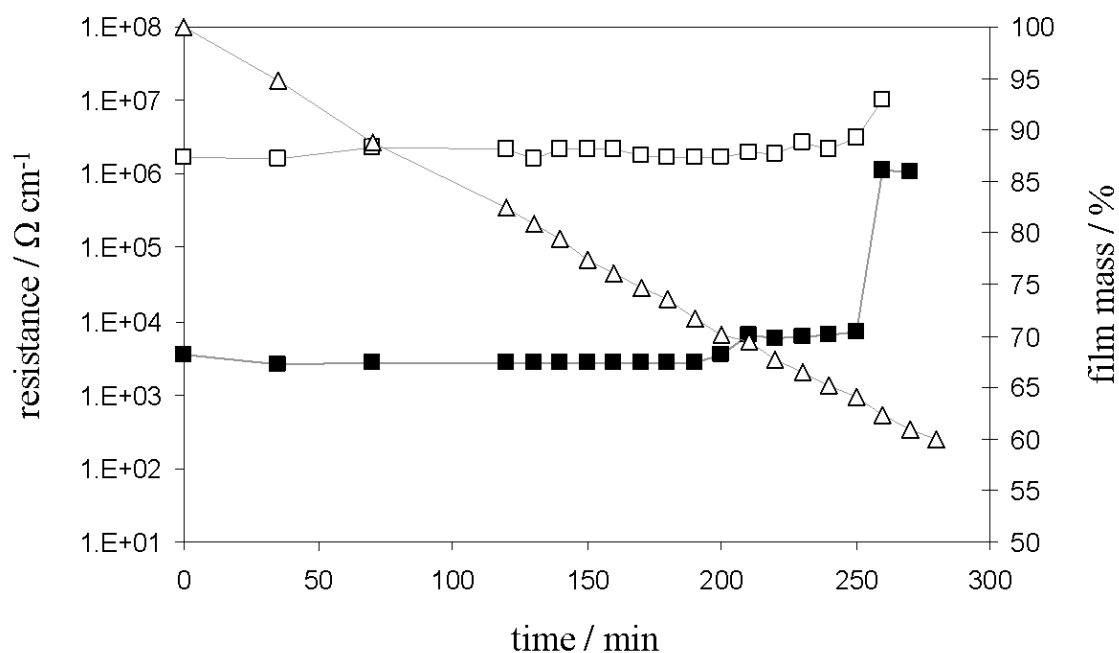


Figure 6.16 Plot of the resistance (LHS axis) and the mass (RHS axis) of an agarose gel (0.50 % w/v) with an encapsulated microwire assembled from 50 nm diameter Ag NWs (0.50 % w/v) over time. Resistance is measured through the electrodes A-A (filled squares) and B-B (empty squares), while the mass of the film as a percentage of its initial mass is also shown (empty triangles).

The data in Figure 6.16 shows that, as discussed earlier, the resistance measured through the microwire (electrodes A-A) is approximately 3 orders of magnitude lower than the resistance measured perpendicular to the assembled microwire (electrodes B-B). This anisotropic nature of the gel remains over a period of just over 4 hours, at which point we observe a sharp rise in the resistance measured through the electrodes A-A. This rise brings the resistance measured through those electrodes close to that measured through the electrodes B-B, showing that the gel has now become isotropic with respect to its electrical character. Visual inspection of the gel after four hours revealed that cracks had formed, leaving large gaps in the gel that had led to the microwire breaking in several places. These cracks are attributed to drying effects caused by evaporation of water from the gel. We can see that the gel loses mass at quite a steady rate over the course of the four hours, with the mass dropping to approximately 65 % of its original value at the point at which the electrical anisotropy, and therefore

the integrity of the microwire, is lost. To prevent this drying effect from disrupting the microwire and causing the loss in anisotropy from the gel, we conducted another experiment in which we stored a gel with its encapsulated microwire under controlled humidity. These conditions were achieved by placing the cell in a Petri dish lined with tissue paper that had been soaked in Milli-Q water, in an attempt to either significantly slow down or stop the loss of water from the gel. The effect of this on the anisotropy of the gel is shown in Figure 6.17.

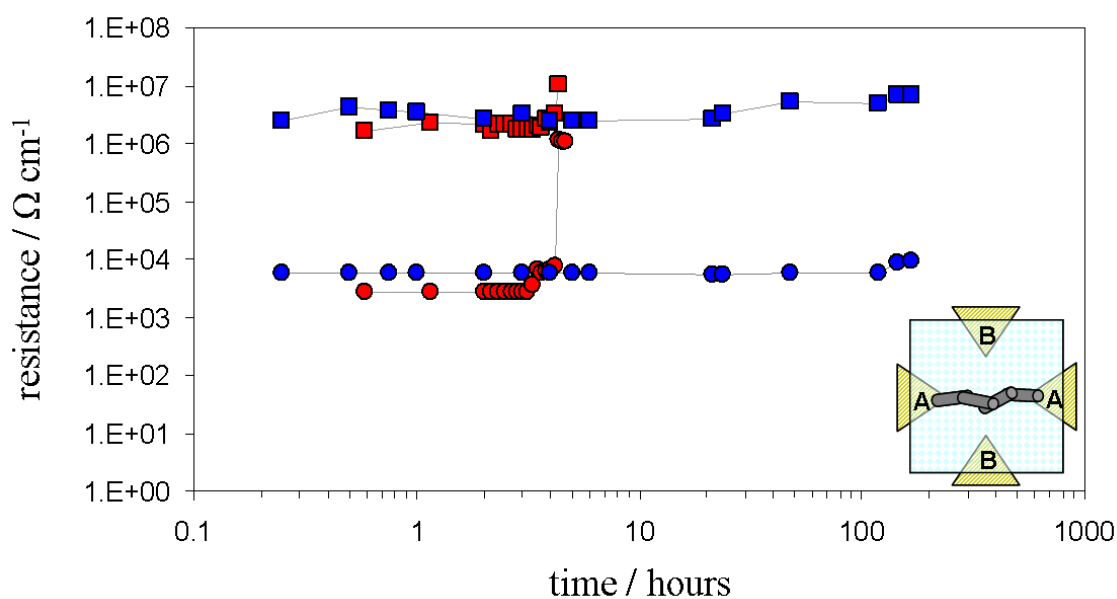


Figure 6.17 Plot of the resistance of agarose gels (0.50 % w/v) with an encapsulated microwire assembled from 50 nm Ag NWs (0.50 % w/v). Circles represent the resistance measured through the electrodes A-A, and squares represent the resistance measured through the electrodes B-B. Data in red is for a gel held at room humidity, data in blue is for a gel held in humid conditions (Petri dish lined with damp tissue paper). Inset is a schematic of the electrodes and the anisotropic gel.

The data shown in red in Figure 6.17 is that of the gel at room temperature and humidity, also shown in Figure 6.16, where the gel anisotropy was lost after approximately four hours. By placing the gel in a more humid environment however, we were able to preserve the anisotropy within the gel to over seven days. At this point

the experiment was stopped through user intervention, though the anisotropy would probably have remained for a longer period of time. This extension of the anisotropic nature of the gel is attributed to the slow down or prevention of loss of water from the gel in the more humid environment. We could not measure the mass of the film accurately, as the mass increased due to water condensing on the cell, but visual inspection by microscope showed no visible cracks in the gel, even after seven days.

We have therefore demonstrated a novel technique to arrest structures formed through DEP, by carrying out the assembly in an agarose solution above its gelling temperature and then cooling to encapsulate the assembled structure within the gel. Through this new method, we have fabricated gel materials that contain up to 99 % w/w water, but possess similar structural integrity to a solid and exhibit anisotropic electrical properties. We have studied this technique in some detail with regards to the formation of microwires assembled from Ag NWs in agarose gel, at a fixed temperature and field voltage.

6.4 Fabrication of a novel biosensor from Ag NWs assembled with DEP

The electrical anisotropy of the gels was then exploited in an attempt to fabricate a novel sensor based on these materials. This was achieved by functionalising the Ag NWs with thiolated biotin molecules, with the thiol group acting as an anchor onto the NW surface. The gel, after dielectrophoretic assembly of the functionalised NWs, was then exposed to a solution containing streptavidin, which has a high binding affinity for up to four biotin molecules. It was envisaged that streptavidin binding to the biotin might result in a change in the electrical properties through the assembled microwire, though not perpendicular to the microwire, hence the use of our electrically anisotropic gels.

6.4.1 NW functionalisation and strategy for novel biosensor fabrication

The sensor was fabricated as described in Section 6.3.1 and in Figure 6.9, using the four electrode cell shown in Figure 6.10. The novel part of the method however comes from the functionalisation of the Ag NWs with the thiolated biotin, prior to their dispersion and assembly within the agarose solution. Functionalisation was achieved through incubating the NWs (50 nm diameter, 3.0 mg) dispersed in a solution of biotin (0.50 mL, 4.225 μ M) for 24 hours. Functionalisation was monitored using UV-vis

spectroscopy, as Sastry and co-workers have previously reported a reduction in the plasmon resonance peak (at ~ 400 nm) for solutions of silver colloids functionalised with thiolated biotin.³⁰ They report that an incubation time as short as one minute is sufficient for functionalisation at a biotin concentration of $100 \mu\text{M}$, and 40 minutes at a concentration of $1 \mu\text{M}$. Therefore, 24 hours should be sufficient in this study. Figure 6.18 shows the UV-vis spectra of Ag NW dispersions, both un-functionalised and functionalised with thiolated biotin, shortly after their preparation.

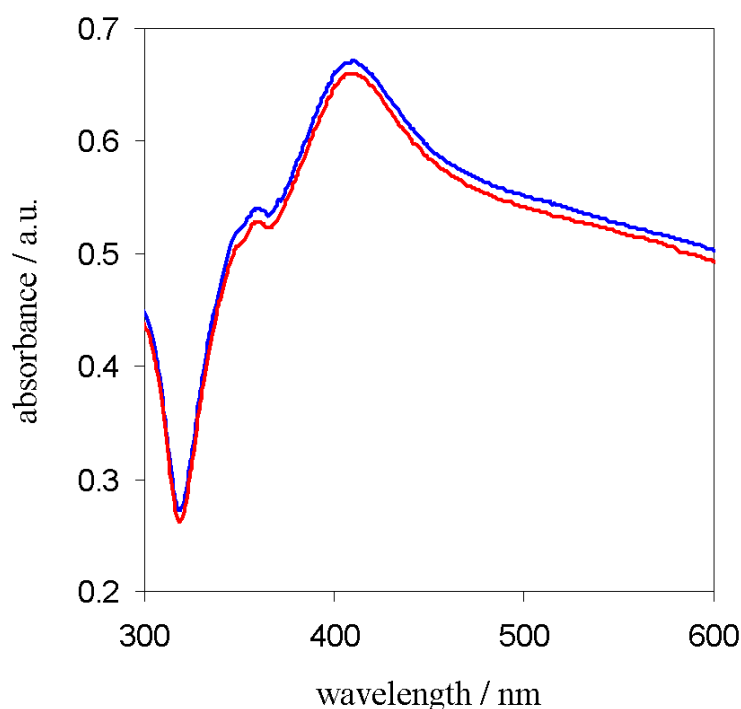


Figure 6.18 UV-vis spectra of Ag NW (50 nm diameter) dispersions, un-functionalised (blue line) and functionalised in $1 \mu\text{M}$ thiolated biotin (red line). Spectra recorded shortly after dispersion preparation.

For the biotin-functionalised Ag NWs in Figure 6.18, there is a small reduction of the peak at ~ 410 nm, suggesting a degree of functionalisation has been achieved. The results of Sastry and co-workers suggest that the degree of functionalisation increases over time, so it is envisaged that after 24 hours incubation, additional functionalisation will have taken place.

The functionalised Ag NWs were then dispersed in agarose gel, at a NW concentration of 0.50 % w/w and an agarose concentration of 0.50 % w/w.

Dielectrophoretic assembly of a continuous microwire was achieved with an AC field of 5 kHz frequency and strength of 250 V cm^{-1} . Cooling resulted in agarose gelation, entrapping the assembled, functionalised microwire and preventing its disassembly on removal of the field.

6.4.2 Sensitivity of the novel biosensor to streptavidin

The functionalised Ag NW gel showed electrical anisotropy, with a resistance of $3.1 \text{ k}\Omega \text{ cm}^{-1}$ through the electrodes A-A (through which the field was applied) and $5.67 \text{ M}\Omega \text{ cm}^{-1}$ through the electrodes B-B (perpendicular to the field). As observed with the un-functionalised Ag NWs, the resistance through the assembled microwire is around three orders of magnitude lower than it is perpendicular to the assembled microwire.

To remove excess biotin, the gel was washed by incubating the gel in 20 ml of Milli-Q water for 30 minutes. This was repeated three times, changing the water after each wash to remove the biotin from the system. The gel was then incubated in 19.5 ml Milli-Q water for 30 minutes, before streptavidin (0.1 mg) dissolved in 0.5 mL Milli-Q water was added. Figure 6.19 shows the % resistance change over the course of the three hours.

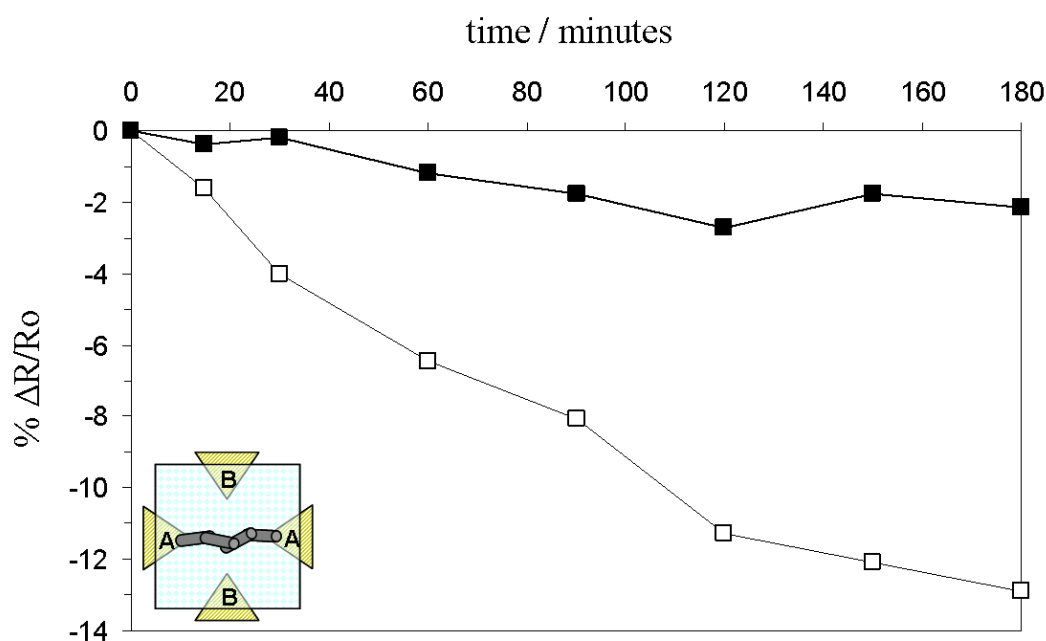


Figure 6.19 Plot showing the % change in the resistance of the agarose gel through the electrodes A-A (empty squares) and B-B (filled squares), upon exposure to streptavidin. Inset is a schematic of the electrodes and the anisotropic gel.

On the introduction of streptavidin to the solution surrounding the gel, the resistance through the electrodes A-A steadily decreased over the three hour examination period, hence the negative change in the % resistance change shown in Figure 6.19. The resistance measured through the electrodes B-B also showed a general decrease, but some rises in the resistance were also observed and the general decrease was not as large as that measured through the assembled microwire (electrodes A-A). By the end of the three hour period, the % change of the resistance through the electrodes A-A was almost 13 %, while the % change through the electrodes was just over 2 %. Clearly therefore the gel has responded to the streptavidin, but has given different responses due to the anisotropy of the gel. As the microwire is a continuous structure, we might expect that the streptavidin-biotin interaction would result in a greater change in the resistance here compared to measurements made perpendicular to the microwire, where the functionalised NWs remain as discrete or small aggregates.

We have thus demonstrated a novel sensor based on functionalised Ag NWs, assembled into microwires using DEP and entrapped within an agarose gel. The sensitivity of the gel has been shown to vary according to the electrical anisotropy of the gel, which might be attributed to the continuous and non-continuous nature of the functionalised NWs.

6.5 Assembly of yeast cell ‘strings’ through DEP in agarose gel

One of the advantages of using a gellation process to arrest the structures formed through DEP is that no functionalisation of the building blocks or substrates is required. This means that this method should find widespread use for any number of building blocks that are to be assembled into organised structures. Here, we demonstrate the viability of this method as we assemble ‘strings’ of living yeast cells. In this work the yeast cells are first coated in polyelectrolytes using the layer-by-layer (LbL) approach, and then assembled into strings of cells in a solution of a gelling agent using DEP, rather than using a template. After the gel has set, holding the cells together, the gel is exposed to a solution of the oppositely charged polyelectrolyte to the one used last to coat the cells. This is expected to act as a glue, holding the cells together so that when the gel is removed, the cells remain chained together.

6.5.1 Strategy for the assembly of yeast cell strings through DEP

Figure 6.20 shows a schematic to represent the proposed method for the fabrication of yeast cell strings, utilising the technique we have developed for dielectrophoretic assembly within a gel.

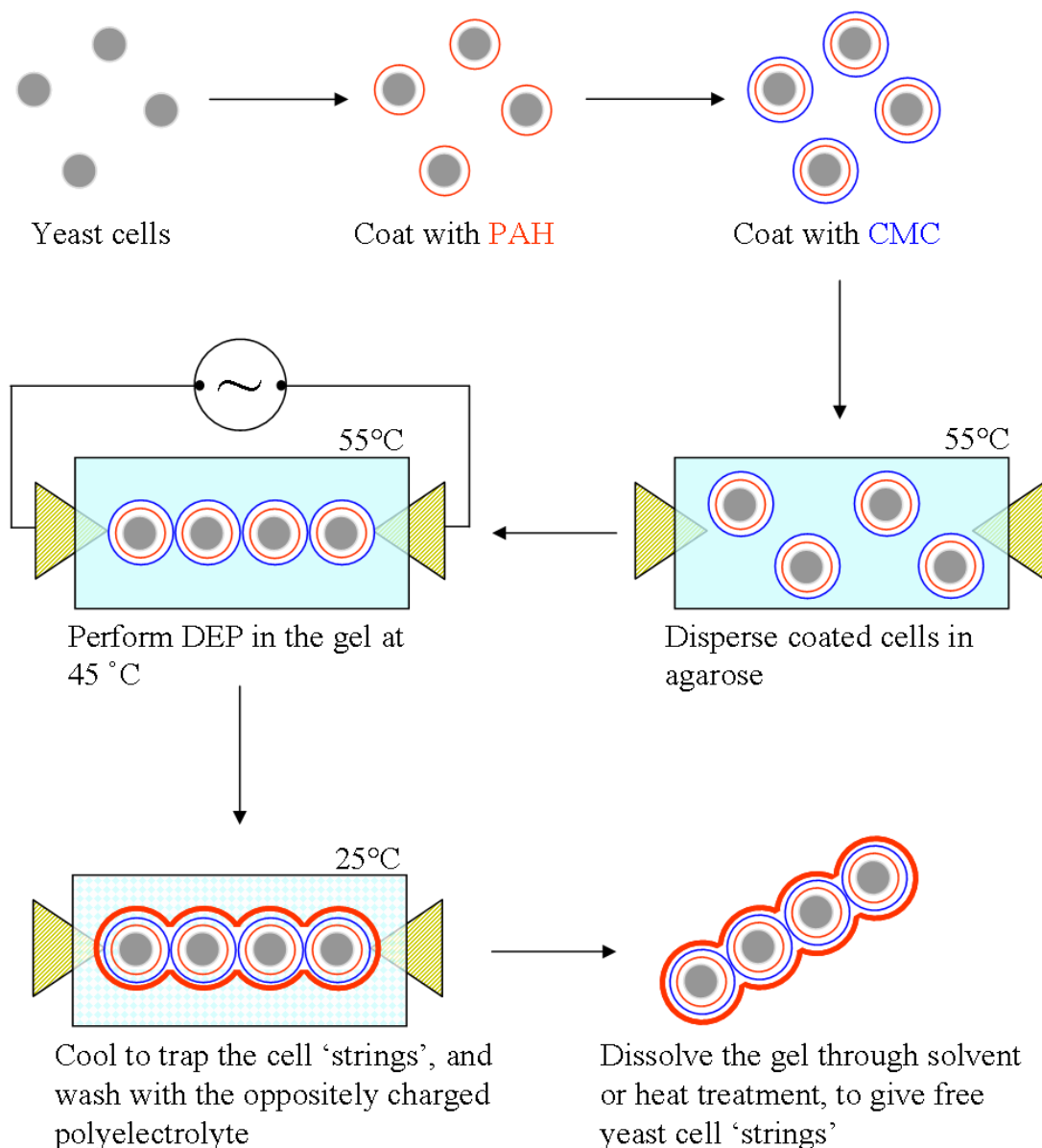


Figure 6.20 Schematic of the preparation of yeast cell ‘strings’, using dielectrophoretic assembly within a gel.

In order to produce strings of yeast cells, we first had to coat the cells with polyelectrolytes using the LbL approach. As the yeast cells carry a native negative charge, the cells were first coated in poly(allylamine hydrochloride) (PAH) and then carboxymethyl cellulose (CMCell), using an incubation, centrifugation and washing

cycle (described in Chapter 2). The yeast cells were then suspended in agarose solution, and kept at a temperature of 45 °C (the temperature could not be too high so as to harm the cells). A few drops of the yeast/agarose suspension were then introduced to the DEP cell, which was also held at 45 °C, and DEP was performed as described earlier, resulting in the yeast cells aligning to form strings. The field was then lowered while the temperature was lowered below the gelling temperature of the solution. The sample was then incubated in a solution of PAH for three hours, allowing the electrolyte to migrate through the gel and adsorb onto the assembled yeast cell strings. The gel was then washed in water, before it was dissolved with gentle heating to release the cell strings from the gel. The strings were collected and washed in water, and then tested with fluorescein diacetate (FDA), again employing a cycle of incubation, centrifugation and washing. FDA is a non-fluorescent derivative of fluorescein, which readily crosses the cell membrane due to its non-polar nature. Once inside the cytoplasm, FDA is hydrolysed by diesterase enzymes and produces a fluorescein derivative that is fluorescent. This happens only if the cellular membrane is intact. This results in the accumulation of fluorescein in living cells, which can then be visualised through fluorescence microscopy if the fluorescein is present in sufficient concentration.³¹ The strings were analysed with fluorescence microscopy, which allows the viability of the cells to be determined.

6.5.2 *DEP of yeast cells in an unmodified agarose gel*

Initial experiments were performed with the same agarose gel that was used for the encapsulation of Ag microwires. The concentration of yeast cells was 0.20 % w/v, in an agarose solution at a concentration of 0.50 % w/v agarose. The frequency of the field was fixed at 20 kHz, while the voltage between the electrodes was increased until the cells started to assemble into strings. Typical optical microscopy images of the yeast cells, aligned with DEP, are shown in Figure 6.21.

The images in Figure 6.21 show that the yeast cells align to form strings in a dielectrophoretic field. The field strength required for assembly to take place, at a frequency of 20 kHz, was approximately 600 V cm⁻¹, although raising the voltage further resulted in more rapid assembly. The string assembly started with the cells aggregating into small strings comprising two or three cells, with these small strings gradually joining together to form increasingly large assemblies.

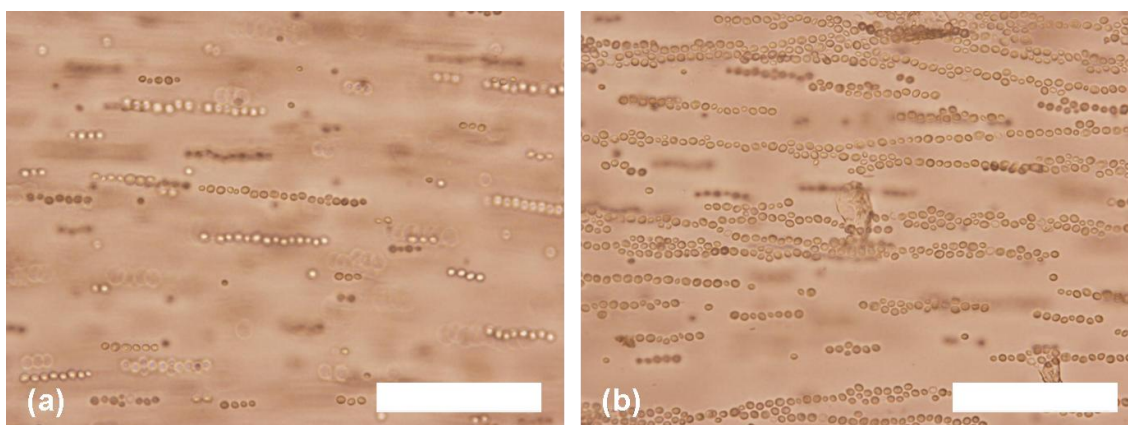


Figure 6.21 Optical microscopy images of yeast cells (0.20 % w/v) in agarose solution (0.50 % w/v) undergoing dielectrophoretic assembly (20 kHz, 600 V cm^{-1}). Images captured (a) 30 s and (b) 2 minutes after the field was applied. Scale bars $100 \mu\text{m}$ in both images.

The length of the string was dependant on the length of time that the field was applied for, as shown by the longer assemblies observed in Figure 6.21b after the field had been applied for two minutes. Eventually, two or more strings joined together to form parallel ‘belts’ of yeast cells. Yeast cells that were not coated in any polyelectrolyte did not assemble in the electric field, even at much higher field strengths. A possible explanation for this is that the formation of the strings is a result of the dielectrophoretic effect on the electric double layers of the cell. The presence of two polyelectrolyte layers deposited on the cell surface may enhance the polarisation and the magnitude of the effective dipole-dipole interactions, resulting in string formation.

After the cells assembled in chains, the field was lowered to 100 V cm^{-1} and the temperature was cooled to $25 \text{ }^\circ\text{C}$. This resulted in gelling of the agarose, which prevented the cells from moving away from each other when the field was finally removed. Such disorganisation of the yeast cells was observed in water and gels above the gelling temperature, if the field was removed. The gel maintained its structural integrity and did not break apart when it was introduced to a solution of PAH, and optical microscopy of the washed gel after three hours incubation in PAH revealed that the yeast cell strings remained intact. A problem was encountered in the next stage however, as even at a concentration as low as 0.50 % w/v agarose gel, the gel would not undergo a transition to its ‘liquid’ state unless heated in excess of $55 \text{ }^\circ\text{C}$. This meant that the yeast cells could not be removed from the gel without heating them up to a

temperature that resulted in their death. Another attempt was made to dissolve the agarose in a solution of urea, but the concentrations required (> 6 M) also proved fatal to the yeast cells. It seemed therefore that conventional agarose, although providing a good medium for dielectrophoretic assembly to take place and sufficient structural integrity to stop the assemblies from disassembling, was not suitable for the eventual release of the cell assemblies from the gel.

6.5.3 *DEP of yeast cells in a hydroxyethylated agarose gel*

The dielectrophoretic assembly of yeast cells was then attempted in another type of agarose gel, which had been modified by substituting some of the agarobiose units with a hydroxyethyl group (HE-agarose).³² Depending on the degree of substitution, the presence of hydroxyethyl groups results in a lowering of the gelling temperature (and subsequent melting temperature, though some hysteresis remains), reduction in gel strength and an increase in the optical transparency of the gel.

Dielectrophoretic assembly was carried out at a yeast cell concentration of 0.20 % w/v, and at several HE-agarose concentrations. Again, the cells were first coated in PAH and then CMCell before suspending them in a warm agarose solution. The field frequency was fixed at 20 kHz, and the temperature of the DEP cell was held at 45 °C. At an HE-agarose concentration of 0.50 % w/v the yeast cells assembled into long strings, but because of the reduction in mechanical strength, the gel at this concentration could not prevent the cells from disassembling when cooled to below the gelling temperature. At an HE-agarose concentration of 1.50 % w/v however, the solution appeared to be too viscous to allow dielectrophoretic assembly to take place even at quite high field strengths and for long time periods. Only very small assemblies, two to three yeast cells long, were assembled, though the gel now had sufficient mechanical strength to prevent the assemblies from disbanding.

A compromise between the length of the assemblies and the gel strength was reached at an HE-agarose concentration of 1.00 % w/v. Here, the cells formed strings that were on average 5 - 15 yeast cells in length, as shown in Figure 6.22.

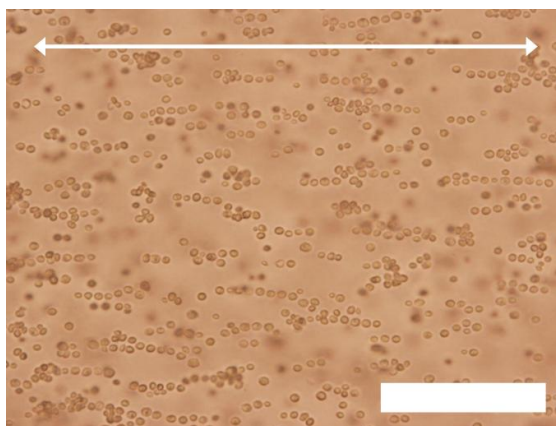


Figure 6.22 Optical microscopy images of yeast cells (0.20 % w/v) in HE-agarose solution (1.00 % w/v) undergoing dielectrophoretic assembly (20 kHz, 1250 V cm^{-1}). The field was applied for 20 minutes. Arrow denotes direction of electrodes in relation to the yeast cell assemblies. Scale bar 100 μm .

The reduction in length of the strings is attributed to the different type of agarose gel in which the dielectrophoretic assembly is being carried out. The concentration here (1.00 % w/v) is higher than that used previously (0.50 % w/v), hence the medium viscosity is higher, which inhibits movement of the yeast cells towards each other. In addition, the hydroxyethylation of the HE-agarose may alter its electrical properties, which would alter the dielectrophoretic force required for the yeast cells to assemble.

At a concentration of 1.00 % w/v the gelling temperature of the HE-agarose was approximately $17 \text{ }^\circ\text{C}$, so the sample was cooled to below this temperature to set the gel while the voltage was lowered to 100 V cm^{-1} . When the field was then removed, the cells remained chained together and did not undergo disassembly. After incubating the sample in a PAH solution for three hours, the gel was washed and then dissolved by gently heating to $45 \text{ }^\circ\text{C}$, resulting in the cell strings freeing themselves from the gel. The yeast cell strings were then separated from the agarose solution by centrifugation, and washed several times with water before incubating in an FDA solution (described in Chapter 2). The cell strings were then washed with water to remove excess FDA, and re-suspended in water. Figure 6.23 shows optical microscopy of some of the yeast cell strings, re-suspended in Milli-Q water.

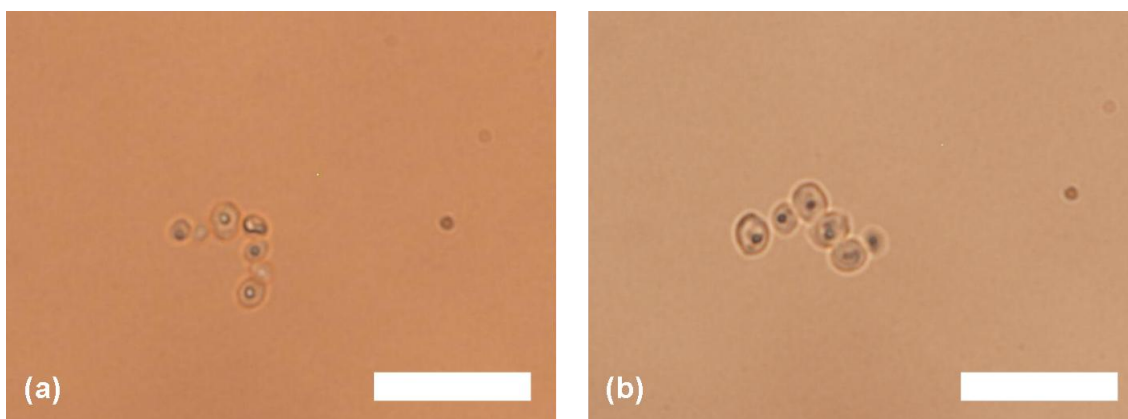


Figure 6.23 Optical microscopy images of yeast cell strings re-suspended in Milli-Q water. Scale bars 25 μm in both images.

The images in Figure 6.23 are typical of the strings that were recovered from the gels. These particular strings are seven and six yeast cells long (Figure 6.23a and b, respectively), and the average length of the strings recovered was in good agreement with the lengths of the assemblies that were being formed in Figure 6.22. This suggests that the strings are not undergoing any significant shortening, or cutting, during any part of the process (incubating in PAH, dissolving the gel, washing, incubating in FDA) after the AC electric field is switched off. Applying light pressure to the microscope cover slip caused the cell strings to move through the solution, revealing two interesting observations. One observation was that the strings were quite flexible, as they bent and wrapped around static objects that they encountered as they moved. This is demonstrated in Figure 6.23a, where the string has undergone a change in its orientation from linear to ‘L-shaped’. The second observation is that the strings also did not break apart under low shear, or as they encountered static objects, suggesting that they are well adhered together by the polyelectrolytes. Fluorescence microscopy images of the yeast cell strings, which are between six and eight yeast cells in length, are shown in Figure 6.24.

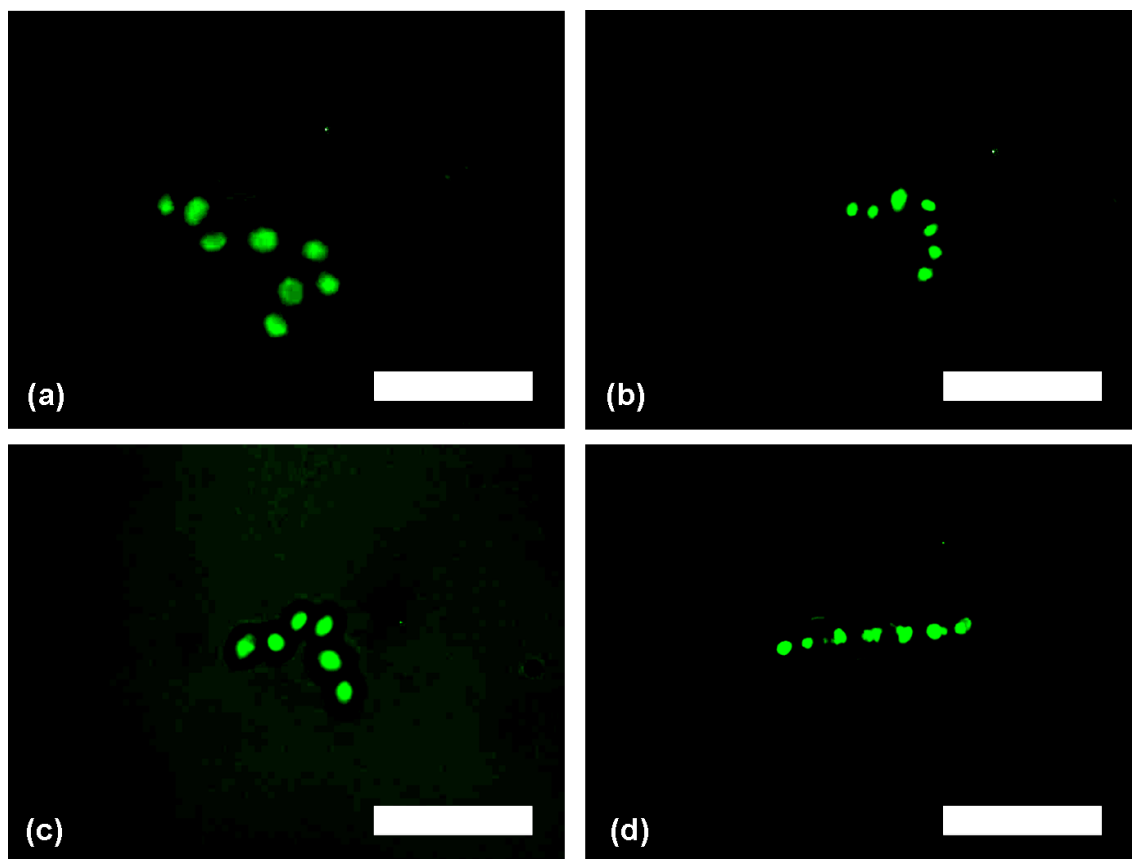


Figure 6.24 Fluorescence microscopy images of yeast cell ‘strings’, stained with FDA and re-suspended in water. Scale bars 25 μm in all images.

In Figure 6.24 we can see that the yeast cells in the strings are all emitting a bright green light, indicating the presence of fluorescein within the cells. This in turn suggests that the cells are still vital, and have not been harmed by the electric field or at any other stage in the process of assembling the cells together into strings.

We have thus demonstrated that the technique developed for assembling and encapsulating building blocks in agarose solution can be applied to the assembly of strings of yeast cells. So far we have only been able to release short strings from the gel (no more than ten yeast cells in length), though the assembly of much longer strings, which we were not able to release from the gel without damaging the cells, has also been achieved. It therefore remains a challenge in the future to remove these longer yeast cell strings from the gel successfully. These cell strings can be considered as a first step towards the assembly of artificial multicellular organisms.

6.6 Conclusions

With a view to carrying out dielectrophoretic assembly of nano- and micro-building blocks within agarose solutions, we have studied the effects that an applied AC electric field (5 kHz, 500 V cm^{-1}) has on the gelling transition of agarose gel. It was found that the field appeared to induce optical anisotropy in the agarose gel when it was applied, but that this anisotropy was lost over a short period of time after the field was switched off. Initial results suggested that the agarose gelling transition was shifted to lower temperature in the presence of the electric field, though this shift was later attributed to a fast cooling rate, which gave the impression that the gelling transition was shifted. Measurements at a slower cooling rate showed that the AC field did not have a profound effect on the gelling temperature, though its presence slowed down the gelling, *i.e.* it has a kinetic effect on the gelling of agarose. By performing the dielectrophoretic assembly of silver microwires within an agarose solution above its gelling temperature, followed by gelling of the agarose to encapsulate the microwires, we prevented them from disassembling when the field was removed. This represents a novel method for arresting the structures fabricated through dielectrophoretic assembly, without the need to modify the building blocks (Ag NWs) or the substrate in any way. By fixing the field frequency and temperature of the cell we were able to construct a microwire growth diagram, comparing the assembly of microwires at various combinations of agarose and NW concentration, and at each NW diameter. This revealed that the assembly and encapsulation of a microwire was dependant on the concentration of both the NWs and the agarose, with assemblies formed at intermediate concentrations of each. With the assembly of a microwire, the resistance through the gel was lowered by three to four orders of magnitude when compared to the resistance measured perpendicular to the microwire formation. We have thus created hydrogels that display electrical anisotropy, which can be sustained for several hours at ambient room conditions. We were able to extend in the gel anisotropy for up to seven days by storing the gel in humid conditions to prevent drying.

Following these findings we were then able to fabricate a novel sensor based on these anisotropic gels, by functionalising the NWs prior to their assembly with thiolated biotin. These functionalised NWs thus formed a continuous sensing element throughout the gel when assembled using DEP, which showed a measurable decrease in the resistance when exposed to a complementary molecule, streptavidin. The response

perpendicular to the microwire was not so large, emphasising the anisotropic nature of the gels. We then showed that the method developed could be used to align and encapsulate yeast cells, so that they formed strings of cells entrapped in the gel. By functionalising the cells with polyelectrolytes before and after their alignment and then dissolving the gel, we could release free-standing yeast cell strings, which we have shown are still vital following this treatment. This demonstrates the applicability of this method that we have developed for other systems, and is also an interesting development towards producing living multi-cellular assemblies. This can be considered as a practical step towards the assembly of a simple multicellular organism of living cells.

6.7 References

- 1 Pohl, H. A., *J. Appl. Phys.*, 1951, **22**, 869.
- 2 Pohl, H. A., *J. Appl. Phys.*, 1958, **29**, 1182.
- 3 Dimaki, M. and Bøggild, P., *Nanotechnology*, 2004, **15**, 1095.
- 4 Huang, Y. and Pethig, R., *Measur. Sci. Technol.*, 1991, **2**, 1142.
- 5 Wang, X.-B., Yang, J., Huang, Y., Vykoukal, J., Becker, F. F. and Gascoyne, P. R. C., *Anal. Chem.*, 2000, **72**, 832.
- 6 Hermanson, K. D., Lumsdon, S. O., Williams, J. P., Kaler, E. W. and Velez, O. D., *Science*, 2001, **294**, 1082.
- 7 Barsotti Jr, R. L., Vahey, M. D., Wartena, R., Chiang, Y.-M., Voldman, J. and Stellaci, F., *Small*, 2007, **3**, 488.
- 8 Gierhart, B. C., Howitt, D. G., Chen, S. J., Smith, R. L. and Collins, S. D., *Langmuir*, 2007, **23**, 12450.
- 9 Ozturk, B., Blackledge, C., Flanders, B. N. and Grischkowsky, D. R., *Appl. Phys. Lett.*, 2006, **88**, 073108.
- 10 Bernard, L., Calame, M., van der Molen, S. J., Liao, J. and Schönenberger, J., *Nanotechnology*, 2007, **18**, 235202.
- 11 Wissner-Gross, A. D., *Nanotechnology*, 2006, **17**, 4986.
- 12 Tang, J., Gao, B., Geng, H., Velez, O. D., Qin, L.-C. and Zhou, O., *Adv. Mater.*, 2003, **15**, 1352.
- 13 Tang, J., Yang, G., Zhang, Q., Parhat, A., Maynor, B., Liu, J., Qin, L.-C. and Zhou, O., *Nano Lett.*, 2005, **5**, 11.
- 14 Suehiro, J., Hidaka, S.-I., Yamane, S. and Imasaka, K., *Sensor. Actuat. B-Chem*, 2007, **127**, 505.
- 15 Papadakis, S. J., Gu, Z. and Gracias, D. H., *Appl. Phys. Lett.*, 2006, **88**, 233118.
- 16 Liu, J. and Rörgren, R., *J. Electron. Manufact.*, 1993, **3**, 205.
- 17 Ramkumar, S. M. and Srihari, K., *J. Electron. Pack.*, 2007, **129**, 149.
- 18 Jin, S., Tiefel, T. H., Wolfe, R., Sherwood, R. C. and Mottine Jr, J. J., *Science*, 1992, **255**, 446.
- 19 Jin, S., Tiefel, T. H. and Wolfe, R., *IEEE Trans. Magn.*, 1992, **28**, 2211.
- 20 Chen, C. L., Sun, L., Tanase, M., Bauer, L. A., Hultgren, A., Silevitch, D., Meyer, G. J., Searson, P. C. and Reich, D. H., *J. Magn. Magn. Mater.*, 2002, **249**, 146.

-
- 21 Agarwal, R., Ladavac, K., Roichman, Y., Yu, G., Lieber, C. M. and Grier, D. G., *Opt. Express*, 2005, **13**, 8906.
- 22 Shang, L., Clare, T. L., Eriksson, M. A., Marcus, M. S., Metz, K. M. and Hamers, R. J., *Nanotechnology*, 2005, **16**, 2846.
- 23 Snoswell, D. R. E., Brill, R. K. and Vincent, B., *Adv. Mater.*, 2007, **19**, 1523.
- 24 www.Isbu.ac.uk, checked 25th April 2009.
- 25 Labropoulos, K. C., Niesz, D. E., Danforth, S. C. and Kevrekidis, P. G., *Carbo. Polym.*, 2002, **50**, 393.
- 26 Narayanan, J., Xiong, J.-Y. and Liu, X.-Y., *J. Phys.: Conf. Ser.*, 2006, **28**, 83.
- 27 Powell, R. L., *J. Stat. Phys.*, 1991, **62**, 1073.
- 28 Powell, R. L., Morrison, T. G. and Milliken, W. J., *Phys. of Fluids*, 2001, **13**, 588.
- 29 Small, W. R. and Paunov, V. N., *J. Mater. Chem.*, 2008, **18**, 2082.
- 30 Sastry, M., Lala, N., Patil, V., Chavan, S. P. and Chittiboyina, A. G., *Langmuir*, 1998, **14**, 4138.
- 31 Chrzanowski, T. H., Crotty, R. D., Hubbard, J. G. and Welch, R. P., *Microb. Ecol.*, 1984, **10**, 179.
- 32 SeaPrep® Agarose product information sheet, Lonza, www.lonza.com, checked 25th April 2009.

CHAPTER 7

MAIN CONCLUSIONS AND FUTURE WORK

7.1 Main conclusions

The main objective of this thesis has been to develop novel sensors based on nanomaterials, which will contribute to a deeper understanding of how these materials can be incorporated into applications that make use of their exceptional qualities. This thesis has presented work showing that novel sensors have been fabricated, comprising nanomaterials such as carbon nanotubes (CNTs) and silver nanowires (Ag NWs), using diverse techniques such as inkjet printing and dielectrophoretic assembly. As well as describing the fabrication and characterisation of these novel sensors, we also aimed to study other aspects regarding the development of nanomaterials as components in sensors. The synthesis of nanomaterial composites and the interactions between nanomaterials and functional dispersants have been studied, which are of importance for understanding sensing mechanisms and attaching functional groups to sensors. Solution-based processing methods for sensor fabrication have also been studied, such as deposition of a sessile drop onto a substrate, inkjet printing and dielectrophoretic assembly.

Chapter 3: Thin films comprising single wall carbon nanotubes (SWNTs) have been fabricated, by dispersing SWNTs in aqueous sodium dodecyl sulphate (SDS) solutions, and then depositing sessile drops of the dispersions onto different substrates and allowing the solvent to evaporate. It was found that two of the factors that affect the morphology of the films and distribution of CNTs within the film are the state of the dispersion and the hydrophobicity of the substrate. Aggregates in as-prepared dispersions pin the contact line, resulting in circular deposits of nanotubes at the perimeter of the drop, similar in appearance to ‘coffee-stains’. Removal of these aggregates allows the contact line to recede unimpeded, resulting in the formation of a film. The hydrophobicity of the substrate also greatly affects both the size and morphology of the films, due to the different drop sizes formed initially and the

subsequent drying mechanisms. Films on hydrophilic substrates have a heterogeneous morphology, and appear to be susceptible to gravity-induced pinning or pinning by a single aggregate. Films on hydrophobic substrates are more homogeneous, due to the apparently more uniform motion of the contact line during evaporation of the drop.¹ These findings may prove to be useful not just in CNT processing, but in any situation where a dispersion of solid particles is deposited on a substrate, a process which forms the base of many solution-based fabrication techniques.

Chapter 4: This chapter describes the synthesis and characterisation of three different CNT composites, prepared with conducting polymers. Polyaniline (PAni)-MWNT composites have been prepared with *in situ* polymerisation, where optical activity in the composites has been generated during the polymerisation, rather than by post-synthesis treatment of the composite. These composites are soluble in organic solvents, show optical activity both in solution and as supported films and have enhanced thermal properties due to the presence of the nanotubes.²

A water soluble polymer, poly(2-methoxyaniline-5-sulfonic acid) (PMAS), was employed to see which of the properties of the CNTs, such as their diameter or graphitisation, most affected their ability to become dispersed. This was also carried out through ultrasonic mixing, characterising the extent of nanotube dispersability by studying the absorption spectra of the dispersions as they underwent increasing amounts of mixing. Although no real trend was observed with respect to the ease of nanotube dispersability on their properties, multi wall carbon nanotubes (MWNTs) produced by the chemical vaporur deposition (CVD) method were found to be become dispersed with the least amount of mixing required. They were also the most stable with regards to aggregation, compared to dispersions with SWNTs prepared by the ‘high pressure decomposition of carbon monoxide’ (HiPco) method.

While the synthesis of water soluble PMAS-CNT composites prepared through *in situ* polymerisation was not possible, a composite prepared from the polymerisation of PAni in the presence of PMAS-stabilised MWNTs was achieved. Using this method, high loading fractions of MWNTs could be achieved in the composites (up to 32.0 % w/w) which showed good stability to aggregation. Supported films of the composites also showed that they retained electroactivity and, due to the presence of the nanotubes, increased conductivity.³

Chapter 5: This chapter describes the development of inkjet printing as a method for processing CNT composite dispersions into films with interesting properties. Gellan gum is an efficient dispersant for CNTs, stabilising dispersions at concentrations that are an order of magnitude lower than required for the dispersant SDS. This has been attributed to gellan gum forming a loose structural network throughout the dispersion that physically separates the nanotubes, rather than adsorbing to their surfaces in a dense layer like SDS. Through the addition of NaOH and, to an extent NaCl, the amount of CNTs dispersed was further improved by manipulating the charge of the gellan gum chains. Gellan gum-CNT films printed with a desktop printer showed excellent transparency and sensitivity to water vapour.⁴

PMAS-CNT films show sheet resistances of approximately $130 \text{ k}\Omega \text{ cm}^{-1}$ for a *single* printed layer. We have shown that these films are also sensitive to alcohol vapours, showing a linear response to increasing vapour concentration.⁵ These films therefore can be used in sensing devices. PMAS-PAni-MWNT composites prepared with high nanotube loading fractions have also been printed, using a Dimatix Materials Printer rather than an ordinary desk-top printer. These composites did not need filtering prior to printing, ensuring that the same fraction of nanotubes present in the dispersion was transferred to the substrate. These printed films showed the lowest sheet resistance of inkjet printed CNT films to date (to the best of the authors knowledge), of approximately $500 \Omega \text{ cm}^{-1}$. They also displayed electroactivity, and at low nanotube loading fractions, electrochromic behaviour.

Chapter 6: This chapter reports the novel use of dielectrophoretic assembly carried out within the confines of a gelling solution as a tool to assemble nanomaterials. By performing the assembly in agarose solution above its gelling temperature, and then cooling to below this point, it is possible to prevent the assembled structures from undergoing disassembly due to Brownian motion when the electric field is removed. This has led to the dielectrophoretic alignment and assembly of Ag NWs in agarose solution, and we have studied this assembly at a range of agarose and nanowire concentrations to produce a ‘microwire growth diagram’ for this system. In achieving this assembly, hydrogels that have very high water content but which display electrical anisotropy have been fabricated, where the anisotropic resistance of the gel differs by three to four orders of magnitude. These anisotropic gels can retain their structure, and hence electrical anisotropy, for several hours in ambient conditions, and up to a week if

they are kept in humid environments.⁶ It was then shown that these novel gel materials can act as sensors, when the building blocks are first functionalised with appropriate functional groups. This was demonstrated by attaching thiolated biotin molecules to the Ag NW building blocks, and then exposing the assembled microwires to streptavidin, to which biotin has a high binding affinity. Our sensor displayed a high electrical conductivity through the assembled microwire, but a much lower conductivity when measured at 90° to the assembled microwire.

This novel method of assembling structures by using dielectrophoresis was then applied to yeast cells, which have been assembled into ‘strings’ of linearly connected cells followed by gelling of the continuous phase. The cells were first coated with polyelectrolytes which acted as a coating to which an oppositely charged polyelectrolyte could be used to lock the cells together, following cell assembly but before their release from the gel. The cell strings were then incubated in fluorescein diacetate so that the viability of the cells could be determined, and it was found that the cells are still vital after their treatment with the polyelectrolytes and subsequent dielectrophoretic assembly. This can be considered as a practical step towards the assembly of a simple multicellular organism of living cells based on this assembly method.

7.2 Future work

The research described in this thesis has raised a number of interesting questions. For instance, while we have addressed the effects of substrate hydrophobicity and dispersion state (*i.e.* with or without aggregates) on the formation of CNT films from evaporating drops, there are other factors to consider. Other surfactants could be employed to disperse the nanotubes, to see if the presence of a surfactant film is essential for nanotube deposition over the entire drop area. It would also be of interest to investigate whether larger dispersed particles might become aligned in the linear assemblies formed by the surfactant perpendicular to the drop contact line, as this may provide a simple route to self assembly.

Inkjet printing and the CNT dispersions used in this process could be further developed, to enhance the transparency and sheet resistance of these films so that they can be used in electrically transparent coatings. The sensing mechanism of the printed films with conducting polymers should also be further investigated, as greater understanding might allow sensing of other analytes and at lower concentrations.

Actuators are one of the most exciting potential applications of both conducting polymers and CNTs, and so it would also be of interest to employ inkjet printing as a method to quickly and reproducibly fabricate thin film actuators.

The dielectrophoretic assembly of nanomaterials and their entrapment within a gel is an area that could potentially find use in a number of different areas. We have shown that they can be used as sensors, and further development could be aimed at increasing the sensitivity and response times of these materials. The study of different analytes and functional groups would also be of interest, perhaps combining more than one functional group on the surfaces of the building blocks. As the study with yeast cells showed, this technique can readily be applied to other building blocks, and it might be desirable to fabricate even longer, perhaps branched, assemblies or strings with two or more different types of cells. These might then be used for studying intercellular transfer, where exchanges or processes occurring between adjacent cells takes place.

7.3 References

- 1 Small, W. R., Walton, C. D., Loos, J. and in het Panhuis, M., *J. Phys. Chem. B*, 2006, **110**, 13029.
- 2 Sainz, R., Small, W. R., Young, N. A., Vallés, C., Benito, A. M., Maser, W. K. and in het Panhuis, M., *Macromolecules*, 2006, **39**, 7324.
- 3 Small, W. R., Masdarolomoor, F., Wallace, G. G. and in het Panhuis, M., *J. Mater. Chem.*, 2007, **17**, 4359.
- 4 in het Panhuis, M., Heurtematte, A., Small, W. R. and Paunov, V. N., *Soft Matter*, 2007, **3**, 840.
- 5 Small, W. R. and in het Panhuis, M., *Small*, 2007, **3**, 1500.
- 6 Small, W. R. and Paunov, V. N., *J. Mater. Chem.*, 2008, **18**, 2082.